Chemical Looping Combustion of Victorian Brown Coal using Fe-based Oxygen Carriers

Sharmen Rajendran

B.Eng (Honours) in the field of Chemical Engineering

Monash University

A thesis submitted in fulfilment of the requirements for the degree of

Doctor of Philosophy

Department of Chemical Engineering

Monash University

August 2015

Declaration

I hereby declare that this thesis contains no material which has been accepted for the award of any degree or diploma at any university or other equivalent institution.

To the best of my knowledge and belief, this thesis contains no material previously published or written by another person, except when due reference is made in the text of the thesis.

Sharmen Rajendran

Department of Chemical Engineering

Monash University

31st August 2015

Notice 1

Under the Copyright Act 1968, this thesis must be used only under normal conditions of scholarly fair dealing. In particular no results or conclusions should be extracted from it, nor should it be copied or closely paraphrased in whole or in part without the written consent of the author. Proper written acknowledgement should be made for any assistance obtained from this thesis.

Notice 2

I certify that I have made all reasonable efforts to secure copyright permissions for third-party content included in this thesis and have not knowingly added copyright content to my work without the owner‘s permission.

Acknowledgements

I would like to dedicate this thesis to my Lord and Saviour Jesus Christ as I would not have gotten the opportunity to undertake and complete this PhD without Him. Only He has granted me the ability to persevere through this trialling journey. I would like to thank my family (Mr Rajendran Ramachandran, Mrs Elizabeth Vasanthi Hunt, Ms Theresa Rajendran and Ms Joyce Rajendran) for their support over the course of my PhD.

Next, I would like to thank my supervisor, Professor Sankar Bhattacharya, for his guidance and Professor Klaus Hein for his inputs during the initial stages of my PhD. I graciously acknowledge Dr Wei Lit Choo and Dr Maggie Chen for their help during my candidature. I would also like to acknowledge the assistance from the members of my research group. In particular, I would like to thank David Stokie for being the best officemate and Makarios Wong for being a helpful junior CLC student. Brown Coal Innovation Australia, Energy Australia, the Department of Chemical Engineering and Monash University are graciously acknowledged for their financial support for this project and for my living allowance. I would like to acknowledge the individuals from the aforementioned bodies who have assisted me during my PhD: Dr Phil Gurney, David McManus, Geoffrey Gay, Dr Steve Pascoe, Jill Crisfield, Lilyanne Price, Rebecca Bulmer, Kim Phu, Ronald Graham, Harry Bouwmeester, Martin Watkins, Ross Ellingham, Chloe Priebee, Gamini Ganegoda, Mark Symonds, Garry Thunder and Paurnami Chandran. I would also like to thank the Dr Xi-Ya Fang, Dr Flame Burgmann, Renji Pan and Dr Russell King at Monash Centre for Electron Microscopy for their help with the use of the electron microscopes. I am grateful to the Australian Synchrotron for giving me the opportunity to use their facilities and am thankful for the assistance I obtained from Dr Helen Maynard-Casely and Dr Justin Kimpton. I would also like to thank Professor Rui Xiao for allowing me to use the facilities at Southeast University, China. I would like to take this opportunity to thank Shuai Zhang and Tove Karlsson for being excellent colleagues in the field of Chemical Looping Combustion. I am also grateful for the assistance I obtained from the following summer research students: Ashley Jake Marshall, Marthinus Stephanus Jacobs, William Huggett, Jonathan Leung and Shaun Lim. I would also like to acknowledge my church family and growth group members for being highly supportive through my PhD.

Abstract

The vast reserves of Victorian brown coal (VBC), over 400 years at the current rate of consumption, is predominantly used for power generation with over 80% of Victoria's electricity generated from the combustion of this fuel. This results in the emission of vast amounts of greenhouse gases such as CO_2. Hence, it is important to investigate carbon dioxide capture and storage technologies for use in power stations employing fossil fuels.

Chemical Looping Combustion (CLC) is an emerging CO_2 capture technology which is capable of inherently capturing CO_2. In CLC, the Oxygen Carrier (OC) provides the oxygen for the combustion of the fuel hence eliminating dilution with N_2 from air. Once the oxygen in the OC is depleted, it is regenerated through oxidation in air and is then sent back to react with another batch of fuel. The vast majority of research in the field of CLC has been focussed on gaseous fuels such as natural gas and syngas due to the simplicity of such a process. In recent times, there has been a shift towards the use of solid fuels due to their abundance, widespread availability and lower cost. As such, there are a number of gaps in the field of CLC employing solid fuels; additionally, the only information relating to CLC of VBC is limited to experiments using small scale laboratory equipment. This thesis serves to fill some of the gaps in the field of VBC-fuelled CLC.

The first study investigated the effect of inherent coal minerals on the performance of a CLC system; a high ash Canadian lignite was also used as part of this comparative study. The results highlighted that the low ash VBC was more suitable for use as a fuel in CLC as it was highly reactive and its low ash content led to a smaller amount of ash deposition on the OC.

The second study involved using synchrotron radiation to perform in-situ X-ray Diffraction studies of a VBC-fuelled CLC process to understand both the changes that the OC undergoes as part of the redox reaction as well as carbon deposition on the OC. The results showed that the reduction of Fe_2O_3 beyond Fe_3O_4 was not favourable over long periods of time when using CO_2 as the gasification agent as it led to carbon deposition on the OC.

The third study is a first-of-its-kind investigation, where the reduction kinetics of an Fe-based OC was determined in the presence of a char derived from VBC. The Shrinking Core Model (SCM) and the Modified Volume Reaction Model (MVRM) were used to model the reduction of the OC. The results showed that both models were capable of predicting the reduction of Fe_2O_3 in the presence of a solid fuel. The calculations also verified that the rate limiting step in CLC was that of char gasification.

The fourth study investigated the effect of the reactor configuration on the performance of the CLC system as such a comparison has never been attempted. A fluidized bed reactor, an atmospheric fixed bed reactor and a pressurized fixed bed reactor operated at 5 bar were used. The amount of the fuel and the OC together with the flow rates of the gases were kept constant so that the results from the different setups could be compared accurately. It was found that using the fluidized bed reactor allowed for the fastest gasification of the fuel due to better contact between the gasification agent and fuel. Although the CO_2 yield and carbon conversion in the fluidized bed reactor was lower compared to the other two fixed bed reactors, it is expected that the use of a circulating fluidized bed (CFB) reactor with cyclones, a carbon stripper and a taller expanded freeboard would improve these two parameters.

The fifth study involved fabricating and trialling 18 synthetic OCs in which NiO, CuO and Mn_2O_3 were supported on Fe_2O_3. This was done as most studies in literature utilize an inert support that is not able to take part in the redox reaction; as such a greater quantity of the OC is needed to provide the necessary oxygen. The results highlight that impregnated OCs were more reactive relative to their physically mixed counterparts. The use of high levels of CuO should be avoided as it led to the defluidization of the bed. Although NiO performed well, it may not be suitable for use due to its toxicity. Taking numerous considerations into account, the use of Mn_2O_3 was recommended as it led to a synergistic effect with Fe_2O_3.

The sixth and final study of this thesis utilized a 10 kW_{th} alternating fluidized bed reactor to trial the performance of VBC in a large scale reactor. A number of studies on the effects of temperature, fuel type, OC particle size range and long term operation on the performance of the CLC system were done. The NO_x emissions were quantified and a carbon balance was also performed. The NO_x emissions were found to average around 25 ppm over the course of the reduction reaction. Based on the carbon balance, 6.8% of the introduced carbon was unaccounted for due to the low capture efficiency of the cyclones. The optimum parameters were found to be 900°C for the temperature, 150-350 µm for the OC particle size range and VBC for the fuel. The average carbon conversion and CO_2 yield over 35 reduction reactions was found to be 86% and 81% respectively for the conditions optimized for this reactor setup.

These studies show that the use of Fe-based OCs is highly promising with VBC. The main recommendation from this thesis is the use of VBC in a CFB reactor as this is expected to significantly improve the carbon conversion and CO_2 yield.

List of Abbreviations

AAEM	Alkali and Alkaline Earth Metal
AR	Air Reactor
ASAP	Accelerated Surface Area and Porosimetry
ASTM	American Society for Testing and Materials
ASU	Air Separation Unit
BET	Brunauer, Emmett and Teller
CFB	Circulating Fluidized Bed
CFD	Computational Fluid Dynamics
CGSM	Changing Grain Size Model
CIF	Crystallographic Information File
CLC	Chemical Looping Combustion
CLOU	Chemical Looping with Oxygen Uncoupling
CVRD	Companhia Vale do Rio Doce
EDS	Energy Dispersive X-ray Spectroscope
FR	Fuel Reactor
GC	Gas Chromatography
HPLC	High Performance Liquid Chromatography
iG-CLC	in-situ Gasification Chemical Looping Combustion
IPCC	Intergovernmental Panel on Climate Change
MEA	Monoethylamine
Me_xO_y	Oxidized Oxygen Carrier
Me_xO_{y-1}	Reduced Oxygen Carrier
MFC	Mass Flow Controller
MVRM	Modified Volume Reaction Model
NMR	Nuclear Magnetic Resonance
OC	Oxygen Carrier
SCM	Shrinking Core Model
SCMg	Shrinking Core Model in the grains
SEM	Scanning Electron Microscope
TGA	Thermogravimetric Analyzer
VBC	Victorian Brown Coal
XRD	X-ray Diffraction
XRF	X-ray Fluorescence

List of Symbols

Δt	Incremental time (s)
Δm	Mass loss/gain over Δt (kg)
$\overline{b}$	Stoichiometric coefficient for reaction of the reducing gas with the OC
C_g	Gas concentration
E_a	Activation energy (kJ/mol)
f_i	Instantaneous gas fraction
G_r	Global reduction rate (s^{-1})
k	Reaction rate ($mol^{1-n}m^{3n-2}s^{-1}$)
K_{eq}	Equilibrium constant
k_o	Pre-exponential factor ($mol^{1-n}m^{3n-2}s^{-1}$)
m	Instantaneous mass at any point during the reduction (kg)
m_f	Final mass of the sample in the crucible (kg)
m_i	Initial mass of the sample in the crucible (kg)
m_o	Mass of the fully oxidized OC (kg)
m_r	Mass of the fully reduced mixture containing coal, ash and the OC (kg)
n	Reaction order
$n_{c,coal}$	Amount of carbon in coal (mol)
R	Universal gas constant (J/mol.K)
r_c	Carbon conversion rate (s^{-1})
r_g	Gasification rate (s^{-1})
r_g	Grain radius of Fe_2O_3 (m)
r_{inst}	Instantaneous reaction rate (s^{-1})
R_o	Oxygen carrying capability
T	Temperature (°C/K)
X	Conversion
X_c	Carbon conversion
x_i	Molar fraction of species i
X_o	Fractional oxidation
X_r	Fractional reduction
ρ_m	Molar density of Fe_2O_3 (mol/m^3)
τ	Time for complete conversion of solids (min)
Ω_{OD}	Oxygen demand

Table of Contents

List of Figures

List of Tables

Chapter 1 Introduction

Climate change is a real global problem and is caused by a multitude of factors, one of which is greenhouse gas emissions from the combustion of fossil fuels. As such, solutions are needed to prevent catastrophic and irreversible changes to the environment. Since CO_2 represents the largest anthropogenic greenhouse gas emissions and that the largest point-source of CO_2 emissions is the combustion of fossil fuels, these emissions have to be curtailed. While the obvious solution is to phase-out the use of carbon intensive fossil fuels, this will not be possible in the near future as alternative power generation technologies have not matured and are still very costly. Additionally, power generation from options such as wind, solar, nuclear and renewables are promising but complete reliance on these for power generation will not be a reality for the coming decades. Also, fossil fuels are comparatively cheaper and relatively abundant across the globe. Therefore, if fossil fuels are to be used for power generation, ways to capture the generated CO_2 and store it away from the atmosphere is necessary.

This chapter will provide an introduction to carbon dioxide capture and storage followed by potential solutions, including Chemical Looping Combustion, as well as an introduction to the fuel of interest, Victorian brown coal.

1.1 Carbon Dioxide Capture and Storage

The concept of carbon dioxide capture and storage involves separating CO_2 and storing it in reservoirs away from the atmosphere. This is a promising concept to prevent the release of excessive anthropogenic CO_2 into the atmosphere, which would then inhibit its contribution to the greenhouse effect. Ideally, this allows fossil fuels to be used without adversely affecting the climate. The steps which are involved include sequestration, transportation and storage of CO_2. This is currently being trialled in various parts of the world due to its efficacy in reducing the impact on climate change while decelerating the increase in atmospheric CO_2.

1.1.1 CO_2 Capture

The primary aim of CO_2 capture is to obtain high purity CO_2 so that additional separation steps further downstream are not necessary before transportation and storage. Three main routes have been proposed to capture the generated CO_2 from power stations utilizing fossil fuels and this can be found in Figure 1-1. The three categories are post-combustion capture, pre-combustion capture and oxyfuel combustion. These are described below:

Post-combustion:

The generated CO_2 is separated from the flue gas and captured after the combustion process. Post-combustion capture systems can be retrofitted to currently available power stations without requiring much alteration to the design. Examples of this technology include absorption, adsorption and membranes.

Pre-combustion:

The carbon that is present in the fuel is separated prior to combustion. This is done either via steam reforming or partial oxidation of the fuel to generate syngas containing CO and H_2. The water-gas shift reaction is then employed to convert the CO to CO_2 while reducing the steam to H_2. Once the CO_2 has been separated, the H_2 can then be used as a carbon-free fuel.

Oxyfuel combustion:

In this process, oxygen is mixed with steam and CO_2 instead of air. This gas mixture is then introduced into the reactor to combust the fuel. In this method, N_2 is not present at the inlet and is thus absent in the flue gas. Hence, the gas at the outlet consists mostly of CO_2 and steam, of which the latter can be condensed out. The oxygen is typically obtained using a cryogenic Air Separation Unit (ASU), which is a costly operation.

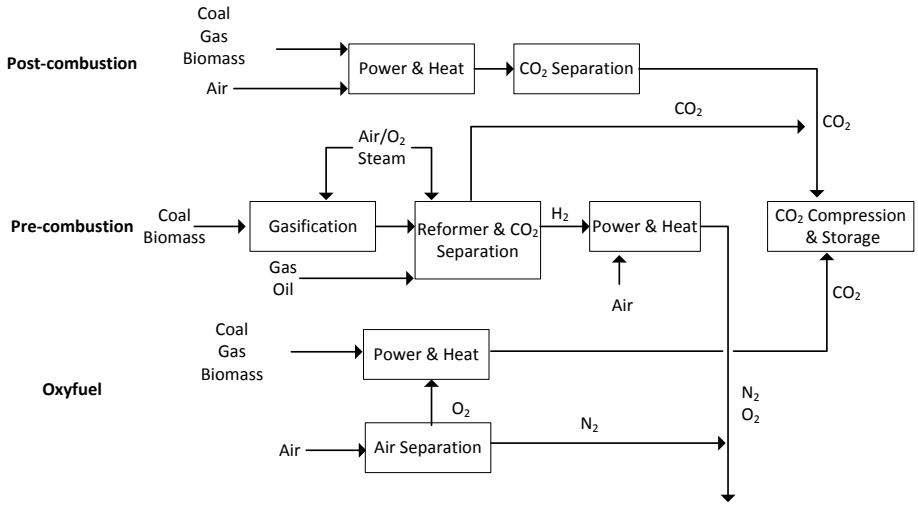

Figure 1-1 Possible routes for CO_2 capture

1.1.2 Cost of Carbon Dioxide Capture and Storage

It is estimated that the cost of capture would be the largest contributor to the overall cost of carbon dioxide capture and storage. While the pathways mentioned above provide the means for capturing the generated CO_2, they incur a significant cost and energy penalty.

Additionally, most of the technologies are not entirely suitable for retrofitting to existing power stations. The implementation of these current technologies would result in an efficiency penalty of around 5-16% for a pulverized coal fired power station [1], depending on the type of system employed and this is not favourable from an economic standpoint. Additionally, the estimated cost of CO_2 capture is around $30-90 per tonne [2]. The Intergovernmental Panel on Climate Change (IPCC) has estimated that this would increase the cost of electricity generation by around 43-91% relative to a pulverized coal fired power station without CO_2 capture [2]. Comparatively, the cost of transportation would be around $11 per tonne [3], while the cost for geological storage is expected to be in the range of $0.6-8.3 per tonne of CO_2 stored [2]. What this shows is that the capture of CO_2 is the most costly process and alternatives are required to significantly reduce this value to make carbon dioxide capture and storage more economically viable.

Therefore, to make carbon dioxide capture and storage more appealing, technologies that can significantly reduce the cost of CO_2 capture are needed. It is worthwhile mentioning that adsorption technologies would probably only be capable of capturing around 90% of the generated CO_2. While oxyfuel combustion can theoretically yield nearly 100% CO_2 capture, it requires pure O_2, the separation of which from air is a costly and energy intensive process. Hence, in addition to being cost effective, carbon dioxide capture and storage technologies should also be capable of obtaining near complete CO_2 capture to make the subsequent downstream processing easier and cheaper. Such a requirement can be met by expanding on the oxyfuel combustion system wherein no N_2 is introduced into the reactor, making the CO_2 capture step inherent to the system. A new technology has been envisioned that satisfies both the aforementioned criteria and is called Chemical Looping Combustion (CLC), which this thesis is based upon.

1.2 Basics of Chemical Looping Combustion (CLC)

CLC is an alternative CO_2 capture technology with N_2 not being present in the reactor containing the fuel to allow for inherent CO_2 capture. This is achieved using an Oxygen Carrier (OC) to provide the required oxygen for the combustion of the fuel. Circulating fluidized bed (CFB) reactors are typically employed to facilitate this and a schematic can be found in Figure 1-2 below. The OC is typically a transition element-based metal oxide. The basic principle is that the OC provides the oxygen to combust the fuel in the Fuel Reactor (FR). The outlet gas consists primarily of CO_2 and H_2O, without N_2 present. Hence, inherent

CO_2 separation is achieved upon condensation of the steam, yielding an almost pure stream of CO_2. Depending on the type of the coal, S- or N- containing gases may also be emitted together with CO and H_2 from incomplete combustion of the fuel. Once the oxygen in the OC is depleted, it then enters the Air Reactor (AR) to be oxidized. The flue gas from the AR consists of oxygen depleted air which can be safely vented. The oxidized OC is then reintroduced into the FR to combust more fuel. The path of travel of the OC between the two reactors forms a loop, hence the term CLC. Since the OC is alternatively reduced in the FR and oxidized in the AR, the cyclic behaviour is termed reduction-oxidation or redox for short.

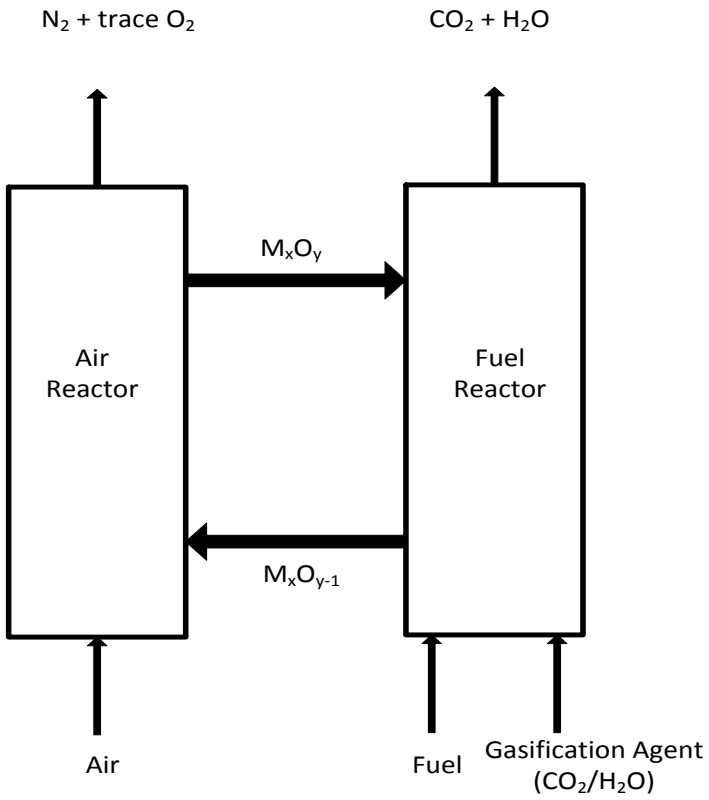

Figure 1-2 Schematic representation of the CLC system

The following equations represent the reactions which occur in the FR and AR respectively whereby Me_xO_y signifies the OC in its oxidized state while the OC in its reduced state is denoted by Me_xO_{y-1} and C_nH_{2m} represents the carbonaceous fuel.

$$(2n+m)Me_xO_y + C_nH_{2m} \rightarrow (2n+m)Me_xO_{y-1} + nCO_2 + mH_2O \quad 1.1$$

$$Me_xO_{y-1} + \tfrac{1}{2}O_2 \rightarrow Me_xO_y \quad 1.2$$

Combining these two equations yields the following:

$$C_nH_{2m} + \left(n + \tfrac{1}{2}m\right)O_2 \rightarrow nCO_2 + mH_2O \quad 1.3$$

The above equation is actually the fuel combustion equation. What this tells us is that the amount of energy evolved using the CLC process is exactly the same as that in conventional combustion.

1.2.1 Background

The concept behind CLC was first presented by Lewis and Gilliland in 1954 as a method for producing CO_2 [4]. Four decades later, in 1994, this concept was expanded upon by Ishida *et al.* [5] as a means for capturing CO_2 while incurring a lower exergy loss and they coined the term CLC. After that, Lyngfelt *et al.* [6] proposed a design for gas-fuelled CLC based on the CFB technology. This system was chosen to enable the circulation of the OC between the two reactors and is shown in Figure 1-3 below. The OC would transfer the oxygen from air to the fuel for combustion. Once the oxygen in the OC has been depleted, it would then be sent to the AR where it would be regenerated by the oxygen present in air. This OC would then be transported back to the FR to begin the next combustion reaction. The configuration for the AR necessitated it to act as a riser to provide the driving force for circulation, which is why a high velocity fluidized bed was chosen. The FR was designed to be a bubbling fluidized bed to provide sufficient residence time for the fuel in the reactor so that it has sufficient time to react with the OC particles.

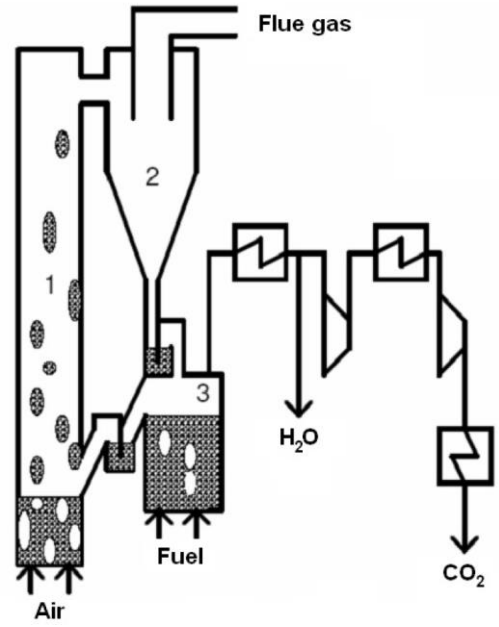

Figure 1-3 CLC process as envisioned by Lyngfelt *et al.* [6]

1.2.2 Types of CLC

Since different types of fuels are used for power generation, a few variants of CLC have been proposed that are specific to the desired outcome and fuel used. The most widely researched form of CLC is for gaseous fuels as it is the simplest to operate; this is basically what Lyngfelt *et al.* [6] proposed. This has been expanded in recent times to include solid fuels and two forms have been proposed. The first is called syngas-fuelled CLC (Syngas-CLC) and involves the fuel first being gasified to generate syngas. This is done using oxygen to provide the necessary energy for the endothermic reaction as well as to ensure that nitrogen is not present to dilute the CO_2 stream. Such a configuration would require the use of an ASU, similar to that in oxyfuel combustion and is unfavourable due to the incurred cost and energy penalties. Therefore, the direct use of solid fuels in the FR was proposed and this variant is termed in-situ gasification CLC (iG-CLC). Such a configuration would be able to function without the requiring pure oxygen, which is beneficial. Additionally, since solid fuels such as coal and petroleum coke are much cheaper and more abundant than gaseous fuels, there is a strong incentive to use solid fuels in CLC. In an iG-CLC system, the solid fuel is introduced into the FR, which is fluidized by gases such as CO_2 and H_2O. These two gases also act as gasification agents and convert the solid fuel into gaseous constituents within the FR. These combustible gases then go on to react with the OC, similar to the aforementioned CLC systems. The next system is called Chemical Looping with Oxygen Uncoupling (CLOU) and this operates in a different process, using OCs having select characteristics. OCs for CLOU must be able to release oxygen in an oxygen-deficient environment such as that in the FR. The released oxygen reacts with the solid fuel to combust it without necessitating it being first gasified. The differences between the three systems are shown in Figure 1-4. In principle, CLC is a highly efficient technology that does not incur significant costs relative to other CO_2 capture technologies such as absorption. The issue with CLC is that it has a lower technological maturity compared to other carbon dioxide capture and storage options, which results in a lower confidence level in the technology. Therefore, more research has to be undertaken to study this technology in greater detail to assess its viability.

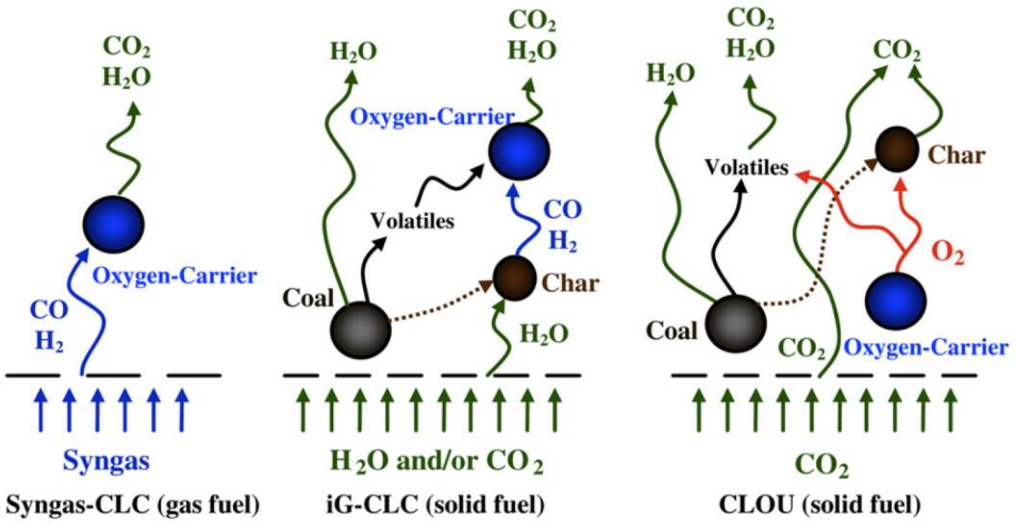

Figure 1-4 Main processes in the FR for the three different options proposed for solid fuel combustion in CLC [7]

1.3 Fuel

The available fuel types vary from country to country depending on natural reserves. Some countries have large reserves of coal while others have access to great amounts of natural gas. Figure 1-5 shows the types of fuel used for electricity generation around the globe in 2012. It can be seen that fossil fuels account for 68% of the generated electricity with the balance being made up of nuclear, hydro as well as 'Other'. The 'Other' category includes electricity generated using geothermal, solar, wind and heat energy. Of the fossil fuels that were used, around 60% was coal/peat. The reason for this is that coal and peat are more abundant, widespread and cheaper compared to the other options.

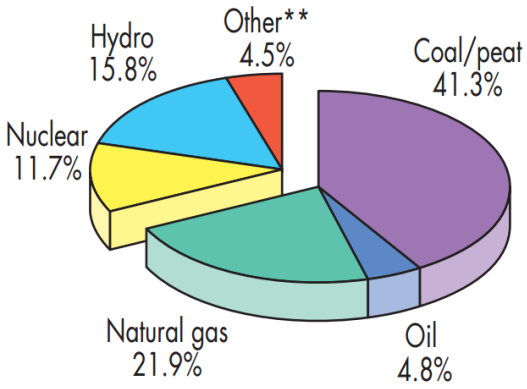

Figure 1-5 2012 Electricity generation by fuel [8]; 'Other' includes geothermal, solar, wind and heat

1.3.1 Victorian Brown Coal (VBC)

Victorian brown coal is a type of young coal with large reserves in Australia. The characteristics of brown coals are between that of peat and sub-bituminous coal. Brown coals generally have a higher moisture content, volatile matter and reactivity relative to other coals. At the current rate of consumption, it is expected that the brown coal reserves in Victoria would last for over four centuries [9]. The main source of energy in Victoria is derived from the combustion of brown coal and it is expected that this will continue to serve as a cheap source of fuel for the foreseeable future. While around 40% of global electricity is generated from coal, this figure is around 85-90% in Victoria due to the low cost and availability of VBC. Presently, VBC is used in conventional pulverized coal-fired power stations, which generate vast amounts of CO_2.

VBCs differ in composition depending on the location of the mine, as shown in Table 1-1. The moisture content on an as received basis is between 60-65%. On a dry basis, VBCs contain approximately 50% volatile matter and have an ash content of about 2% [10]. Since VBC has undergone a low degree of coalification, it contains low amounts of carbon (~65%) and high levels of oxygen (~20%). These coals typically have low amounts of nitrogen and sulphur present as well. The main difference between these brown coals lies in their ash composition. Typically, ash of Yallourn coal has high amounts of iron, while ash of Morwell coal has high levels of calcium and the ash of Loy Yang coal is rich in silicon and aluminium.

Various carbon dioxide capture and storage technologies are presently being researched to capture the CO_2 from the combustion of VBC at a reasonable cost due to the harmful environmental effects that greenhouse gases pose to the environment. Very little work has been done to date with respect to understanding the use of VBC in the CLC process. Thus, the applicability of the CLC process to VBC needs to be investigated further.

Table 1-1 Composition of three major VBCs

Components	Yallourn	Morwell	Loy Yang
HHV, MJ/kg	24.5 – 26.1	24.8 – 25.4	25.7 – 26.4
Moisture, % ar	~65	~60	~60
Proximate Analysis (% db)			
Ash	1.9 - 2.4	1.7 – 3.0	1.1 – 2.8
Volatile Matter	48.0 – 50.5	48.3 – 51.4	49.0 – 50.6
Fixed Carbon	47.0 – 49.1	46.9 – 49.2	47.9 – 49.5
Ultimate Analysis (% db, ash free)			
C	64.9 - 66.6	64.9 – 69.3	66.1 – 69.6
H	4.0 - 4.6	4.4 – 5.1	4.6 – 5.2
N	0.4 - 0.5	0.4 – 0.6	0.6 – 0.7
S	0.2 – 0.3	0.2 – 0.4	0.3 – 0.4
O	~22.5	~22.2	~22.7
Na	~0.1	~0.1	0.1 – 0.2
Cl	~0.1	~0.1	~0.1
Ash Composition (%)			
SiO_2	5.3 – 15.0	2.28 – 12.8	4.8 – 41.6
Al_2O_3	3.0 – 5.0	3.44 – 12.4	5.4 – 26.7
Fe_2O_3	34.1 – 40.4	10.5 – 30.2	2.03 – 10.9
TiO_2	0.1 – 0.44	0.20 – 10.4	0.26 – 1.1
K_2O	0.3 – 1.0	0.2 – 0.4	0.2 – 0.5
MgO	14.2 – 17.2	11.7 - 17.2	5.1 – 15.3
Na_2O	4.8 – 6.0	3.6 – 5.1	2.6 – 13.5
CaO	6.3 – 8.3	14.1 – 35.6	3.2 – 28.9
SO_3	13.7 – 17.0	20.8 – 23.0	8.08 – 22.1

ar: as received; db: dry basis; HHV: Higher Heating Value

The next chapter will provide a review of literature in the field of CLC, with a particular focus on CLC of solid fuels.

1.4 References

1. Ghoniem, A.F., *Needs, resources and climate change: Clean and efficient conversion technologies.* Progress in Energy and Combustion Science, 2011. **37**(1): p. 15-51.
2. *IPCC special report on carbon dioxide capture and storage*. 2005.
3. Allinson, G., Y. Cinar, W. Hou, and P.R. Neal, *The Costs of CO2 transport and injection in australia.* CO2TECH Consultancy, Report, 2009.
4. Lewis, W.K., Gilliland, E.R., *Productions of pure carbon dioxide*. 1954.
5. Ishida, M. and H.G. Jin, *A New Advanced Power-Generation System Using Chemical-Looping Combustion.* Energy, 1994. **19**(4): p. 415-422.
6. Lyngfelt, A., B. Leckner, and T. Mattisson, *A fluidized-bed combustion process with inherent CO2 separation; application of chemical-looping combustion.* Chemical Engineering Science, 2001. **56**(10): p. 3101-3113.
7. Adanez, J., A. Abad, F. Garcia-Labiano, P. Gayan, and L.F. de Diego, *Progress in Chemical-Looping Combustion and Reforming technologies.* Progress in Energy and Combustion Science, 2012. **38**(2): p. 215-282.
8. *Key World Energy Statistics 2014*. 2014, International Energy Agency.
9. Chen, L. and S. Bhattacharya, *Sulfur Emission from Victorian Brown Coal Under Pyrolysis, Oxy-Fuel Combustion and Gasification Conditions.* Environmental Science & Technology, 2013. **47**(3): p. 1729-1734.
10. Saha, C. and S. Bhattacharya, *Chemical looping combustion of low-ash and high-ash low rank coals using different metal oxides - A thermogravimetric analyser study.* Fuel, 2012. **97**: p. 137-150.

Chapter 2 Literature Review

Since the conceptualization of CLC in the mid-nineties, it has now developed to investigations on pilot scale units and still has significant room for improvement. This chapter will detail the advancements in the field of CLC, including the OC selection criteria.

This chapter will provide a review of the information in literature on OC selection, in-situ gasification CLC including design considerations, modelling of OC reduction kinetics as well as economics. This chapter will end with the objectives and structure of this thesis, followed by a list of publications arising from this thesis.

2.1 Oxygen Carriers (OC)

The OC plays a very important role in the CLC process. Typically, the OCs which have been researched in the past decade are transition element metals from groups 7-11; examples include oxides of Fe, Mn, Cu and Ni. Such materials have the capability of being reduced and oxidized easily by giving off and accepting oxygen into their lattice structure. The selection of a good OC is paramount to the success of the CLC process and as such needs to fulfil certain criteria which are listed below:

- High reactivity in both reduction and oxidation cycles
- High oxygen carrying capacity to minimize the solids inventory in the reactors
- Ability to completely combust the fuel to obtain maximum fuel combustion efficiency
- Resistance to attrition to reduce OC loss via elutriation
- High mechanical strength to withstand cyclic frictional stress due to the high particle circulation rates
- Resistance to agglomeration to avoid defluidization of the bed
- Resistance to sintering, which may lead to deactivation of the OC
- Ability to withstand a certain degree of contamination by the reactants or products while retaining its reactivity
- Negligible carbon deposition on the OC to maximize the carbon capture efficiency
- Environmentally benign
- Acceptable disposal
- Inexpensive

The following subsections will describe each of these aspects in detail to determine the most suitable metal oxide for use as an OC.

2.1.1 Reactivity

High reactivity is one of the most important criteria of an OC as it dictates the time required to completely combust a given amount of fuel. Based on the commonly used OCs, pure NiO has low reactivity due to its lack of porosity. It is for this reason that numerous studies have been undertaken on the preparation of highly reactive Ni-based OCs by using a support material to increase its dispersion [1, 2]. Cu-based OCs are extremely proficient at converting the fuel at low temperatures. Fe-based materials have sufficient reactivity with CO and H_2 but are not proficient at converting CH_4. On the other hand, Mn-based samples typically have poor reactivity, even when syngas is used as the fuel. This shows that the pure form of the metal oxide generally has poor reactivity and is typically used in combination with a porous inert support. This leads to the fabrication of synthetic OCs having enhanced surface area, mechanical strength and attrition resistance. It is worthwhile mentioning that the method used for the preparation of a synthetic OC has an impact on the properties of the final product. The distribution of the metal oxide over the surface of the support as well as potential interactions between the two materials will have an effect on the reactivity of the OC. Several methods exist in literature for the production of synthetic OCs and these can be broken down into three distinct types. The first type is when the metal oxide and support are in a solid state and the final product is generated via mechanical mixing, freeze granulation or spray drying. The second method involves using a solution containing both the desired metal and support material. This solution is then converted into a solid by using techniques such as co-precipitation, dissolution, sol-gel or solution combustion. The last method involves depositing the metal that is in a liquid state onto the surface of a solid support through impregnation. The downside to all of the aforementioned methods is that such a combination would generally increase the cost of the OC and a larger amount of bed material would be required to provide the same amount of the active metal oxide. Also, from a practical viewpoint, the use of synthetic OCs in large scale applications is not favourable as these OCs are costly and could reduce the economics of the process.

2.1.2 Oxygen Carrying Capacity

The oxygen carrying capacity of an OC measures the maximum amount of oxygen that the OC can release and this is dependent on the oxidation states between which it alternates. Whilst this value can be measured experimentally, the theoretical limits can be defined by Equation (1.1), where R_o represents the oxygen carrying capacity between its various oxidation states, while m_o and m_r represent the mass of the fully oxidized and reduced OCs respectively.

$$R_o = \frac{m_o - m_r}{m_o} \qquad 2.1$$

The oxygen carrying capacity of some the most commonly used oxygen carriers are shown in Figure 2-1 below:

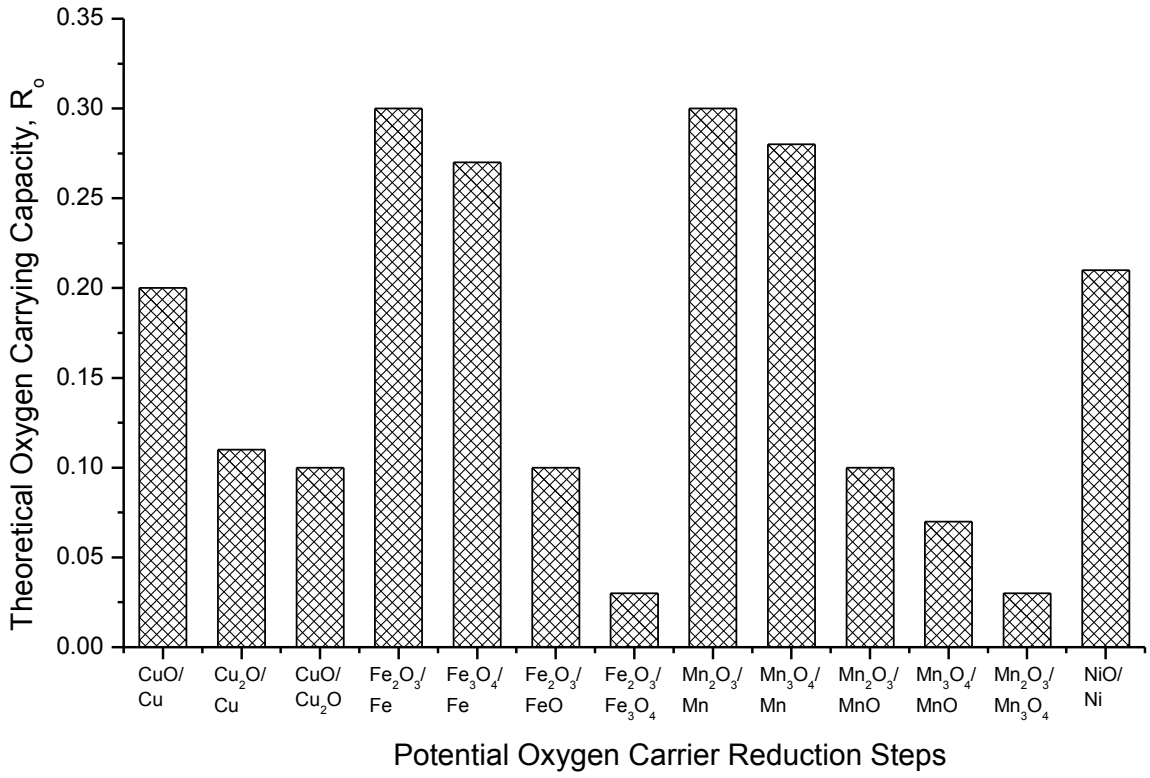

Figure 2-1 Oxygen carrying capacity of common oxygen carriers

Based on the above figure, it can be seen that both Fe_2O_3 and Mn_2O_3 have the highest oxygen carrying capacity followed by NiO and CuO. While these OCs can be theoretically reduced to their lowest oxidation stages, thermodynamics would dictate if these oxidation stages are able to fully convert the fuel.

2.1.3 Extent of Fuel Combustion

Thermodynamic analysis can be used to predict the efficiency of an OC to convert combustible gases such as CO and H_2, which are the most prevalent gases in a CLC system. As mentioned, the reactivity of the OC is of paramount importance and it must show an affinity towards the conversion of the combustible gases into CO_2 and H_2O. Such an analysis has been performed by Jerndal *et al.* [3] for various redox systems and this has been compiled by Adanez *et al.* [4]; this compilation can be found in Figure 2-2. The abscissa shows the reaction temperature while the ordinate shows the equilibrium constant, K_{eq}, for the reaction between the fuel, CO and H_2, and the different OC redox pairs. The larger the K_{eq} value, the higher the conversion of the reactant, which is the reducing gas in this case. A redox system having a K_{eq} value higher than $1e^{+3}$ corresponds to a conversion of the reducing gas in excess of 99.9%. This means that less than 0.1% of the gas is unconverted, which is acceptable. The only OC pairs that fulfil this criterion are CuO-Cu, Mn_3O_4-MnO and Fe_2O_3-Fe_3O_4. If the K_{eq} is further dropped, the NiO-Ni system becomes a potential candidate with around 99.5% conversion for H_2 and 98.5% for CO in the temperature range of 900-1000°C, which is the typical operating temperature of a CLC system. It can be seen that in terms of reactivity, Fe-, Mn-, Cu- and Ni-based metal oxides are suitable for use as OCs.

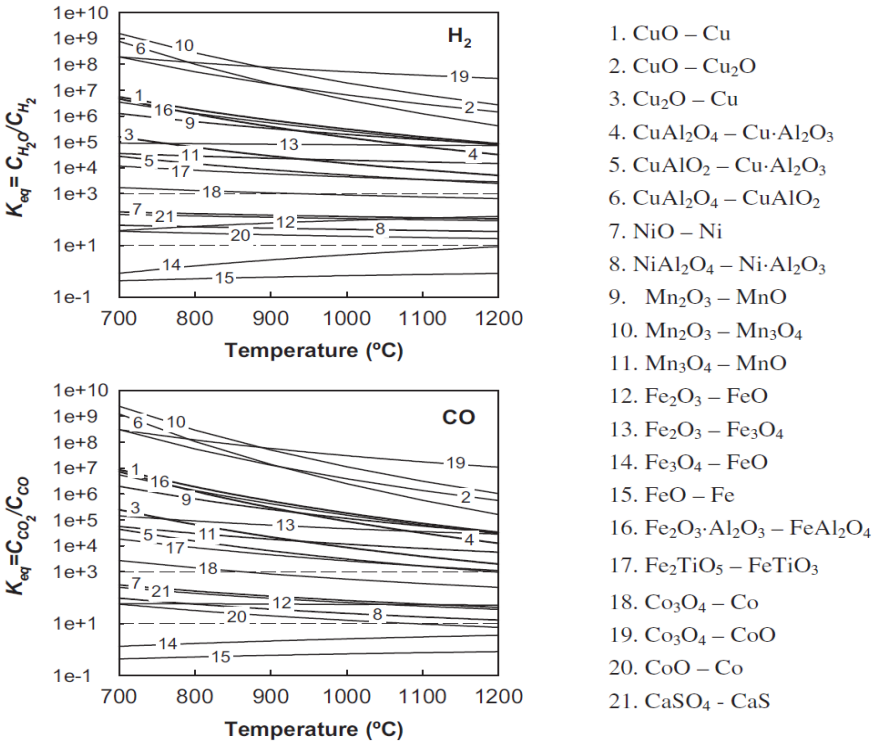

Figure 2-2 Equilibrium constants for the reduction reaction between both H_2 and CO with different OC pairs [4]

2.1.4 Attrition and Mechanical Strength

The resistance to attrition and high mechanical strength are related characteristics. These reduce the breakage rate of the OC particles as well as allow it to withstand the frictional stresses arising from circulating the particle between the FR and AR. High mechanical strength and attrition resistance of the OC would lead to a reduction in elutriation losses. Various studies [5-7] have found that the use of either an inert support or a natural ore results in mechanically stronger and attrition resistant OCs. Materials such as Al_2O_3 [5, 8, 9], TiO_2 [10, 11], MgO [6, 7, 12] and ZrO_2 [13-15] have been widely researched and the findings suggest that these materials are indeed capable of increasing the durability of the OC. Ores such as iron ore [16, 17], manganese ore [18, 19] and ilmenite [20-22], a titanium-iron oxide, have been used and proven to be reactive while having acceptable mechanical strength. Adanez *et al.* [4] consolidated and tabulated the attrition data of a few OCs from different sources and this is shown in Table 2-1 below. Since a vast difference is observed between the Fe- and Ni-based samples, a simple comparison between the two was performed. Taking the best lifetime value for NiO gives 40,000 hours while iron ore has a lifetime of 1,600 hours. The cost of the metal oxides is roughly \$15/kg for NiO and \$0.15/kg for iron ore [4]. The most important parameter from an economic viewpoint is the cost of the OC over its lifetime. Taking this ratio gives \$0.00038/hr for NiO and \$0.000094/hr for iron ore. This means that iron ore is at least four times more economical compared to the NiO-based OC as this cost does not include the cost of Al_2O_3 and the cost associated with the preparation of the NiO/Al_2O_3 OC. The other way of considering it would be to just use pure NiO, but a pure metal oxide would have a lifetime much lesser than 40,000 hours due to having a lower mechanical strength. Therefore, attrition or the lifetime of the OC is not as important as the cost over its lifetime.

Table 2-1 Projected lifetime of OCs based on attrition data [4]

Carrier	Capacity (kW_{th})	Operation time (h)	Temperature (°C)		Attrition rate (%/h)	Lifetime (h)
			Fuel Reactor	Air Reactor		
NiO/Al_2O_3	10	100	~900	1000	0.0023	40000
$NiO/NiAl_2O_4$ + $MgAl_2O_4$	10	1016	~940	1000	0.003	33000
$NiO/NiAl_2O_4$	10	160	~940	1000	0.022	4500
$NiO/\alpha\text{-}Al_2O_3$	0.5	70	880	950	0.01	10000
$CuO/\gamma\text{-}Al_2O_3$	10	100	800	800	0.04	2400
$CuO/\gamma\text{-}Al_2O_3$	0.5	60	800	900	0.09	1100
$CuO/NiO\text{-}Al_2O_3$	0.5	67	900	950	0.04	2700
Iron ore	1	10	950	1010	0.0625	1600

2.1.5 Sintering and Agglomeration

The resistance to sintering and agglomeration are two important characteristics of an OC. Materials having a low melting point are more susceptible to agglomeration, which leads to the formation of larger particles. Additionally, the interaction with ash from solid fuels or the support material, in the case of synthetic OCs, can also cause this through the formation of low melting point compounds termed eutectics and this will be discussed in the following subsection. A small degree of agglomeration can cause disturbances in the solids circulation as well as channelling of gases through the bed and this reduces the contact between the fuel and the OCs; excessive agglomeration can lead to bed defluidization, which must be avoided at all costs. Among the typically used metal oxides, CuO has the lowest melting point when it is reduced to Cu as it has a melting point of 1085°C. Even though this is higher than the temperatures at which the CLC system is typically operated at, metal oxides often soften at temperatures lower than their melting point and this can lead to agglomeration. The agglomeration tendency of Cu has been documented to occur at temperatures as low as 950°C but was absent when the temperature was reduced to 800°C [23]. The operation at such a low temperature would lead to a reduction in the turbine efficiency and hence the energetic efficiency of the system. To circumvent this, the use of inert supports has been proposed. Some studies were performed by Gayan *et al.* [24] in a $500W_{th}$ CFB reactor and they found

that the use of supports such as α-Al_2O_3, γ-Al_2O_3, $MgAl_2O_4$ and $NiAl_2O_4$ were capable of preventing the Cu-based OC from agglomerating. Hence, if CuO was to be used as an OC, it should be supported to increase its thermal stability. On the other hand, Ni-, Fe- and Mn-based OCs were found to be resistant to agglomeration at temperatures of interest in CLC.

2.1.6 Oxygen Carrier Contamination

Contamination of the OC by the reactants or products is inevitable in CLC and can be caused by both gases and solids, such as the ash from the solid fuel. Of the gaseous contaminants, sulphur compounds are of particular interest. The presence of sulphur compounds in the exhaust of the FR would warrant additional clean-up as it affects the compression, transport and storage of the CO_2. With respect to the OC, the sulphur present in the fuel may react with it, which could lead to a decrease in reactivity through the formation of unreactive metal sulphides. Additionally, certain metal sulphides have a low melting point which could lead to agglomeration and subsequent bed defluidization. To investigate this potential issue, Tian *et al.* [25] performed experiments in a thermogravimetric analyzer (TGA) using Fe-, Ni-, Mn- and Cu-based OCs. They found that the reactivity of all the OCs decreased with time with NiO experiencing the highest decrease while Mn_2O_3 had the least reduction in reactivity. Garcìa-Labiano *et al.* [26] performed experiments in a 500 W_{th} CLC using NiO and found that Ni_3S_2 was formed under all the operating conditions tested. This led to a decrease in the reactivity with time, signalled by the decrease in CO_2 concentration at the outlet with an accompanied increase in H_2S. Upon oxidation of the OC, it was found that the Ni_3S_2 decomposed to SO_2 and NiO. They recommended the implementation of a desulfurization step for high sulphur fuels when using NiO. Using a Cu-based OC, Forero *et al.* [27] found that the formation of copper sulphides was absent except when the OC to fuel ratio was less than 1.5. This shows that OCs containing Cu, Fe and Mn are resistant to interaction with sulphur compounds typically found in fuels while Ni-based samples could be deactivated upon contact with such compounds. With respect to interaction with ash, Keller *et al.* [28] investigated the potential interactions between Cu-, Mn-, Fe-, Ni- and ilmenite-based OCs with the ash from thermal treatment of the minerals commonly found in coal. They performed experimental and thermodynamic simulations and found that the Cu- and Mn-based samples were most susceptible to interaction with minerals while the Ni- and Fe-based OCs were more resistant to such interactions; they found that ilmenite was the best candidate with respect to this criterion. Therefore, if a mineral-rich fuel is to be used, ilmenite is the preferred metal oxide followed by Ni- and Fe-based OCs.

2.1.7 Environmental Impact and Waste Disposal

The next characteristic is that the OC should be environmentally benign and this is tied to the OC having an acceptable disposal. Of the four most commonly used metal oxides in an OC, Ni poses significant environmental and health issues. This is due to the fact that compounds containing nickel have carcinogenic properties and that Ni is toxic. Additionally, the use of Cu can be challenging, as inhaling it can lead to irritation while ingesting it could cause irreversible damages to the body. On the other hand, Fe- and Mn-based materials are non-toxic and are most suitable for use in a CLC system. In an iG-CLC system, the OCs will experience attrition and would be elutriated and captured by the cyclones, which would also capture the fly ash from solid fuels. Therefore, if NiO is used as an OC, it would need to be separated from the fly ash and disposed of in a responsible manner.

2.1.8 Carbon Deposition

Deposition of carbon on the OC is unfavourable as the deposited carbon can enter the AR before being combusted by air. This causes the CO_2 capture efficiency to reduce and should be avoided where possible. Additionally, the deposited carbon could react with some metal oxides, leading to its deactivation. This phenomenon is highly correlated with the amount of available oxygen for the combustion of the fuel, with an observed acceleration in the rate of carbon deposition with a reduction in the available oxygen. Cho *et al.* [29] used a batch fluidized bed reactor and found that when more than 80% of the available oxygen in a Ni-based OC had been consumed, the deposition of carbon became more prominent. Using a similar configuration, de Diego *et al.* [8] found that when more than 75% of the available oxygen had been consumed from a copper-based OC, carbon deposition was prevalent. Such an observation has not been made with respect to iron-based OCs.

2.1.9 Cost

The last aspect with regards to the selection of an OC is also a highly important one and revolves around the cost of the metal oxide. Since attrition and elutriation of the OCs are both inevitable in CLC, it is preferable that the cost of the OC is low from an economic standpoint. Figure 2-3 shows the cost of some of the metals which can be used as OCs. It can be seen that both Mn and Fe are the most economical options for use as OCs when compared to Ni, Cu or Co. Based on the statistics provided, Fe and Mn are approximately two to four orders of magnitude cheaper when compared to the other three materials.

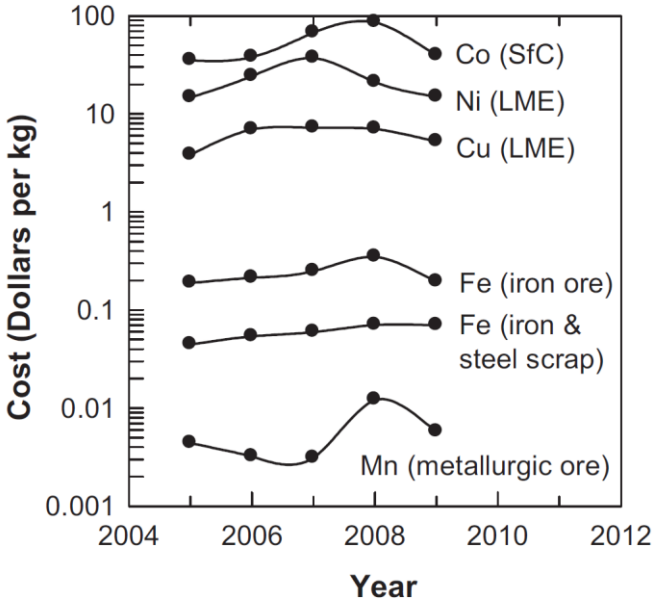

Figure 2-3 Average annual cost of materials which can be used as OCs [4];
SfC: Spot for cathodes; LME: London Metal Exchange

Therefore, amongst the four most commonly used OC materials, it can be seen that Fe_2O_3 is the best candidate with manganese-based materials coming in second. The issues with Mn-based samples are its low reactivity towards the fuel and that they have a high tendency of reacting with the minerals from solid fuels. The Cu- and Ni-based samples are good OC candidates but are costly materials; also, the former has a low melting point and the latter is carcinogenic as well as being susceptible to sulphur poisoning.

2.2 In-Situ Gasification CLC (iG-CLC)

As mentioned in the introduction chapter, while CLC was initially investigated with gaseous fuels, there has been a shift in recent times towards the use of solid fuels due to its abundance, widespread availability and low cost. The focus of this section will be on the iG-CLC system, which is an attractive option for use with the highly reactive VBC.

The reactor scheme most commonly used for the iG-CLC process employs the CFB technology and is shown in Figure 2-4 below, with MeO and Me representing the oxidized and reduced OCs respectively. The benefit of such an arrangement is the fuel flexibility associated with the use of CFB boilers and that the use of such a technology allows for the continuous generation of energy under steady-state operation. The feasibility of this process has been successfully proven in continuously operating CLC units with output capacities ranging from 500 W_{th} [30] to 12 MW_{th} [31].

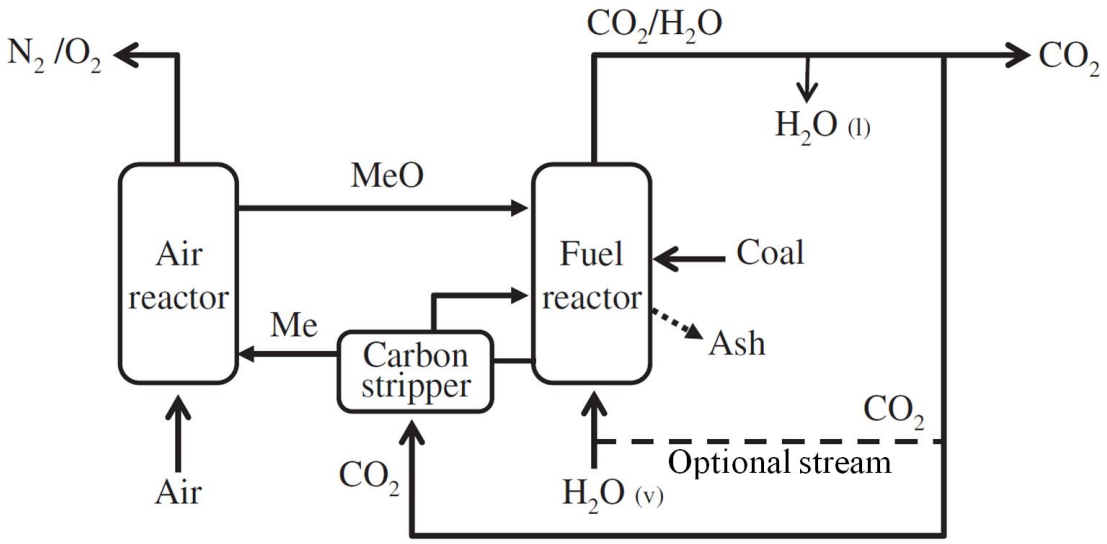

Figure 2-4 Reactor scheme for the iG-CLC process [4]

Although the reactions occurring in the FR and AR have been highlighted in the introduction chapter for any hydrocarbon-based fuel, this part will discuss the specificities relating to the use of a solid fuel. The first step that occurs in the FR is the devolatilization of the solid fuel, as shown in Equation (2.2). This leaves behind char which cannot be readily combusted and needs to be gasified as the solid-solid reaction between the char and OC does not occur at an appreciable rate [32]. The in-situ gasification of the solid fuel is highly endothermic and is accomplished using either steam or CO_2 as the gasification agents, which also act as the fluidization agents. This produces gasification intermediates, CO and H_2, which are shown in Equations (2.3) and (2.4) respectively. The volatiles and gasification products then react with the OC, Me_xO_y, as shown in Equation (2.5). The first four reactions occur in the FR and the net heat balance around this reactor is typically endothermic due to the heat required for char gasification. While this is true for most metal oxides, usage of Cu-, Mn- and Co-based OCs result in the heat balance in the FR being exothermic. This is due to the very low bond energy between the oxygen and Cu-, Mn- and Co- atoms, which results in an overall exothermic reaction. Finally, the reduced OC, Me_xO_{y-1}, is transferred to the AR where it is oxidized by the oxygen from air as shown in Equation (2.6). This process is exothermic for all OCs as it involves the conversion of the metal oxide to a more stable oxidation state. The regenerated OCs then enter the FR to complete one redox cycle. Performing a net energy balance over both the reactors, the total extractable energy from this system is exactly the same as in conventional combustion. The subsequent subsections will deal with the intricacies relating to the use of solid fuels in an iG-CLC process.

$$\text{Solid fuel} \rightarrow \text{Volatile matter} + \text{Char} \quad (2.2)$$

$$\text{Char} + H_2O \rightarrow H_2 + CO \quad (2.3)$$

$$\text{Char} + CO_2 \rightarrow 2\,CO \quad (2.4)$$

$$H_2, CO, \text{Volatile matter} + n\,Me_xO_y \rightarrow CO_2 + H_2O + n\,Me_xO_{y-1} \quad (2.5)$$

$$Me_xO_{y-1} + \tfrac{1}{2}\,O_2 \rightarrow Me_xO_y \quad (2.6)$$

2.2.1 Coal Conversion

Alongside the fabrication of suitable OCs for the iG-CLC process, much research is being focused on the aspect of fuel conversion with respect to solid fuels. Preliminary in-situ experiments were performed using a thermogravimetric analyzer (TGA) with OCs comprising Cu, Ni, Mn and Fe. Although it has been claimed that the solid-solid reaction between the OC and the solid fuel proceeds at an unappreciable rate, in actuality it may be masked when a gasification agent is used as is typical in CLC. This was found to not be true when an experiment was performed using ilmenite as the OC in a fluidized bed reactor where it was shown that the gasification rate of bituminous coal and petcoke with CO_2 or steam was more prevalent compared to direct solid-solid reaction with the OC [32, 33]. Additionally, Leion *et al.* [32] performed an experiment using only N_2 as the fluidizing gas without any CO_2 or steam as gasification agents for the fuel, petroleum coke. They found that the fuel conversion was very slow and after a period of 90 minutes, only 30% of the fuel had been converted. This was most likely due to the release of volatile matter during the initial stages of the reaction. Hence, the reaction between the OC and the gasification products is more significant compared to the solid-solid reaction and therefore gasification agents are needed to increase the rate of reaction in an iG-CLC system.

Char from low rank coals are known to be more reactive from a gasification point of view. The reactivity of any given char can be attributed to its chemical structure, inorganic constituents and porosity [34]. Comparing CO_2 and steam as gasification agents, it is a well-known fact that steam gasification of char proceeds at a faster rate than CO_2 gasification and this is ascribed to the larger size of the CO_2 molecule resulting in slower gas-solid diffusion [35]. An experiment conducted with a bituminous Colombian coal showed that the conversion of char was five times slower when CO_2 was used compared to when steam was employed as the gasification agent, confirming the previous statement [36]. It was found that steam gasification completely consumed the sample in minutes while complete gasification

using CO_2 was in the order of hours. On the other hand, there is a divergence from the theory put forth above where it has been found that the CO_2 gasification rate of low rank coals is as high as that of steam [37]. Experimentally, in a CLC system, it has been proven that the gasification of a lignite [38] using CO_2 proceeds as fast as the steam gasification of bituminous coal [36]. Therefore, the usage of low rank fuels are of advantage in a CLC system as the generated CO_2 can be recirculated back into the FR as a fluidizing gas and gasification agent.

In-situ gasification is favourable in the presence of an OC as it leads to an increase in the gasification rate, which is due to the continuous removal of the gasification intermediates through the reaction with the OC [32, 39]. It has been well documented that the gasification intermediates, H_2 and CO, are known char gasification inhibitors as they form a layer around the char particle, increasing the resistance to diffusion. This impedes the gasification agents from penetrating this layer to reach the surface of the char particle [40]. This inhibitory factor decreases as the OC conversion efficiency of CO and H_2 increases.

Gasification is also highly temperature dependant and it has been found that temperatures between 900 - 1000°C greatly enhance the rate of char gasification. Additionally, Leion *et al.* [32] found that increasing the reaction temperature from 850°C to 1000°C resulted in an increase in gasification reactivity by a factor of four. The second reason for the accelerated char gasification rate is that both the CO and H_2 are converted by the OC at a faster rate at higher temperatures due to faster OC reduction kinetics.

2.2.2 Unconverted Char Particles

The main effect of low gasification rates is the increased char concentration in the FR, which will cause the stream exiting the FR to contain more unconverted char. The unreacted char particles can exit the CLC system by being combusted in the AR or exiting the FR with the combustion products. To prevent the char from entering the AR, the particles can be separated from the OC by using a carbon stripper, as shown in Figure 2-4, which recycles the unreacted fuel back into the FR. Since the char particles entering the carbon stripper have a smaller size and lower density than the OC particles, by operating at an appropriate fluidization velocity, the char particles can be elutriated and recirculated back while the OC particles are sent to the AR. The separation in the carbon stripper occurs due to differences between the terminal velocities of the char and OC particles. The transfer of char to the AR does not reduce the energetic efficiency of the process but will decrease the amount of CO_2

that is captured, which will in turn reduce the carbon capture efficiency. The second means by which the fuel particles can be lost is through elutriation out of the FR with the combustion products, which is due to attrition of the fuel particles. These elutriated particles need to be recaptured and this can be achieved through the use of a cyclone.

2.2.3 Coal Ash Removal

The use of a solid fuel in the iG-CLC system results in the formation and accumulation of ash from the gasification of the char. These ash particles can be elutriated out of the FR and subsequently captured using a cyclone. As mentioned, it is likely that some of the char particles would also be present in the cyclone alongside the ash. The ash and unreacted fuel particles can then be separated based on the difference in densities. The unreacted fuel particles can then be redirected back into the FR while the ash is drained from the system.

Ash may be detrimental to the OC as there is a possibility for both particles to interact with each other and this could lead to agglomeration or a reduction in the OC reactivity. A few researchers have found that agglomeration and reactivity loss of the OC in the presence of ash was insignificant when the ash concentration in the fuel was lower than 5% [41, 42]. This means that such interactions are less likely to occur when low rank coals such as VBC are used as fuel in CLC, making such fuels highly favourable feedstock for the CLC process.

2.2.4 Investigated OCs

OCs for use in an iG-CLC system should ideally have the characteristics mentioned in the previous section to make it attractive for use. Importantly, these traits should be maintained over repeated redox cycles to make a viable OC. The paragraphs to follow will highlight some of the main findings in literature relating to the four previously discussed metal oxides.

In terms of reactivity, Cu-based materials are known to be very reactive and capable of achieving almost complete combustion of gasification products at temperatures beyond 850°C [43]. As previously mentioned, the use of this metal oxide is one of the few that results in the total energy evolved in the FR to be exothermic. This means that the heat released during the reduction of CuO can be used to compensate for the endothermic gasification reaction of the coal. Reduction of CuO to Cu is not favoured at temperatures beyond 800°C as this is close to the melting point of Cu, which is 1050°C. While the difference is significant, Cu starts to soften at temperatures much lower than its melting point, causing it to agglomerate. Experiments using CuO have been performed using a Victorian brown coal,

Loy Yang [23]. The findings reported here were similar to the others in literature whereby CuO was found to sinter at temperatures of around 950°C and could not be reoxidized, rendering it unusable. Few experiments were repeated at a lower temperature of 800°C and at this temperature the OC was found to perform well. While this result is favourable, this is not practical, as using such a low temperature for the combustion process reduces the energetic efficiency of a power station.

Ni-based OCs have also shown good reactivity with gasification products but are highly temperature dependant [44]. This has been shown in continuous operations with bituminous coals as the fuel, but full conversion of the gasification products were not observed due to the design of the FR which prevented the gases from efficiently contacting the OC [45, 46]. The use of Ni-based materials must be restricted to low-sulphur fuels as nickel is known to deactivated in the presence of sulphur [47, 48]. Thermogravimetric analysis were performed using Loy Yang brown coal and the authors found a reduction in the reactivity of NiO over the course of the reaction and concluded that it is not a suitable option for use with Loy Yang brown coal [49, 50]. Additionally, OCs containing NiO are not favoured due to their high price and toxicity, with the latter necessitating extreme safety protocols for disposal.

There is limited information pertaining to the use of Mn-based materials in an iG-CLC process compared to syngas-CLC. An investigation using manganese containing ores was performed with petcoke as the fuel and the authors found that it performed better compared to ilmenite in terms of its reactivity towards CO and H_2 [51]. They also found that some manganese ores were capable of increasing the rate of char gasification. Since the ore contained appreciable amounts of alkali-minerals, these were found to volatilize and deposit on the surface of the char. This led to the formation of channels and cavities, which is typical of catalytic gasification. Such an observation was apparent in this case as the petcoke contained very low levels of minerals and it was hypothesized that it had insignificant amounts of catalytic minerals to enhance its gasification rate, making the rate enhancement by the mineral deposition more pronounced.

Fe-based OCs generally have lower reactivity when compared to Ni-based materials, but it is capable of complete combustion of the gasification products to CO_2 and H_2O [38]. Leion *et al.* [32] found that the CO concentration at the exit of the FR was around 0.5% when using Fe_2O_3 as the OC. The reactivity of ilmenite was analysed in a batch fluidized bed reactor and it was found to have good conversion of the gasification products [52]. They also established that the reactivity of ilmenite was in the same order of magnitude as highly reactive OCs such

as Ni-based materials [48]. A 10 kW_{th} iG-CLC unit was operated by Berguerand and Lyngfelt [53-56] using coal and petroleum coke as the fuel; it was found to perform well, leading them to conclude that ilmenite is a suitable OC for the process. Experiments performed in a 500 W_{th} small scale CLC unit showed that neither volatile matter nor unburnt tars were present at the reactor exit [57]. A natural iron ore was used in a 1 kW_{th} unit operated continuously and Wu *et al.* [58] found that the coal combustion efficiency was similar to that of a very reactive Ni-based OC [45]. Zhang *et al.* [59] investigated the use of Fe containing materials in a fixed bed reactor operated under both atmospheric and pressurized conditions of up to 0.5 MPa. They found that the performance of the OC was strongly pressure dependent, obtaining higher CO_2 concentrations at higher pressures. Additionally, the carbon conversion rate and extent was improved at higher operating pressures. Experiments performed using Loy Yang coal in a TGA led the authors to conclude that Fe_2O_3 was able to retain its reactivity over repeated cycles [50]. This is proof that Fe-based oxygen carriers are promising for use in the iG-CLC process as they are cheap, environmentally benign and show sufficient reactivity with all types of coal, particularly Victorian brown coal.

A summary of recent studies on iG-CLC systems can be found in Appendix A.

2.3 iG-CLC Design Considerations

Since one of the objectives of this thesis is to design and operate a 10kW_{th} iG-CLC unit, this section will detail the aspects that need to be considered to accomplish this task. The smallest scale unit that can be used for preliminary investigations is a TGA. Here, a certain amount of the OC is mixed with the fuel and the system is operated in a batch mode. The weight loss curve as a function of time can be used to determine the temperatures at which certain components are evolved. Then, the experiments are scaled-up to a more complex level using either a bench-scale fixed or fluidized bed reactor. This is used to study the behaviour of the OC in a manner that closely simulates an actual iG-CLC system. When results from such a scale prove to be satisfactory, the fuel and OC are ready to be trialled in a pilot scale reactor. Here the fluid flow properties are studied to see the effect of particle circulation between the FR and AR. Then, when most if not all of the issues have been resolved, a demonstration plant is constructed to study the performance of the system on a larger scale, which closely mimics that of a commercial power station. Upon completion, the last step involves commercialization of the process. This is the typical progression followed by many technologies prior to their commercialization and CLC is presently at the pilot reactor scale.

Kronberger *et al.* [60] developed a comprehensive design procedure for a CLC system. This involved the fuel and OC feed rates, R_O of the OCs as well as the reaction kinetics in both the AR and FR. This procedure also factors in aspects relating to hydrodynamics such as particle entrainment, pressure drop, CO_2 leakage via the AR as well as residence time of the fuel and OC. The proposed design procedure is shown in Figure 2-5 below to gain a better understanding of the steps necessary in designing a CLC reactor system. Wolf and Kemiteknik [61] provided a listing, pointing out the essential features of an efficient CLC system and this is described below:

- Adequate particle circulation between the AR and FR to ensure complete combustion
- Sufficient contact between the OC and the fuel in the FR as well as air in the AR to attain maximum conversion
- Minimum CO_2 leakage from the FR to the AR
- High temperature operation which will increase the energetic efficiency of the system

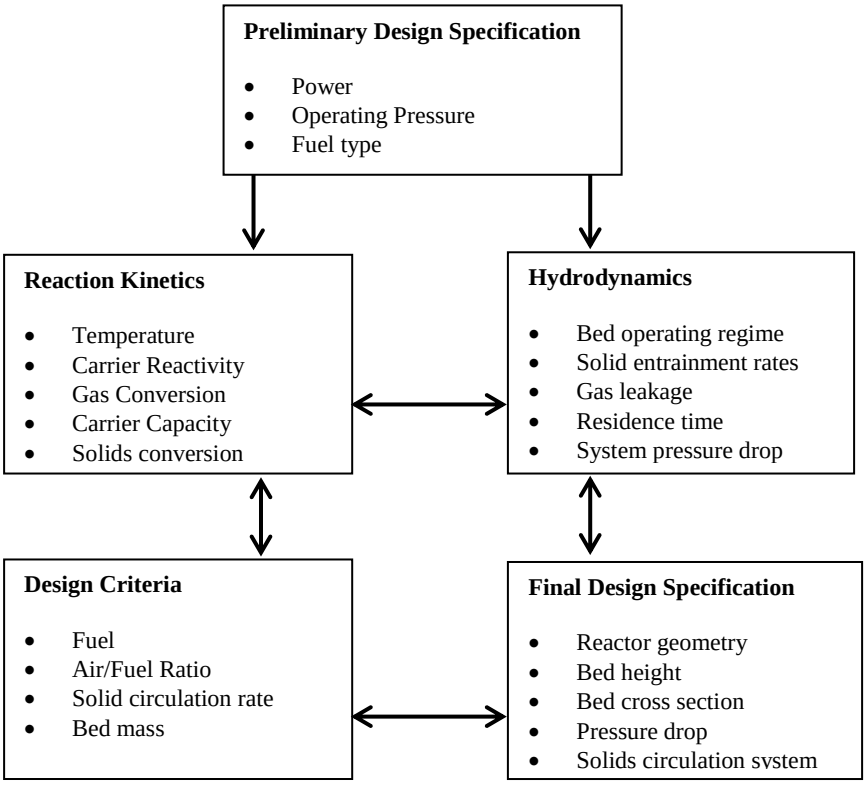

Figure 2-5 Design procedure of a CLC reactor system [62]

2.4 Modelling

Upon fabrication and operation of a reactor system, modelling is an important aspect to be considered next. Performing modelling or simulation allows for a prediction to be drawn out in the initial phase, which will then set the scene for model validation or nullification based on the acquired data.

2.4.1 Kinetic Modelling

A kinetic model can be used to predict the solids inventory in the FR and AR whereby the output from the model is highly dependent on the reactivity of the OC and its oxygen carrying capability [63]. Kinetic data exists for many metal oxides as catalyst in other processes but this cannot be directly used for the metal oxides employed in an iG-CLC system. This is because the metal oxides used in a CLC system are reactants and are subjected to repeated reduction and oxidation cycles, causing its properties and reactivity to change with time. OC reduction kinetics data is available in literature but only for when gaseous fuels are used [64]. Although the OCs in the iG-CLC system are reacting with the volatile matter and gasification products from the coal, the amount of these components changes from one fuel to another unlike when natural gas is used. Thus, kinetic data needs to be generated for each coal alongside its gasification conditions.

In terms of kinetic modelling, the interactions that occur in the FR and AR are assumed to be non-catalytic gas-solid reactions and this is justifiable for the development of a preliminary model. Different models have been proposed for the gas-solid reactions to predict the conversion of the OC particles as a function of time as well as to study the effect of operating conditions on the reaction rate. The three most commonly used models are the Changing Grain Size Model (CGSM), the Shrinking Core Model (SCM) as well as the nucleation and nuclei growth model, which are shown in Figure 2-6. Additionally, the Modified Volume Reaction Model (MVRM) can also be used. These models are described in detail below.

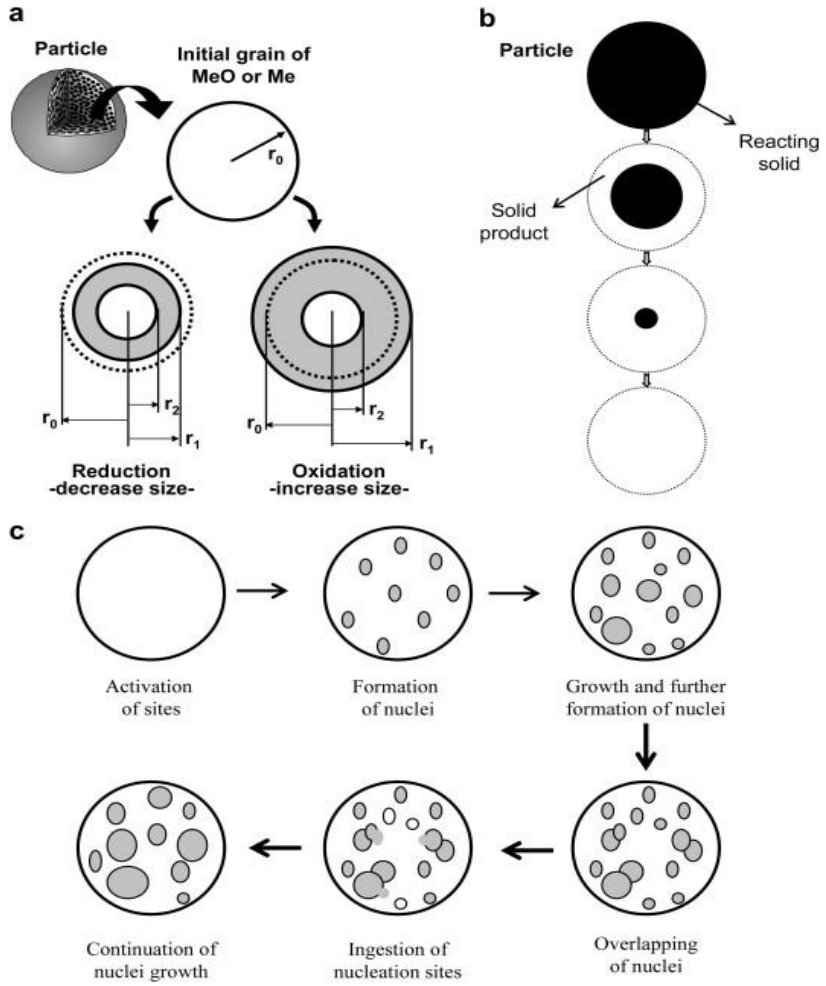

Figure 2-6 Representation of the various reaction models on a particle: a) Changing Grain Size Model; b) Shrinking Core Model; c) Nucleation and nuclei growth model [65]

2.4.1.1 Changing Grain Size Model (CGSM)

A feature that is present in all gas-solid reactions is that the overall process involves several intermediate steps and these are mentioned below:

1) Gaseous diffusion of the reactants from the bulk of the gas phase to the surface of the reacting solid particle
2) Diffusion of gaseous reactants through the pores of the solid particle or the product layer formed during the gas-solid interaction
3) Adsorption of gaseous reactants onto the solid surface
4) Chemical reaction between the gas and solid

If the reaction generates gaseous compounds, diffusion of the molecules into the bulk gas phase occurs by means of steps (1) to (3). The progress of the gas-solid reactions can be affected if the surface structure changes or if sintering occurs.

The CGSM considers the steps mentioned above and operates on the assumption that the particle consists of non-porous grains with a uniform characteristic length, r_o [66]. During the course of the reaction, the grain size, r_1, changes while the unreacted core, r_2, shrinks due to differences in the volume of product formed per unit volume of reactant. Here the integration of the SCM comes into play as it is used to model each grain, which is assumed to follow the ascribed model. The reaction initiates on the surface of the grain and as the reaction proceeds, a layer of the solid product is formed around an unreacted core, resulting in the reduction of the unreacted core size. The border at which the product layer and unreacted core coincide is the region where the chemical reaction occurs. The reacting gas has to overcome various resistances, which are steps (1) to (3), before any reaction can occur.

An approximation to the mass balances was developed by Szekely *et al.* [67] in which they hypothesized that the time taken to overcome all the resistances is a summation of each individual resistance. Typically the rate of diffusion through the film, pores and product layer is deemed to present an insignificant resistance with the only significant factor being the chemical reaction occurring in the grain. The reaction time for the complete reaction with the reducing gas at the grain corresponds to a Shrinking Core Model in the grains (SCMg).

Dueso *et al.* [68] used the CGSM to determine the oxidation and reduction kinetics of Ni-based OCs in the presence of syngas and natural gas. They found that the model was capable of adequately predicting the conversion of the OC. Also, Abad *et al.* [69] used the same model to determine the redox kinetics of pre-oxidized and activated ilmenite in the presence of the same gases above. They found that the activation energies for the reduction reaction varied depending on the type of fuel and OC used, and obtained values between 65-165 kJ/mol. Additionally, they found the activation energy for the oxidation of the reduced OC to be much lower, between 11-25 kJ/mol.

2.4.1.2 Shrinking Core Model (SCM)

This has been briefly discussed in the previous subsection and is typically employed when the resistance to gas diffusion in the unreacted particle is very high. This is due to the formation of a layer of solid product around an unreacted core inside the particle. This method was found to be unsuitable for highly porous small particles in the order of 100 µm and as such either the CGSM or SCMg are used to model such particles. On the other hand, this model was found to be suitable for larger particles having low porosities.

Song *et al.* [70] utilized the SCM to determine the redox characteristics of a bimetallic OC consisting of Ni and Fe with CO as the fuel. Their findings showed how the obtained kinetic parameters of the individual OCs could be used to predict the kinetic parameters of the bimetallic OCs. Saha and Bhattacharya [71] determined the redox characteristics of a Cu-based OC using the same model as well and found that the SCM was able to sufficiently predict the conversion of CuO in the presence of CO.

2.4.1.3 Nucleation and Nuclei Growth Model

This model states that the oxidation and reduction of the OC particles can be assumed to follow a nucleation process whereby metallic nuclei are formed which then grow and overlap. The reaction rate increases as the generation of the nuclei increases during the initiation of the reaction and this is termed the induction period. Beyond this period, the reaction occurs uniformly over the solid surface and the reaction front advances into the inner part of the grain [72].

The simplification of this model occurs when the reaction order with respect to the solid concentration is one, yielding a model for a homogenous particle. The nucleation process is directly proportional to the temperature of the reduction/oxidation of the particle and for the temperatures typically used in CLC, the nucleation process is thought to occur relatively fast. It has been shown that both the SCM and this model fitted experimental data obtained using gaseous fuels reasonably well [73].

2.4.1.4 Modified Volume Reaction Model (MVRM)

The MVRM is a simple model capable of calculating the conversion of a solid as a function of time. The MVRM ignores the characteristics of the solid and is only concerned with the conversion of the OC with time. Unlike the SCM which assumes the resistance to gas diffusion is high, the assumption in the MVRM is that there is negligible resistance. To date, no one has reported the use of the MVRM for modelling the redox characteristics of an OC.

There are many references in literature where the reduction of the OC was modelled in the presence of gaseous fuels [74-77]. Adanez *et al.* [4] mentioned that the effect of the gas product concentration on the reduction rate of the OC has been barely analysed and this is required to study the interaction and potential inhibition that may arise due to the presence of the product gases. This requires an in-depth investigation so that the required OC mass for a

given system can be estimated. The conclusion obtained from this subsection is that there has not been any research into the reduction kinetics of an OC in the presence of a solid fuel.

2.5 Economics

The economics of a CLC system is an important aspect to consider for the implementation of this system in the long run. This section will briefly discuss cost estimations that have been performed by various researchers and governmental bodies on the operation of a CLC system. There are various economic factors involved in the design and operation of a CLC system, some of which are similar and others different from a typical pulverized coal power station. Putting aside the differences in the design of the two systems, the OC is one of the most significant factors in terms of costing. It is for this reason that the OC should be cheap and readily available as large volumes will be used in the operation of the CLC system. Synthetic OCs are typically not favoured as the fabrication of such a material incurs additional costs such as the cost of the support material and manufacturing process. Thus an OC that can be used in its natural form, such as an ore, would be ideal for the CLC process.

Abad *et al.* [74] evaluated the impact of the cost of the metal oxide on the CO_2 capture cost based on the lifetime and reactivity of the particles. The authors found the main cost to be associated with the makeup flow of the particles and concluded that using an OC with a lifetime of 300 hours would have the same cost as the amine makeup required in the monoethylamine (MEA) process for the same level of CO_2 capture. It is estimated that future CO_2 capture processes should have a cost of between USD 20-30 for the capture and sequestration of a tonne of CO_2 to be considered feasible. This can be achieved by OCs having a lifetime of 100 hours and such a lifetime is easily accomplished by most OCs [4]. Thus, comparing with other CO_2 capture technologies, it can be inferred that the cost of the OC would not present a limitation to the CLC process.

The research group at ALSTOM Power Plant Laboratories in Windsor, CT, USA tried to determine if CO_2 can be captured at a cost of USD 10 per tonne CO_2 avoided [78]. They predicted that the total capital cost will be relatively low due to the fast reactions that occur in both reactors. The cost of electricity was plotted against the CO_2 allowance price for various CO_2 capture technologies and this is shown in Figure 2-7 where it can be seen that the lowest costs were obtained with the CLC system. This shows that CLC is one of the cheapest methods to capture the CO_2 generated from the combustion of coal. The cost of electricity for

CLC does not change with increasing CO_2 allowance because at least 95% of the emitted CO_2 can be inherently captured by the process.

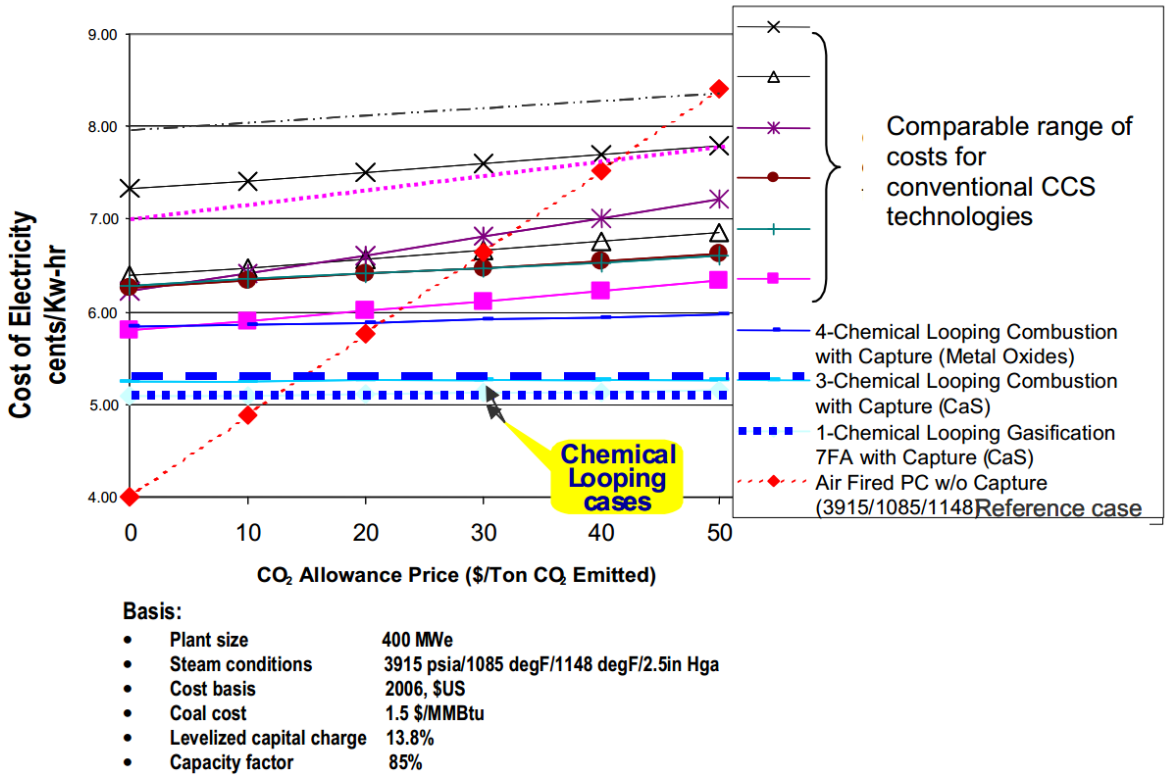

Figure 2-7 Cost of electricity for various carbon dioxide capture and storage technologies [79]

2.6 Summary of Literature Review

It is clearly evident from literature that there are still many aspects which have not been fully investigated, leading to the generation of knowledge gaps in the field. This is intensified in the case of VBC as there has only been one study prior to this and it was predominantly undertaken using a TGA [80].

In terms of cost, literature suggests that CLC is a viable and cost effective carbon dioxide capture and storage technology relative to other options. Researchers have found that the cost of the OC is not expected to be a showstopper in the operation of a CLC system if its lifetime is higher than 100 hours.

Literature shows that both Fe_2O_3 and Mn_3O_4 are promising materials for use as an OC in the CLC process after taking into account the theoretical oxygen carrying capacity, thermodynamic analysis as well as cost and environmental impact. Additionally, Fe_2O_3 has been found to be a very suitable OC for use with VBC compared to CuO and NiO. Although

some of these materials have been experimentally investigated, most of the studies were undertaken using a TGA; this does not simulate a fluidized bed reactor, which is the typical configuration in commercial power stations.

Most of the experiments that have been performed to date deal with the identification of suitable OC materials and proof of concept in large bench scale units. Experimentally, detailed investigations pertaining to certain intrinsic aspects of the process have not been sufficiently researched, such as the fate of nitrogen containing pollutant gases as well as the impact of coal minerals on the overall performance of the CLC system. The effect of coal ash on the OC is also an area which has not been adequately investigated.

In-situ XRD pertaining to the reduction of Fe-based OCs have not been reported in literature. Such an investigation would allow for aspects such as the lattice parameters and the crystallite sizes to be investigated as a function of temperature and time. This information is important as it allows the changes in the OC to be studied as it is reduced and oxidized.

There have been many reactor configurations that have been proposed in literature for use in an iG-CLC system. These include fluidized bed reactors, atmospheric fixed bed reactors as well as pressurized fixed bed reactors, but no study has been undertaken to compare the performance of these three systems in the presence of a solid fuel.

While many OC reduction kinetics models exist in literature, these are limited to gaseous fuels such as natural gas and syngas. To date, there has not been any study on the reduction kinetics of the OC in the presence of a solid fuel such as that in an iG-CLC system.

While some studies have looked into the fabrication and performance of synthetic OCs, most of these studies revolve around supporting the metal oxide on an inert support. There are limited studies on supporting one metal oxide on another and this represents a knowledge gap.

As previously mentioned, most of the preliminary studies on VBC were performed in a TGA and there is no information on the performance of this fuel in a large fluidized bed reactor.

The aforementioned statements represent gaps of knowledge in the field of iG-CLC. Thus, research is still needed in this field to generate information to obtain a comprehensive understanding of the applicability of using VBC in CLC. The following subsections will list the objectives and thesis structure based on the identified gaps.

2.7 Objectives and Thesis Structure

The objective of this work is to determine the applicability of the CLC process using VBC as the fuel and to find out any potential issues with using said fuel.

Chapter 1 provides an introduction to the thesis and deals with carbon dioxide capture and storage, CLC and VBC. The objectives, thesis structure and list of journal publications are also shown.

Chapter 2 centres on a review of the information in literature, focussing on the utilization of solid fuels in an iG-CLC process as well as some of the important characteristics of an ideal OC. This chapter also details the investigations that have been done on the different OCs for iG-CLC such as NiO, CuO, Fe_2O_3 and Mn_2O_3. Since part of the work involves the fabrication and construction of a $10kW_{th}$ CLC reactor, some design considerations are included. This is then followed on with a review of kinetic modelling that has been reported in literature. Next, the economics of the CLC process is reviewed and is followed by a summary.

Chapter 3 details the methodology employed in this thesis. This includes the steps involved in the experiments using the various setups as well as the methodology employed for the analytical analysis using the different instruments for the characterization of the OC. The derivation and application of the kinetic models are also detailed.

Chapter 4 marks the start of the results chapters. Here, the effect of coal minerals on the performance of VBC as well as the potential interactions between the ash formed from the thermal treatment of the minerals and the OC is discussed. Since VBC has a very low ash content, a comparative study was performed with a high ash Canadian lignite to provide a better understanding of ash interaction.

Chapter 5 describes the reduction of the OC using synchrotron-based in-situ X-ray Diffraction (XRD) for iG-CLC using VBC as the fuel. In this chapter, the carbon deposition phenomenon is also discussed.

Chapter 6 involves modelling the reduction of the OC. Two models were generated to predict the reduction of the OC as a function of time. Since such a study has never been performed before, this serves to fill a very important gap in knowledge.

Chapter 7 details the various modes of reactor operation that can be used in CLC. Three modes were investigated including atmospheric fixed bed, pressurized fixed bed and

fluidized bed. This was a comparative assessment on how the mode of operation affected the performance of the CLC system.

Chapter 8 investigates the performance of synthetically fabricated bimetallic OCs which was then compared to a monometallic Fe_2O_3 OC. The synthetically fabricated OCs contained various amounts of the secondary metal oxide (NiO, CuO and Mn_2O_3) supported on Fe_2O_3. The OCs were fabricated using physical mixing and impregnation.

Chapter 9 investigates the performance of VBC-fuelled CLC in a sub-pilot scale $10kW_{th}$ setup. Here, the fuel type was varied alongside the temperature and OC particle size. A carbon balance was performed together with a study on NO_x emissions. Also, a 35 cycle experiment was conducted over 40 hours to study the performance of the OC over longer durations.

Chapter 10 highlights the conclusions from the various studies in this thesis alongside some practical implications. The chapter will be closed by providing some recommendations for future work to advance CLC with VBC.

Figure 2-8 shows an overview of the structure of this thesis.

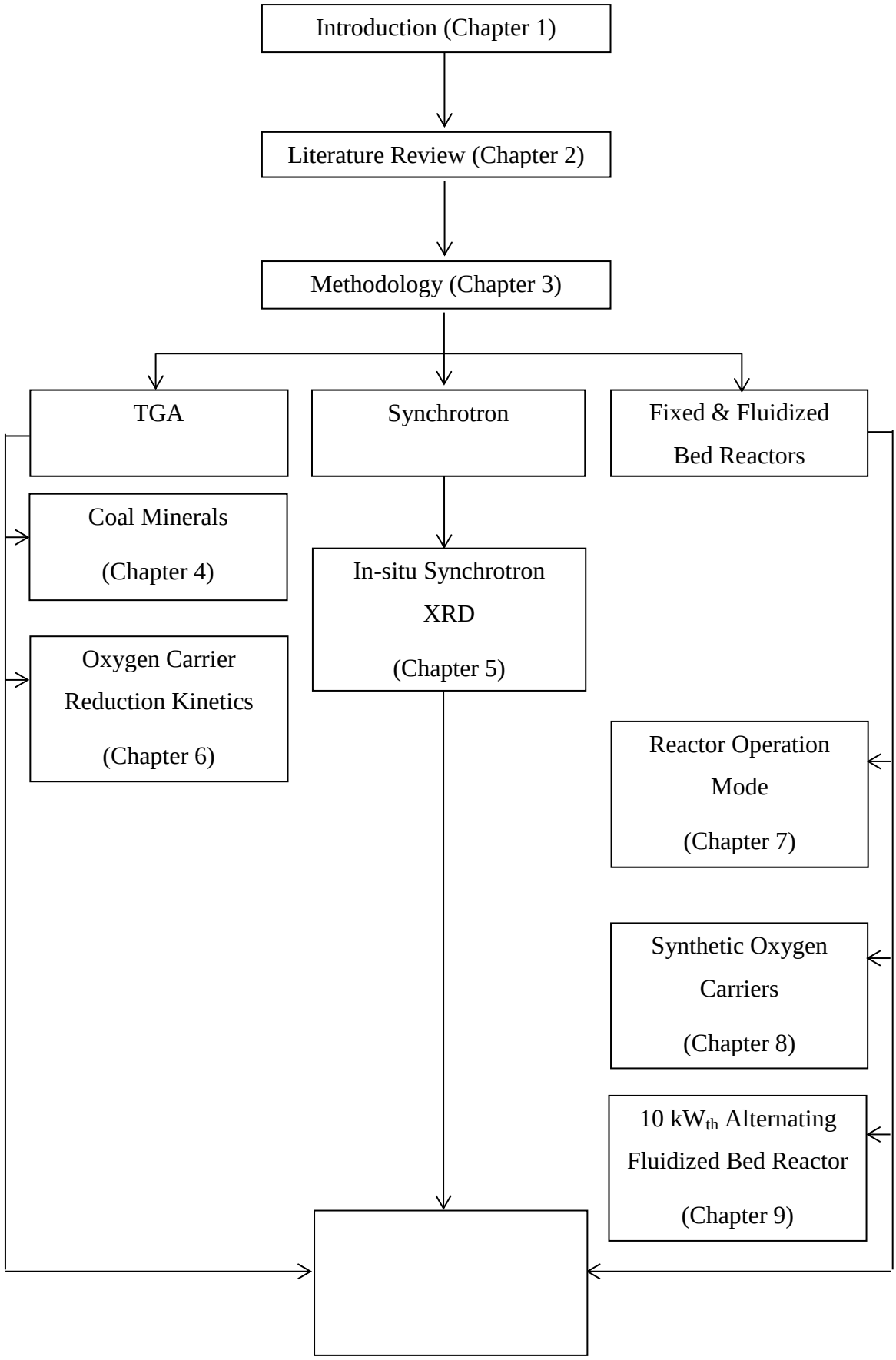

Figure 2-8 Thesis structure

2.8 List of Publications from this Research

The following subsections list the journal and conference papers that have been published during the course of this research project as well as some others that have been prepared.

2.8.1 Journal Paper Publications

1. Use of Synthetic Oxygen Carriers for Chemical Looping Combustion of Victorian Brown Coal
   (S Rajendran, S Zhang, R Xiao, S Bhattacharya, Proceedings of the Combustion Institute)
2. Use of Pyrite Cinder as an Iron-Based Oxygen Carrier in Coal-Fuelled Chemical Looping Combustion
   (*S Zhang, S Rajendran, S Henderson, D Zeng, R Xiao, S Bhattacharya, Energy & Fuels)*
3. Chemical Looping Combustion of Coal in a 5 kWth Interconnected Fluidized Bed Reactor Using Hematite as Oxygen Carrier
   (J Ma, H Zhao, X Tian, Y Wei, S Rajendran, Y Zhang, S Bhattacharya, C Zheng, Applied Energy)

2.8.2 Conference Proceedings

1. Reduction Characteristics of Hematite- Victorian Brown Coal And Char Pellets For Applications To Chemical Looping Combustions
   (C Saha, S Rajendran, S Bhattacharya, International Workshop on Clean Technologies of Coal and Biomass Utilization, June 2012, Anshan, China)
2. Experimental Investigation of Chemical Looping Combustion of Victorian Brown Coal using Hematite
   (C Saha, S Rajendran, K Hein, S Bhattacharya, Chemeca, September 2012, Wellington, New Zealand)
3. Chemical Looping Combustion of Victorian Brown Coals – Scientific and Technical Issues
   (S Rajendran, C Saha, K Hein, S Bhattacharya, 2nd International Conference on Chemical Looping, September 2012, Darmstadt, Germany)

4. Chemical-Looping Combustion of Victorian Brown Coal using Mixed Oxygen Carriers of Iron and Manganese Oxides
   (S Zhang, S Rajendran, R Xiao, S Bhattacharya, Chemeca, September 2013, Brisbane, Australia)
5. Chemical Looping Combustion of Victorian Brown Coal Using Iron Ores
   (*T Karlsson, J Ma, S Rajendran, S Bhattacharya, The 39th Clearwater coal conference, June 2014, Florida, USA)*
6. Chemical Looping Combustion of Coal in a 5 kW_{th} Interconnected Fluidized Bed Reactor Using a Hematite Oxygen Carrier
   (*J Ma, H Zhao, X Tian, Y Wei, S Rajendran, Y Zhang, S Bhattacharya, C Zheng, The 3rd International Conference on Chemical Looping, September 2014, Goteborg, Sweden)*
7. Chemical Looping Combustion of Victorian Brown Coal with Hematite and Ilmenite as Oxygen Carriers
   (*M Wong, S Rajendran, S Bhattacharya, International Conference on Coal Science & Technology, September 2015, Victoria, Australia)*

2.8.3 Draft Journal Papers Prepared

1. Effect of Inherent Coal Minerals on the Performance of Chemical Looping Combustion – A Thermogravimetric Analyzer Study
   (*S Rajendran, S Zhang, M Rahman, R Xiao, R Gupta, S Bhattacharya)*
2. Use of Mn-, Cu- and Ni-based Synthetic Oxygen Carriers Supported on Fe_2O_3 in Chemical Looping Combustion of Victorian Brown Coal
   (S Zhang, S Rajendran, S Bhattacharya, R Xiao)
3. In-situ Synchrotron Study of Fe_2O_3 Reduction with Victorian Brown Coal
   (*S Rajendran, S Zhang, H Casely, R Xiao, S Bhattacharya)*
4. Reduction kinetics of Fe_2O_3 in the presence of Victorian Brown Coal
   (*S Rajendran, A Marshall, M Jacobs, S Bhattacharya*)

The next chapter will provide details pertaining to the methodology employed for the various experimental and modelling studies undertaken in this thesis.

2.9 References

1. Johansson, M., T. Mattisson, and A. Lyngfelt, *Use of NiO/NiAl2O4 particles in a 10 kW chemical-looping combustor.* Industrial & Engineering Chemistry Research, 2006. **45**(17): p. 5911-5919.
2. Linderholm, C., E. Jerndal, T. Mattisson, and A. Lyngfelt, *Investigation of NiO-based mixed oxides in a 300-W chemical-looping combustor.* Chemical Engineering Research and Design, 2010. **88**(5–6): p. 661-672.
3. Jerndal, E., T. Mattisson, and A. Lyngfelt, *Thermal Analysis of Chemical-Looping Combustion.* Chemical Engineering Research and Design, 2006. **84**(9): p. 795-806.
4. Adanez, J., A. Abad, F. Garcia-Labiano, P. Gayan, and L.F. de Diego, *Progress in Chemical-Looping Combustion and Reforming technologies.* Progress in Energy and Combustion Science, 2012. **38**(2): p. 215-282.
5. Zhang, J.S., Q.J. Guo, Y.Z. Liu, and Y. Cheng, *Preparation and Characterization of Fe2O3/Al2O3 Using the Solution Combustion Approach for Chemical Looping Combustion.* Industrial & Engineering Chemistry Research, 2012. **51**(39): p. 12773-12781.
6. Jerndal, E., T. Mattisson, I. Thijs, F. Snijkers, and A. Lyngfelt, *NiO particles with Ca and Mg based additives produced by spray-drying as oxygen carriers for chemical-looping combustion.* Greenhouse Gas Control Technologies 9, 2009. **1**(1): p. 479-486.
7. Baek, J.I., J.W. Kim, J.B. Lee, T.H. Eom, J. Ryu, C.K. Ryu, and J. Yi, *Effects of Support on the Performance of NiO-Based Oxygen Carriers.* Oil & Gas Science and Technology-Revue D Ifp Energies Nouvelles, 2011. **66**(2): p. 223-234.
8. de Diego, L.F., P. Gayan, F. Garcia-Labiano, J. Celaya, M. Abad, and J. Adanez, *Impregnated CuO/Al2O3 oxygen carriers for chemical-looping combustion: Avoiding fluidized bed agglomeration.* Energy & Fuels, 2005. **19**(5): p. 1850-1856.
9. He, F., H. Wang, and Y. Dai, *Application of Fe2O3/Al2O3 Composite Particles as Oxygen Carrier of Chemical Looping Combustion.* Journal of Natural Gas Chemistry, 2007. **16**(2): p. 155-161.
10. Mattisson, T., M. Johansson, and A. Lyngfelt, *Multicycle reduction and oxidation of different types of iron oxide particles - Application to chemical-looping combustion.* Energy & Fuels, 2004. **18**(3): p. 628-637.
11. Wang, S.Z., M. Luo, G.X. Wang, L.F. Wang, and M.M. Lv, *Analysis of Reactivity of a CuO-Based Oxygen Carrier for Chemical Looping Combustion of Coal.* Energy & Fuels, 2012. **26**(6): p. 3275-3283.
12. Erri, P. and A. Varma, *Solution combustion synthesized oxygen carriers for chemical looping combustion.* Chemical Engineering Science, 2007. **62**(18-20): p. 5682-5687.
13. Johansson, M., T. Mattisson, and A. Lyngfelt, *Investigation of Mn3O4 with stabilized ZrO2 for chemical-looping combustion.* Chemical Engineering Research & Design, 2006. **84**(A9): p. 807-818.
14. Ryden, M., E. Cleverstam, M. Johansson, A. Lyngfelt, and T. Mattisson, *Fe2O3 on Ce-, Ca-, or Mg-Stabilized ZrO2 as Oxygen Carrier for Chemical-Looping Combustion Using NiO as Additive.* Aiche Journal, 2010. **56**(8): p. 2211-2220.
15. Ksepko, E., R.V. Siriwardane, H.J. Tian, T. Simonyi, and M. Sciazko, *Effect of H2S on Chemical Looping Combustion of Coal-Derived Synthesis Gas over Fe-Mn Oxides Supported on Sepiolite, ZrO2, and Al2O3.* Energy & Fuels, 2012. **26**(4): p. 2461-2472.
16. Gu, H.M., L.H. Shen, J. Xiao, S.W. Zhang, T. Song, and D.Q. Chen, *Iron ore as oxygen carrier improved with potassium for chemical looping combustion of anthracite coal.* Combustion and Flame, 2012. **159**(7): p. 2480-2490.

17. Xiao, R., L.Y. Chen, C. Saha, S. Zhang, and S. Bhattacharya, *Pressurized chemical-looping combustion of coal using an iron ore as oxygen carrier in a pilot-scale unit.* International Journal of Greenhouse Gas Control, 2012. **10**: p. 363-373.
18. Arjmand, M., H. Leion, A. Lyngfelt, and T. Mattisson, *Use of manganese ore in chemical-looping combustion (CLC)-Effect on steam gasification.* International Journal of Greenhouse Gas Control, 2012. **8**: p. 56-60.
19. Pour, N.M., *Production and examination of oxygen carrier materials based on different manganese ores with addition of calcium hydroxide or iron oxide in chemical-looping combustion.* 2013.
20. Azis, M.M., E. Jerndal, H. Leion, T. Mattisson, and A. Lyngfelt, *On the evaluation of synthetic and natural ilmenite using syngas as fuel in chemical-looping combustion (CLC).* Chemical Engineering Research and Design, 2010. **88**(11): p. 1505-1514.
21. Cuadrat, A., A. Abad, F. García-Labiano, P. Gayán, L.F. de Diego, and J. Adánez, *Ilmenite as oxygen carrier in a chemical looping combustion system with coal.* Energy Procedia, 2011. **4**(0): p. 362-369.
22. Linderholm, C., P. Knutsson, M. Schmitz, P. Markström, and A. Lyngfelt, *Material balances of carbon, sulfur, nitrogen and ilmenite in a 100kW CLC reactor system.* International Journal of Greenhouse Gas Control, 2014. **27**: p. 188-202.
23. Saha, C. and S. Bhattacharya, *Comparison of CuO and NiO as oxygen carrier in chemical looping combustion of a Victorian brown coal.* International Journal of Hydrogen Energy, 2011. **36**(18): p. 12048-12057.
24. Gayan, P., C.R. Forero, A. Abad, L.F. de Diego, F. Garcia-Labiano, and J. Adanez, *Effect of Support on the Behavior of Cu-Based Oxygen Carriers during Long-Term CLC Operation at Temperatures above 1073 K.* Energy & Fuels, 2011. **25**(3): p. 1316-1326.
25. Tian, H.J., T. Simonyi, J. Poston, and R. Siriwardane, *Effect of Hydrogen Sulfide on Chemical Looping Combustion of Coal-Derived Synthesis Gas over Bentonite-Supported Metal-Oxide Oxygen Carriers.* Industrial & Engineering Chemistry Research, 2009. **48**(18): p. 8418-8430.
26. Garcia-Labiano, F., L.F. de Diego, P. Gayan, J. Adanez, A. Abad, and C. Dueso, *Effect of Fuel Gas Composition in Chemical-Looping Combustion with Ni-Based Oxygen Carriers. 1. Fate of Sulfur.* Industrial & Engineering Chemistry Research, 2009. **48**(5): p. 2499-2508.
27. Forero, C.R., P. Gayan, F. Garcia-Labiano, L.F. de Diego, A. Abad, and J. Adanez, *Effect of gas composition in Chemical-Looping Combustion with copper-based oxygen carriers: Fate of sulphur.* International Journal of Greenhouse Gas Control, 2010. **4**(5): p. 762-770.
28. Keller, M., M. Arjmand, H. Leion, and T. Mattisson, *Interaction of mineral matter of coal with oxygen carriers in chemical-looping combustion (CLC).* Chemical Engineering Research and Design, 2014. **92**(9): p. 1753-1770.
29. Cho, P., T. Mattisson, and A. Lyngfelt, *Carbon Formation on Nickel and Iron Oxide-Containing Oxygen Carriers for Chemical-Looping Combustion.* Industrial & Engineering Chemistry Research, 2005. **44**(4): p. 668-676.
30. Cuadrat, A., A. Abad, F. Garcia-Labiano, P. Gayan, L.F. de Diego, and J. Adanez, *Effect of operating conditions in Chemical-Looping Combustion of coal in a 500 W-th unit.* International Journal of Greenhouse Gas Control, 2012. **6**: p. 153-163.
31. Thunman, H., F. Lind, C. Breitholtz, N. Berguerand, and M. Seemann, *Using an oxygen-carrier as bed material for combustion of biomass in a 12-MW< sub> th</sub> circulating fluidized-bed boiler.* Fuel, 2013. **113**: p. 300-309.

32. Leion, H., T. Mattisson, and A. Lyngfelt, *The use of petroleum coke as fuel in chemical-looping combustion.* Fuel, 2007. **86**(12–13): p. 1947-1958.
33. Brown, T.A., J.S. Dennis, S.A. Scott, J.F. Davidson, and A.N. Hayhurst, *Gasification and chemical-looping combustion of a lignite char in a fluidized bed of iron oxide.* Energy and Fuels, 2010. **24**(5): p. 3034-3048.
34. Laurendeau, N.M., *Heterogeneous kinetics of coal char gasification and combustion.* Progress in Energy and Combustion Science, 1978. **4**(4): p. 221-270.
35. Balsamo, M., F. Di Natale, A. Erto, A. Lancia, F. Magri, F. Montagnaro, and L. Santoro, *Steam-and CO2-Gasification of Coal Combustion Ash Aimed at its Utilization in Adsorption Processes.*
36. Leion, H., A. Lyngfelt, and T. Mattisson. *Effects of steam and CO 2 in the fluidizing gas when using bituminous coal in chemical-looping combustion*. in *Proceedings of the 20th International Conference on Fluidized Bed Combustion*. 2010. Springer.
37. Peters, W. *Fundamentals of coal gasification*. in *Gasification and Liquefaction of Coal*. 1976.
38. Scott, S.A., J.S. Dennis, A.N. Hayhurst, and T. Brown, *In situ gasification of a solid fuel and CO2 separation using chemical looping.* AIChE Journal, 2006. **52**(9): p. 3325-3328.
39. Cao, Y., B. Casenas, and W.-P. Pan, *Investigation of Chemical Looping Combustion by Solid Fuels. 2. Redox Reaction Kinetics and Product Characterization with Coal, Biomass, and Solid Waste as Solid Fuels and CuO as an Oxygen Carrier.* Energy & Fuels, 2006. **20**(5): p. 1845-1854.
40. Leion, H., T. Mattisson, and A. Lyngfelt, *Chemical looping combustion of solid fuels in a laboratory fluidized-bed reactor.* Combustion de charges solides avec la boucle chimique dans un lit fluidisé de laboratoire, 2011. **66**(2): p. 201-208.
41. Shen, L., J. Wu, Z. Gao, and J. Xiao, *Reactivity deterioration of NiO/Al2O3 oxygen carrier for chemical looping combustion of coal in a 10 kWth reactor.* Combustion and Flame, 2009. **156**(7): p. 1377-1385.
42. Dennis, J.S. and S.A. Scott, *In situ gasification of a lignite coal and CO2 separation using chemical looping with a Cu-based oxygen carrier.* Fuel, 2010. **89**(7): p. 1623-1640.
43. Müller, C., T. Brown, C. Bohn, S. Chuang, J. Cleeton, S. Scott, and J. Dennis. *Experimental Investigation of Two Modified Chemicallooping Compustion Cycles Using Syngas from Cylindersand the Gasification of Solid Fuels*. in *Proceedings of the 20th International Conference on Fluidized Bed Combustion*. 2010. Springer.
44. Gao, Z., L. Shen, J. Xiao, C. Qing, and Q. Song, *Use of Coal as Fuel for Chemical-Looping Combustion with Ni-Based Oxygen Carrier.* Industrial & Engineering Chemistry Research, 2008. **47**(23): p. 9279-9287.
45. Shen, L., J. Wu, Z. Gao, and J. Xiao, *Characterization of chemical looping combustion of coal in a 1 kWth reactor with a nickel-based oxygen carrier.* Combustion and Flame, 2010. **157**(5): p. 934-942.
46. Shen, L., J. Wu, and J. Xiao, *Experiments on chemical looping combustion of coal with a NiO based oxygen carrier.* Combustion and Flame, 2009. **156**(3): p. 721-728.
47. Forero, C.R., P. Gayán, F. García-Labiano, L.F. de Diego, A. Abad, and J. Adánez, *Effect of gas composition in Chemical-Looping Combustion with copper-based oxygen carriers: Fate of sulphur.* International Journal of Greenhouse Gas Control, 2010. **4**(5): p. 762-770.
48. Leion, H., A. Lyngfelt, and T. Mattisson, *Solid fuels in chemical-looping combustion using a NiO-based oxygen carrier.* Chemical Engineering Research and Design, 2009. **87**(11): p. 1543-1550.

49. Saha, C., B. Roy, and S. Bhattacharya, *Chemical looping combustion of Victorian brown coal using NiO oxygen carrier.* International Journal of Hydrogen Energy, 2011. **36**(4): p. 3253-3259.
50. Saha, C. and S. Bhattacharya, *Chemical looping combustion of low-ash and high-ash low rank coals using different metal oxides - A thermogravimetric analyser study.* Fuel, 2012. **97**: p. 137-150.
51. Arjmand, M., H. Leion, T. Mattisson, and A. Lyngfelt, *Investigation of different manganese ores as oxygen carriers in chemical-looping combustion (CLC) for solid fuels.* Applied Energy, 2014. **113**(0): p. 1883-1894.
52. Leion, H., T. Mattisson, and A. Lyngfelt, *Solid fuels in chemical-looping combustion.* International Journal of Greenhouse Gas Control, 2008. **2**(2): p. 180-193.
53. Berguerand, N. and A. Lyngfelt, *Design and operation of a 10 kWth chemical-looping combustor for solid fuels – Testing with South African coal.* Fuel, 2008. **87**(12): p. 2713-2726.
54. Berguerand, N. and A. Lyngfelt, *The use of petroleum coke as fuel in a 10kWth chemical-looping combustor.* International Journal of Greenhouse Gas Control, 2008. **2**(2): p. 169-179.
55. Berguerand, N. and A. Lyngfelt, *Operation in a 10 kWth chemical-looping combustor for solid fuel—Testing with a Mexican petroleum coke.* Energy Procedia, 2009. **1**(1): p. 407-414.
56. Berguerand, N. and A. Lyngfelt, *Chemical-Looping Combustion of Petroleum Coke Using Ilmenite in a 10 kWth Unit−High-Temperature Operation.* Energy & Fuels, 2009. **23**(10): p. 5257-5268.
57. Cuadrat, A., A. Abad, F. García-Labiano, P. Gayán, L.F. de Diego, and J. Adánez, *The use of ilmenite as oxygen-carrier in a 500 Wth Chemical-Looping Coal Combustion unit.* International Journal of Greenhouse Gas Control, 2011. **5**(6): p. 1630-1642.
58. Wu, J., L. Shen, J. Hao, and H. Gu. *Chemical Looping Combustion of Coal in a 1 kWth reactor with Iron Ore as an Oxygen Carrier*. in *Proc. 1st Int Conf on Chemical Looping. Lyon, France*. 2010.
59. Zhang, S., C. Saha, Y.C. Yang, S. Bhattacharya, and R. Xiao, *Use of Fe2O3-Containing Industrial Wastes As the Oxygen Carrier for Chemical-Looping Combustion of Coal: Effects of Pressure and Cycles.* Energy & Fuels, 2011. **25**(10): p. 4357-4366.
60. Kronberger, B., A. Lyngfelt, G. Löffler, and H. Hofbauer, *Design and Fluid Dynamic Analysis of a Bench-Scale Combustion System with CO2 Separation−Chemical-Looping Combustion.* Industrial & Engineering Chemistry Research, 2005. **44**(3): p. 546-556.
61. Wolf, J. and K.T.h.I.f. kemiteknik, *CO2 Mitigation in Advanced Power Cycles: Chemical Looping Combustion and Steam-based Gasification*. 2004.
62. Hossain, M.M. and H.I. de Lasa, *Chemical-looping combustion (CLC) for inherent separations—a review.* Chemical Engineering Science, 2008. **63**(18): p. 4433-4451.
63. Lyngfelt, A., B. Leckner, and T. Mattisson, *A fluidized-bed combustion process with inherent CO2 separation; application of chemical-looping combustion.* Chemical Engineering Science, 2001. **56**(10): p. 3101-3113.
64. Lyngfelt, A., M. Johansson, and T. Mattisson. *Chemical-looping combustion-status of development*. in *9th International Conference on Circulating Fluidized Beds May 13-May 16, Hamburg 2008*. 2008.

65. Hossain, M.M. and H.I. de Lasa, *Reduction and oxidation kinetics of Co–Ni/Al2O3 oxygen carrier involved in a chemical-looping combustion cycles.* Chemical Engineering Science, 2010. **65**(1): p. 98-106.
66. Georgakis, C., C. Chang, and J. Szekely, *A changing grain size model for gas—solid reactions.* Chemical Engineering Science, 1979. **34**(8): p. 1072-1075.
67. Szekely, J., J.W. Evans, and H.Y. Sohn, *Gas-solid reactions*. Vol. 66. 1976: Academic Press New York.
68. Dueso, C., M. Ortiz, A. Abad, F. Garcia-Labiano, L.F. de Diego, P. Gayan, and J. Adanez, *Reduction and oxidation kinetics of nickel-based oxygen-carriers for chemical-looping combustion and chemical-looping reforming.* Chemical Engineering Journal, 2012. **188**: p. 142-154.
69. Abad, A., J. Adanez, A. Cuadrat, F. Garcia-Labiano, P. Gayan, and L.F. de Diego, *Kinetics of redox reactions of ilmenite for chemical-looping combustion.* Chemical Engineering Science, 2011. **66**(4): p. 689-702.
70. Song, H., E. Doroodchi, and B. Moghtaderi, *Redox Characteristics of Fe-Ni/SiO2 Bimetallic Oxygen Carriers in CO under Conditions Pertinent to Chemical Looping Combustion.* Energy & Fuels, 2012. **26**(1): p. 75-84.
71. Saha, C. and S. Bhattacharya, *Determination and Comparison of CuO Reduction/Oxidation Kinetics in CLC Experiments with CO/Air by the Shrinking Core Model and Its Characterization.* Energy & Fuels, 2014. **28**(5): p. 3495-3510.
72. Moghtaderi, B. and H. Song, *Reduction properties of physically mixed metallic oxide oxygen carriers in chemical looping combustion.* Energy & Fuels, 2010. **24**(10): p. 5359-5368.
73. Sedor, K.E., M.M. Hossain, and H.I. de Lasa, *Reduction kinetics of a fluidizable nickel–alumina oxygen carrier for chemical ‐looping combustion.* The Canadian Journal of Chemical Engineering, 2008. **86**(3): p. 323-334.
74. Abad, A., J. Adánez, F. García-Labiano, L.F. de Diego, P. Gayán, and J. Celaya, *Mapping of the range of operational conditions for Cu-, Fe-, and Ni-based oxygen carriers in chemical-looping combustion.* Chemical Engineering Science, 2007. **62**(1–2): p. 533-549.
75. Abad, A., F. García-Labiano, L.F. de Diego, P. Gayán, and J. Adánez, *Reduction Kinetics of Cu-, Ni-, and Fe-Based Oxygen Carriers Using Syngas (CO + H2) for Chemical-Looping Combustion.* Energy & Fuels, 2007. **21**(4): p. 1843-1853.
76. García-Labiano, F., L.F. de Diego, J. Adánez, A. Abad, and P. Gayán, *Reduction and Oxidation Kinetics of a Copper-Based Oxygen Carrier Prepared by Impregnation for Chemical-Looping Combustion.* Industrial & Engineering Chemistry Research, 2004. **43**(26): p. 8168-8177.
77. Abad, A., J. Adánez, F. García-Labiano, L.F. de Diego, and P. Gayán, *Modeling of the chemical-looping combustion of methane using a Cu-based oxygen carrier.* Energy Procedia, 2009. **1**(1): p. 391-398.
78. Marion, J.L. and N.y. Nsakala, *Greenhouse gas emissions control by oxygen firing in circulating fluid bed boilers (Phase II – Evaluation of the Oxyfuel CFB Concept)*. 2003, US Power Plant Laboratories, ALSTOM Power, Inc. 2000 Day Hill Road Windsor, Connecticut 06095.
79. Andrus, H., J. Chiu, P. Thibeault, and A. Brautsch. *Alstom's calcium oxide chemical looping combustion coal power technology development*. in *The 34th International technical conference on clean coal & fuel systems, Clearwater, Florida, USA*. 2009.
80. Saha, C., *Chemical-looping combustion of Victorian brown coal*.

Chapter 3 Methodology

This chapter will detail the various equipment used in this study together with the different analytical instruments used for the characterization of the fuels as well as the fresh and used OC particles. The two kinetic models, Shrinking Core Model and Modified Volume Reaction Model, will also be described in detail. Also, a summary of the experimental conditions employed in each of the studies will be provided at the start of the chapter.

This chapter will detail the methodology of the work carried out in this thesis.

3.1 Materials

In this thesis, a few different OCs have been used alongside a Victorian brown coal, Yallourn, which was the primary fuel used in all of the investigations. A high ash Canadian lignite was used in one of the studies for comparison purposes. The materials that were used will be described in the following subsections.

3.1.1 Fuel

The fuel predominantly used in this study is Yallourn coal from the La Trobe Valley in Victoria, Australia. The properties of this fuel can be found in Table 3-1 below. As can be seen in the proximate analysis, around 50% of the fuel is composed of volatile matter, with around 47% fixed carbon and around 2% ash. Herein lies the important characteristics of this fuel, it has very low ash and high amounts of volatiles. A low ash content is favourable in combustion and even more so in CLC as this would reduce the potential interactions with the OC. A high volatile content means that a significant amount of the fuel is released in gaseous form, which can readily react with the OC. This would leave behind a smaller amount of char, which will then need to be gasified before it can react with the OC. As such, VBC would require less time to be gasified relative to high rank fuels such as bituminous coals and anthracite. The ultimate analysis shows that around 70% of the mass of the coal is comprised of carbon with around 24% oxygen, 5% hydrogen and less than half a percent each of nitrogen and sulphur. The low levels of sulphur and nitrogen are highly advantageous, as this would reduce the generated amount of sulphur and nitrogen containing gases. These would need to be separated and removed prior to compression and storage of the CO_2. With respect to the ash composition, it can be seen that around 40% is Fe_2O_3 with appreciable amounts of SiO_2, MgO, CaO, Na_2O and Al_2O_3. The amount of TiO_2 and K_2O are minimal in Yallourn coal.

A Canadian lignite with a much higher ash content was also employed in a comparative study using a thermogravimetric analyzer (TGA). This coal sample was obtained from Boundary Dam, Alberta and the composition of this coal can be found in Table 3-1. A significant difference can be seen here with the ash content being almost an order of magnitude larger compared to Yallourn coal. Additionally, the fixed carbon and volatile matter content is around 10% lesser here compared to the VBC. The levels of carbon, hydrogen and oxygen are relatively similar to Yallourn coal with higher levels of sulphur and nitrogen. Unlike Yallourn coal, the ash in this coal is predominantly composed of SiO_2 at around 42% with significant amounts of Al_2O_3 and CaO.

Table 3-1 Composition of fuels

Components	Victorian brown coal	Char from Victorian brown coal	Canadian lignite
Proximate Analysis (% db)			
Ash	2.4	4	19.8
Volatile Matter	50.4	0.7	39.6
Fixed Carbon	47.2	95.3	40.6
Ultimate Analysis (% db, ash free)			
C	70.6	96.3	69.1
H	4.6	0.8	5.0
N	0.4	0.7	1.5
S	0.2	0.2	0.9
O	24.2	2.0	23.5
Ash Composition (%)			
SiO_2	10.4	4.4	41.6
Al_2O_3	4.0	3.4	25.5
Fe_2O_3	40.2	43.6	3.7
TiO_2	0.2	0.1	1.0
K_2O	0.6	0.3	0.5
MgO	15.7	14.4	2.0
Na_2O	5.6	4.2	6.0
CaO	7.8	11.8	12.7
SO_3	15.5	17.8	7.0

db: dry basis

Some of the investigations involved the use of Yallourn char and the composition of this can be found in the above table. The coal was first placed into a fixed bed reactor having an internal diameter of 50 mm. The reactor was placed into a tubular furnace which was then heated to 1000°C at a rate of 10°C/min with N_2 as the sweep gas. The use of N_2 served to reduce the diffusion of oxygen into the reactor and provided an inert atmosphere to drive off the volatile matter present in the coal. The temperature was isothermally held for 8 hours, after which the furnace was switched off while retaining the N_2 sweep gas. Once ambient temperatures were reached, the char was removed.

3.1.1.1 Demineralization

To study the effect of coal minerals on the performance of CLC, coal demineralization processes were employed to significantly reduce the amount of minerals present in the coal matrix. The demineralization would also lead to a reduction in the amount of ash formed from the thermal treatment of the coal. Yallourn coal was subjected to a three step demineralization process while the Canadian coal was demineralized using a solvent extraction process [1]. Although different demineralization methods were used, this was not the focus of the study and the final outcome, demineralized coal, was the same.

The chemicals utilized for the demineralization of the Yallourn coal were NaOH, H_2SO_4 and HNO_3. The demineralization process used was similar to that used by Yang *et al.* [2] with slight modifications. 100 mg of Yallourn coal was mixed with 600 mL of 10% NaOH solution and maintained at a temperature of 90°C for 90 minutes. This was then cooled down to room temperature and centrifuged to separate the NaOH from the coal. The coal was washed thoroughly with distilled water and subsequently filtered until a pH of 5 was reached in the filtrate. This coal was then mixed with 500 mL of 4% H_2SO_4 at a temperature of 80°C for 60 minutes. Following this duration, the mixture was diluted with distilled water and filtered until the filtrate had a pH of 5. Finally, the coal was mixed with 500 mL of 20% HNO_3 solution for 60 minutes at a temperature of 80°C. When this was completed, the mixture was diluted and filtered as above but to a pH of 6.5. The retentate, demineralized coal, was dried to remove the moisture. The ash content of the demineralized coal was determined according to the AS 2434.8-2002 method and was found to be 0.46%. Since a very small amount of sample was generated, ash analysis could not be performed and as such it was assumed that the extent of demineralization of the different minerals was similar to that of Yang *et al*. [2]. The authors reported that approximately 90% of the silica and alumina

were removed during the caustic digestion, while 75% of the pyrite reacted with the caustic acid. The sulphuric acid leaching reduced the levels of organic sulphur and hematite. Lastly, the nitric acid leaching step removed a large proportion of the pyrite.

The demineralization process of the Canadian coal required the use of hydrotreated solvent (heavy aromatic hydrocarbons) containing 58% aromatic proton as measured by ^{1}H-NMR (Proton Nuclear Magnetic Resonance) and 84% aromatic carbon as measured by ^{13}C-NMR (Carbon Nuclear Magnetic Resonance) using a Varian Inova-400 Nuclear Magnetic Resonance (NMR) spectrometer that was operated at 399.794 MHz for proton and 100.54 MHz for carbon. The process involved heating the coal-solvent slurry to a temperature of 400 °C under an inert nitrogen atmosphere with an initial and final pressure of 10 and 30 bar in an autoclave. The ash content of the demineralized coal samples was found to be 0.04% as determined according to the American Society for Testing and Materials (ASTM) D3174 method

3.1.1.2 Drying and Sieving

As different studies had different requirements, the coal and char samples were crushed to the required size fraction and then dried overnight in a muffle furnace at 110°C. This was done to remove the moisture present in the fuel sample. Three different particle size ranges were used and this depended on the requirements of the study; the three particle size ranges were: 106-150, 125-180 and 600-1000 µm.

3.1.2 Oxygen Carriers

As mentioned previously, a few different OCs were investigated and these are listed in the following subsections.

3.1.2.1 Commercial Fe_2O_3

Commercial Fe_2O_3 was employed in some of the studies and these were procured from Chem Supply. These were laboratory grade samples with a minimum assay of 96%, the remainder being predominantly moisture; these samples were sieved to a size range of 106-150 µm. Such a sample was used to limit the interactions of the coal ash to Fe_2O_3, as an iron-based ore would contain other minerals which may also interact with the ash. For one of the studies, this sample was calcined overnight at 950°C in the presence of air through the use of a muffle furnace.

3.1.2.2 Synthetic Oxygen Carriers

Several synthetic OCs were fabricated by supporting a secondary metal oxide (CuO, NiO and Mn_2O_3) on the primary metal oxide, Fe_2O_3, to yield bimetallic OCs. Two methods of preparation were employed, which were physical mixing and wet impregnation. These two methods were employed as the former is simple mechanical process while the latter provides a high degree of dispersion for the secondary metal oxide. Three different loading contents of the secondary metal oxide were investigated, which were 5, 10 and 20 wt%.

The impregnated samples were prepared by mixing stoichiometric amounts of $Ni(NO_3)_2$, $Cu(NO_3)_2$ and $Mn(NO_3)_2$, all of which were commercially obtained, with Fe_2O_3 in a beaker to yield a final product containing 5, 10 and 20 wt% of the secondary metal oxide. Alternatively, the physically mixed samples were generated by mixing 5, 10 and 20 wt% of NiO, CuO and Mn_2O_3, all reagent grade samples, with Fe_2O_3 in 500 mL of distilled water in a beaker. The Fe_2O_3 used in both methods of preparation was of reagent grade and was commercially obtained as well. A beaker containing the slurry was then placed atop a heated magnetic stir plate operated at a temperature of 80°C with the stirrer rotating at 400 RPM to ensure good contact between the various reagents while ensuring quick evaporation of the liquid. To ensure consistency, the Fe_2O_3 sample was also mixed with water and subjected to the same procedure as the other samples. After 6 hours of mixing, the samples were air dried overnight at 110°C using an oven. These samples were then calcined at 900°C in a muffle furnace over a period of 8 hours to increase the mechanical strength. Once the samples had cooled down, they were crushed and sieved to a size range of 150-350 µm.

The samples are denoted by the preparation method, followed by the percentage mass loading of the secondary metal oxide and terminated with the primary metal oxide. A sample called I-20Mn-Fe represents an OC having 20 wt% of Mn_2O_3 impregnated onto Fe_2O_3.

3.1.2.3 Natural Ores

Two natural ores were used in two separate studies in this thesis. The first was obtained from Companhia Vale do Rio Doce (CVRD) in Brazil. The OC particles were calcined at 1000°C, after which they were sieved to a particle size range of 90-180 µm. The composition of this iron ore can be found in Table 3-2. It can be seen that this ore only contains Fe_2O_3 as the active metal oxide with minor amounts of SiO_2 and Al_2O_3 making up the balance.

The second ore was obtained from Western Australia. The fresh sample was predominantly composed of geothite (FeO(OH)), hematite (Fe_2O_3) and silica (SiO_2). Upon calcination, the geothite was found to oxidize to hematite and the composition of the calcined sample can be found in Table 3-2. The calcined OC can be seen to primarily contain Fe_2O_3 with small amounts of SiO_2 and Al_2O_3. Additionally, some Na was present in the OC matrix. While CuO was also present, the amount was considered to be negligible as it was less than 0.02%. This OC was sieved to a size range of 150-350 µm for the vast majority of the experiments; to investigate the effect of the OC particle size, some were sieved to a size range of 106-150 µm.

Table 3-2 Ore composition

Compound	Western Australian ore	CVRD ore
	wt%	
Fe_2O_3	95.15	94.8
SiO_2	2.21	4.3
Na_2O	1.20	-
Al_2O_3	1.11	0.9
MgO	0.20	-
P_2O_5	0.07	-
SO_3	0.02	-
CuO	0.02	-
As_2O_3	0.01	-
ZnO	0.01	-

3.2 Experimental Equipment and Analytical Instruments

A number of different experimental equipment were used in this thesis, including a thermogravimetric analyzer (TGA), a bench scale fluidized bed reactor, a multipurpose reactor and a 10 kW_{th} sub-pilot scale fluidized bed reactor. These will be described in detail in the following subsections.

3.2.1 TGA

A NETZSCH STA 449 F3 Jupiter TGA, as shown in Figure 3-1, was used in a few studies as it allows for the generation of precise mass loss and gain profiles. Additionally, the amount of sample required for an investigation in a TGA is in the order of mg, enabling preliminary results to be obtained before a larger sample size is used in a fluidized bed reactor.

The coal and OC mixture was placed into an alumina crucible having an 18 mm ID, a 10 mm depth and a 1 mm wall thickness with a tolerance of ±0.5 mm. The OC to fuel ratios ranged from 6:1 to 120:1 depending on the investigation. Once the OC and fuel mixture was prepared and placed into the crucible, it was then supported on a microbalance within the TGA. The TGA was then closed and the chamber evacuated by means of a vacuum pump to remove the contained air. Once a sufficient vacuum level was reached, the pump was switched off and the chamber filled with N_2. Once atmospheric pressure was reached, it was ready to be used.

A temperature program was then created to allow the temperature ramp rate and hold time to be specified. The gases to be introduced into the reactor during the reduction and oxidation periods were specified in the software. CO_2 was used as the reducing gas while air was used as the oxidizing agent in all of the experiments. Once the experiment was over, the sample was allowed to cool to room temperature before either being reused in a multicycle investigation or stored for characterization studies. The following subsections, based on the titles of the result chapters, describe the conditions used in the different investigations.

Figure 3-1 NETZSCH STA 449 F3 Jupiter TGA

3.2.1.1 Effect of Coal Minerals on the Performance of CLC (Chapter 4)

The Fe_2O_3 to coal ratio used was 6:1, similar to that used by Saha and Bhattacharya [3], which corresponds to the stoichiometric amount of oxygen needed to completely reduce the coal; 20 mg of coal was mixed with the corresponding amount of Fe_2O_3. A gas flow rate of 23 mL/min consisting of 13% CO_2 and 87% N_2 by volume was used as the reducing

environment. These values were selected as they were used in a previous study on CLC [4]. The sample was subjected to this environment while the temperature of the furnace was increased at a rate of 5°C/min from ambient to a temperature of 200°C where it was held for five minutes to ensure the complete removal of the inherent moisture present in coal. Subsequently, the temperature was ramped up to a value of 950°C at a rate of 10°C/min and held isothermally for 1 hour. The gases were then switched to allow for oxidation of the reduced OC by introducing air and N_2 at a 13:87 ratio by volume, with a total flow rate of 23 ml/min, for a period of 1 hour. Finally, the sample was allowed to cool down to room temperature. Upon completion, another batch of 20 mg of coal was added to the crucible which contained the reoxidized OC and ash from the combusted coal. This ash could not be separated and hence accumulated in the crucible over the course of the experiment. A total of five redox reactions were performed for each test. Some tests were conducted in absence of the OC to study the catalytic effect of Fe_2O_3 on the gasification of coal.

3.2.1.2 In-situ Synchrotron Study of Fe_2O_3 Reduction with Victorian Brown Coal (Chapter 5)

The Fe_2O_3 OC was mixed with coal at a ratio of 6:1, corresponding to the stoichiometric amount of oxygen needed to completely reduce the coal. Coal totalling 20 mg was mixed with 120 mg of Fe_2O_3 and placed into the crucible. A gas flow rate of 23 mL/min consisting of 13 v/v% CO_2 and balance N_2 was used for the reduction reaction with the former as the gasification agent. The crucible was placed into the TGA at ambient temperature and the temperature of the furnace was then increased to 200°C at a rate of 5°C/min after which it was held at the set temperature for five minutes. The temperature was then gradually increased to the experimental temperature of 950°C at a rate of 10°C/min and then isothermally held for one hour to provide sufficient time for the reduction reaction. The CO_2 gas was then replaced with air at the same flow rate to initiate the oxidation reaction and this was carried out for one hour to completely reoxidize the OC sample. Finally, the sample was cooled down to room temperature and retrieved for subsequent characterization. To fully study the OC carbon deposition phenomenon, the experiment was terminated at three different points during the reduction period (110, 135 and 160 minutes from the start of the reaction) and the sample was removed to allow for its characterization. These values were chosen as the first point denoted the lowest point in the TGA curve. Subsequently, a weight gain was observed, which continued until the 160^{th} minute mark after which it was stable;

this was the third point. The second point was taken to better understand what was occurring to the sample between the first and third points.

3.2.1.3 Reduction Kinetics of Fe_2O_3 with Victorian Brown Coal (Chapter 6)

A ratio of 80:1 between the OC and char was used and this corresponded to the stoichiometric amount necessary to ensure that the OC was not reduced beyond Fe_3O_4. A factor of 1.5 was used to this ratio to provide excess OC, yielding a ratio of 120:1. Char totalling 2 mg was mixed with 240 mg of Fe_2O_3 and placed into the crucible. Subsequently, this was positioned in the TGA. A gas flow rate totalling 100 ml/min was used throughout this study with N_2 introduced at the initial stages as an inert gas. The temperature was increased from ambient at a rate of 10°C/min to the experimental temperature, which ranged from 725°C to 900°C. Once the set point was reached, the gas was switched to a mixture of CO_2 and N_2. The concentration of CO_2 was varied from 5% to 50%; this affected the gasification rate of the char, leading to a variation in the reduction of the OC. While it would have been simpler to just increase the amount of the fuel, this would have resulted in the reduction of the OC beyond Fe_3O_4, which was not part of the scope of this study. The temperature was isothermally held until the reduction was complete and this varied from 10 minutes at 900°C to 6 hours at 725°C. Upon completion of the reaction, the furnace was allowed to cool down and the sample removed and stored for characterization.

3.2.1.4 Performance of Synthetic Oxygen Carriers (Chapter 8)

Experiments were performed in a TGA to study the performance of the OC. The experiments were performed with a gas flow rate of 60 mL/min of which 10 mL/min was CO_2 and the balance N_2. This corresponds to 17% CO_2 and 83% N_2, which is slightly different from the 13:87 which has been used previously. The OC mass was maintained at 900 mg while the mass of the coal sample was varied depending on the desired OC-coal ratio. The experiments were performed at 800, 850 and 900°C. These were done to perform sensitivity analyses on the OC's reactivity as a function of the amount of fuel, temperature and loading content.

3.2.2 Bench Scale Fluidized Bed Reactor

After the OCs were tested in the TGA, some were used in a bench scale fluidized bed reactor. The picture of the reactor can be found in Figure 3-2. This fluidized bed reactor was capable of batch fuel feeding and was operated in an alternating mode, cycling between the reduction and oxidation reactions. The schematic of the reactor can be found in Figure 3-3 below. The

reactor was constructed of 253MA high-temperature stainless steel to withstand the high reaction temperatures that were used. It has an internal diameter of 50 mm and a length of approximately 1 m, with a sintered plate as the distributor. A thermocouple with a diameter of 3.2 mm was positioned atop the distributor plate to monitor the temperature of the bed material. The fuel was fed from the top using a ball valve and isolated from the atmosphere by means of a stainless steel cap. The gas outlet was located at the top of the reactor, where a portion of the outlet gases were directed through an online gas analyser with the balance vented. The reactor was enclosed within an electrically heated furnace that could be operated up to 1000°C. The next subsection details how this reactor was used in the various studies.

Figure 3-2 Bench scale fluidized bed reactor

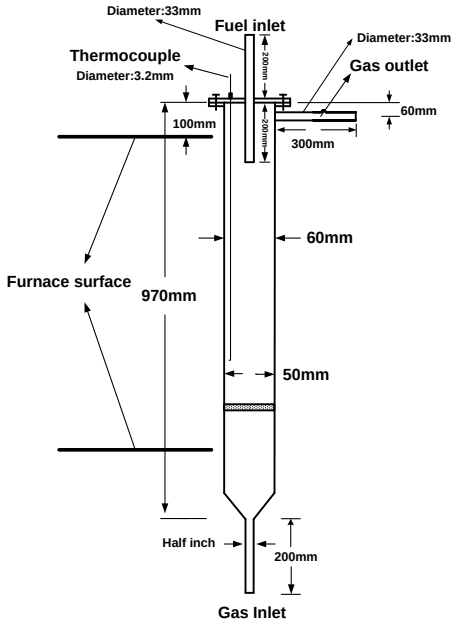

Figure 3-3 Schematic of the bench scale fluidized bed reactor

3.2.2.1 Performance of Synthetic Oxygen Carriers (Chapter 8)

Initially, 50 g of sand was added into the reactor followed by 60 g of the OC. The furnace was then heated to 900°C and gases totalling 6 L/min of 20 v/v% CO_2 with balance N_2 were introduced into the reactor. Once the set temperature was reached, 0.6 g of Yallourn coal was added into the reactor. This translates to an OC to fuel ratio of 100:1, which is in excess of the stoichiometric amount of 80:1 that is necessary for the reduction of Fe_2O_3 to Fe_3O_4. The exhaust gases from the reactor passed through moisture and particulate matter traps before entering an online gas analyser with the capability of measuring CO_2, CO, CH_4, O_2 and H_2. When the reduction reaction was complete, the CO_2 line was shut off and N_2 was introduced into the reactor to prevent back mixing of the gases. After five minutes, air was introduced into the reactor to oxidize the reduced OC particles. Once the O_2 concentration reached a steady value, the oxidation was deemed to be complete. The second reduction experiment was initiated after switching the gas from air to CO_2, followed by the addition of another batch of fuel. Ten redox reactions were performed with the last run terminated after the 10^{th} reduction. The furnace was then switched off and the samples were collected once the reactor reached ambient temperatures. It is acknowledged that while this design will not ensure intimate contact between the OC and coal volatiles, it will provide a platform for the relative comparison of the performance of the OCs.

3.2.2.2 Operational Experience with a $10kW_{th}$ Alternating Fluidized Bed Reactor (Chapter 9)

Here, 50 g of sand was added into the reactor before the addition of 100 g of the Western Australian ore. The furnace was operated at 900°C with a fluidizing gas flow rate of 6 L/min consisting of 20 v/v% CO_2 and balance N_2. Similar to the above, an OC to fuel ratio of 100:1 was used. Hence, 1 g of coal was added into the reactor. Upon completion of the reduction step, N_2 was used to purge the reactor before the CO_2 stream was replaced by air to oxidize the OC. The gases at the exhaust were directed through an online gas analyser. Ten redox reactions were performed and the experiment was terminated at the 10^{th} reduction reaction.

3.2.3 Multipurpose Reactor

A multipurpose reactor was used in one of the studies and the schematic for the operation of the fixed bed reactor mode can be found in Figure 3-4 below. During fluidized bed operation, the inlets and outlets for the gases were swapped to allow for the fluidization gas to be introduced from the bottom. This reactor is located in Southeast University and the

investigations performed using this reactor was done in collaboration with project partners from said university. The reactor was constructed of stainless steel, with a design pressure of 2 MPa at 1000°C. The reactor has an inner diameter of 30 mm and a length of 950 mm, with the distributor plate located around the halfway mark, lengthwise. The furnace temperature was controlled based on the temperature readings obtained using a K-type thermocouple enclosed within the furnace. The temperature within the reactor was manipulated by observing the temperature measured by a second K-type thermocouple inside the reactor.

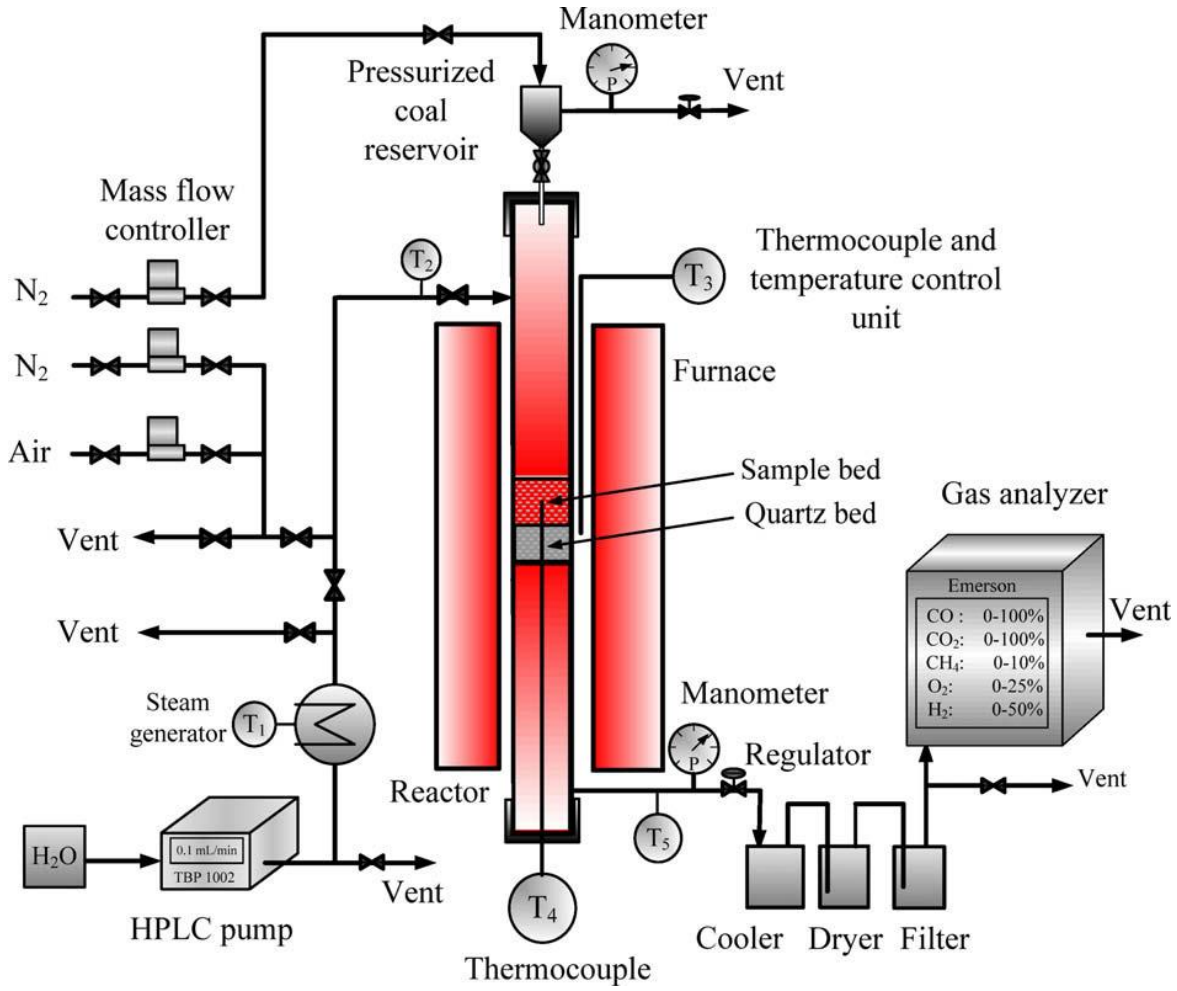

Figure 3-4 Schematic of multipurpose reactor (fixed bed mode) located in Southeast University [5]

3.2.3.1 Effect of Reactor Operating Mode (Chapter 7)

Three modes of operation were investigated using this reactor: Fluidized bed, atmospheric fixed bed and pressurized fixed bed. The pressurized experiment was conducted at a pressure of 5 bar. The temperature was kept at 970°C for all the conditions to provide a standard for comparing the different operating modes with one another and with experiments previously

done by Zhang *et al.* [6] using a Chinese bituminous coal. The experiments were conducted in a cyclic manner, alternating between reduction and oxidation reactions.

During the atmospheric and pressurized fixed bed experiments, gases were fed from the top of the reactor. The gases used for the reduction experiments consisted of steam for the gasification of the coal and N_2 as the carry gas. With respect to the operation of the fluidized bed reactor, the same gases were introduced through the distributor plate at the bottom. The flow rate of N_2 was controlled using a mass flow controller (MFC) while a High Performance Liquid Chromatography (HPLC) pump was used to deliver a precise and accurate amount of distilled water into a steam generator operated at 250°C. The pump could deliver a flow rate of up to 10.0 mL/min with an accuracy of ±1%. The total gas flow rate used in all three reactor configurations was 1040 ml/min, with steam accounting for 74% of the flow rate.

Before the start of the experiment, 40 g of quartz sand having a size range of 600-1000 µm was introduced into the reactor and placed on the distributor plate. This was done to ensure that none of the coal or OC particles channelled through the perforations of the distributor plate. An OC to coal ratio of 100:1 was used in all modes of operation. This is in excess of the stoichiometric amount of oxygen necessary to completely combust the fuel while ensuring that the OC was not reduced beyond Fe_3O_4. Initially, 40g of the CVRD ore, having a particle size range of 90-180 µm, was introduced into the reactor. Subsequently, the reactor was heated to the operating temperature while a gas mixture consisting of 5 v/v% O_2 with balance N_2 at a flow rate of 1000 mL/min was introduced into the reactor. As soon as the experimental conditions were reached, the gases in the reactor were changed to steam and N_2.

With respect to the operation of all three reactor modes, 0.4 g of coal having a size range of 125-180 µm was placed into the isolation valve and then introduced into the reactor. For the pressurized fixed bed reactor, a pressure regulator at the gas outlet was manually manipulated to maintain a pressure of 5 bar in the reactor. As soon as coal was introduced into the reactor, the generated gases caused the pressure within the reactor to increase. Hence, the valve had to be opened to relieve the pressure. Therefore, the work with the pressurized fixed bed unit was done on the basis of an averaged pressure of 5 bar.

After the coal was introduced into the reactor, it underwent devolatilization and in-situ gasification by steam. The generated gases then reacted with the OC to form CO_2 and steam. The flue gases then exited the reactor and went through a particle trap and steam condenser. This was done to generate clean dry gas by removing the particulate matter and condensing

the steam. These gases were then diluted with 1500 mL/min of N_2 after which the mixture was fed into an Emerson online gas analyser capable of detecting CO_2, CO, CH_4, H_2 and O_2. The gases were diluted to provide a sufficient flow rate into the gas analyser. The reactions were deemed to be complete as soon as the gas concentration fell below the detection limit of the gas analyser. This was found to be around 30 minutes for the reduction reaction. Subsequently, 1000 mL/min of N_2 was introduced to purge the reactor for 10 minutes. This was done to ensure that there was no mixing between the gases from the reduction and oxidation steps. Upon completion, the oxidation of the OC was initiated by introducing 1000 mL/min of a gas mixture consisting of 5 v/v% O_2 with 95 v/v% N_2. The oxidation was found to also complete within 30 minutes. The low concentration of oxygen was chosen in place of air to prevent excessive localized heating of the OC due to the strong exothermic nature of the reaction between O_2 and the reduced OC. Once the oxidation was complete, the reactor was again purged with N_2 for 10 minutes to drive off the oxygen contained within. This point marks one completed reduction-oxidation cycle. The next cycle is initiated by introducing the steam and N_2 mixture. Upon stabilization of the online gas analyser readings, the coal was introduced and this was repeated 10 times. After the tenth reduction reaction, the reactor was cooled down in the presence of N_2 and the OC samples were collected for analysis once the reactor reached ambient temperatures. The gas flow rates during the reduction, oxidation and purge periods were kept constant to minimize pressure fluctuations in the reactor during the operation of the pressurized fluidized bed reactor.

3.2.4 10kW$_{th}$ Fluidized Bed Reactor

The schematic for the 10 kW$_{th}$ fluidized bed reactor can be found Figure 3-5, while a photograph of the setup can be found in Figure 3-6. The reactor was constructed using 253MA stainless steel, which has excellent thermal stability and corrosion resistance. The main reactor zone has a diameter of 100 mm and a height of 1.5 m. The distributor used in this setup was a collection of tuyeres. Beyond the main zone, there is an expanded freeboard section with a diameter of 150 mm and a height of 2 m. Two cyclones were designed and installed to capture the generated fines, with the secondary cyclone purposed at increasing the solids capture efficiency. The primary cyclone has a cyclone diameter (D_c) of 250 mm, while the secondary cyclone has a D_c of 150 mm. A sampling point was introduced between the primary and secondary cyclones to enable a small amount of the gases to be extracted for analysis. These gases passed through a series of particulate filters and moisture traps before entering an online gas analyser.

The flow rates of N_2 and CO_2 were controlled using MFCs and a rotameter was used to obtain the desired flow rate of air. The solids were fed into the main reactor zone using a screw feeder that was connected to a hopper containing the solids; N_2 was used to aid the delivery of the solids into the reactor.

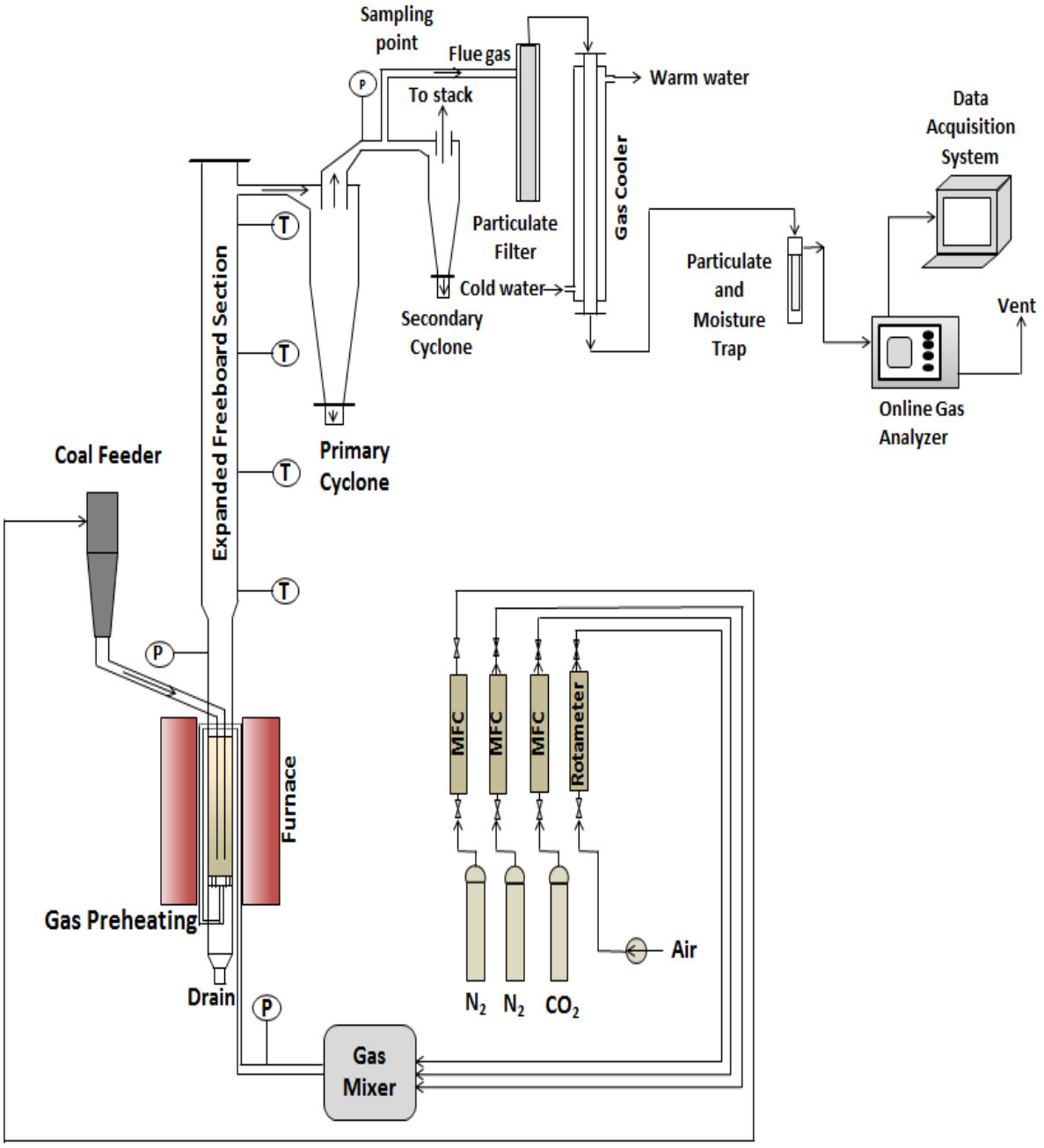

Figure 3-5 Schematic of the 10 kW_{th} fluidized bed reactor

Figure 3-6 Photograph of the 10 kW_{th} fluidized bed reactor

3.2.4.1 Operational Experience with a 10 kW_{th} Alternating Fluidized Bed Reactor (Chapter 9)

A gas manifold housed the MFCs and rotameters that were used to control the flow rates of the gases. The flow rates of the N_2 and CO_2 gases was controlled using MFCs while a rotameter was used to manipulate the volumetric flow rate of air to obtain the desired value. The gases were then homogeneously mixed in a gas mixer. A two pass heat exchanger system was implemented to preheat the gases and this was achieved by enclosing the gas line within the furnace. The preheated gas then entered the reactor through tuyeres which acted as distributors. The bed material consisted of a layer of sand followed by the OC. The gases then entered and passed through the main reactor zone into the expanded freeboard and through

the cyclones before being vented. Between the first and second cyclones, a sampling point was introduced and a fraction of the gases, around 1-2 L/min, was then vacuumed through the slipstream. The gases then went through a particulate filter to remove the remainder of the solids and then entered a gas cooler which was a one pass heat exchanger with water as the cooling medium. The cooled and cleaned gas then entered a particulate and moisture trap to ensure complete removal of all the solids and condensed liquids.

The gases were then introduced into an online gas analyser connected to a data acquisition system before being vented. The online gas analyser was made by Fuji Electric Co., Ltd. It had the capability of measuring the concentrations of CO_2, CO, CH_4, H_2 and O_2. It should be noted that the concentration readout does not add up to 100% due to dilution by N_2. All along the setup, three pressure transducers and four thermocouples were installed to monitor changes in these two values to help identify regions wherein issues were developing.

With respect to the solids in the reactor, firstly 1 kg of sand with a particle size range of 1000-2000 μm was introduced into the reactor and this acted as an inert layer on the distributor as well as a secondary distributor for the gases. Then, 5 kg of the OC was introduced into the reactor over a period of 1 hour. The sand and OC were added using the same screw feeder that is used to introduce the coal into the reactor. The following section will detail the daily operating protocols for the experiments.

Firstly, with respect to the gas analyser, a zero calibration for all gases and a span calibration for O_2 were performed. The gases were introduced into the reactor at a total flow rate of 25 L/min, consisting of 80 v/v% air and 20 v/v% N_2. Then, the sand and OC were introduced into the reactor. This was done to oxidize and calcine the OC particles prior to utilizing it. Four different temperatures were investigated in this study at 100°C intervals between 700-1000°C. Once the temperature set point was reached, the gases were switched over to the mixture consisting of CO_2 and N_2. The flow rate used was 25 L/min with 20 v/v% CO_2 and balance N_2. After the gas concentration was found to have stabilized based on the online gas analyser readout, the fuel was introduced into the reactor. A point to note here is that the fuel was introduced into the OC bed. 50 g of the fuel was fed into the reactor at an average rate of 16.6 g/min. This translates to an initial OC to fuel ratio of 100:1, which would ensure that the OC was not reduced beyond Fe_3O_4 while combusting the fuel. The fuel first devolatilized and these gases reacted with the OC; subsequently, the carbon in the fuel was gasified by CO_2 to produce CO which then reacted with the OC to form CO_2. The generated gases were then vacuumed through the slipstream in between the two cyclones and passed through the various

traps and coolers before entering the online gas analyser. The reduction was allowed to occur over a period of 30 minutes, after which the CO_2 MFC was shut off and N_2 was used as a sweep gas to remove the residual gases in the system. After ten minutes, 20 L/min of air and 5 L/min of N_2 was introduced into the reactor to oxidize the reduced OC particles, which took place over a course of 30 minutes. A low oxygen concentration was employed to prevent excessive localized temperatures on the OC particles during the oxidation reaction, which is highly exothermic and could potentially lead to sintering. This marked one complete redox cycle and this was repeated another five times, yielding a total of six redox reactions in one experiment. The reason the experiment was terminated at the sixth reduction was due to the fact that operational experience has shown that the operation stabilizes around the fifth/sixth cycle. The sixth run was terminated at the reduction step, after which the furnace was turned off while the reactor was fluidized and also cooled by N_2 to prevent oxidation by air which may enter the reactor. The reduced samples were collected the next morning by draining them out of the reactor and these were stored in sealed containers. The samples from the catch pots were also collected and stored. Besides the temperature variation study, one study was dedicated to investigating the effect of the OC particle size. Then, a study was undertaken to investigate the effect of the fuel on the performance of CLC and this was done by using char instead of coal. Lastly, an experiment was conducted over 35 redox cycles to study the OC performance over a period of 40 hours; this was accomplished over a period of 6 days.

3.3 Gas Phase Measurement

The analysis of the gases generated during the operation of the reactors is important as it allows for the quantification of the performance of the OC in a given setup. From the concentration of the various gases, the carbon conversion of the fuel as well as the CO_2 yield can be calculated and this will be discussed in the subsections to follow. These parameters allowed for the comparison of the different OCs that were used. Additionally, the concentration of N containing gases such as NO_2, NO and N_2O were also quantified.

3.3.1 Online Gas Analysis

Two different online gas analysers were used in the various studies in this thesis involving the fluidized and fixed bed reactors. Experiments in the TGA were not subjected to such an analysis, as the flow rate of the generated gases was insufficient for use in an online gas analyser.

The first gas analyser was from Fuji Electric Co., Ltd. This gas analyser was used for all the studies employing a fluidized bed reactor, except for the study involving the multipurpose reactor. This unit consisted of two parts. It had a ZRE Non-Dispersive Infra-Red type gas analyser coupled with a ZAF3 thermal conductivity gas analyser. The ZRE unit was used to measure the concentrations of CO_2, CO, CH_4 and O_2 while ZAF3 was used to detect and quantify the concentration of H_2. CO_2 had a span of 100%, O_2 had a span of 25% while both CO and CH_4 had a span of 10%. On the other hand, the span for H_2 was 50%.

The second gas analyser was only used in the study employing the multipurpose reactor. It was an Emerson unit capable of detecting and quantifying the concentrations of CO_2, CO, CH_4, H_2 and O_2. This unit is located in Southeast University.

3.3.2 NO, NO_2 and N_2O Analysis

The concentrations of NO and NO_2 were measured using Dräger-Tubes®, which allowed for the measurement and quantification of gases even at levels of parts per million (ppm). The gases evolved in the study using the 10 kW_{th} reactor were collected in a gas bag for analysis. A Dräger Accuro® gas detector pump was used to draw 100 mL of gas per stroke of the pump through the Dräger-Tube®. Depending on the gas being analysed, the number of strokes of the pump and the time period over which it was drawn varied. The gases that were drawn in through each stroke of the pump then entered the Dräger-Tube® and reacted with the chemicals contained within the tubes. Upon completion, the gas concentration was read off the graduation on the tube, which was found along its length. The number that was read off the graduation was based on the length of the colour change of the chemicals in the Dräger-Tube®.

The gases which were collected in the gas bag were also analysed for N_2O. A small amount of the gas was drawn out using a gas syringe and then evacuated into an exetainer. The exetainer was then placed into a Varian Gas Chromatograph (GC) to obtain the concentration of N_2O present in the gas sample.

3.4 Sample Characterization

The OC samples that were collected from each of the different studies were subjected to a variety of analytical analyses to characterize both the fresh and used particles. Instruments such as a Scanning Electron Microscope (SEM), an Energy Dispersive X-ray Spectroscope (EDS), an X-ray Diffraction (XRD) unit, an X-ray Fluorescence (XRF) unit, an Accelerated

Surface Area and Porosimetry (ASAP) unit and a particle size distribution unit allowed for the used OCs to be characterized and compared to the fresh samples. Such a comparison yielded useful information that helped to understand and explain the experimental results. The following subsections will detail each of these analytical techniques.

3.4.1 Scanning Electron Microscope (SEM)

The use of an SEM allows for the investigation of the changes in the morphology of the OC particles. Such an analysis can show if the OC particles had undergone sintering, attrition or even agglomeration. A JOEL 7001F SEM, as shown in Figure 3-7, was used to characterize the fresh and used OC samples. The working distance used was 6 mm while an accelerating voltage of 30 kV was employed. With regards to the sample preparation, a few variants were used and this was due to the updating of the operating protocols by the scientists at the Monash Centre for Electron Microscopy. In some studies, a carbon strip on the sample stub was used to secure the OC samples. In others, a thin layer of cyanoacrylate was smeared on the sample stub and the OC particles were placed on it. Once the samples were placed onto the sample stub, they were coated with a thin layer of either Iridium or Platinum, having thicknesses of 2-3 nm. This was done to minimize the charging of the samples by the X-rays. The sample stub was then loaded into the instrument to begin the analysis. A few different levels of magnifications were used to get a better understanding of the changes in the morphology of the particles. A lower magnification was used to obtain the entire OC particle in the micrograph to study changes in its structure to determine if it had undergone attrition or agglomeration; a higher magnification was employed to study the changes in the grain structure to investigate if the grains had undergone sintering.

3.4.2 Energy Dispersive X-ray Spectroscope (EDS)

The use of an EDS allows for the changes in the chemical composition of the OC to be investigated. An Oxford Instruments X-Max 80 Silicon Drift EDS detector coupled with the aforementioned JOEL 7001F SEM was used. An image of this setup can be found in Figure 3-7. The same sample stub used in the SEM analysis was also used when performing the EDS studies. The only differences are that a larger working distance of 10 mm was used while the accelerating voltage was reduced to 15 kV. The instrument allowed for a variety of analysis to be performed, such as a single point scan, an area scan and elemental mapping of the different elements present on the sample. An area scan was performed for most of the samples, as this provided a statistically better surface elemental analysis compared to a single

point analysis. In the study employing the synthetic OCs, elemental mapping was done to study the distribution of the secondary metal oxide on the synthetic OC.

Figure 3-7 JOEL 7001F SEM with an Oxford Instruments X-Max 80 Silicon Drift EDS detector [7]

3.4.3 X-ray Diffraction (XRD)

An XRD was used to determine the presence of crystalline phases on the surface of the OC particle. A Rigaku Miniflex 600, as shown in Figure 3-8, was used to perform the XRD analysis. A Cu target with Kα radiation was used at 40 kV and 15 mA. To secure the sample onto the sample holder, a thin layer of silicon was used. This was done to prevent the sample from falling off the holder as it was spun during the analysis. The analysis was conducted in a step-scan manner over a 2θ range of 3-80° with a step size of 0.02°.

Figure 3-8 Rigaku Miniflex 600 [8]

3.4.4 Synchrotron High-Temperature In-Situ X-ray Diffraction

The XRD beamline at the Australian Synchrotron was used for in-situ studies on the phase changes of the OC in the presence of VBC. The technical details of the setup can be found in a work by Wallwork *et al.* [9], while an image of the setup can be found in Figure 3-9.

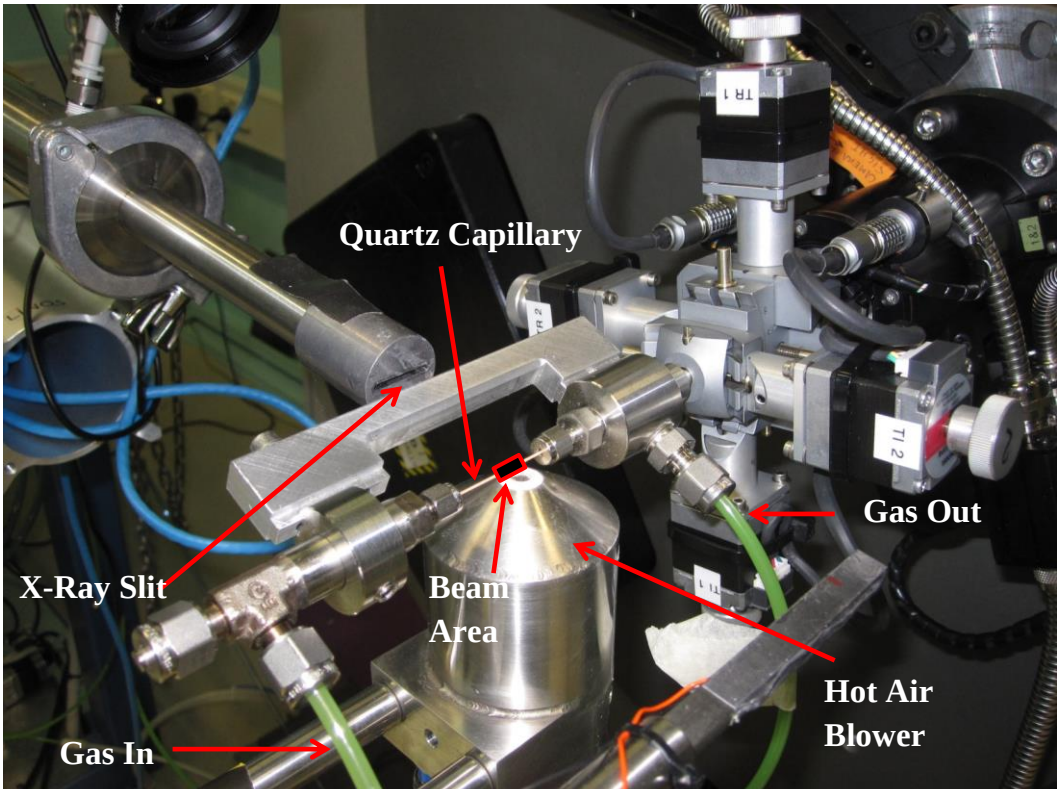

Figure 3-9 Synchrotron XRD beamline

The OC-coal sample was loaded into a 0.5 mm ID (0.6 mm OD) quartz capillary. This was then placed into a flow cell that was later loaded into the flow cell holder. The X-ray beam, having dimensions of 1 mm by 1.2 mm, was focused vertically and the capillary was aligned to the centre of this beam. The flow cell and capillary were then continually oscillated in 10° arcs to average out any preferred orientation in the sample and enhance the powder diffraction patterns collected by the MYTHEN-II strip detector [10]. The temperature of the capillary area probed by the X-ray beam was controlled using a hot air blower that went from ambient to 950°C at a rate of 10°C/min. The wavelength used was 0.95362Å and this was obtained through Rietveld refinement of a NIST LaB_6-660b standard diluted with powdered diamond; the Rietveld refinement of the standard was performed using the software TOPAS [11]. Diamond was added as LaB_6 is a strong absorber of X-rays, especially when the beam is at low energies, such as the beams generated by a synchrotron. The first diffraction pattern was collected at room temperature and served as a baseline, while subsequent data were

collected from 300°C to 950°C at 50°C intervals. These data were acquired over 1 minute at each interval. A gas flow rate of 1 L/min was used during the reduction reaction, of which 20 v/v% was CO_2 and the balance N_2. The temperature was then held isothermally until the diffractograms stabilized, which took around 15-25 minutes. Upon stabilization, the CO_2 was replaced by air to oxidize the reduced OC and this was only done for the first set of conditions due to time constraints.

Three different sets of experiments were performed. The first was done to compare with the results obtained from the TGA analysis and involved using a 6:1 ratio of homogeneously mixed Fe_2O_3 and coal. The second and third experiments were done to study the extent of reduction of Fe_2O_3 using a maximum loading of the fuel. For this, the second experiment was undertaken with coal and the third with char prepared at 950°C. The fuel and OC in the second and third experiments were segregated; the ratio used was approximately 2.6 parts of fuel to 1 part OC. This was done as the amount of sample that can be contained in the 5 mm long heated zone was very small; by doing this, a greater extent of reduction could be studied. Rietveld refinement was done using the GSASII software [12] to obtain the cell parameters (lattice parameters) and microstructure (crystallite size). The lattice parameter refers to the physical dimensions of a unit cell in a crystal lattice; the lattices are typically three-dimensional and have three lattice constants which are denoted by a, b and c. On the other hand, the crystallite size represents the size of a single crystal in the powder form.

3.4.5 X-ray Fluorescence (XRF)

To determine the bulk composition of the OC, particularly the fresh sample, XRF was used. Firstly, the sample was mixed with Hoechst wax C powder from Merck at a ratio of 1:4. Next, the powdered mixture was placed into a sample holder having an inner diameter of 31 mm. Subsequently, this was placed into a SPEX SamplePrep 3635 pelletiser. The sample holder was subjected to a pressure of 20 tonnes for 2 minutes after which the pressure was slowly released over a course of 30 seconds. Next, the pellet was placed into a Rigaku NEX CG XRF unit as shown in Figure 3-10. This unit has an X-ray tube with a Palladium anode. The sample was then analysed and compared to a standard database to obtain the concentration of each of the elements.

Figure 3-10 Rigaku NEX CG [13]

3.4.6 Accelerated Surface Area and Porosimetry (ASAP)

One of the factors that affect the reactivity of an OC is its surface area as this roughly translates to the amount of area available for reaction with the combustible gases. Hence, a Micromeritics ASAP 2010 unit, as shown in Figure 3-11, was used to obtain the Brunauer, Emmett and Teller (BET) surface area as well as the cumulative pore volume and average pore size. These values allow the fresh and used OC particles to be compared quantitatively.

Figure 3-11 Micromeritics ASAP 2010

3.4.7 Particle Size Distribution

To investigate changes in the particle size distribution of the OC before and after a reaction, a Malvern Mastersizer 2000 with a Scirocco 2000 dry cell operated using air as the dispersant was utilized; an image of this instrument can be found in Figure 3-12. This instrument was used to obtain the particle size distribution of the OC alongside the surface weighted mean diameter. Additionally, the d(0.1), d(0.5) and d(0.9) diameters were also obtained.; these represent the volume mean diameter at which 10%, 50% and 90% of the distribution is below.

Figure 3-12 Malvern Mastersizer 2000 with a Scirocco 2000 dry cell

3.5 Modelling

Modelling, such as thermodynamic and kinetic modelling, is an important component in any research. Models enable quick predictions of the outcomes for a given set of parameters without the need to conduct individual experiments and this saves cost and time. Two different models were used in this thesis and are described below.

3.5.1 Thermodynamic Modelling

Thermodynamic modelling allows the equilibrium concentration of the products in a reaction to be determined. Such a model provides information relating to the extent of consumption and generation of certain compounds, but disregards reaction kinetics. Typically, in a thermodynamic model, the prevailing assumption is that the reactants are in perfect contact with one another for an infinite amount of time, hence discounting reaction kinetics.

FactSage 6.4 [14] and HSC Chemistry [15], both thermodynamic equilibrium modelling software, were used to determine the equilibrium product concentrations for reactions

mimicking the experiments that were performed. FactSage 6.4 was used to generate phase diagrams as well as to predict and quantify the formation of possible phases from the interaction between the fuel ash and the OC. HSC Chemistry, on the other hand, was used to generate an Ellingham diagram, which shows the variation in the Gibbs free energy as a function of temperature. The results from these models were then compared to the experimental results to determine the degree of similarity between the two results.

Thermodynamic models generated using FactSage can be found in Section 4.6 of Chapter 4 and Section 5.4.2 in Chapter 5. An Ellingham diagram was generated using HSC Chemistry and this can be found in Section 5.4.1 in Chapter 5.

3.5.2 Kinetic Modelling

As mentioned in the literature review chapter, to date, no model is capable of simulating the reduction kinetics of an OC in the presence of a solid fuel; there have been publications on the OC reduction kinetics in gas-fuelled CLC systems [16, 17]. Unlike thermodynamic models, kinetic models are capable of determining the time required for a given reaction to complete. Additionally, the obtained kinetic parameters from the model can be used in Computation Fluid Dynamics (CFD) modelling to study the hydrodynamics of a system.

Two kinetic models, the Shrinking Core Model (SCM) and the Modified Volume Reaction Model (MVRM), were employed to map the reduction of the OC under a number of different conditions. To obtain sufficient data for the models, four experiments were performed at temperatures of 750°C, 800°C, 850°C and 900°C with a constant CO_2 concentration of 10 v/v%. Subsequently, the CO_2 concentration was varied between 5 v/v%, 10 v/v%, 20 v/v% and 30 v/v% at a constant temperature of 850°C. These seven experiments formed the basis for the generation of the model and are referred to as the model data experiments. To validate the model, experiments with the following conditions were performed: 850°C and 15 v/v% CO_2; 850°C and 40 v/v% CO_2; 825°C and 25 v/v% CO_2; 800°C and 20 v/v% CO_2. The details relating to the generation of these models are shown in Section 3.6.3 below.

3.6 Data Processing

The processing of raw experimental data is an important aspect, as it allows for the acquisition of certain important information, such as carbon conversion and CO_2 yield. The subsections to follow will detail how the obtained raw data were processed.

3.6.1 Thermogravimetric Analyzer

As mentioned, a TGA allows for precise and accurate mass loss and gain measurements to be performed. Hence, the following parameters were calculated using the data from the TGA.

Fractional reduction, $X_r = \frac{m_i - m}{m_i - m_r}$ 3.1

Fractional oxidation, $X_o = \frac{m - m_r}{m_f - m_r}$ 3.2

Global reduction rate, $G_r = \frac{dX_r}{dt}$ 3.3

Instantaneous reaction rate, $r_{inst} = \frac{\Delta m}{M \Delta t}$ 3.4

Conversion, $X = \frac{m_i - m}{m_i - m_f}$ 3.5

Symbol definition:

m Instantaneous mass of the sample at any point during the reaction (kg)

m_i Initial mass of the sample (kg)

m_r Mass of the reduced sample (kg)

m_f Final mass of the sample (kg)

Δt Incremental time

Δm Mass loss/gain over an incremental time (kg)

3.6.2 Fluidized Bed and Fixed Bed Reactors

The instantaneous gas fraction during the reduction reaction is obtainable using the following:

$$f_i = \frac{x_i}{(x_{CO} + x_{CO_2} + x_{CH_4} + x_{H_2})} \quad 3.6$$

Symbol definition:

f_i Fraction of the desired component *i* (CO_2, CO, CH_4, H_2) at any given point in time

x_i Molar fraction of the desired species.

The CO_2 yield equation calculates the amount of CO_2 evolved relative to all the carbonaceous gases and is shown below, where $\dot{n}_{out}$ (mol s^{-1}) denotes the outlet molar gas flow rate:

$$CO_2\ Yield = \frac{\int_0^t \dot{n}_{out} \times x_{CO_2} dt}{\int_0^t \dot{n}_{out} \times (x_{CO} + x_{CO_2} + x_{CH_4})\, dt} \quad 3.7$$

The carbon conversion, X_c, is an important parameter and shows the fraction of carbon present in coal that has been converted to a carbonaceous gas. The equation to calculate this value can be found below, where $n_{C,coal}$ (mol) represents the amount of carbon in coal:

$$X_C = \frac{\int_0^t \dot{n}_{out} \times (x_{CO} + x_{CO_2} + x_{CH_4})\, dt}{n_{C,coal}} \quad 3.8$$

The first derivative of the carbon conversion with respect to time yields the carbon conversion rate, r_c (s^{-1}), which is shown in the equation below:

$$r_c = \frac{dX_c}{dt} \quad 3.9$$

To obtain the gasification rate of the fuel, r_g (s^{-1}), the following equation is used and it is dependent on the amount of unreacted char as well as the carbon conversion rate [18]:

$$r_g = \frac{1}{1-X_c} \frac{dX_c}{dt} \quad 3.10$$

The oxygen demand, Ω_{OD}, denotes the fraction of oxygen required to completely oxidize the remaining combustible gases leaving the reactor during the reduction stage. The equation for the oxygen demand can be found below:

$$\Omega_{OD} = \frac{0.5\, x_{CO} + 0.5\, x_2 + 2\, x_{CH_4}}{x_{CO_2} + x_{CH_4} + x_{CO}} \quad 3.11$$

3.6.3 Kinetic Modelling

Before delving into how the data for the two models were processed, the assumptions that were made will be listed first as they enabled the simplification of the model.

3.6.3.1 Model Assumptions

The assumptions used in both models are listed below:

- The particles are spherical
- The reaction occurs under isothermal conditions
- The porosity of the particles are not considered
- The char is fully reacted by the end of the experiment
- Negligible amounts of unreacted CO
- Negligible external film mass transfer
- Negligible resistance to gas diffusion (MVRM)
- High resistance to gas diffusion (SCM)

It is worth noting that since char was used in the investigation, it is impossible to separate the mass of the char from that of the OC. Taking into account the fourth and fifth assumptions, it is acceptable to say that the weight loss of the OC is directly proportional to that of the char. The validity of this statement is confirmed by delving into the chemistry behind the OC reduction process. The OC can only reduce in the presence of a reducing gas, such as those formed during gasification of the char. Hence, if there are negligible amounts of unreacted CO, it would mean that the OC was reduced by the CO from char gasification. To confirm this major assumption, gas samples were collected in gas bags and analysed during the course of the reaction. It was found that the percentage of CO in the gas relative to the amount of generated CO_2 was never more than 5%. Since conversion is a ratio and most of the generated CO reacted with the OC, there is no reason to isolate the mass loss of the OC from that of the char. Hence, m, m_i and m_f refer to the mass of the OC and char mixture.

3.6.3.2 Shrinking Core Model (SCM)

The governing equation for the SCM is as follows:

$$\frac{t}{\tau} = 1 - (1 - X)^{\frac{1}{3}} \qquad 3.12$$

Symbol definition:

τ Time required for complete conversion of the solids (min)

X OC reduction conversion at time t

τ was determined experimentally from a conversion versus time plot for the reduction of the OC by the char gasification intermediates. A plot of the linearized conversion $[1 - (1 - X)^{\frac{1}{3}}]$ against t yields a straight line with a gradient of $\frac{1}{\tau}$. The gradient was taken from X=0 to X=0.65 for all the cases. The obtained τ values were then used to model the behaviour of τ as a function of T and C_g, the latter of which represents the concentration of CO_2. It is proposed that the relationship of τ with C_g and T are as follows:

$$\tau = f(C_g) \times f(T) \qquad 3.13$$

where $f(C_g)$ has the following form:

$$f(C_g) = \frac{a}{C_g^n} \qquad 3.14$$

with n being the order of reaction.

On the other hand,

$$f(T) = b \cdot e^{\frac{(\frac{E_a}{R})}{T}} \quad 3.15$$

which follows the form of the Arrhenius equation typically represented by:

$$k = k_o e^{\frac{-E_a}{RT}} \quad 3.16$$

with k as the reaction rate, k_o as the pre-exponential factor, E_a as the activation energy and R as the universal gas constant. Combining the two results in the following equation:

$$\tau = \frac{a}{C_g^n} b \cdot e^{\frac{(\frac{E_a}{R})}{T}} = \frac{c \cdot e^{\frac{(\frac{E_a}{R})}{T}}}{C_g^n} \quad 3.17$$

For comparison, the τ equation used by Abad *et al.* [16] is shown below:

$$\tau = \frac{\rho_m r_g e^{\frac{E_a}{RT}}}{\bar{b} C_g^n k_0} \quad 3.18$$

In the current derivation, c accounts for most of the constants and takes the following form:

$$c = \frac{\rho_m r_g}{\bar{b} k_0} \quad 3.19$$

Symbol definition:

ρ_m Molar density of Fe_2O_3

r_g Grain radius of Fe_2O_3

$\bar{b}$ Stoichiometric coefficient for the reaction between the reducing gas and the OC

The values for these constants were taken to be 14,000 mol/m^3, 0.5x10^{-6} m and 3 respectively. The first two values are similar to that found in Abad *et al.* [16] with the molar density being slightly higher in this study as the specific gravity of hematite is higher than that of ilmenite.

Using the equations above, the pre-exponential factor, k_o, can be calculated since ρ_m, r_g and b are all constants. Conversely, c, E_a and n can be obtained from the experimental data. Based on the experimentally obtained τ values, the value for n can be determined from the gradient of the plot of ln (τ) against ln (C_g). The activation energy can be obtained by first plotting ln (τ) against $\frac{1}{T}$ followed by determining the line of best fit and its gradient; the negative of this gradient is E_a. With the calculated values for n and E_a, the constant c can then be calculated by fixing the aforementioned values and using the Generalized Reduced Gradient

(GRG) nonlinear solving method to obtain the best fit for the experimental data. Once the constant c is determined, the pre-exponential factor can then be obtained.

3.6.3.3 Modified Volume Reaction Model (MVRM)

The MVRM is an upgraded form of the typical Volumetric Reaction Model (VRM) which has the following form:

$$\frac{dX}{dt} = k_{VM}(1 - X) \tag{3.20}$$

The MVRM replaces the constant k_{VM} with a function that allows for a wider range of conversion profiles to be modelled and this is shown below:

$$\frac{dX}{dt} = k(X)(1 - X) \tag{3.21}$$

Based on the conversion-time plot obtained from the experimental data, the following equation is proposed:

$$X = 1 - \exp(-at^b) \tag{3.22}$$

Upon differentiation, the following is obtained:

$$\frac{dX}{dt} = \frac{d}{dt}(1 - \exp(-at^b))$$

$$= 0 + \frac{d}{dt}(-\exp(-at^b))$$

$$= -\exp(-at^b) \times \frac{d}{dt}(-at^b)$$

$$= -\exp(-at^b)\,(-abt^{b-1})$$

$$\frac{dX}{dt} = (abt^{b-1})\exp(-at^b) \tag{3.23}$$

Substituting the above equation into the governing equation yields the following conversion equation:

$$k(X)(1 - (1 - \exp(-at^b)\,) = (abt^{b-1})\exp(-at^b) \tag{3.24}$$

Rearranging the terms in order to substitute X back into the equation gives:

$$k(X) = ab\left[\left[\ln\left((1 - X)^{-\frac{1}{a}}\right)\right]^{\frac{1}{b}}\right]^{b-1} \tag{3.25}$$

Rearranging again to have the equation as a function of time results in a simpler equation:

$$k(t) = ab[t]^{b-1} \quad 3.26$$

Here, the variables (a) and (b) were calculated by fitting the experimental conversion-time plots. These values were then used to obtain a model which predicted the behaviour of (a) and (b) over a range of temperatures and CO_2 concentrations.

Based on the proposed equation, it was first linearized and rearranged to yield the following equation with a simple X-t dependency:

$$at^b = -\ln(1 - X) \quad 3.27$$

The right hand side of the equation can be obtained by plotting the experimental results while the variables (a) and (b) on the left hand side were given initial values. The difference between the values on the left and right hand sides were then computed to give a residual as shown below:

$$r = [at^b - (-\ln(1 - X))]^2 \quad 3.28$$

The values of (a) and (b) were then varied to find the minimum value of r and these were then designated as the calculated values of (a) and (b), as they closely model the experimental data. The model was terminated at a conversion of 95% as the remaining 5% can be predicted sufficiently well. In addition, the residual above a conversion of 95% significantly affected the final prediction, as it tried to better predict the last 5% of the conversion, causing the results in the intermediate section to deteriorate.

The next chapter, the first of six results chapters, will investigate the effect of the coal minerals on the performance of a CLC system.

3.7 References

1. Rahman, M., A. Samanta, and R. Gupta, *Production and characterization of ash-free coal from low-rank Canadian coal by solvent extraction.* Fuel Processing Technology, 2013. **115**: p. 88-98.
2. Yang, R.T., S.K. Das, and B. Tsai, *Coal demineralization using sodium hydroxide and acid solutions.* Fuel, 1985. **64**(6): p. 735-742.
3. Saha, C. and S. Bhattacharya, *Chemical looping combustion of low-ash and high-ash low rank coals using different metal oxides - A thermogravimetric analyser study.* Fuel, 2012. **97**: p. 137-150.
4. Saha, C., *Chemical-looping combustion of Victorian brown coal*. 2012
5. Xiao, R., Q.L. Song, M. Song, Z.J. Lu, S.A. Zhang, and L.H. Shen, *Pressurized chemical-looping combustion of coal with an iron ore-based oxygen carrier.* Combustion and Flame, 2010. **157**(6): p. 1140-1153.
6. Zhang, S., C. Saha, Y.C. Yang, S. Bhattacharya, and R. Xiao, *Use of Fe2O3-Containing Industrial Wastes As the Oxygen Carrier for Chemical-Looping Combustion of Coal: Effects of Pressure and Cycles.* Energy & Fuels, 2011. **25**(10): p. 4357-4366.
7. *Specification Sheets (SEM)*. 2015 [cited 2015 30 March]; Available from: http://www.jeol.co.jp/en/products/spec_sem.html.
8. *Benchtop X-ray diffraction (XRD) instrument*. 2015 [cited 2015 25 March]; Available from: http://www.rigaku.com/en/products/xrd/miniflex.
9. Kia S. Wallwork, B.J.K., David Wang. *The High Resolution Powder Diffraction Beamline for the Australian Synchrotron*. in *SYNCHROTRON RADIATION INSTRUMENTATION: Ninth International Conference on Synchrotron Radiation Instrumentation*. 2006. Daegu, Korea: AIP Publishing.
10. Bergamaschi, A., A. Cervellino, R. Dinapoli, F. Gozzo, B. Henrich, I. Johnson, P. Kraft, A. Mozzanica, B. Schmitt, and X. Shi, *The MYTHEN detector for X-ray powder diffraction experiments at the Swiss Light Source.* Journal of synchrotron radiation, 2010. **17**(5): p. 653-668.
11. Coelho, A., *TOPAS 4.1. Bruker AXS Inc*. 2008: Madison, Wisconsin, USA.
12. Toby, B.H. and R.B. Von Dreele, *GSAS-II: the genesis of a modern open-source all purpose crystallography software package.* Journal of Applied Crystallography, 2013. **46**(2): p. 544-549.
13. *Cartesian geometry energy dispersive X-ray fluorescence spectrometer*. 2015 [cited 2015 21 March]; Available from: http://www.rigaku.com/en/products/xrf/nexcg.
14. Bale, C., E. Bélisle, P. Chartrand, S. Decterov, G. Eriksson, K. Hack, I.-H. Jung, Y.-B. Kang, J. Melançon, and A. Pelton, *FactSage thermochemical software and databases—recent developments.* Calphad, 2009. **33**(2): p. 295-311.
15. Roine, A., *Outokumpu HSC chemistry for windows: chemical reaction and equilibrium software with extensive thermochemical database.* Pori, Finland: Outokumpu, 1999.
16. Abad, A., J. Adanez, A. Cuadrat, F. Garcia-Labiano, P. Gayan, and L.F. de Diego, *Kinetics of redox reactions of ilmenite for chemical-looping combustion.* Chemical Engineering Science, 2011. **66**(4): p. 689-702.
17. Monazam, E.R., R. Siriwardane, R.W. Breault, H.J. Tian, L.J. Shadle, G. Richards, and S. Carpenter, *Kinetics of the Reduction of CuO/Bentonite by Methane (CH4) during Chemical Looping Combustion.* Energy & Fuels, 2012. **26**(5): p. 2779-2785.

18. Gu, H.M., L.H. Shen, J. Xiao, S.W. Zhang, T. Song, and D.Q. Chen, *Iron ore as oxygen carrier improved with potassium for chemical looping combustion of anthracite coal.* Combustion and Flame, 2012. **159**(7): p. 2480-2490.

Chapter 4 Effect of Coal Minerals on the Performance of CLC

As mentioned in the literature review chapter, the contamination of the OC is an important aspect to be considered in the operation of a CLC system. This contamination is intensified in the presence of solid fuels, whereby the coal ash could interact with the OCs. There have been a few studies on the interaction between OCs and the ash prepared from the combustion of coal [1, 2], but there are limited investigations using the coal itself instead of just the ash. Since some ash compounds have low melting points, these may have evolved and exited the reactor system used to prepare the ash. Alternatively, the generated ash would differ depending on if a reducing or oxidizing gas was used. Hence, studies using just the ash from the combustion of coal will not account for some interactions that may occur in a CLC system.

Therefore, in this chapter, four fuels were used to study the impact that the minerals have on the performance of CLC. Two parent coals, one from Victoria and the other from Canada, were used alongside their demineralized counterparts. The primary difference between the two parent coals is the ash content with the Canadian coal having about 8 times more ash relative to the Victorian coal. The demineralized coals were used to study how the inherent minerals affect the gasification performance of the coal.

This chapter serves to quantify the effect of coal minerals on the performance of a CLC system.

4.1 Experimental Conditions

A TGA was used in this study, as described in Chapter 3, and it was operated at a temperature of 950°C. A total of five redox reactions were performed. The parent and demineralized Victorian and Canadian coals were used as the fuel. The Victorian coal, Yallourn, is denoted by the initial ‘V’ while the Canadian coal is represented by the initial ‘C’.

The OC used was the commercially procured Fe_2O_3 and this was selected to prevent the interaction between the coal ash and other compounds typically found in ore-based OCs. A gas mixture containing 13 v/v% CO_2 with balance N_2 was used during the reduction reaction, having a total flow rate of 23 mL/min. During the oxidation reaction, the CO_2 was switched to air while keeping the flow rates and concentrations constant. The OC to coal ratio used

was 6:1 with the mass of coal being 20 mg. A point to note is that the ash could not be separated at the end of each of the redox reactions and hence accumulated in the crucible.

In terms of characterization, a Scanning Electron Microscope (SEM) was used to study the morphology of the OC particles while an Energy Dispersive X-ray Spectroscope (EDS) was used to obtain the elemental composition. An X-ray Diffraction (XRD) unit was also used to identify the crystalline phases present on the OC.

A thermodynamic equilibrium simulation was done using FactSage 6.4 to predict and quantify the formation of possible phases between the interaction of the OC and ash. This was done to obtain the theoretical prediction for comparison with the experimental results.

4.2 Baseline Tests with the Coal Samples

Baseline tests were conducted with both the parent and demineralized coals in absence of the OC. Figure 4-1 shows the weight loss and instantaneous reaction rate curves for both the parent and demineralized Victorian coals while Figure 4-2 shows the trends observed using both the Canadian coals.

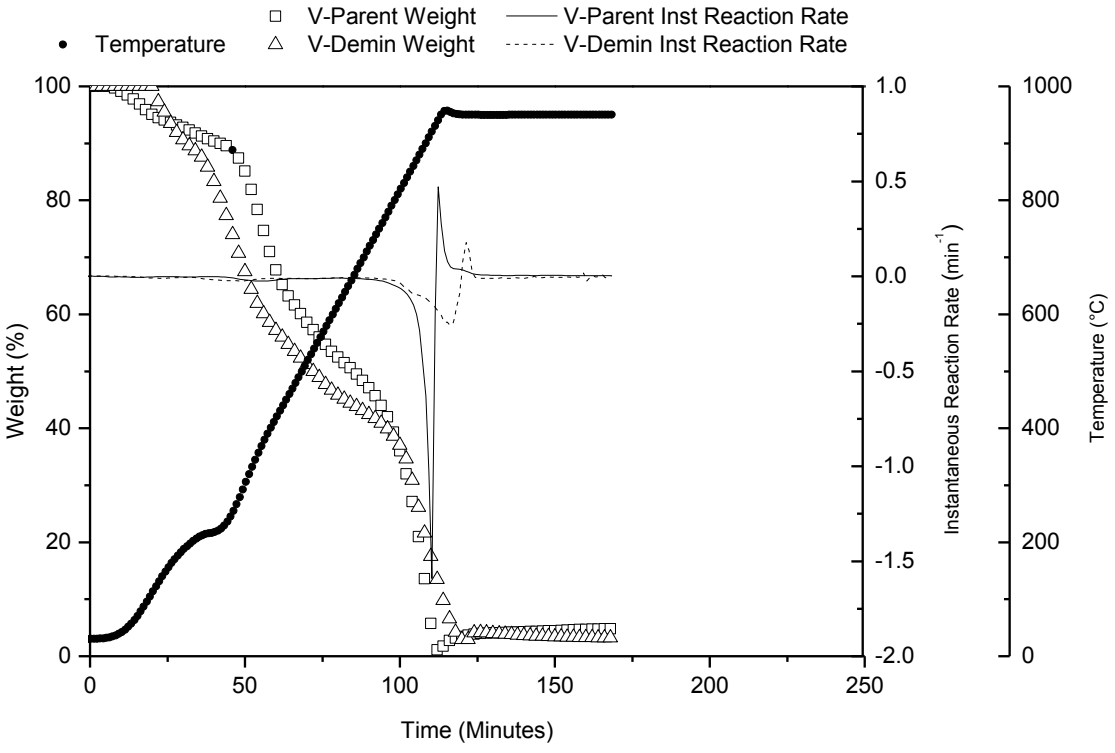

Figure 4-1 Weight loss of parent and demineralized Victorian coals during gasification

Figure 4-1 shows the first weight loss to occur at around 80°C and this continued until a temperature of 200°C. This was due to the removal of moisture from the coal. Beyond this temperature, an appreciable weight loss was observed and this can be attributed to the devolatilization of the coals. The weight loss experienced by the demineralized coal during this period was higher than that of the parent coal and this was due to its higher volatile content (58.7%) relative to the parent coal (50.4%). A sharp instantaneous reaction rate peak was observed at 840°C for the parent Victorian coal while this occurrence was delayed to 950°C for the demineralized coal. This signifies the peak reduction rate of the coal samples; the peak reduction rate of the parent coal is approximately 6 times larger than that of the demineralized coal. This observation can be explained by the presence of inherent coal minerals, typically those of Alkali and Alkaline Earth Metal (AAEM) species such as Na, K, Mg and Ca as well as transition element metals such as Fe in the parent coal; these are known to function as gasification catalysts [3]. These minerals are also responsible for the peak gasification rate of the parent coal to occur 110°C earlier compared to when the demineralized coal was used. When coal is thermally processed, the minerals transform into ash, which accounts for 2.4% and 0.46% of the mass of the parent and demineralized coals respectively. The reduction in the bulk mineral matter between the parent and demineralized coal was 81% and based on the results shown in Figure 4-1, this corresponds to an 83% decrease in the peak gasification rate.

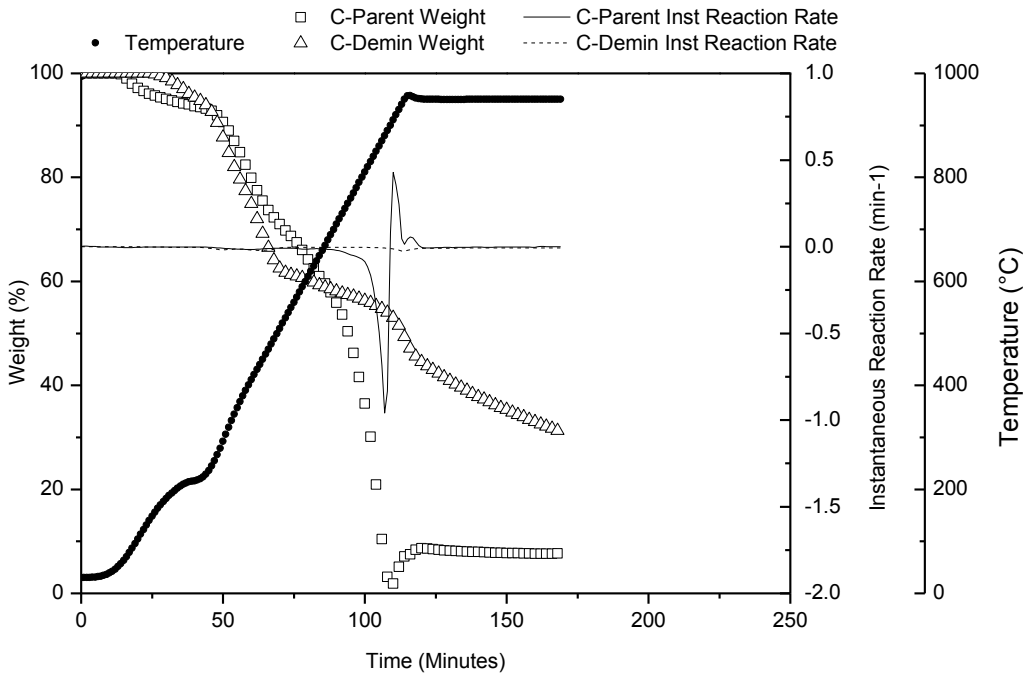

Figure 4-2 Weight loss of parent and demineralized Canadian coals during gasification

Figure 4-2 shows the weight loss and instantaneous reaction rate profiles for the two Canadian coals. The drying of the coals followed a similar profile to the Victorian coals, but the devolatilization of the demineralized coal appeared to proceed up to a temperature of 850°C after which a slight change in the profile can be seen, signalling an increase in the gasification rate. The peak instantaneous reduction rate for the parent coal occurred at a temperature of 890°C while this value increased to 950°C for the demineralized coal; the peak gasification rate of the parent coal was found to be 38 times higher than that of the demineralized coal. The ash content of the parent coal was 19.8% while the demineralized coal had only 0.04% translating to a 98% decrease in the ash content. This subsequently led to a 97.4% decline in the peak gasification rate of the demineralized coal. It can be seen that the demineralized Canadian coal had not completely reduced at the end of the 170-minute mark, highlighting the significant reduction in its reactivity relative to the parent coal.

Comparing the instantaneous reaction rates of both parent coals, the peak value obtained from using the parent Victorian coal is approximately 1.6 times higher relative to when the parent Canadian coal was used. This is due to the fact that the Victorian coal has catalytic inorganic minerals which are organically bound and hence more easily accessible [4] unlike those in the Canadian coal. Also, it can be seen that both coals exhibited similar trends whereby the peak gasification of the parent coals occurred at an earlier time relative to their demineralized counterparts. Although the main reason revolves around the presence or absence of the catalytic minerals, such as those mentioned in Section 4.2, it is also possible that the demineralization process may have altered the physical and chemical structure of the coal. Moreover, this behavioural change is more apparent with the demineralized Canadian coal as the demineralization process involved the use of high temperatures and pressures. Comparing both the coals with their demineralized counterparts, it can be seen that the decrease in the peak gasification rate is fairly proportional to the reduction in the amount of mineral matter.

4.3 Experimental Tests with Fe_2O_3 and Coal Samples (Fifth Cycle)

In this subsection, the behaviour of both the parent and demineralized Victorian and Canadian coals in a CLC system is presented. The first reaction cycle was not selected as the OC underwent conditioning and drying in this period. Additionally, in the first cycle, the OC underwent morphological changes that affect its reactivity. Beyond the first cycle, the results typically had a consistent and repeatable form. Hence, the fifth cycle was chosen as the representative cycle for each test. Each redox reaction took around four hours to complete.

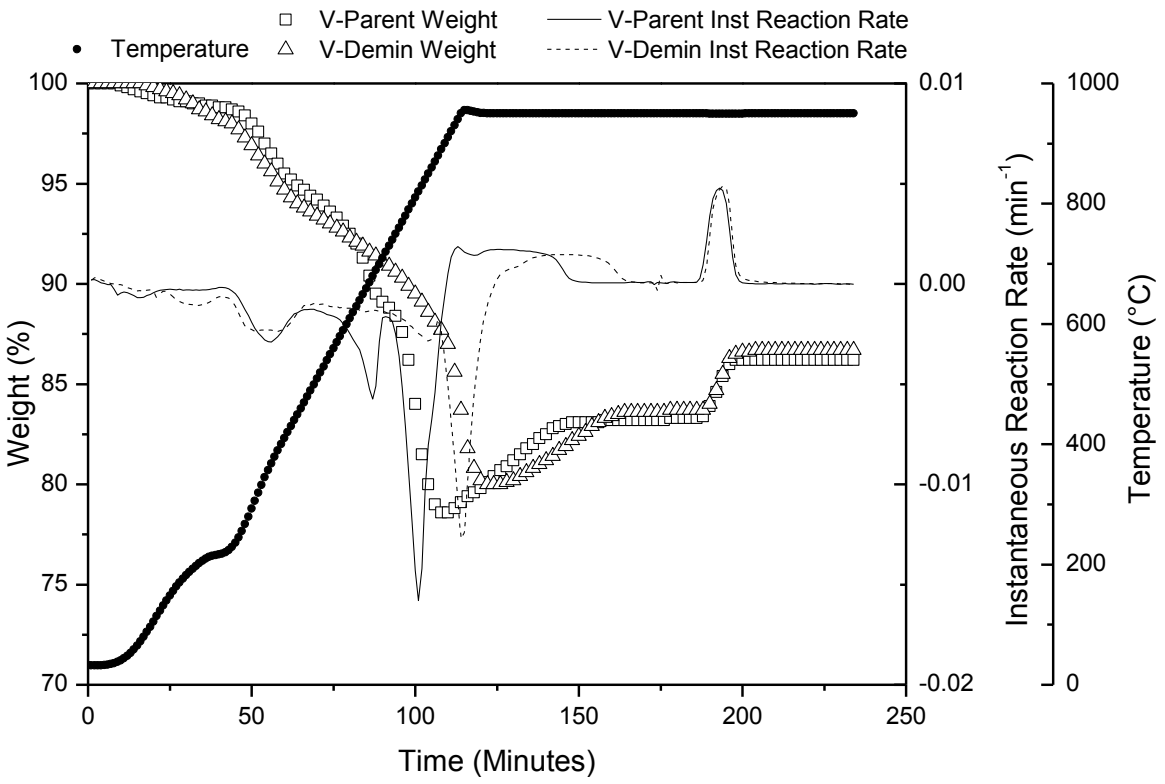

Figure 4-3 Fifth cycle in-situ CLC with parent and demineralized Victorian coals

Figure 4-3 shows the TGA results obtained for the fifth redox experiment performed using both the parent and demineralized Victorian coals. The peak instantaneous reaction rate can be seen to occur at 800°C and 950°C for the parent and demineralized coals respectively. This represents a reduction of roughly 40°C compared to the experiment in which only coal was used and this can be attributed to the presence of Fe_2O_3. This phenomenon is due to the OC's oxidation of the gasification intermediates, H_2 and CO, which are known gasification inhibitors [5]. The peak instantaneous reduction rate exhibits similar characteristics to that observed in the gasification of coal, whereby the peak value obtained using the parent coal was higher than that obtained using the demineralized coal; here, it is higher by a factor of 1.25. The observed difference here is not as apparent when compared to the baseline test and this is due to the equation used for data processing. The instantaneous reaction rate factors in the mass of the sample remaining in the crucible in addition to the rate of mass loss. This caused the difference in the peak rates to close in between the parent and demineralized coals. Since the mass of the OC was included in the calculation, this dictated the magnitude of the reaction rate. A mass gain can be seen to occur between the 105 and 125 minute mark, which was prior to the introduction of the oxidizing agent. Similarly, this was also observed in the

baseline tests as shown in Figure 4-1 and Figure 4-2. The reason for this will be discussed in Chapter 5. At around the 190 minute mark, a steep mass gain can be seen to occur and this is due to the rapid oxidation of the reduced OC. The instantaneous reaction rates for the oxidation step in both cases are very similar and this is due to the reaction being dependent on both the oxidation of the reduced OC as well as the concentration of the oxidizing gas, which were the same for both experiments.

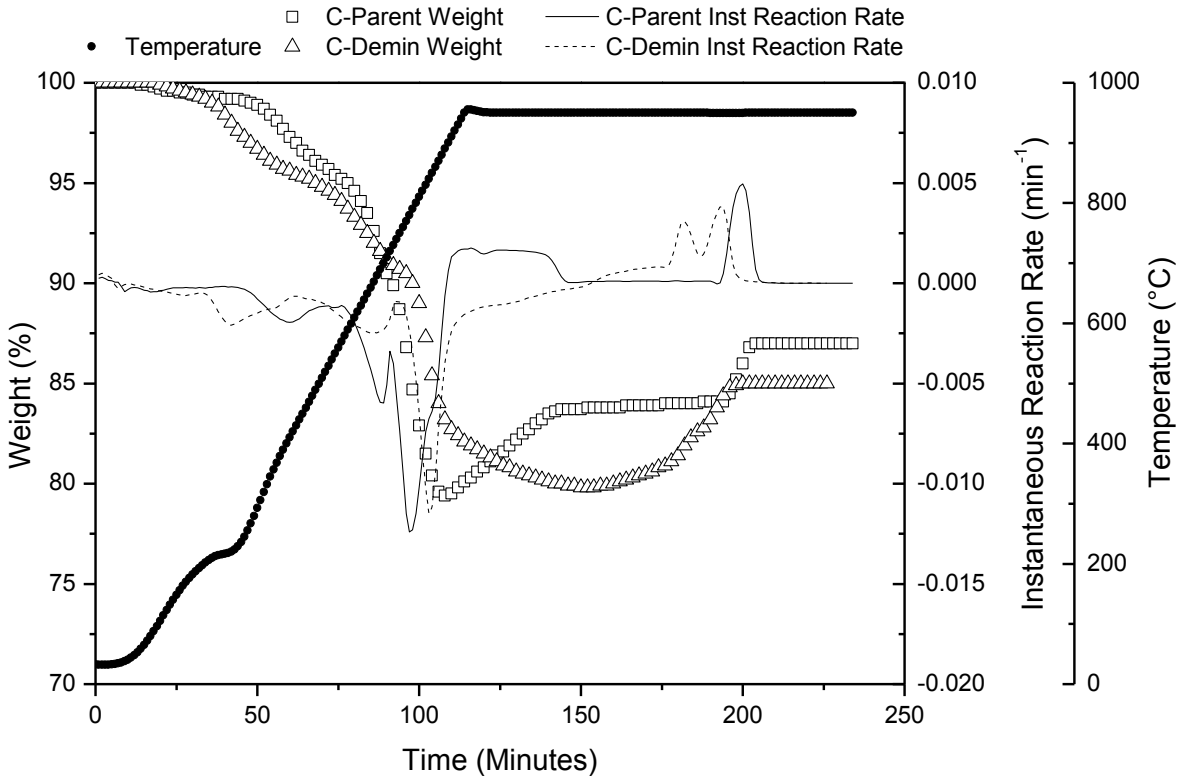

Figure 4-4 Fifth cycle in-situ CLC with parent and demineralized Canadian coals

Figure 4-4 shows the weight loss/gain and instantaneous reaction rate curves for the parent and demineralized Canadian coals. Temperatures of 800°C and 850°C represent the point at which the peak instantaneous reactions rates were observed to occur for the gasification of the parent and demineralized coals respectively. This indicates a decrease of approximately 100°C for both coals relative to the baseline tests in absence of Fe_2O_3. The time for complete reduction of the parent coal in the presence of Fe_2O_3 was approximately 10% less compared to the baseline test in absence of Fe_2O_3. This signifies that the gasification of the parent coal occurred at a faster rate in the presence of the OC for reasons mentioned above, i.e., consumption of the gasification inhibitors by Fe_2O_3. It could also be possible that Fe_2O_3 is

functioning as a catalyst during the oxidation of the gasification intermediates and this requires further investigation.

The faster gasification rate could be ascribed to the higher content of mineral matter in the parent Canadian coal over the demineralized coal, denoting a higher amount of catalytic species and leading to an increase in the gasification rate. The lowest point in the weight loss/gain curve is taken to represent the complete reduction of the coal and OC mixture. From here, it can be seen that the demineralized coal required an additional 50 minutes over the parent coal to undergo complete reduction. Based on the weight loss curve, it can be seen that the reduction rate is quick initially but then decreases significantly after a short duration. An explanation for this behaviour is that the core of the demineralized coal particle is denser or less porous than the surface of the particle, due to the demineralization treatment it underwent, resulting in a decrease in the gasification rate. The peak instantaneous reaction rate of Fe_2O_3 with the demineralized coal is approximately 20% less compared to when the parent coal was used, while the oxidation profiles of both samples were once again similar. A plateau during the reduction stage is not observed with the demineralized coal but it continued to increase in mass after which it was oxidized in the presence of air. With respect to the oxidation step, the OC that reacted with the demineralized coal can be seen to display two distinct reaction rate peaks; this is most likely due to a two-step oxidation of the reduced sample.

Comparing the peak instantaneous reaction rates during the reduction period, the experiment using the parent Victorian coal had a peak rate which was 20% higher relative to when the parent Canadian coal was used. This observation is similar to that seen in the baseline test i.e., without the OC and the reasoning behind this is the same as mentioned earlier.

4.4 Multicycle Redox Experiments

The results obtained from the five redox reaction cycles with the parent and demineralized Victorian and Canadian coals are shown in Figure 4-5 and Figure 4-6 respectively. This was carried out to study the interaction of the coal-Fe_2O_3 mixture in an in-situ CLC environment under CO_2 gasification over five redox cycles, which amounted to a total reaction time of 20 hours. These were also conducted to investigate the effect of multiple redox cycles on the reducing capability of Fe_2O_3 in the presence of coal as well as its re-oxidation potential in the presence of air**.** Finally, the formation of ash from thermal processing of the minerals and its subsequent interaction with Fe_2O_3 was studied.

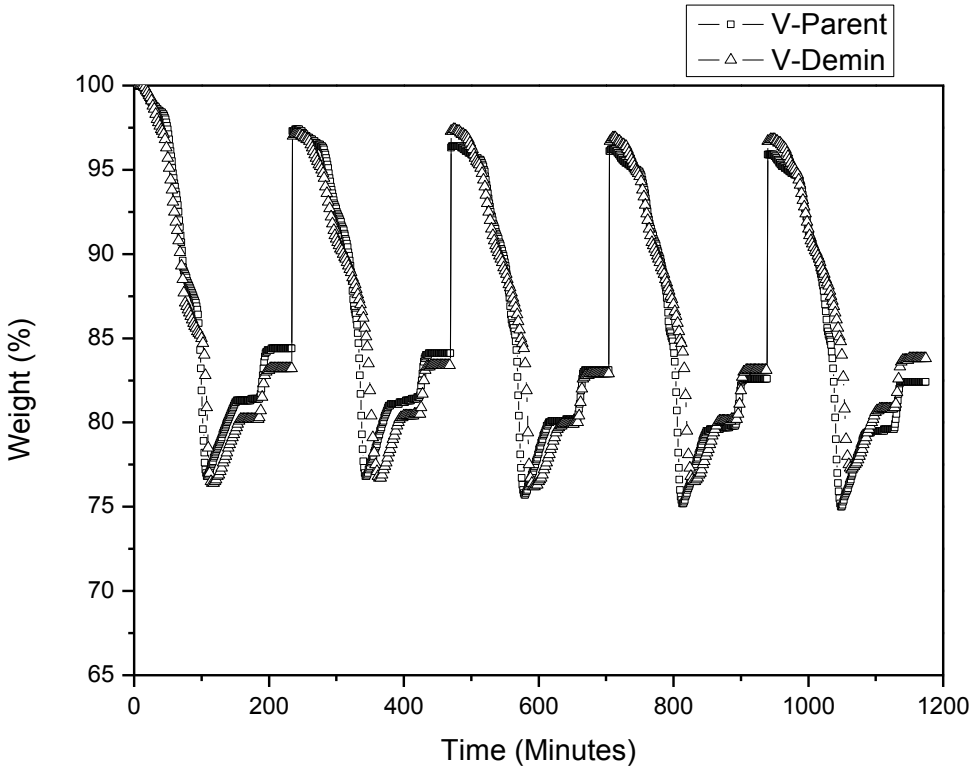

Figure 4-5 Five redox reactions with parent and demineralized Victorian coals

Figure 4-5 shows the weight loss/gain curve of Fe_2O_3 with the parent and demineralized Victorian coals over five redox cycles. There is a slight difference in the results of the first cycle, specifically the initial reduction period, compared to the next four cycles. This is due to the presence of some impurities present in the fresh OC. The OC samples used in all the experiments had a purity of 96%, the remainder of which was predominantly moisture. These compounds were mostly driven off as the temperature was increased during the operation of the first cycle. The starting mass of the second cycle was 97.5% which confirms the aforementioned statement. Beyond the first cycle, repeatability exists in each of the subsequent cycles and this signifies that there was no adverse effect on the performance of the OC over the five cycles due to interactions with ash. The curve representing the results obtained using the parent Victorian coal shows a very slight decrease starting from the second cycle to the fifth cycle. There are two possible explanations for this, the first being due to melting of the ash compounds which then adhered onto the surface of the reduced OC. Upon adhering onto the surface of the OC, the ash prevented these areas from re-oxidizing, making these areas unusable for subsequent reduction reactions. Alternatively, it could be due to the formation of inert and unreactive compounds between the reduced OC and the ash. The second curve, from the reaction with the demineralized Victorian coal, shows no appreciable

mass loss or gain from the second cycle onwards. This confirms the hypothesis mentioned above, as the ash content of the demineralized coal was 81% lesser relative to that in the parent coal, hence decreasing the extent of the interaction between the ash and the OC.

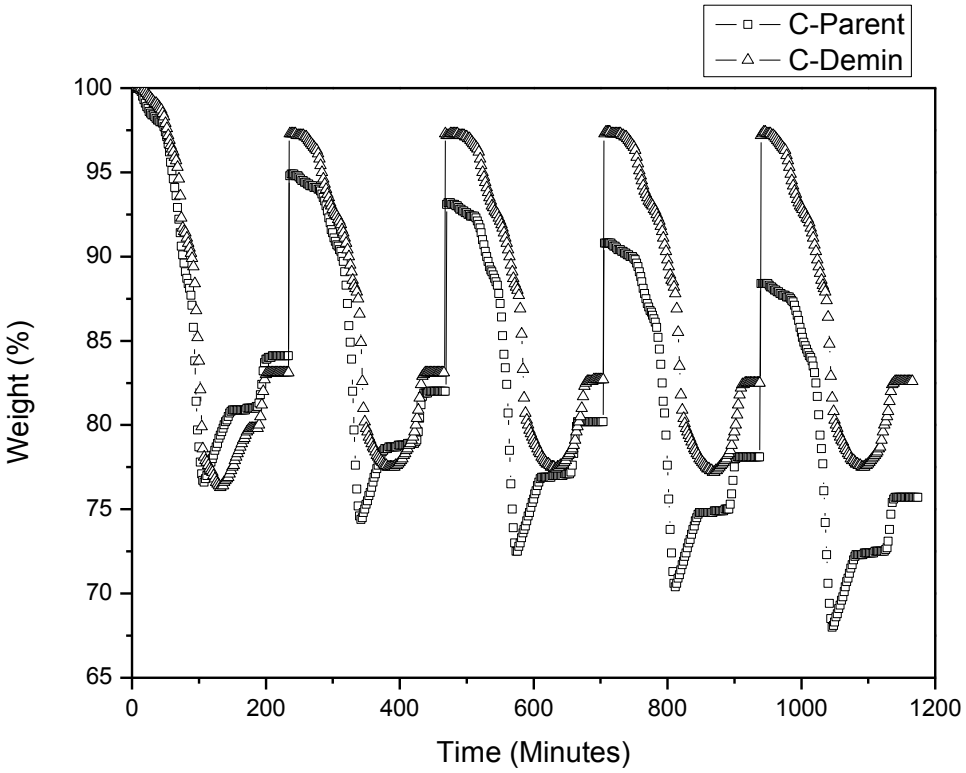

Figure 4-6 Five redox reactions with parent and demineralized Canadian coals

The TGA results for the experiments performed using the parent and demineralized Canadian coals with Fe_2O_3 over five redox reactions are shown in Figure 4-6. It can be observed once again that with the exception of the first cycle, repeatability in the redox curves over the remaining cycles is present. However, there is a significant difference when comparing the results of the parent and demineralized coals. The Fe_2O_3-parent Canadian coal mixture appears to have a significant mass loss from the first cycle onwards. This is due to the substantially higher ash content present in the parent Canadian coal over the parent Victorian coal. XRD and SEM analysis in the subsequent sections will help shed some light on these results. On the other hand, the demineralized Canadian coal does not show any observable decrease in mass over the five redox cycles. While the behaviour of the demineralized Canadian coal is very different from that of the other three coals, the lack of an observable mass loss is in line with the findings obtained using the demineralized Victorian coal, as shown in Figure 4-5.

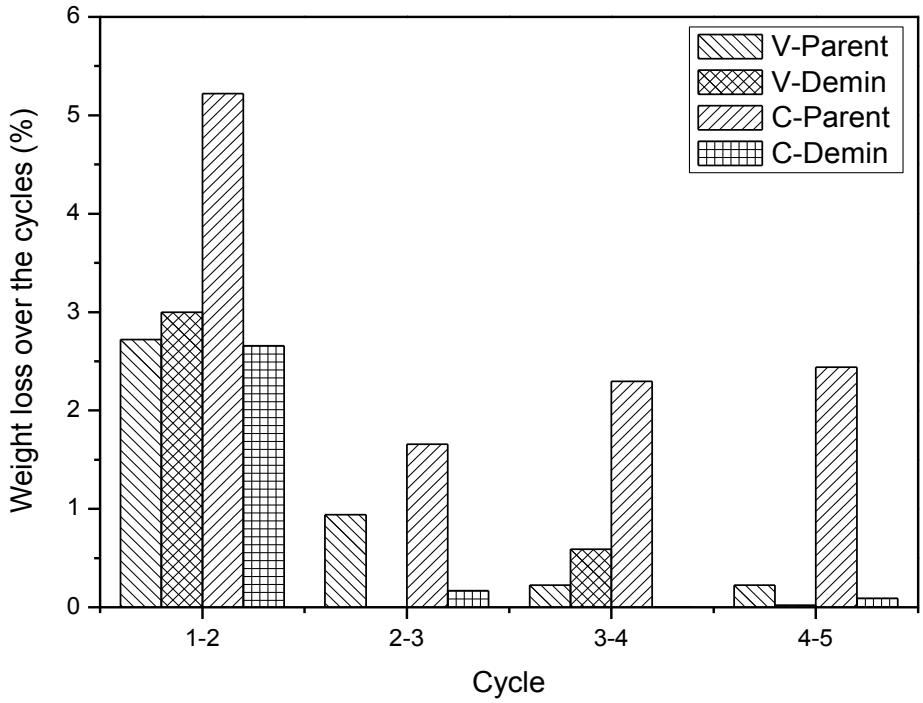

Figure 4-7 Weight loss of the OC across the five redox reactions using the different coals

To further understand the extent of the OC weight loss, the calculated weight loss across each of the cycles was tabulated and can be found in Figure 4-7. A trend can be observed with regards to the mass loss experienced by the OC in the presence of the different coals. While there are some minor fluctuations with the weight loss, the averaged values from the later cycles can be used as representative values. The weight loss across the first cycle is the largest and is approximately 2.5% for most samples, which has been attributed to the impurities present in the fresh OC. In contrast, Fe_2O_3 that reacted with the parent Canadian coal had a weight loss that was approximately three percentage points higher, yielding a total of 5.5%. This excess weight loss corresponds within limits to the weight of the ash accrued over one cycle. Beyond this, the weight loss values between cycles 2-3, 3-4 and 4-5 were relatively similar. The average weight loss over the last two cycles were 2.4%, 0.3%, 0.25% and 0.07% which corresponds to when the parent Canadian, parent Victorian, demineralized Victorian and demineralized Canadian coals were used as the fuel. The weight loss across the cycles shows a strong increasing trend with increasing ash content in the coal. Additionally, a relationship was found between the weight loss of the OC and the ash content of the parent coals. It is clear that the ash content of the parent Canadian coal is higher by a factor of 8 relative to the parent Victorian coal but the interesting aspect is that this same ratio was

observed with the average weight loss of the OC used with both parent coals. This translates to a linear correlation between the ash content of the parent coal and the observed weight loss. It should be noted that this is true for the case studied here and may not be a universal correlation. Based on a study by Bao *et al.* [6], they found that the interactions between Fe_2O_3 and compounds such as SiO_2 and Al_2O_3 in coal ash were prevalent in coals having high levels of these two materials. Around 70% of the Canadian coal's ash consisted of Al_2O_3 and SiO_2. Therefore, the formation of iron silicates and aluminates having poor reactivity is possible.

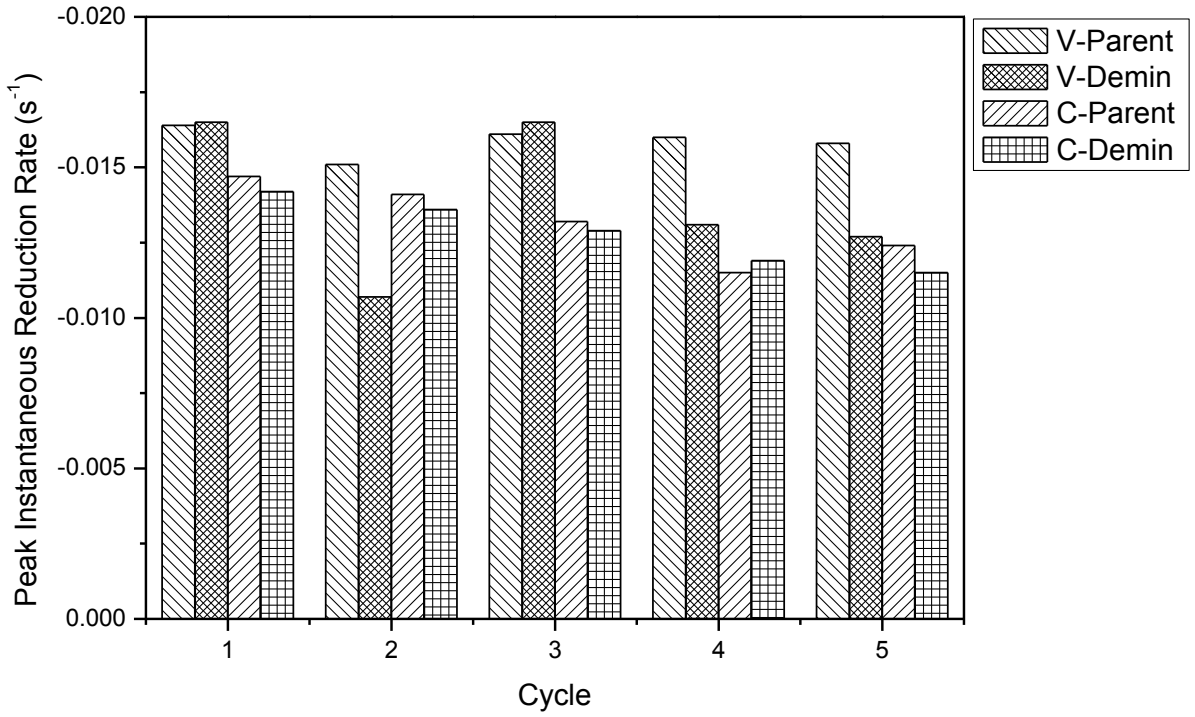

Figure 4-8 Peak instantaneous reduction rates for the four coal types over five redox reactions

Figure 4-8 shows the plot of the peak instantaneous reduction rates over five cycles for the reaction between Fe_2O_3 and the four coals. A general noticeable trend is that in a given parent-demineralized coal pair, the average instantaneous reduction rate over the five cycles is higher when the parent coal was used relative to when its demineralized counterpart was used. Secondly, when considering the last two cycles, the peak reduction rate when using the parent Victorian coal as the fuel was higher by at least 23% compared to when the other fuels were used; this could be due to its high reactivity as previously mentioned. The peak reduction rate was found to decrease slightly going from the first to the fifth reduction reaction. Although the ash could be responsible for this, the fact that all the coal-OC mixtures

experienced this implies that there is another factor at play. A similar phenomenon has also been observed by de Diego *et al.* [7] albeit with gaseous fuels. Although different fuels were used, the principle behind this occurrence still applies as it is caused by the OC being subjected to repeated chemical and thermal stresses. This causes a reduction in its reactivity, leading to a decrease in its peak reduction rate. Although the decline in the peak reduction rate was very small going from the first to the fifth cycle, it is recommended that more cycles be investigated to determine if this trend persists beyond the fifth cycle. A point to note is that an investigation in a TGA leads to significant intimate contact between the OC and coal which would not occur in a fluidized bed reactor. Here, this translates to increased ash deposition and interaction with the OC. What this means is that in a fluidized bed reactor, the reactivity of the OC would most likely be sustained for a longer period of time due to reduced contact and interaction with the ash. On the other hand, the use of a fixed bed system would yield similar results to that obtained in this study and as such would not be a suitable configuration for CLC using high ash fuels. Alternatively, this means that the use of low ash fuels in a fluidized bed iG-CLC process is preferable as this would lead to a lower mass loss of the OC while maintaining the reduction and oxidation rates of the OC over multiple redox reactions.

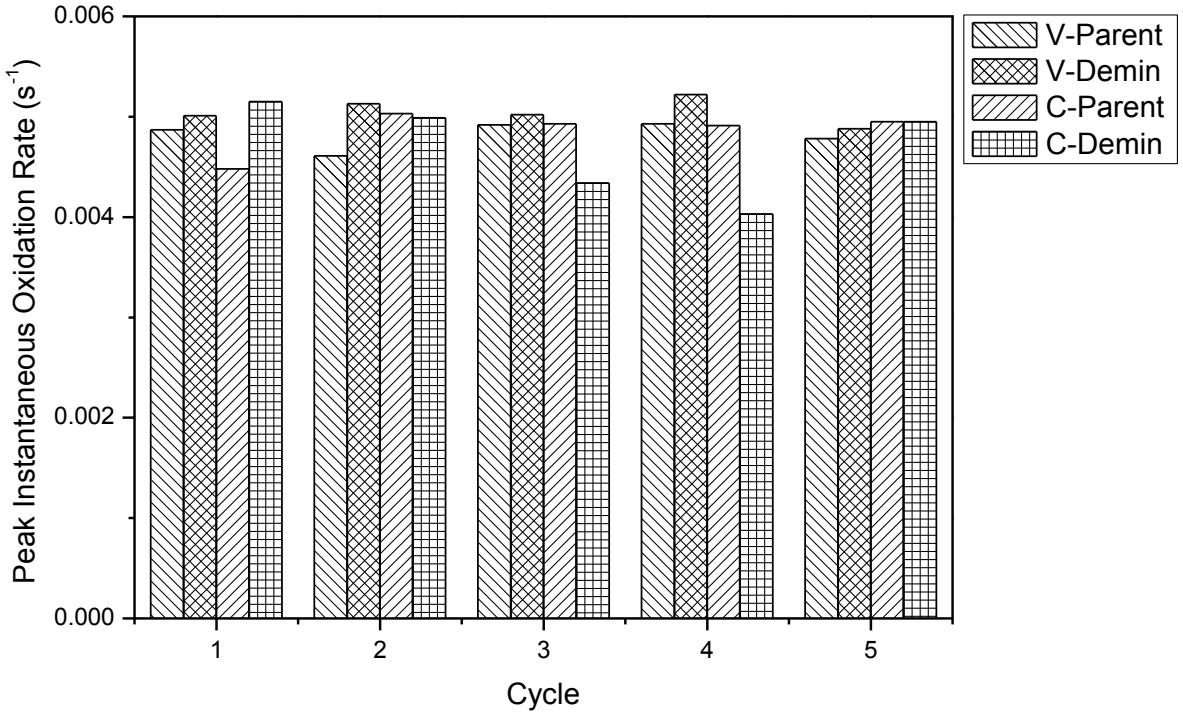

Figure 4-9 Peak instantaneous oxidation rates for the four coal types over five redox reactions

As a comparison, the peak instantaneous oxidation rates were plotted in a similar fashion and are shown in Figure 4-9. Going from one cycle to the next, no discernible difference can be perceived. The reason behind this similarity, although the ash content in the coals varied from 0.04% in the lowest to 19.8% in the highest, is that the peak rate is dependent on the oxidation kinetics, which is initially chemically controlled. This is due to the low concentration of O_2 used, which would dictate the peak rate for all of the oxidation reactions. The low O_2 concentration was used to prevent excessive localized heating on the surface of the OC particle, which may lead to sintering. Since the concentration of the oxidizing gas was constant for all cases, this rate would also be constant. This finding is also similar to that reported by Siriwardane *et al.* [8]. Therefore, the peak oxidation rate would be expected to change if the concentration of the oxidizing gas was altered or if the OC underwent significant sintering or agglomeration, neither of which was observed in this study.

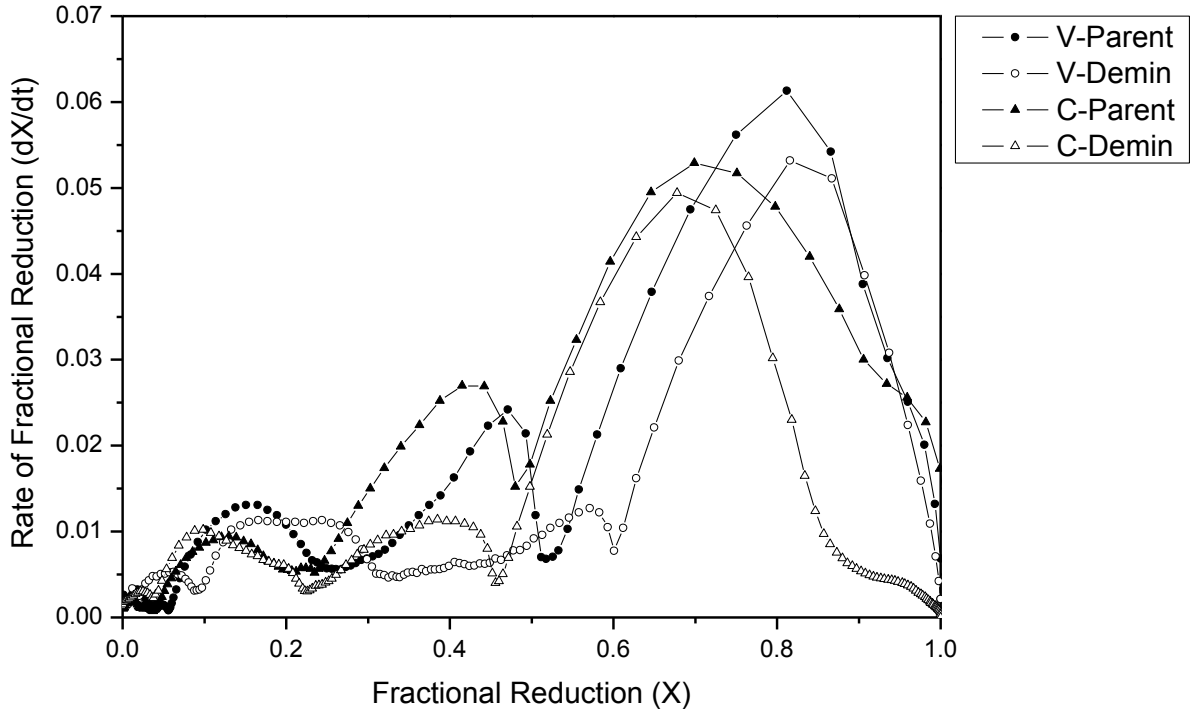

Figure 4-10 Global reduction rate vs fractional reduction of the four Fe_2O_3-coal mixtures during the fifth redox reaction

Figure 4-10 is a plot of the global reduction rate against the fractional reduction of the Fe_2O_3-coal mixture during the fifth cycle for the four coal samples that were investigated. This figure shows the initiation of gasification as well as the peak reduction values on a

normalized scale so that the results from all four samples can be compared on the same basis. It can be seen that the tests that were performed using the parent coals had an earlier initiation point for gasification, which has been attributed to the presence of catalytic minerals in the parent coals. Therefore, the peak fractional reduction rates for the four coals were as follows: V-Parent > C-Parent > V-Demin > C-Demin. Practically, this shows that it is favourable to use low ash, low rank coals over high ash or demineralized coals as low ash low rank coals are more reactive and since they contain a lesser amount of ash, the interactions between the OC and coal ash is also reduced.

4.5 Oxygen Carrier Characterization

The fresh and residual Fe_2O_3 from the end of the fifth redox reaction were characterized using XRD, SEM and EDS to study the changes in crystalline phases, structural and morphological features as well as elemental composition. The fresh Fe_2O_3 served as a baseline so that any differences that arose from the characterization of the residual Fe_2O_3 could be identified.

4.5.1 X-ray Diffraction (XRD)

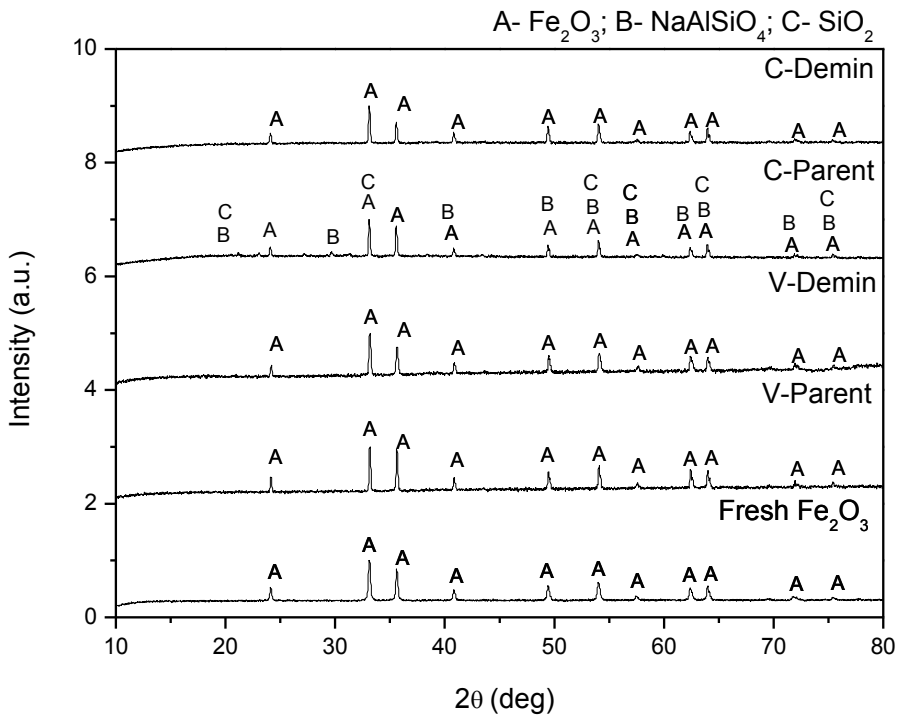

Figure 4-11 Diffractograms of the fresh and residual Fe_2O_3 from the reaction with the four coal samples

The diffractograms of the residual samples obtained from the end of the fifth redox reactions together with fresh Fe_2O_3 are shown in Figure 4-11. The analysis identified the presence of silica (SiO_2) and nepheline ($NaAlSiO_4$) in addition to Fe_2O_3 for the OC that reacted with the parent Canadian coal. It is evident that the ash in the parent Canadian coal consists primarily of SiO_2 and Al_2O_3 with lesser amounts of CaO and Na_2O, justifying the identified phases. This was not evident with the OC that was used with the demineralized Canadian coal as there was only 0.04% ash in it. The diffractograms of the samples that were reacted with both demineralized coals as well as the parent Victorian coal were almost identical to that of the fresh Fe_2O_3 sample. This is possible for both the demineralized coals as they contained very low amounts of ash even if the cumulative amount is taken into consideration. The total mass of ash accrued over the five cycles would be 0.04 mg and 0.46 mg for the demineralized Canadian and Victorian coals respectively; this corresponds to a mass percentage of 0.03% and 0.38% relative to the mass of the OC. These extremely low values could account for the lack of other peaks in the diffractograms. Similarly, the diffractogram of the OC that reacted with the parent Victorian coal coincides with that of the fresh sample even though the total accumulated mass of the ash was 2.2 mg over the five cycles. It is worthwhile mentioning that the ash of the parent Victorian coal consists of approximately 40% Fe_2O_3; as such, the mass of the ash compounds excluding Fe_2O_3 would have been 1.32 mg. The Fe_2O_3 present in the ash would not have led to the formation of a different peak as this would have coincided with the Fe_2O_3 peak of the OC. This means that these samples are similar to the fresh OC with respect to the presence of crystalline compounds, but may very well contain amorphous phases that could not be identified using XRD. Also, compounds with very low concentrations would not have been detected. Therefore, EDS analyses of the OC samples may help identify if other elements are present on the surface in addition to Fe and O.

4.5.2 Scanning Electron Microscope (SEM)

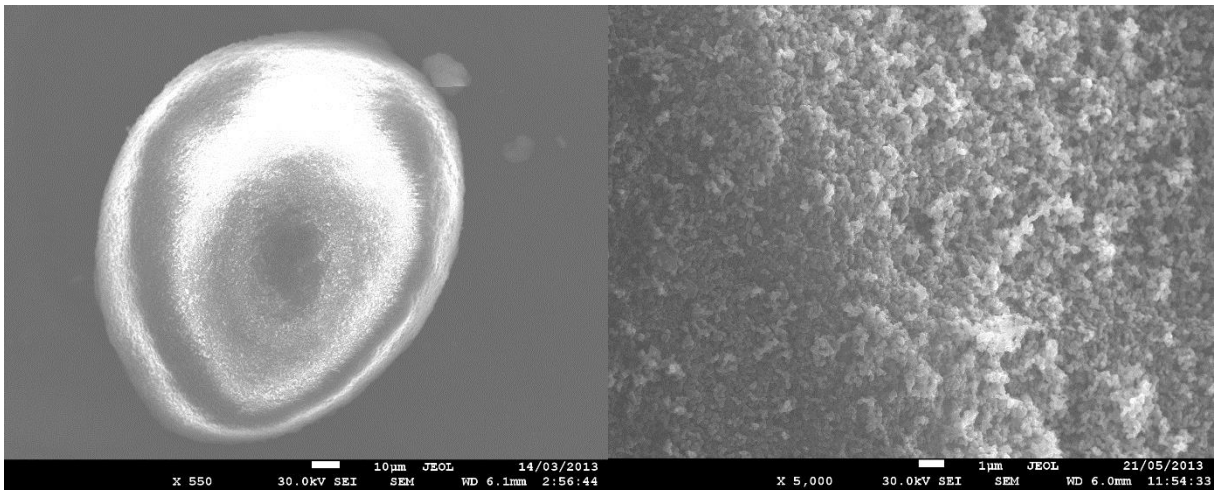

(A) (B)

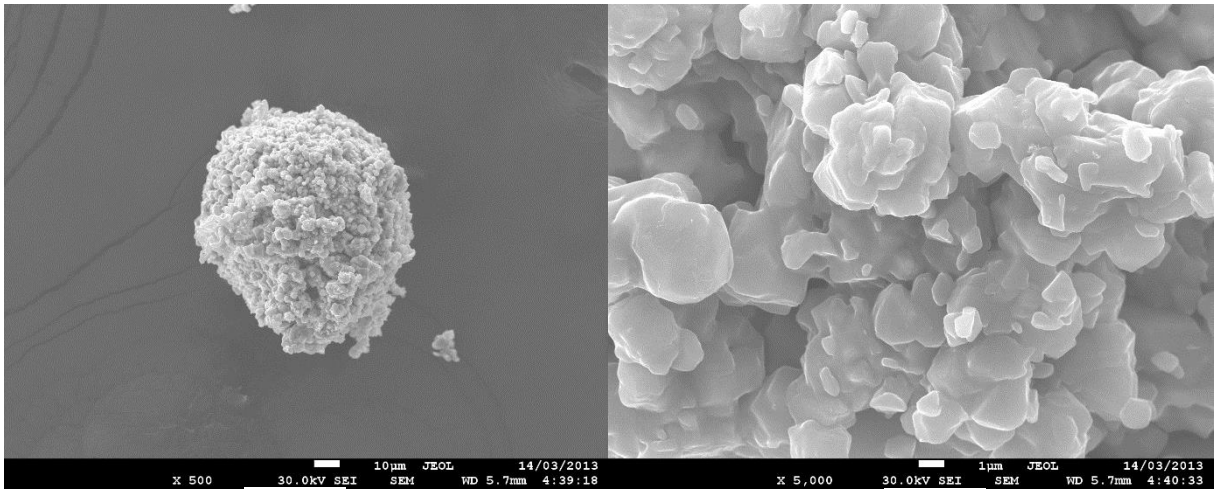

(C) (D)

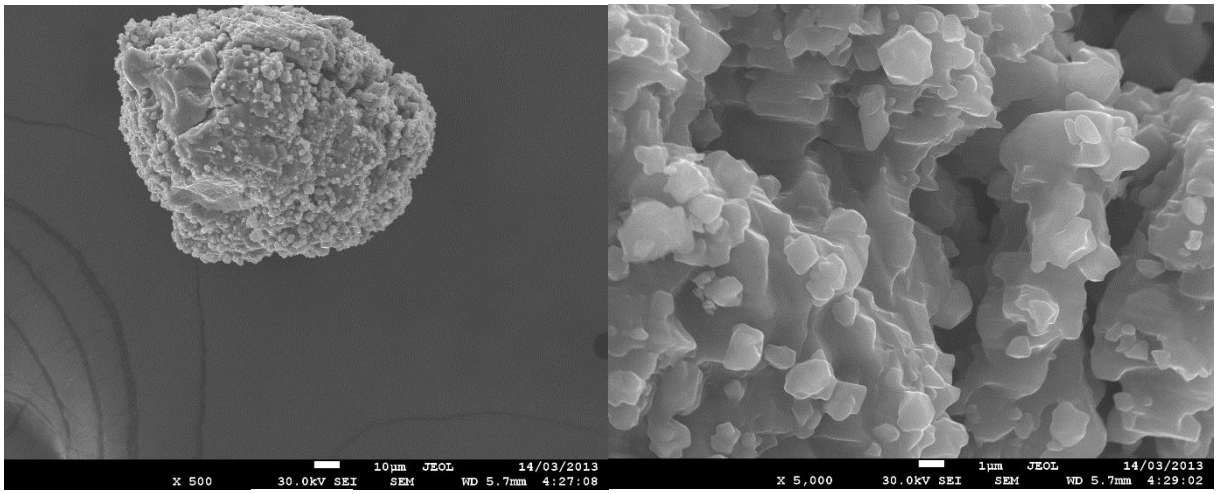

(E) (F)

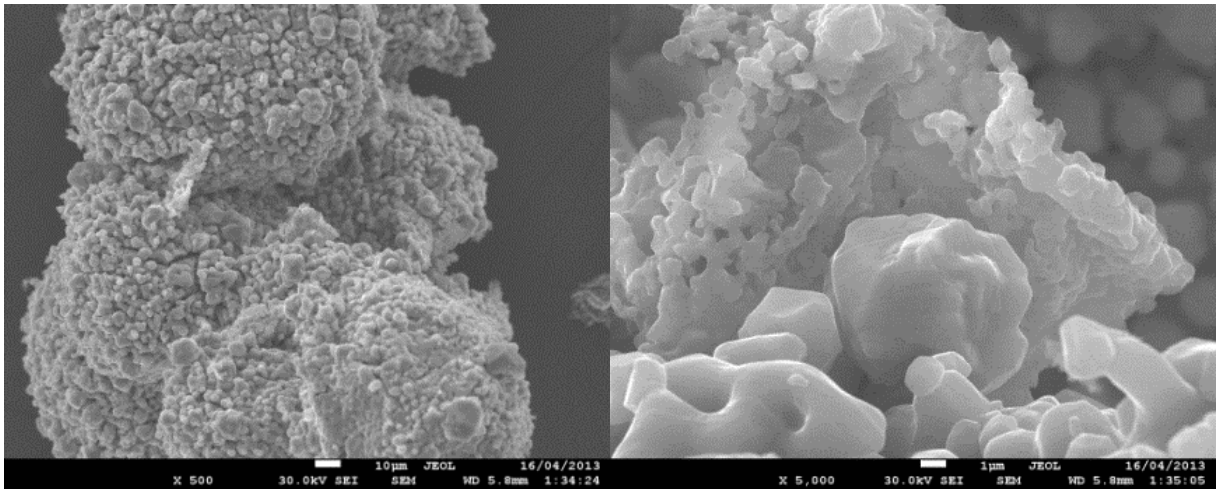

(G) (H)

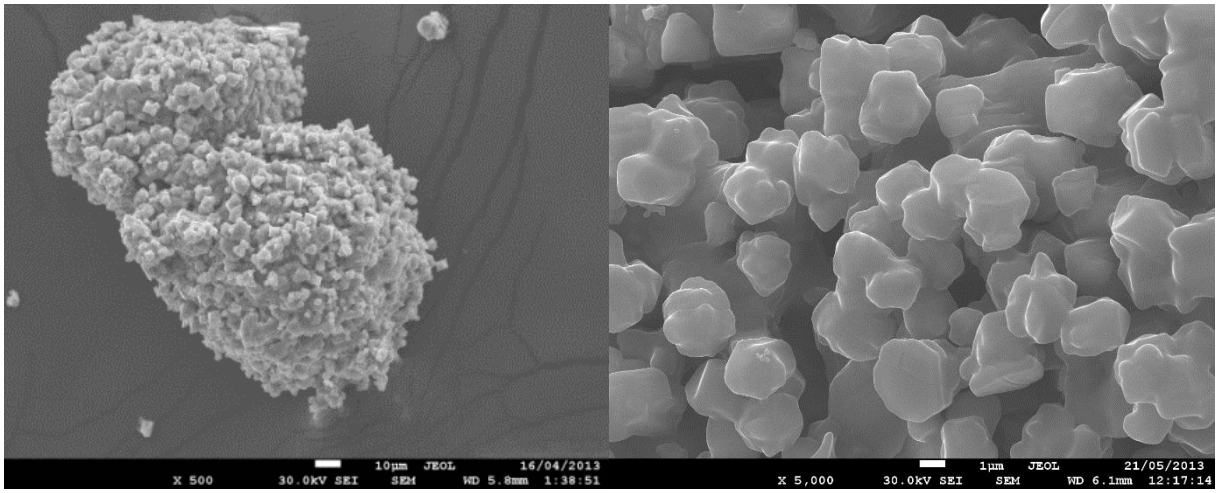

(I) (J)

Figure 4-12 Micrographs of the fresh (A & B) Fe_2O_3 as well as the residual Fe_2O_3 which reacted with the parent Victorian (C & D), demineralized Victorian (E & F), parent Canadian (G & H) and demineralized Canadian (I & J) coals.

Figure 4-12 (A-J) shows the SEM images of the fresh and residual Fe_2O_3 OC samples after five redox reactions. The micrographs on the left and the right represent the images that were taken at a lower (500X) and higher (5000X) magnification respectively. These magnifications were used to obtain a micrograph of the entire particle as well as its microstructure.

The fresh particle under a magnification of 500X appears to be very smooth and rounded, while the fresh particle under a higher magnification appears to contain many small grains. All the residual OC particles, Figure 4-12 (C, E, G, I), are rougher with visible formation of cracks. The images of the residual OC particles from reaction with the parent and demineralized Victorian coals as well as the demineralized Canadian coal show single

particles as being present. Figure 4-12 (G) shows a residual Fe_2O_3 particle from the reaction with the high ash parent Canadian coal and it appears to be agglomerated with multiple particles adhering to one another. This agglomeration behaviour was observed in some and not all of the particles. The melting point of Fe-based metal oxides is lowest when it exists as FeO and has a value of roughly 1400°C; the other three forms, Fe, Fe_3O_4 and Fe_2O_3, have melting points in excess of 1500°C. This indicates that the observed agglomeration is not due to the melting of the OC, but is caused by the minerals present in the coal. A secondary evidence to support this statement is that the OC that reacted with the other three coal types did not appear to be agglomerated and this is due to the low ash content of the coals. Based on the XRD analysis, SiO_2 and $NaAlSiO_4$ were identified in addition to Fe_2O_3. Both of these compounds have melting points in excess of 1400°C as well. There are a few possibilities for this agglomeration phenomenon. Firstly, the AAEM elements such as Na, K, Ca and Mg have melting points lower than 1000°C, which could have caused the observed agglomeration. The parent Canadian coal has around six times the mass of these AAEM compounds compared to the parent Victorian coal. Additionally, the removal of the OC at the end of the 5^{th} redox cycle means that it would be in its oxidized form and as such there may have been lower melting point compounds in the reduced phase. One such compound which could have been formed is fayalite, Fe_2SiO_4, which has a melting point of around 1170°C. While the operating temperature of 950°C may not have caused it to have melted, it may have softened enough to cause the OCs to adhere to one another. Bao *et al.* [6] also reported similar findings with fayalite being responsible for the agglomeration of their samples. Since the parent Canadian coal is rich in SiO_2, this could have occurred but fayalite would not have been identifiable as it would have been oxidized to Fe_2O_3 and SiO_2. Under a higher magnification, Figure 4-12 (D, F, J) shows the residual particles as having much larger grains relative to the fresh particles and this is due to coalescence of the grains. This could be due to the thermal treatment that the OC was subjected to over the course of the five redox reactions. Such an observation implies that the reduced OC particles have a lower surface area. However, the pore size can be seen to have increased after the multiple redox reactions. The reducing gas, CO, repeatedly enters the matrix of the OC particle and exits as CO_2, causing it to be conditioned; as such, this causes the formation of larger pores to facilitate the diffusion of the reactant and product gases. Similarly, this also occurs during the oxidation of the reduced OC particle by O_2. With reference to the agglomerated OC particle mentioned in the previous paragraph, Figure 4-12 (H) shows the magnified image of the same particle. It can be clearly

seen that the porosity has been reduced relative to the OC particles that were reacted with the other three coals. Secondly, it is also evident that the grains in this particle appear agglomerated. It is possible that this is due to low melting point ash compounds or eutectics that have liquefied and adhered onto the surface of the OC particle. This finding supports the results shown in Figure 4-7 whereby the OC that reacted with the parent Canadian coal appears to have undergone a significant mass loss over the five reduction reactions. Ash formation, from the thermal processing of coal minerals, would initiate during the reduction reaction, leading to it being deposited on the reduced OC. Upon oxidation, these compounds prevent the OC from fully re-oxidizing and hence decrease its reactivity, capacity and reusability. This is apparent from Figure 4-8, in which the peak reduction rate of the OC that was used with the parent Canadian coal is significantly lower than that obtained when using the parent Victorian coal as the fuel; this difference is due to the higher ash content of the parent Canadian coal.

4.5.3 Energy Dispersive X-ray Spectroscope (EDS)

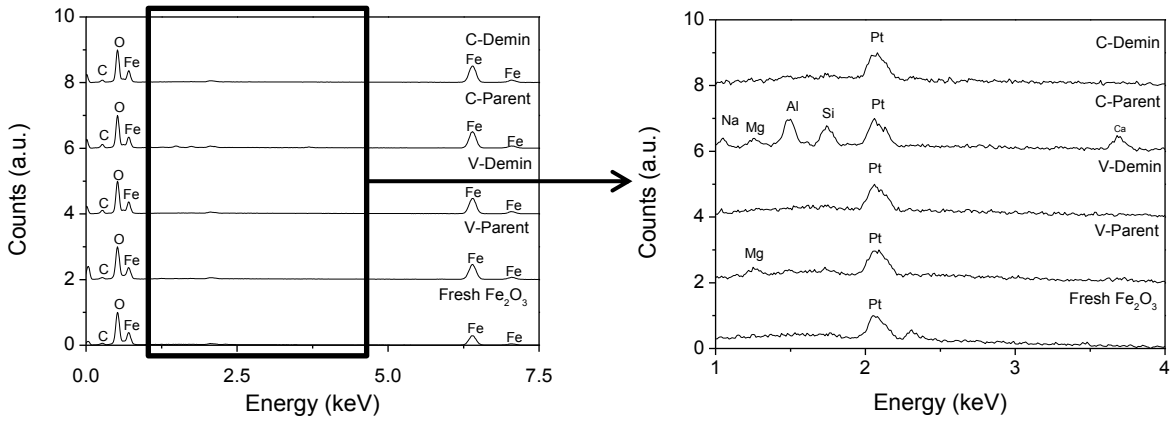

Figure 4-13 Energy dispersive X-ray spectra of the fresh and residual Fe_2O_3 from the reaction with the four coal samples

Figure 4-13 shows the energy dispersive X-ray spectra of the fresh Fe_2O_3 particles as well the residual particles from the reaction with the four different coals. The presence of C and Pt in the spectra is due to the use of carbon tape and platinum coating respectively. The elements with the strongest peak in all the spectra were Fe and O, which account for the majority of the elemental components. The magnified region for energy values between one and four keV are also shown to highlight some of the elements which were found to be present at lower concentrations. Herein, it can be seen that the OCs which reacted with both demineralized

coals show the same behaviour as the fresh Fe_2O_3 particle. However, samples which were reacted with both parent coals show a slightly different behaviour. In addition to the elements mentioned above, the presence of Ca, Si, Al, Na and Mg was observed on the OC that was reacted with the parent Canadian coal while only Mg was present on the OC that reacted with the parent Victorian coal. Although EDS is a semi-quantitative analytical method, it is clear that the amount of these elements were higher in the Fe_2O_3 sample that reacted with the parent Canadian coal over that found in the OC which reacted with the parent Victorian coal. This is once again due to the lower amount of ash in the parent Victorian coal. While all spectra of the residual OCs from reaction with the parent Canadian coal showed the presence of these ash elements, this was not the case for the OCs that reacted with the parent Victorian coal, as only some of the obtained spectra showed the presence of Mg. The reason for this is that Mg is the second most abundant element, after Fe, in the ash of VBC.

The diffractogram of the OC that was used with the parent Canadian coal, as shown in Figure 4-11, was found to have compounds containing Ca, Si, Al and Na, while EDS additionally identified the presence of Mg. The diffractogram of the OC which was reacted with the parent Victorian coal did not show the presence of any crystalline compounds other than Fe_2O_3, but Mg was also identified via EDS. A possible reason for the first observations is that Mg was not present as a crystalline structure and hence unidentifiable using XRD. Additionally, the XRD unit could not identify the deposition of the ash from the parent Victorian coal on the surface of the OC as the amount of ash in the coal was too low, possibly below its detection limit. EDS on the other hand allows for the detection of low concentrations of elements present on the surface of the OC and it was observed that the OCs that reacted with the parent coals had detectable amounts of ash on the surface but this was not the case when the demineralized coals were used.

4.6 Thermodynamic Modelling

Thermodynamic modelling, showing the expected species at equilibrium, was carried out to compare the results of the model with the experimental results identified using XRD.

Table 4-1 Predicted phases formed from the reaction between Fe_2O_3 and the parent coals

Predicted phases	Predicted mass (g/g Fe_2O_3OC)	
	Parent Victorian	Parent Canadian
Fe_2O_3	1.0067	1.0058
$Ca_3MgSi_2O_8$	0.0022	0.0000
$NaAlSiO_4$	0.0019	0.0381
MgO	0.0016	0.0000
Mg_2SiO_4	0.0013	0.0000
$CaAl_2Si_2O_8$	0.0000	0.0697
$CaMgSi_2O_6$	0.0000	0.0179
$NaAlSi_3O_8$	0.0000	0.0131
$CaSiTiO_5$	0.0000	0.0041
$KAlSi_2O_6$	0.0000	0.0031
$Ca_3Fe_2Si_3O_{12}$	0.0000	0.0029

Table 4-1 shows the predicted phases formed from the reaction between the parent Victorian and Canadian coals with Fe_2O_3. The major phase present was Fe_2O_3, in line with the results obtained from the XRD analysis. The reason the predicted mass of Fe_2O_3 is higher than one is due to the Fe present in the ash of the coals. Comparing both samples, it can be seen that the amount of Fe_2O_3 predicted was slightly lower when the parent Canadian coal was used in place of the parent Victorian coal; this is due to the higher amount of Fe in the ash of the Victorian coal relative to the Canadian coal. Based on the model's prediction, it can be seen that $Ca_3Fe_2Si_3O_{12}$ was one of the minor compounds formed when the Canadian coal was used with the OC and contains relatively high amounts of Fe. This could have been formed from the reaction between the reduced OC and the minerals present in the coal ash.

It can be seen from the model that the phases formed using both types of coal were very different. The model predicted that $Ca_3MgSi_2O_8$ and $NaAlSiO_4$ were the dominant phases when the parent Victorian coal was used as the fuel. Besides Fe_2O_3, Victorian coal ash has relatively high amounts of Mg, Si and Ca making the predicted phases a possibility. When

the Canadian coal was used as the fuel, most of the phases identified on the OC contained high levels of Mg, Si, Al and Ca. The ash of the parent Canadian coal is rich in the compounds of these elements, which make up approximately 80% of the total ash content. One of the most dominant compounds predicted when the parent Canadian coal was employed as the fuel was $NaAlSiO_4$. This phase was also found in the X-ray diffraction of the residual Fe_2O_3 sample that had reacted with the parent Canadian coal. There are several possible reasons for the discrepancy between the phases identified by XRD as well as those predicted by FactSage 6.4. Firstly, some of the compounds may not have sufficiently crystallized for it to have been identified by the XRD analysis as the kinetics of some reactions are very slow and FactSage 6.4 only determines equilibrium compositions. Secondly, phases predicted by FactSage 6.4 include both crystalline and amorphous phases, but the XRD unit can only identify the crystalline compounds present with concentrations above its detection limits. Thirdly, some of the compounds deposited on the surface of the OC may have had very small crystal sizes, which XRD is not capable of identifying. Lastly, Factsage 6.4 assumes that all the inputs are perfectly homogenously mixed and hence each compound could react with the material that would result in the formation of the most thermodynamically stable product; this may not be true for the contents in the TGA crucible as there may have been localized surpluses and deficits of certain elements, leading to the formation of less preferred compounds. Although the predicted phases from the thermodynamic modelling did not completely match the XRD results, the prediction serves to identify the formation of thermodynamically favoured compounds.

4.7 Conclusions

This chapter investigated the effect of coal minerals on coal gasification performance as well as the interactions between the ash from the coals and the Fe-based OCs in an in-situ environment. Four main conclusions were drawn from this study and these are mentioned below:

1. The minerals present in coal collectively have a strong catalytic effect on the gasification of both parent coals relative to their demineralized counterparts. The demineralized Victorian coal contains 81% lesser minerals relative to the parent coal and this led to an 83% decrease in its peak gasification rate. Similarly, a 98% mineral reduction in the demineralized Canadian coal caused the peak gasification rate to decrease by 97.4%. This

shows an almost linear correlation between the reduction in mineral matter and peak gasification rate.

2. Thermal processing of the coal minerals led to the formation of ash which then deposited on the surface of the reduced OC, preventing it from re-oxidizing. Additionally, some of the ash reacted with the OC to form unreactive compounds. The ash content of the parent Canadian coal is approximately 8 times higher than that of the parent Victorian coal, 19.8% vs. 2.4% respectively, which led to an observed OC mass loss that was 8 times greater, 2.4% vs. 0.3%. The mass loss in the OCs due to the ash from the parent coals appears to have a 1:1 correlation based on this study.

3. The mass loss of the OC was not significant when the demineralized coals were used, but this led to a loss in their gasification reactivity relative to when the parent coals were utilized. Agglomeration, as evidenced by the SEM micrographs, was not observed when the parent Victorian coal was used but was found to occur when the parent Canadian coal was used. While the lifespan of the OC will be higher when used with demineralized coals, due to lesser interactions with the ash, the cost penalty incurred by the demineralization process and the slower reaction rate that arises from the reduced gasification kinetics renders the use of such coals unfeasible from an economic point of view.

4. The results indicate that the iG-CLC process is more suitable for highly reactive, low ash coals. While the minerals are responsible for the increase in the gasification rate of the coals, it causes a reduction in the OC's oxygen carrying capacity due to ash deposition or interaction with the ash. This means that the lifetime of the OC which is used with Victorian brown coal would be much higher than when it is used with the Canadian lignite. Therefore, this would lead to a reduction in the operating cost of the CLC process, as the frequency of replacing the OC would reduce hence decreasing the make-up cost of the OC.

The obtained results suggest that the use of the low ash Victorian brown coal is more suitable for the CLC process compared to the high ash Canadian coal. Additionally, the Victorian brown coal used here, Yallourn, had the benefit of containing a large amount of iron in the ash with smaller amounts of other minerals, which reduces the interactions of these compounds with the Fe-based OC.

4.8 References

1. Bao, J., Z. Li, and N. Cai, *Interaction between iron-based oxygen carrier and four coal ashes during chemical looping combustion.* Applied Energy, 2014. **115**: p. 549-558.
2. Keller, M., M. Arjmand, H. Leion, and T. Mattisson, *Interaction of mineral matter of coal with oxygen carriers in chemical-looping combustion (CLC).* Chemical Engineering Research and Design, 2014. **92**(9): p. 1753-1770.
3. Li, C.-Z., *Advances in the science of Victorian brown coal*. 2004: Elsevier Science.
4. Bhattacharya, S., K.B. Kabir, and K. Hein, *Dimethyl ether synthesis from Victorian brown coal through gasification–Current status, and research and development needs.* Progress in Energy and Combustion Science, 2013.
5. Johnson, J. and M. Elliott, *Chemistry of Coal Utilization*. Vol. 2nd Supplementary Volume. 1981: John Wiley & Sons. 1491-1598.
6. Bao, J., Z. Li, and N. Cai, *Interaction between iron-based oxygen carrier and four coal ashes during chemical looping combustion.* Applied Energy, 2014. **115**(0): p. 549-558.
7. de Diego, L.F., F. Garcia-Labiano, J. Adanez, P. Gayan, A. Abad, B.M. Corbella, and J.M. Palacios, *Development of Cu-based oxygen carriers for chemical-looping combustion.* Fuel, 2004. **83**(13): p. 1749-1757.
8. Siriwardane, R., H. Tian, G. Richards, T. Simonyi, and J. Poston, *Chemical-Looping Combustion of Coal with Metal Oxide Oxygen Carriers.* Energy & Fuels, 2009. **23**(8): p. 3885-3892.

Chapter 5 In-situ Synchrotron Study of Fe_2O_3 Reduction with Victorian Brown Coal

The reduction of Fe_2O_3 in the presence of Victorian brown coal (VBC) has not been sufficiently investigated. A study was conducted by Siriwardane *et al.* [1] using bituminous coal, char and carbon black with a Cu-based OC. The authors employed in-situ XRD to study the reduction of CuO in the presence of a solid fuel to determine the temperature at which the reduction reaction initiated. To date, in-situ synchrotron-based XRD investigations have not been done using Fe_2O_3, which is a highly promising metal oxide for use as an OC. This is one of the aims in this chapter and this study would provide insights into the mechanistic behaviour of the OC in the presence of VBC.

Additionally, based on the TGA results from the previous chapter, it was found that the OC-coal mixture experienced a weight gain during the reduction period. Therefore, this chapter will also investigate the cause behind this phenomenon through the use of a TGA. Experiments were performed with regular sample removal for characterization to better understand the reasons behind this phenomenon.

This chapter will investigate the extent of reduction of an Fe-based OC as well as the weight gain phenomenon experienced by the OC under reducing conditions, as highlighted in the previous chapter.

5.1 Experimental Conditions

The first part involved using the TGA with an OC to coal ratio of 6:1, similar to that used in the study in Chapter 4. The gas flow rate was 23 mL/min with 13 v/v% CO_2 and balance N_2. The temperature was increased from ambient to 950°C. During the oxidation reaction, air replaced CO_2. The contents in the crucible were removed at three different points (110, 135 and 160 minute mark) during the reduction reaction. The first point denoted the lowest point in the TGA weight profile with the last point being the point at which the weight gain had stabilized during the reduction period; the second point was taken in between the two extremes to help shed some light on this phenomenon.

The second part of this study involved performing three investigations using the powder diffraction beamline at the Australian synchrotron. Here, the commercially obtained Fe_2O_3 was used as the OC. The OC-coal samples were loaded into a quartz capillary and placed into

the setup as shown in Figure 3-9 of Chapter 3. The readings were initially taken at room temperature and then from 300°C to 950°C at 50°C intervals. A reducing gas flow rate of 1 L/min was used, consisting of around 20 v/v% CO_2 with the balance made up of N_2. For the first experiment, the sample remaining at the end of the reduction period was also oxidized and this was done by replacing the CO_2 stream with air, while keeping the flow rates constant. The first experiment was done with an OC-coal ratio of 6:1, the second with a ratio of 1:2.6 and the third with this same ratio but using char as the fuel. The latter two were performed to study the effect of the fuel on the reducing capability of the OC. The collected data were subjected to Rietveld refinement to obtain the lattice parameters and crystallite sizes of the OCs.

SEM, EDS and XRD were employed to characterize the samples from the TGA study as the amount of the samples from the synchrotron study was too little to be characterized.

The experimental results were then compared to theoretical results by using both FactSage 6.4 and HSC Chemistry. The former was used to generate phase diagrams, while an Ellingham diagram was constructed using the latter. The purpose of these two models was to determine the theoretical initiation temperatures for the reduction of Fe_2O_3, Fe_3O_4 and FeO in the presence of CO, which is the main gasification intermediate produced from CO_2 gasification of VBC.

5.2 TGA Experiments

As mentioned, one focus of this chapter is to understand the reason behind the weight gain experienced by the OC-coal mixture during the reduction stage, as mentioned in Chapter 4. To study this, the contents of the crucible were removed at three intervals. Before delving into this, a typical weight loss/gain curve obtained from the reaction between Fe_2O_3 and VBC is first shown and discussed below.

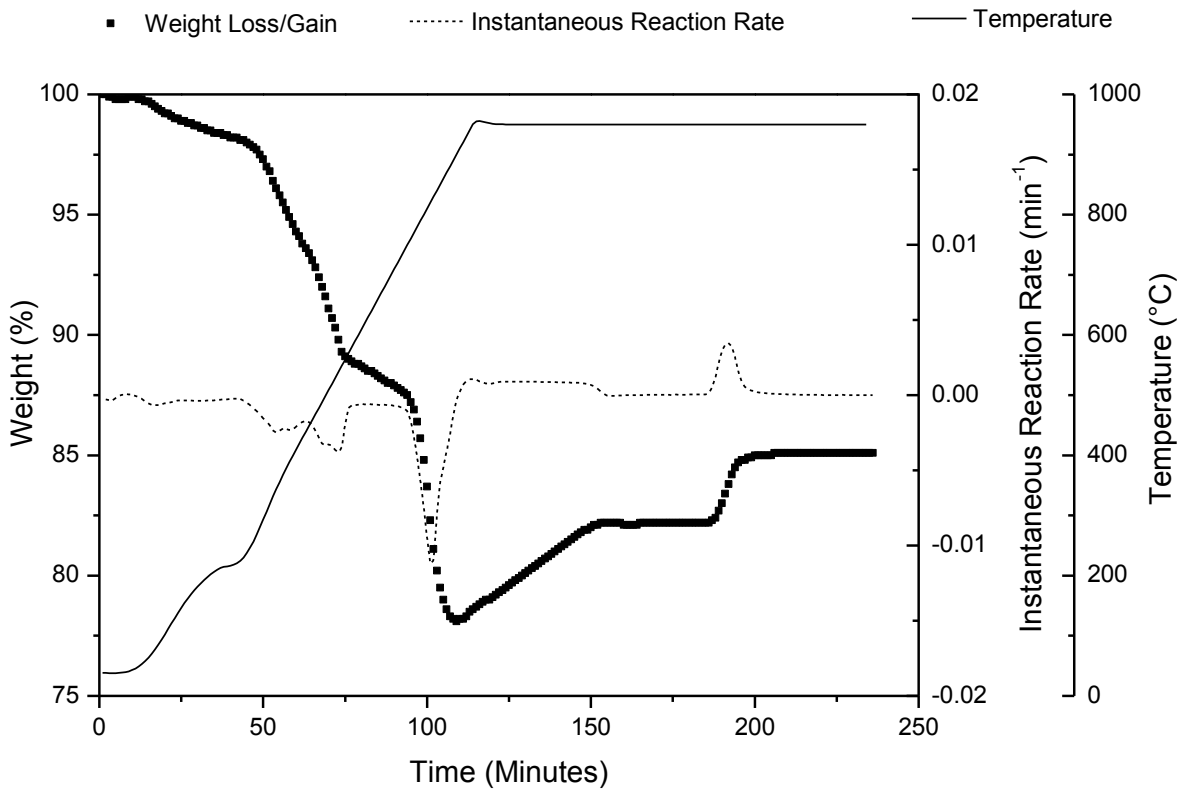

Figure 5-1 Complete redox reaction between Victorian brown coal and Fe_2O_3

Figure 5-1 shows a complete redox reaction using Yallourn coal and Fe_2O_3. Reducing conditions were in effect from the start until the 190th minute, after which the sample was oxidized. The first sign of mass loss occurred around 80°C and continued until a temperature of 220°C; this was due to the removal of moisture from both the OC and coal as well as partial pyrolysis of the coal. Beyond 220°C, the rate of coal devolatilization was found to increase, resulting in an appreciable mass loss. Subsequently, gasification was found to commence around the 550°C mark and this was signalled by the increase in the instantaneous reaction rate at this point. Additionally, it is possible that the OC could have started reacting with the coal gasification products and this will be confirmed in the latter half of this study by means of in-situ XRD.

At 750°C, there is a significant increase in the weight loss, evidenced by the steeper line in the weight loss curve and increased instantaneous reaction rates. The kinetics of the gasification of coal and the reduction of the OC are improved at higher temperatures, resulting in an increase in the rate of both reactions with increasing temperature. This weight loss continued until a temperature of 900°C, at which point the weight loss curve was at a minimum. Typically, under reducing conditions, the weight loss curve should flatten out after

the minima is reached; this was not the case here as the sample in the TGA started gaining weight over a duration of about 40 minutes before the weight loss/gain curve stabilized. Such an occurrence had been observed by Saha *et al.* [2] using Fe_2O_3 as the OC, but no explanation was given for the observed weight gain during the reduction reaction. At around the 190 minute mark, the oxidizing gas was introduced into the TGA to oxidize the reduced OC, resulting in a very quick mass gain.

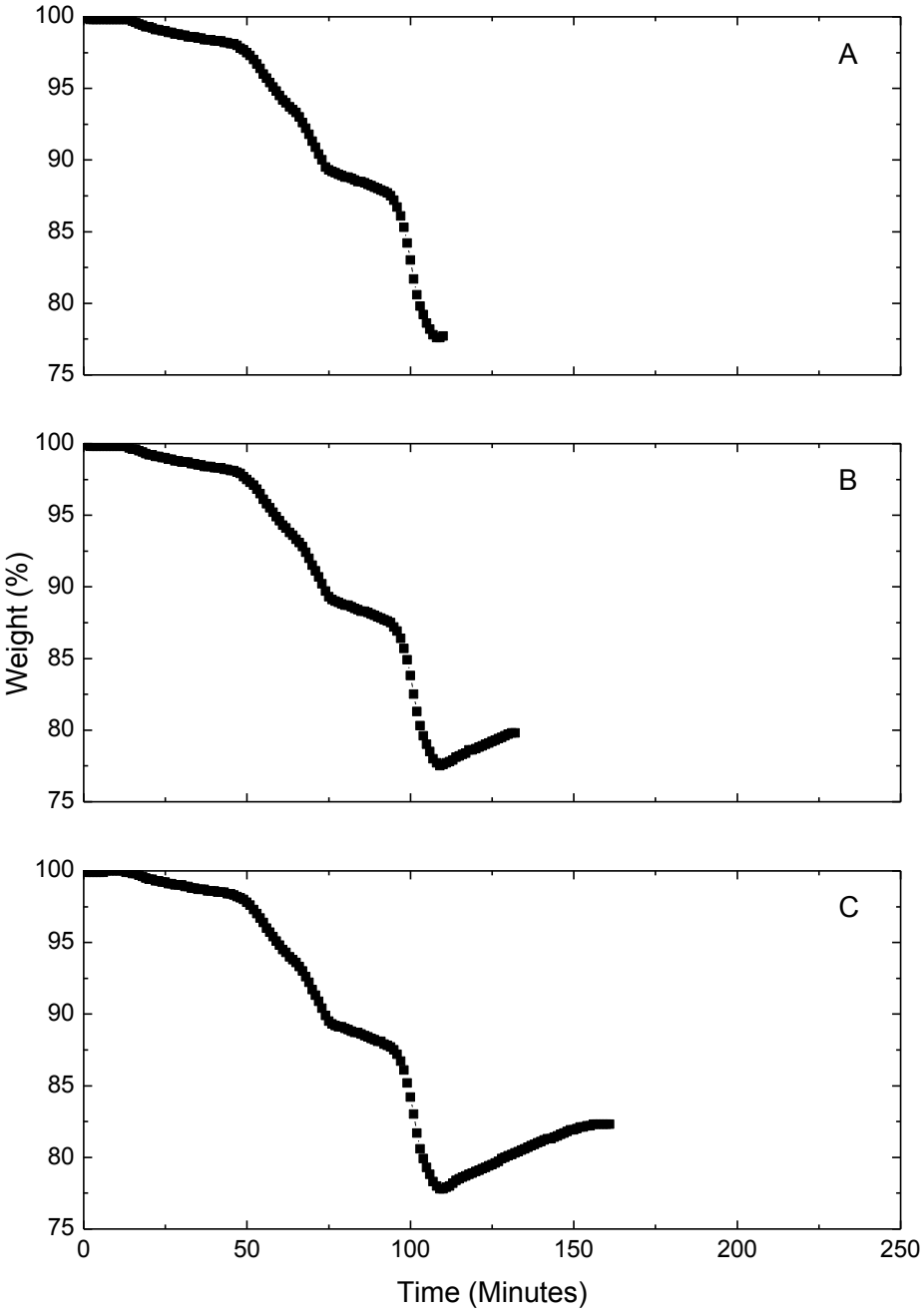

Figure 5-2 Weight loss/gain curves for samples removed at the start (A), midway (B) and end (C) points of the mass gain sections

To investigate this behaviour, the samples in the crucible were removed at three different intervals (110, 135 and 160 minutes), corresponding to the initiation, midway point and termination of the mass gain sections respectively. The obtained weight loss/gain curves are shown in Figure 5-2 (A-C). The gases were switched to N_2 at the end of the experiment to provide an inert environment to prevent the sample from gaining mass as it was being cooled down. The results in Figure 5-2 (A-C) display a similar trend to that shown in Figure 5-1 and will not be discussed further.

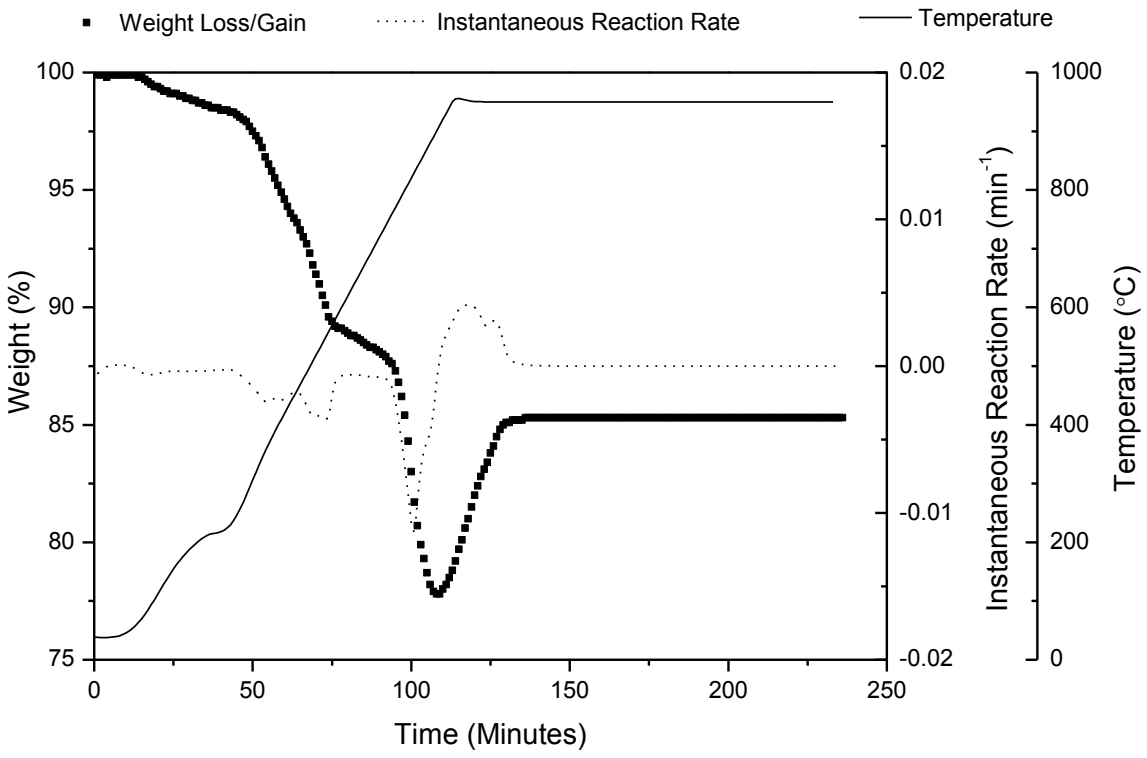

Figure 5-3 Redox reaction curve with oxidizing gas introduced at 110 minutes

Another experiment was also performed and involved switching the reducing environment to an oxidizing environment at the 110 minute mark to determine the extent of oxidation when the sample was at its lowest weight. Figure 5-3 shows that when air was introduced at the 110 minute mark, the contents in the crucible underwent oxidation and stabilized at the same level as observed in Figure 5-1. This signifies that the reactivity of the OC has not been affected as it was capable of re-oxidizing to its fully oxidized state. The results from the TGA still do not explain this behaviour and therefore the residues were characterized to help shed some light on this phenomenon.

5.2.1 Scanning Electron Microscope (SEM)

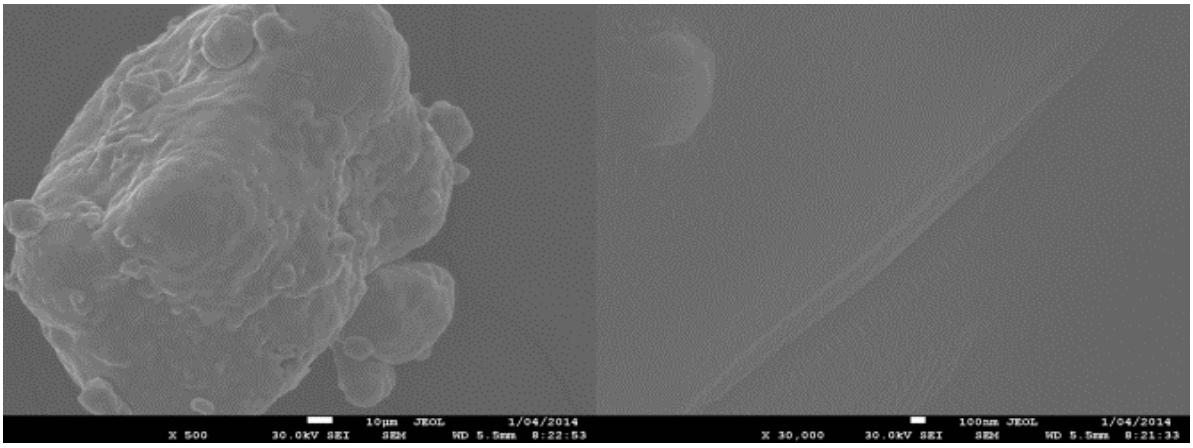

(A) (B)

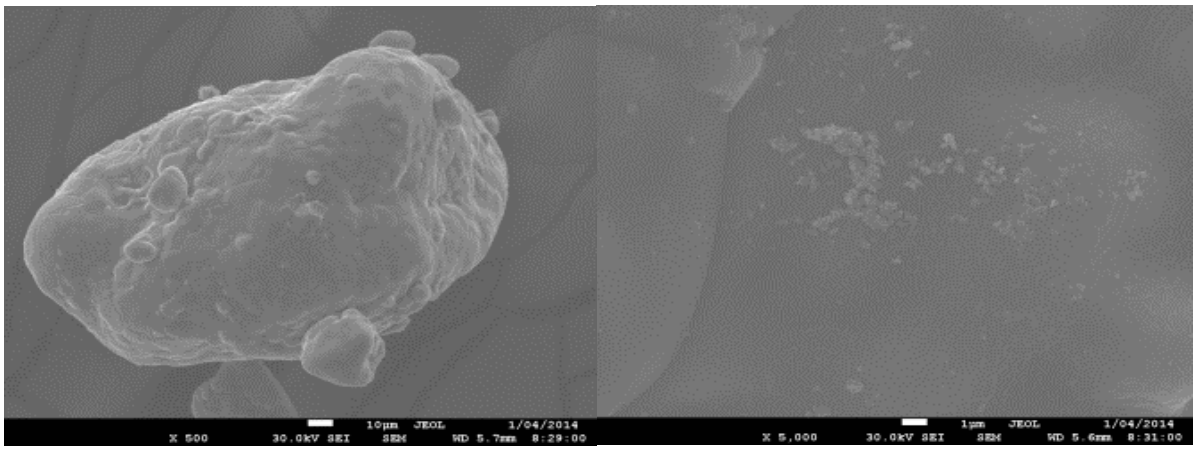

(C) (D)

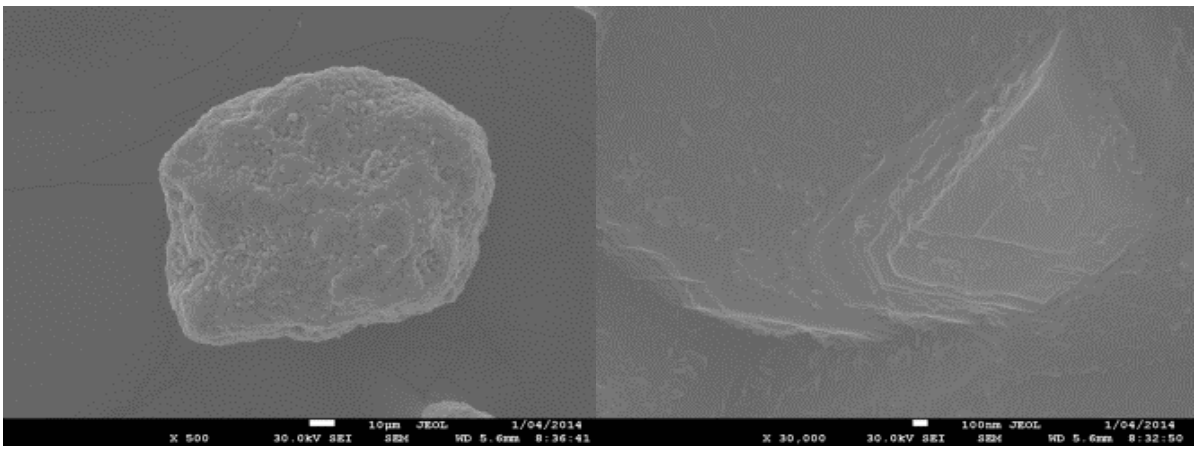

(E) (F)

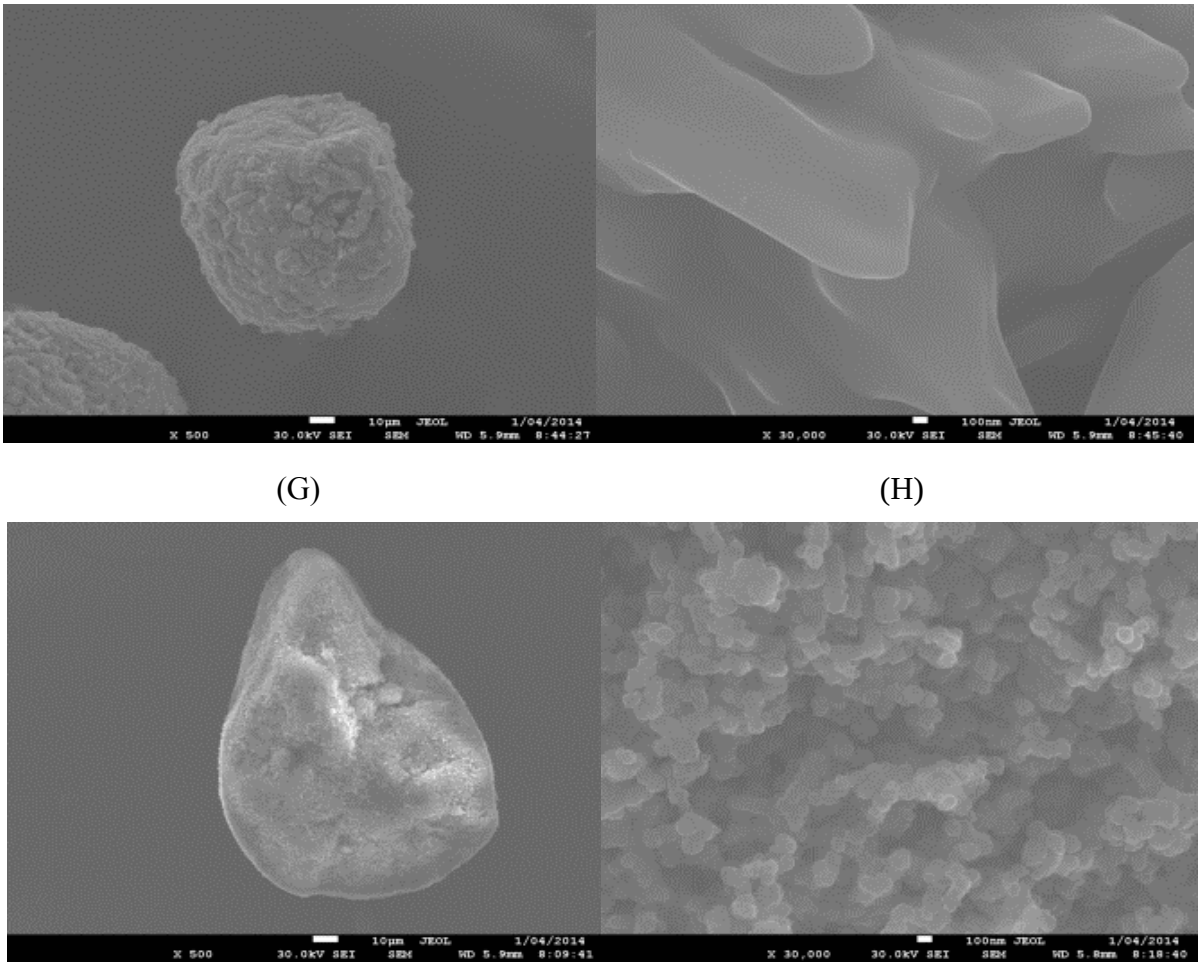

(G) (H)

(I) (J)

Figure 5-4 SEM micrographs of sample residues after 160 minutes (A & B), 135 minutes (C & D), 110 minutes (E & F) and complete redox (G & H); micrographs of fresh Fe_2O_3 (I & J)

Micrographs obtained through use of the SEM are shown in Figure 5-4 (A-J). This technique was used to study the morphology and surface characteristics of the various particles that were removed during the course of the reaction; these were then compared to the micrographs of the fresh and fully oxidized particles. The micrographs on the left were taken at a low magnification of 500X while the ones on the right were captured at a much higher magnification of 10,000X. Micrographs I and J show the images that were taken of the fresh OC particle and it can be seen to have a rough surface consisting of many tiny grains with diameters of 100-200 nm. Images E and F of the particles removed at 110 minutes, corresponding to the lowest point on the weight loss/gain curve, show the particle to have a smooth appearance with a low porosity. Images C and D correspond to the particles which were removed at 135 minutes. At a low magnification, the particle appears smooth with a

lack of porosity, while the image at the higher magnification shows the presence of small deposits on the OC surface. This could be due to carbon deposition and further analysis will be performed to confirm this. The samples that were removed at 160 minute mark are shown in images A and B. The surface of this sample is similar to that of the sample removed at 135 minutes, but at a higher magnification there were no deposits present, implying that the carbon deposits have been potentially consumed. This will be discussed in greater detail in the following subsection. The features present in the fresh sample, as shown in images I and J, is no longer present in the sample that underwent a complete redox reaction, as shown in images G and H. This particle appeared rougher with the presence of satellites on its surface, while the image at the higher magnification shows that the small grains that were initially present have now coalesced to form grains with diameters in the order of microns. The redox process subjects the OC particle to thermal and chemical stresses, leading to grain coalescence and giving rise to wider channels to aid in the diffusion of the gaseous reactants and products into and out of the matrix of the particle. The conclusion from the SEM micrographs is that carbon deposition may have occurred and this will be validated through the use of an Energy Dispersive X-ray Spectroscope.

5.2.2 Energy Dispersive X-ray Spectroscope (EDS)

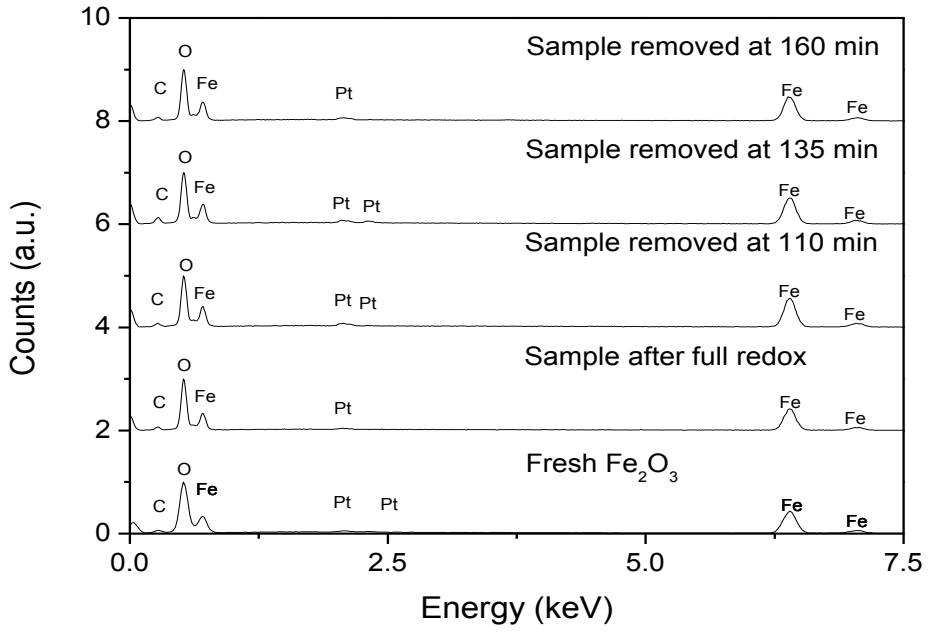

Figure 5-5 Energy dispersive X-ray spectra of the various OC samples

An EDS was used to identify the elements present on the surface of the OC and the spectra can be found in Figure 5-5. Most of the analysed samples, except for the sample that was removed at the 135 minute mark, had a baseline level of carbon and platinum present which was due to the use of carbon tape and platinum coating respectively. Both the fresh sample and the sample after the full redox reaction showed approximately the same peak heights for Fe and O, symbolizing that the OC did return to its initial oxidation state. The samples that were removed at 110, 135 and 160 minutes had higher levels of iron and this is due to it being in a reduced state, containing higher amounts of iron relative to oxygen. As mentioned, the sample removed at 135 minutes had higher levels of carbon present, which could be due to carbon deposition.

5.2.3 X-ray Diffraction (XRD)

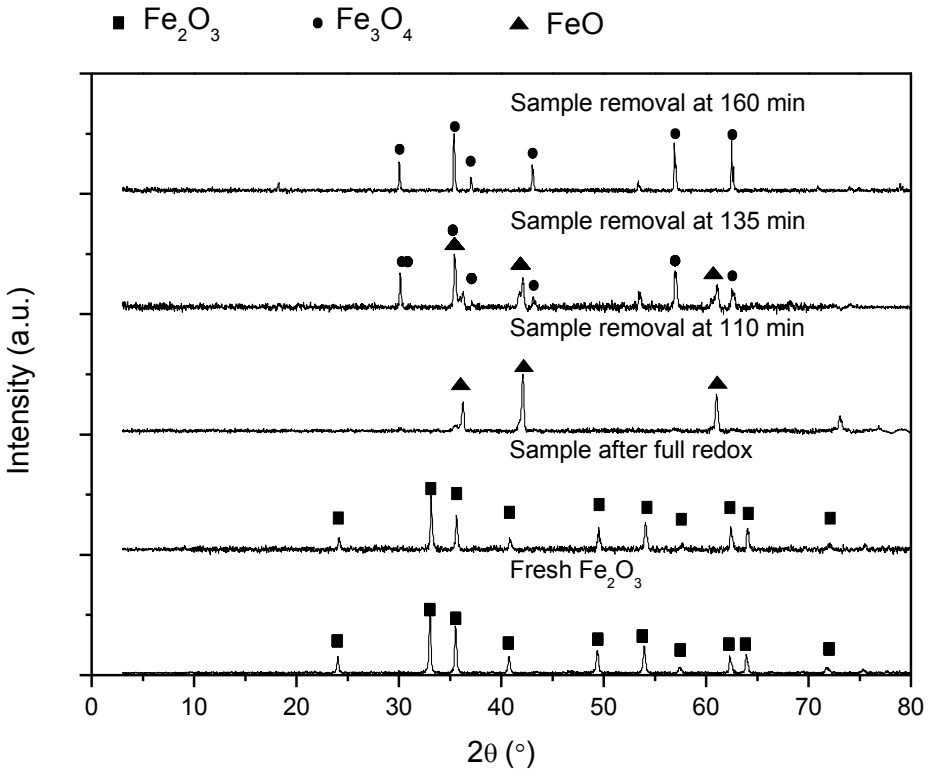

Figure 5-6 Diffractograms of the various OC samples obtained using a laboratory XRD

To better understand this phenomenon, XRD was performed using a bench scale unit to determine the crystalline phases present on the surface; the obtained diffraction patterns are shown in Figure 5-6. Again, both the fresh sample and the sample after the redox reaction were found to contain only Fe_2O_3 on the surface. The samples that were removed during the course of the reaction had varying results. The sample removed at 110 minutes was found to

only contain FeO, while the particles removed at 160 minutes appeared to only have Fe_3O_4. In between, at the 135 minute mark, Fe_3O_4 and FeO were both detected, which represent the intermediate compounds between the first and third points. A study conducted by Zhang *et al.* [3] showed the reduction of CO_2 by wüstite. They found that normal wüstite, $Fe_{0.94}O$, underwent eutectic decomposition at temperatures below 843K to form active wüstite, $Fe_{0.98}O$, as well as magnetite. The authors found that the active wüstite was unstable and was highly reactive towards CO_2, leading to the formation of carbon and magnetite. The mechanism for this was thought to be via the transfer of O^{2-} ions to the surface of wüstite, oxidizing it to magnetite, with simultaneous transfer of electrons from wüstite to CO_2, reducing CO_2 to carbon.

In this investigation, the eutectic decomposition step was not present but CO_2 was found to react with FeO, similar to the active wüstite mentioned above. $Fe_{0.94}O$ was not detected in this investigation as this would have led to its dissociation into $Fe_{0.98}O$ and Fe_3O_4 under the inert N_2 atmosphere during the cooling down period, neither of which was identified in the diffractograms. The FeO then proceeded to consume the CO_2, generating more magnetite and carbon until the 160^{th} minute, at which point it was found to consist purely of magnetite. The difference between this study and that by Zhang *et al.* [3] is that this study was done at a higher temperature and allowed the deposited carbon to be gasified. This explains the presence of carbon as deposits in the micrograph as well as the increased amount of C in the energy dispersive X-ray spectra of the sample that was removed at a 135 minutes; this also explains why carbon was not detected in the other two samples. While some of the CO would have reacted with the OC, other CO molecules would not have had sufficient contact time to do so, which eventually led to the equilibration of the system.

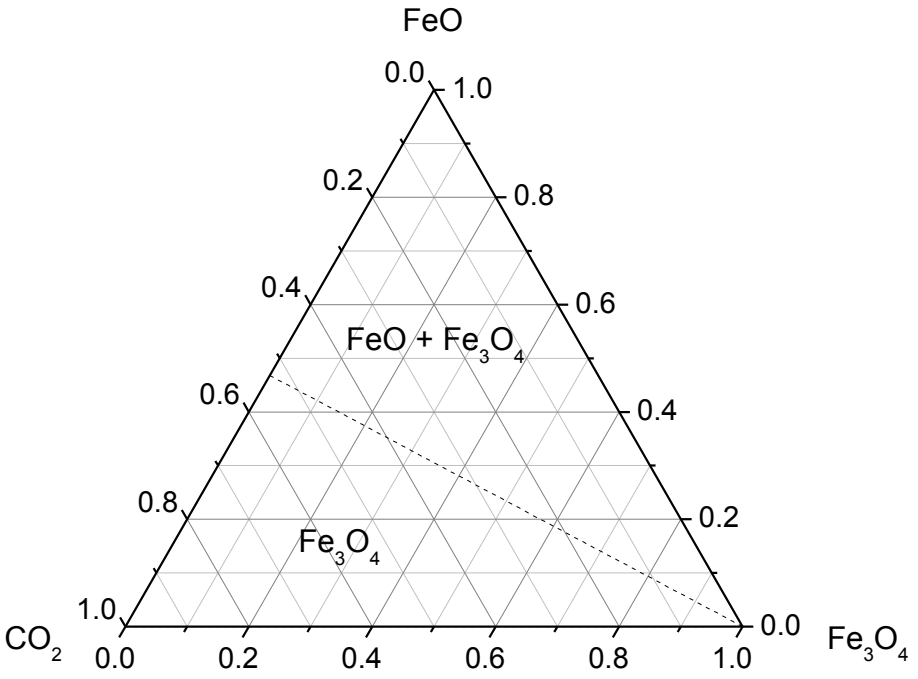

Figure 5-7 FeO-CO_2-Fe_3O_4 phase diagram

To confirm the observed carbon deposition phenomenon, a ternary phase diagram between FeO, CO_2 and Fe_3O_4 was generated using FactSage 6.4 and is shown in Figure 5-7. The model is simple with the diagram split into two parts. When the level of CO_2 is low with high levels of FeO, CO and CO_2 were formed together with FeO and Fe_3O_4. This shows that CO_2 was indeed responsible for oxidizing FeO to Fe_3O_4. When there are high levels of CO_2 and Fe_3O_4, the system equilibrates at Fe_3O_4 with CO and CO_2. This supports the obtained results well because as the reaction progressed, the level of Fe_3O_4 was found to increase as evidenced by diffraction patterns obtained using the XRD. It is worthwhile mentioning that this model did not predict carbon deposition as the model only determines the equilibrium product compositions; this observation is in line with the experimental results as carbon was only present during the transition stages and disappeared when the system equilibrated to consist of only Fe_3O_4. Hence, the carbon would have been converted to CO, which was found to be present in both parts of the ternary phase diagram.

This part of the study has shown the reason behind the observed weight gain phenomenon of the OC-coal system. The weight gain is caused by a mixture of FeO oxidation by CO_2 as well as carbon deposition on the OC. As the reaction progresses, the carbon is gasified and the system equilibrates to only contain Fe_3O_4. Therefore, the CLC system should not be operated to this point as this reaction is less exothermic relative to the oxidation reaction with O_2.

5.3 Synchrotron In-Situ XRD

The methodology employed for this investigation can be found in Section 3.4.4 of Chapter 3. In this part of the study, three different sets of experiments were performed to better understand the reduction of the Fe_2O_3 in the presence of VBC. It should be noted that this setup does not simulate a TGA, but provided intimate contact between the OC and the fuel, mimicking the reaction environment in a TGA. This analysis would help shed light on the initiation temperature at which Fe_2O_3 reduces to its various oxidation states in the presence of VBC. The vertical lines drawn on this figure correspond to the reflections generated using the Crystallographic Information File (CIF), which were obtained for the room temperature samples.

5.3.1 Homogeneously Mixed Fe_2O_3 and Coal at a Ratio of 6:1

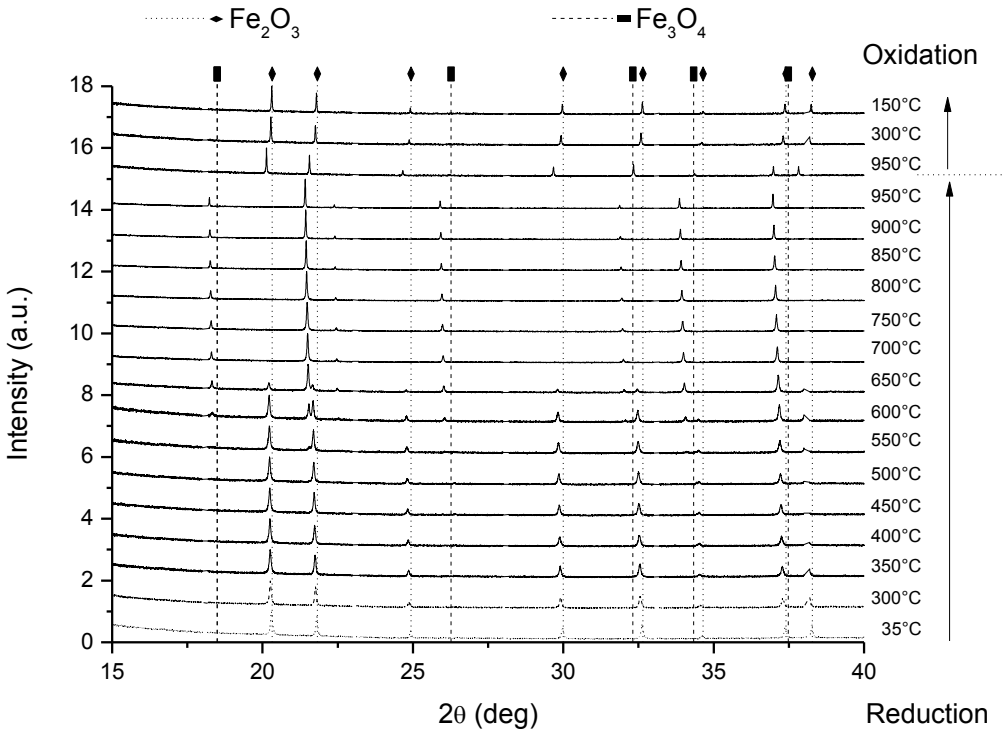

Figure 5-8 Diffraction patterns of homogeneously mixed Fe_2O_3 and coal at a 6:1 ratio

Figure 5-8 shows the powder diffraction patterns which were obtained for the simulated in-situ CLC system. The obtained diffractograms show that from ambient temperature to 500°C, the only phase present was Fe_2O_3. Rietveld refinement is a technique for the characterization of crystalline materials using a least squares system which alters a number of parameters sequentially to refine a theoretical profile until it matches the measured profile. The use of the

Rietveld refinement technique allows for the determination of the cell parameters and microstructure of a material containing crystalline compounds. Based on the Rietveld refinement that was carried out, Fe_3O_4 was found to be present at 550°C alongside Fe_2O_3, which later disappeared at 700°C, which implies that the reduction of Fe_2O_3 to Fe_3O_4 initiated at 550°C; further reduction of the OC to FeO or Fe was not detected. The obtained reduction temperature of Fe_2O_3 by CO falls within the range reported in literature by Hayes and Grieveson [4]. This is also similar to the results obtained in the TGA, whereby the reduction of the OC was found to start occurring around 550°C. Although the sample from the TGA was found to reduce to FeO at around 800°C, the sample in the quartz capillary did not reduce beyond Fe_3O_4. In a TGA, the gases flow over the crucible at a relatively slow rate, which translates to a long residence time; the residence time in the quartz capillary that was used here is short, which explains the difference in the results. Therefore, in the TGA, the CO formed from gasification of the fuel has a longer time around the OC to reduce it relative to when using the quartz capillary. One feature that is noticeable with increasing temperature is that the peak positions tended to shift towards lower angles, which is characteristic of lattice expansion and will be discussed in the following paragraphs. This shifting of the peak positions appears almost linear with respect to temperature. Once the peaks were stable, the gas was switched over to a mixture of air and N_2. After 20 minutes, it was found that the OC had been completely reoxidized to Fe_2O_3. The sample was then cooled down to study any potential changes in the sample on cooling; as such, data were collected at 300°C and 150°C. The data collection was terminated here as no further reactions were expected to occur. Comparing the sample at ambient temperature and that at 150°C, the obtained peaks were found to align perfectly with the data obtained from the CIF file, showing that the effect of lattice expansion and contraction is a function of temperature.

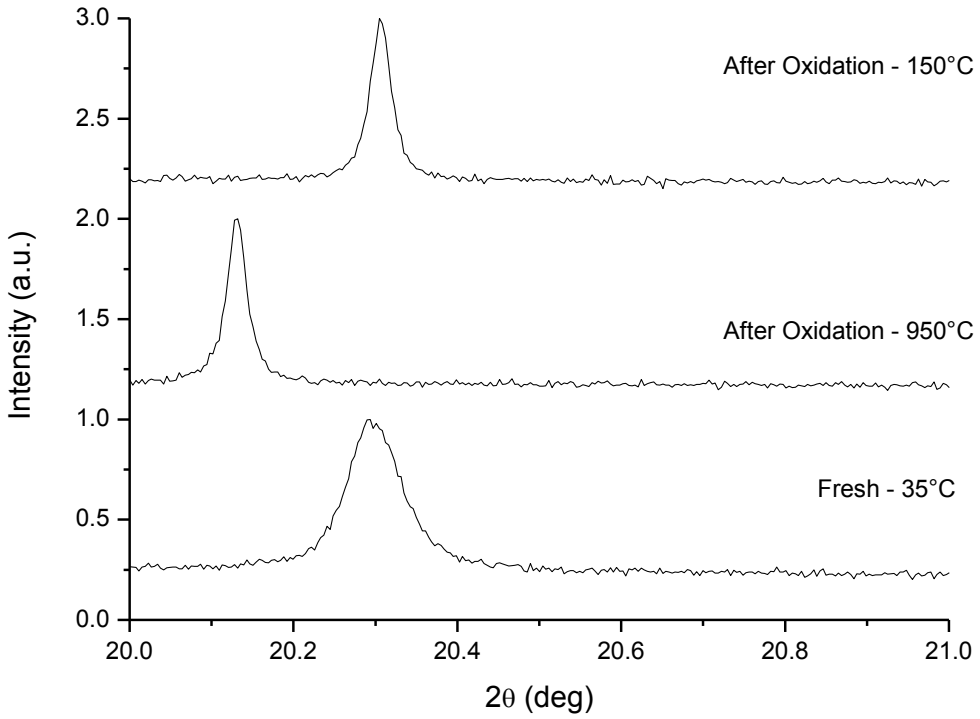

Figure 5-9 Magnified reflection between 2θ of 20-21° (104 hkl plane) for samples at 35°C (before reduction), 950°C (after oxidation) and 150°C (after oxidation)

A magnification of three of the diffraction patterns between 2θ values of 20-21° can be found in Figure 5-9. The diffractograms at 35°C, 950°C and 150°C represent the fresh particles, fully reoxidized particles and reoxidized particles during the cooling down period respectively. The reason these three diffraction patterns were chosen was because they all represent the sample containing only Fe_2O_3 without any Fe_3O_4. It can be observed that there is a peak shift of 0.18° to the left from a 2θ value of 20.31° for the particles at 35°C to 20.13° for the particles at 950°C. Comparing the former with the diffractogram at 150°C, it can be seen that the peaks align well at 20.31°. The reason behind this is the thermal expansion of the OC lattice, which is characterized by a shifting of the peaks to the left. Another obvious difference between diffraction patterns of the fresh particle and the particles after oxidation is that the peaks are better defined and narrower for the latter. Broader peaks either signify a sample has poor crystallinity [5] or that it has very small crystals, making it nanocrystalline. As the temperature was increased and even after it was cooled down at the end of the redox reaction, the peaks appear narrower indicating that the samples have increased in crystallinity, most likely from an increase in crystallite size. This is supported by the SEM images as

shown in Figure 5-4 (J-H) wherein the small crystallite sizes present in the fresh particle were absent in the reoxidized sample.

5.3.2 Segregated Fe_2O_3 and Coal at a Ratio of 1:2.6

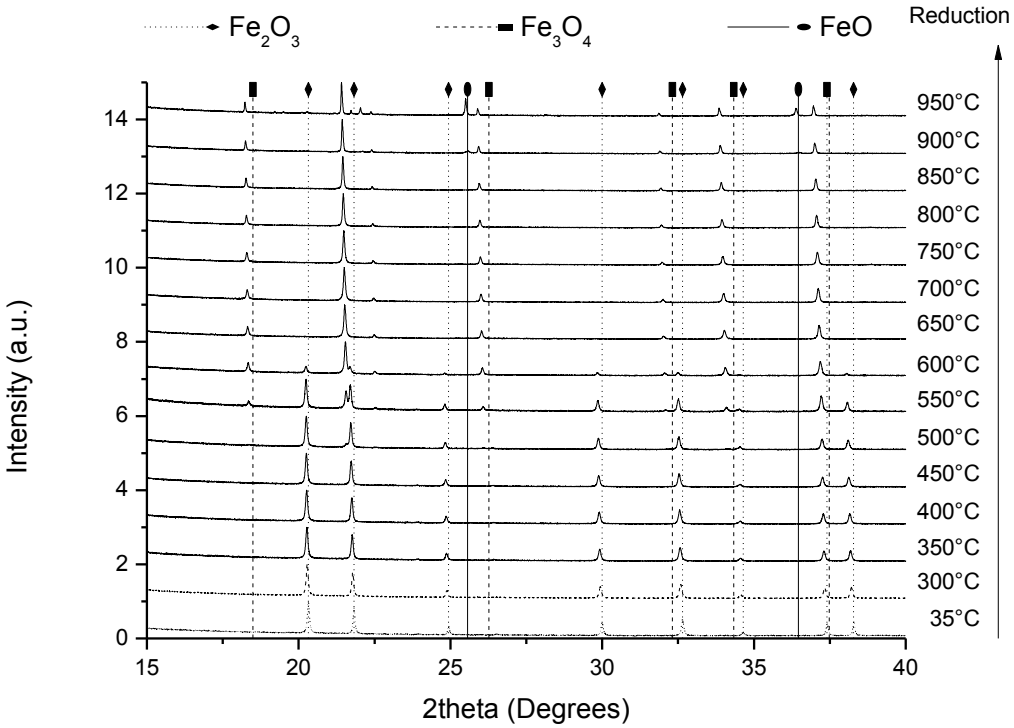

Figure 5-10 Diffraction patterns of segregated Fe_2O_3 and coal at a ratio of 1:2.6

Since a greater extent of reduction was not achievable with the previous experimental condition, different conditions were investigated to enable this to occur. Figure 5-10 shows the collected diffraction patterns for the segregated Fe_2O_3 and coal run. The rationale behind this is that while the quartz capillary had a sizeable volume, the effective isothermal region along the length of the capillary was only around 5 mm while the length of the X-ray beam was even smaller at 1 mm. Hence, the Fe_2O_3 was loaded first and filled to cover the width of the X-ray beam. Then 2.6 parts of coal were added for every part of Fe_2O_3. This led the coal to be within the isothermal zone provided by the hot air blower, enabling its gasification but just outside of the detector beam region. Similar results to that in Figure 5-8 were observed in this experiment. The differences are two-fold with the first being that at 650°C, Fe_2O_3 had been completely reduced to Fe_3O_4 and secondly, the OC was found to further reduce to FeO at 950°C. Both of these differences can be attributed to the fact that there were significantly more reducing gases present in this experiment. Wimmers *et al.* [6] found that the reduction

of Fe_3O_4 occurred at a higher temperature compared to the reduction of Fe_2O_3 through the use of H_2 gas in a Temperature Programmed Reduction (TPR) experiment. This supports the current findings whereby the reduction of Fe_3O_4 occurred at a higher temperature and after a longer time period relative to the reduction of Fe_2O_3. The duration it took for the contents in the quartz capillary to go from 650°C to 950°C was 30 minutes and within this period there were no changes in the phases present on the surface until FeO was detected. Since the penetration depth of X-rays is low, this would imply that the conversion of the OC followed that of the Shrinking Core Model (SCM) with the surface reacting first followed by subsequent reactions in the core of the OC particle. Once the particle had been reduced to Fe_3O_4, the metal oxide on surface started reducing to FeO with Fe_3O_4 still being detectable. The oxidation of the sample was not studied here as it was assumed that it would follow a similar trend to that presented in Figure 5-8.

5.3.3 Segregated Fe_2O_3 and Char at a Ratio of 1:2.6

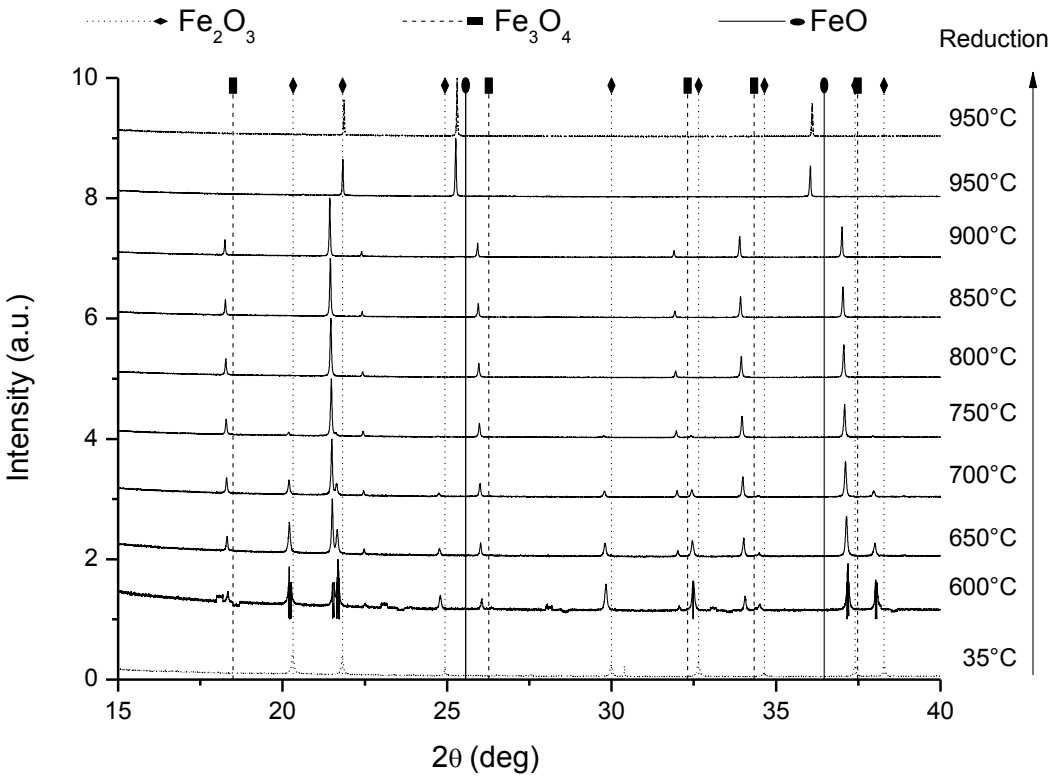

Figure 5-11 Diffraction patterns of segregated Fe_2O_3 and char at a ratio of 1:2.6

VBC contains high levels of volatiles (~50%). Since most of the volatiles would be driven off as the temperature was increased, as evidenced in Figure 5-1, a large fraction of it would not

be able to react with the OC. The reason for this is that the temperature is not high enough for the reaction between Fe_2O_3 and the volatile matter to occur. This is not expected to be the case in a commercial unit as the coal would be introduced into an isothermally operated reactor. Hence, to further investigate the reduction behaviour of the OC, a third experiment was conducted. Figure 5-11 shows the diffraction patterns obtained from the investigation using the segregated Fe_2O_3 and char, at a ratio of 1:2.6. It was found that the reduction of Fe_2O_3 initiated at 600°C, unlike in the previous two experiments. The amount of Fe_3O_4 was found to slowly increase until a temperature of 750°C, after which only Fe_3O_4 was detected. At 950°C, only FeO was detected without any trace of Fe_3O_4, unlike the results obtained with the previous experimental conditions. Comparing Figure 5-8, Figure 5-10 and Figure 5-11, the differences in these results lie in the extent of reduction of the OC coupled with the temperature at which the reductions occurred. The lowest OC reduction temperature, 550°C, occurred when coal was used as the fuel while the reduction of Fe_2O_3 initiated at a temperature of 600°C in the presence of char. The volatiles in VBC begin to release from around 200°C; these can react with the OC, once a sufficient temperature is reached such as 550°C here, leading to its reduction as observed in the cases where coal was used as the fuel. When char was used, instead of coal, the reduction of the OC was observed to initiate at a higher temperature. This is because the gasification of char is a slower process with a higher activation energy, relative to the gasification of coal.

5.3.4 Oxygen Carrier Lattice Parameter

The lattice parameters were obtained through Rietveld refinement of the synchrotron data. The definition of this refinement technique is mentioned in Section 3.4.4.1 of Chapter 3.

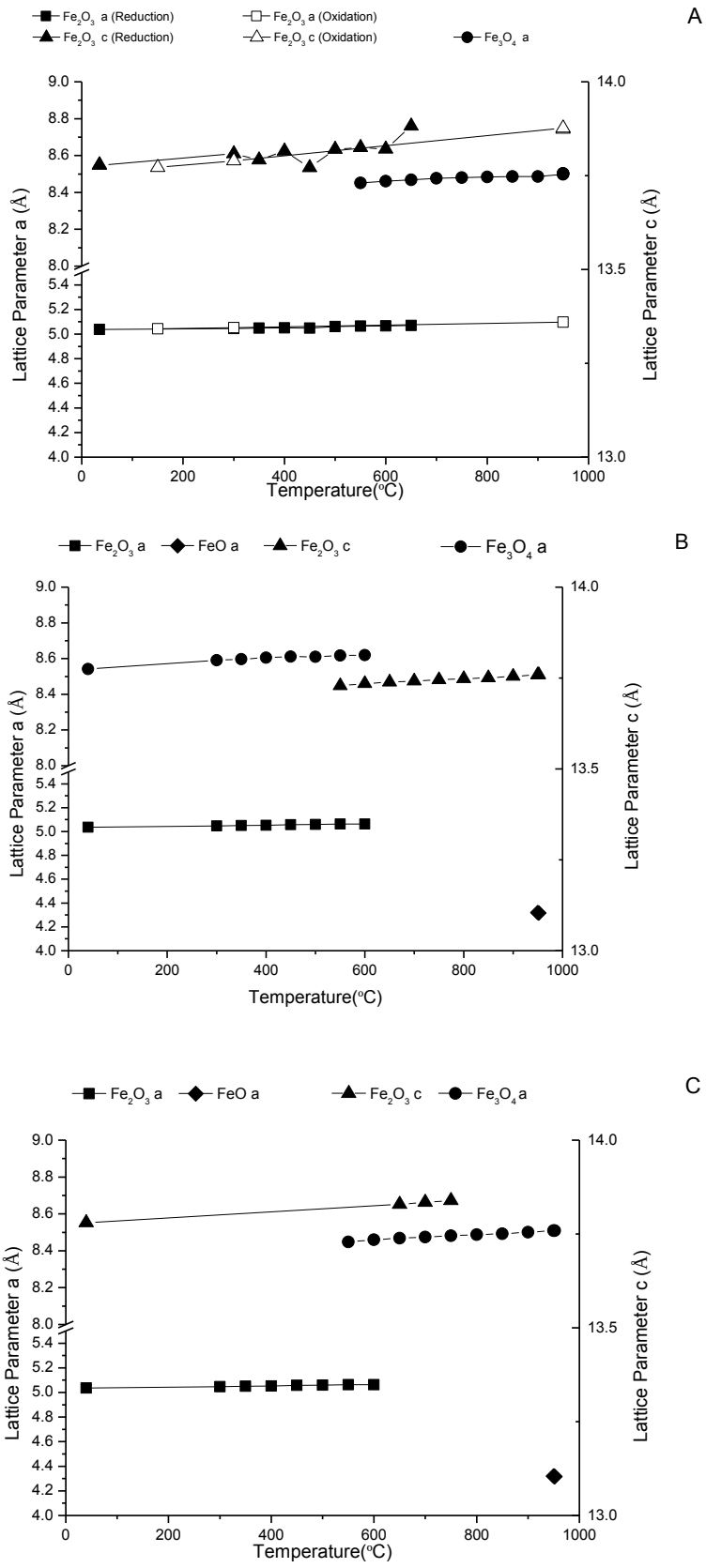

Figure 5-12 Lattice parameters of the OC in the experiment with homogeneously mixed Fe_2O_3 and coal (A), segregated Fe_2O_3 and coal (B) as well as segregated Fe_2O_3 and char (C)

Based on the Rietveld refinements that were performed, the lattice parameters and crystallite sizes of the OCs were obtained. These were plotted against temperature for the three cases that were investigated. Figure 5-12 (A-C) shows the plot of the lattice parameters as a function of temperature. The structure of a phase is defined by the lattice parameter, which describes the dimensions of a unit cell. Typically, a unit cell is represented by three unit cell lengths (*a*, *b and c*) and the angles between these (α, β and γ). For example, when the three unit cell lengths are the same and all the angles are 90°, the unit cell is described as being cubic with the structure having a corresponding symmetry. For the materials found to be present in this study, Fe_2O_3 has a hexagonal structure while both FeO and Fe_3O_4 have a cubic structure. This means that for FeO and Fe_3O_4, the unit cell lengths are all equal i.e., a=b=c. On the other hand, for Fe_2O_3, the unit cell lengths a and b are equal while c is different i.e., a=b≠c. Figure 5-12 (A) shows the lattice parameters obtained for the first experiment with the homogeneously mixed Fe_2O_3 and coal. It can be seen that the OC undergoes thermal expansion based on the increase in the value of the lattice parameters with increasing temperature. The lattice parameter was also found to vary with the oxidation state of the OC. The gradient of the lattice parameters are very similar, which mean that the size of the unit cell increases proportionally across all three axes. As mentioned, Fe_2O_3 is fully consumed by 700°C and at 950°C it is reoxidized back to its initial oxidation state. The open symbols represent the sample as it was being cooled down and it can be seen that these values fit well with those obtained during the reduction period.

The significance of this result is that the expansion and contraction of the lattice is a function of temperature and the extent of reduction of the OC. Figure 5-12 (B-C) show a similar trend with comparable values during the reduction reactions. The volume of the molecular species was obtained using GSASII; as expected, the lattice volume of Fe_3O_4 was the greatest, followed by Fe_2O_3 and lastly FeO.

5.3.5 Oxygen Carrier Crystallite Size

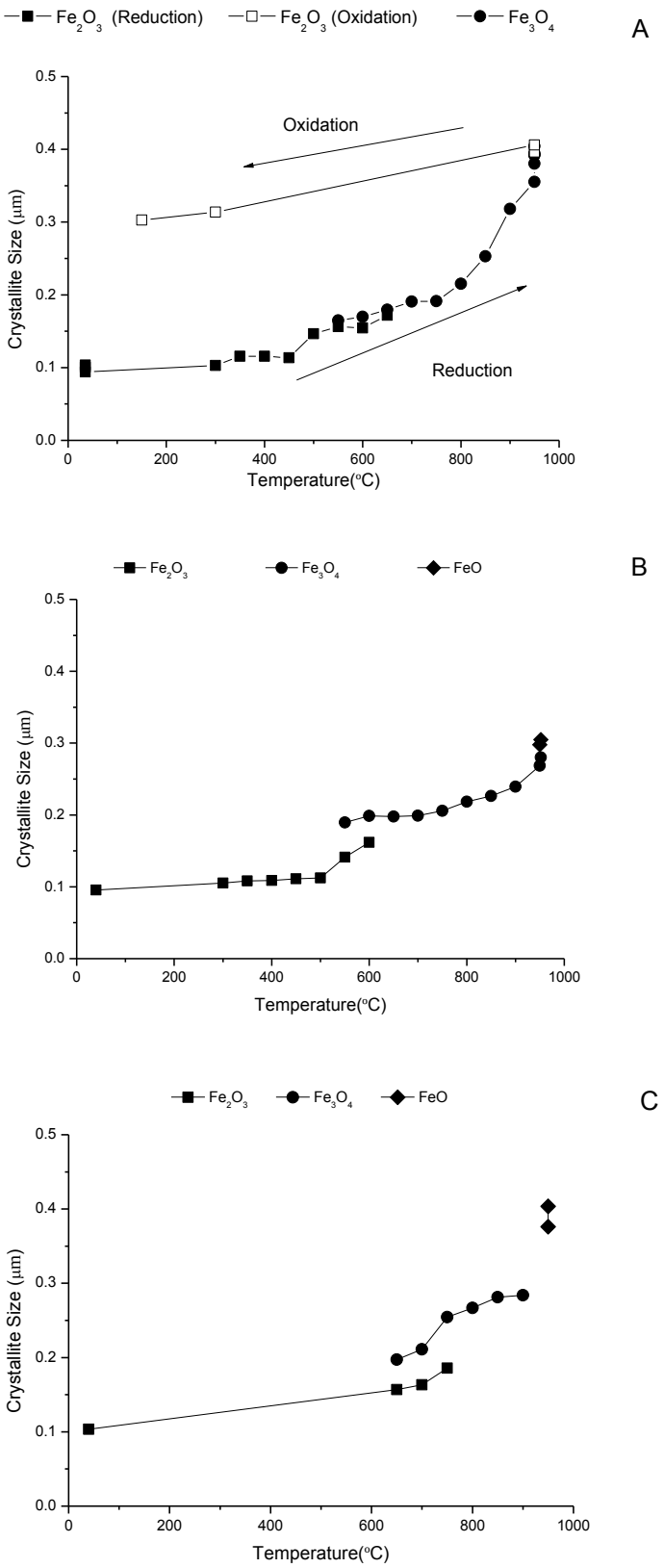

Figure 5-13 Crystallite sizes of the OCs in the experiment with homogeneously mixed Fe_2O_3 and coal (A), segregated Fe_2O_3 and coal (B) as well as segregated Fe_2O_3 and char (C)

Similarly, the crystallite sizes of the OCs were plotted as a function of temperature, as shown in Figure 5-13 (A-C). Figure 5-13 (A) shows the results obtained for the first experiment that was performed. It can be seen that the gradient of the crystallite sizes for a given phase is almost linear and that there is an increase in this gradient as the sample was reduced to lower oxidation states. This is confirmed by the results shown in Figure 5-9, wherein the peaks were found to be narrower, signifying an increase in the crystallite size. Furthermore, as the sample was cooled down, the crystallite size did not return to its initial value, unlike the lattice parameter. This could possibly be due to coalescence, leading to the formation of larger crystallites as evidenced by the SEM images in Figure 5-4. While OCs are typically calcined to increase their mechanical strength, the downside is that the reactivity of the OC is reduced due to a decrease in the surface area caused by the increase in the crystallite size. As the temperature of the reaction was increased, the OC underwent calcination. Similar to the lattice parameters, the crystallite sizes were found to also be a function of the OC's oxidation state and reaction temperature. The crystallite sizes for the second and third conditions that were investigated can be found in Figure 5-13 (B-C). While the trend appears similar, one difference is apparent. There is now a gap between the crystallite sizes going from one oxidation state to another and this is more pronounced in Figure 5-13 (C). The only difference between the first and the latter two experiments was the amount of reducible material in increasing order. It can be seen that the greater the reducing environment, the larger the gap and this translates to the formation of larger crystallite sizes. This is especially true for the third condition with the segregated Fe_2O_3 and char, which led the crystallite size to stabilize at 0.4 µm compared to approximately 0.35 µm for the previous two conditions.

From a practical view point, it would appear that a highly reducing environment is not favourable for the OC in more ways than one. Firstly, this leads to an increase in the crystallite size of the OC, which is unfavourable as this causes a reduction in the surface area. Secondly, reducing Fe_2O_3 beyond Fe_3O_4 leads to a decrease in the thermodynamic equilibrium concentration of CO_2; this would then cause a reduction in the CO_2 capture efficiency, which is unfavourable as it is one of the most important parameters in CLC.

5.4 Thermodynamic Modelling

Thermodynamic equilibrium modelling was done using HSC Chemistry to obtain an Ellingham diagram while FactSage 6.4 was used to generate a phase diagram. An Ellingham

diagram shows the temperature dependence of a compound's stability and can be used to evaluate the ease of reduction of a metal oxide.

5.4.1 Ellingham Diagram

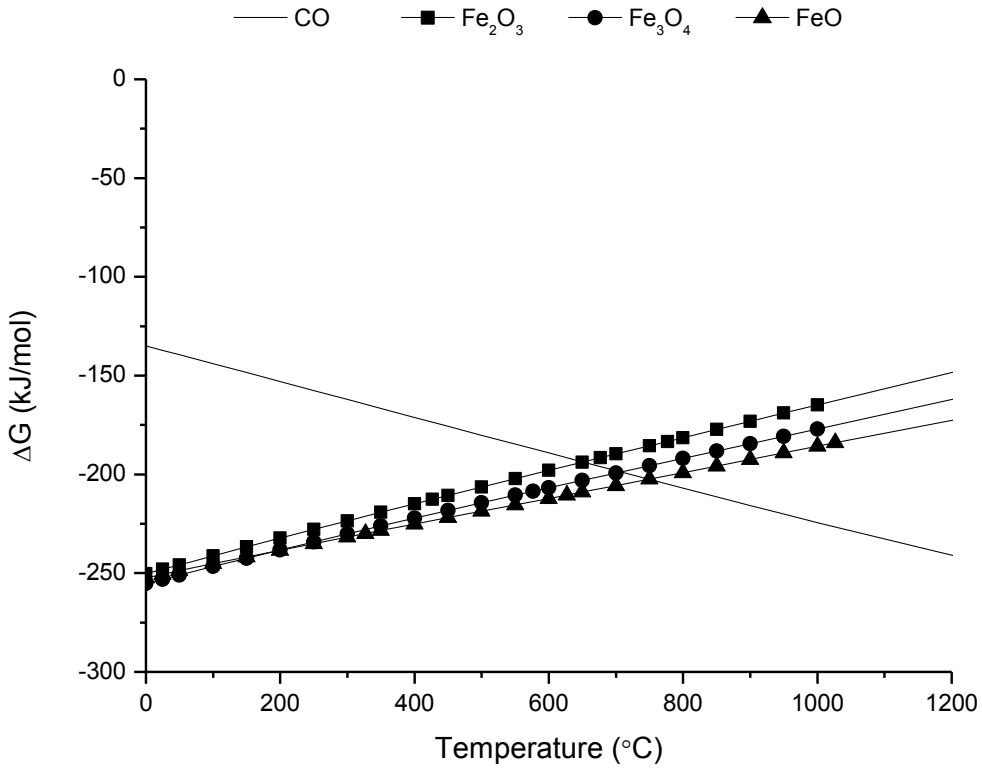

Figure 5-14 Ellingham diagram of the reduction of Fe_2O_3, Fe_3O_4 and FeO by CO

An Ellingham diagram, as shown in Figure 5-14, was constructed for the reduction of Fe_2O_3, Fe_3O_4 and FeO with CO. Based on the model, the initiation temperatures for the reduction of the various oxidation states of iron oxide by CO can be obtained. The initiation temperatures for the reduction of Fe_2O_3, Fe_3O_4 and FeO in the presence of CO were found to be 650°C, 710°C and 750°C respectively. The reduction of Fe_2O_3 at 650°C from the model does not match well with the results from Figure 5-8, Figure 5-10 and Figure 5-11.The reason for this is that the software only considers complete reduction of the OC and not the temperature at which a reaction is first considered thermodynamically feasible. Therefore, while there would have been Fe_3O_4 present prior to 650°C, Fe_2O_3 would also have been present. Hence, the software did not consider it to be feasible.

5.4.2 Phase Diagram

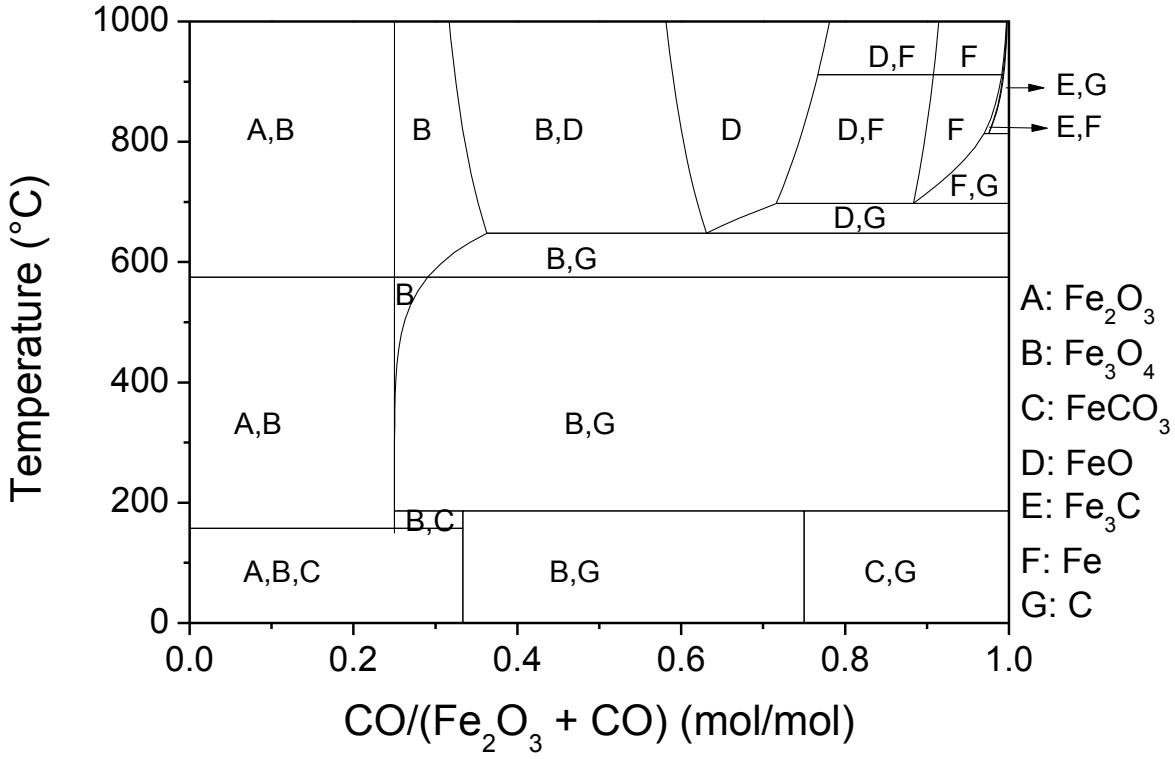

Figure 5-15 Fe_2O_3-CO phase diagram

To further investigate this, a Fe_2O_3-CO phase diagram was constructed using FactSage 6.4 and can be found in Figure 5-15. The model shows that Fe_2O_3 can be reduced to Fe_3O_4 at any temperature depending on the concentration of CO. The model also shows that FeO can only form once a temperature of 650°C is reached. While the model predicts the equilibrium composition for a given amount of reactants, the experiment conducted in this study cannot reach thermodynamic equilibrium as it was not a batch process. Another observation is that the reduction of Fe_3O_4 to FeO occurred only at 950°C, while it was thermodynamically possible to initiate at 650°C. This supports the initial theory that the reactions proceeded according to the SCM.

5.5 Comparison of the TGA and In-Situ XRD Results

A comparison between the experiments performed in the TGA and the first condition investigated in the synchrotron study will be made here. Both the experiments had Fe_2O_3 mixed with coal in a 6:1 ratio, ensuring that the amount of the reducing agent to the OC was constant. The gases used in both the experiments were the same as well. In essence,

everything was the same between the two experiments except for the gas flow rate and the operation mode with the TGA having the gases flow over the OC-coal mixture, while a packed bed reactor was simulated in the quartz capillary that was used in the synchrotron-based experiments. This translates to a difference in the residence time of the reducing gases in the presence of the OC. The gases in the TGA would have had a much larger residence time as the CO_2 flowed over the mixture with some of the gases diffusing through the bed to react with the coal. The generated gases, since not in direct contact with the flow gas, would have to diffuse back to the surface of the mixture, hence resulting in an increased residence time. With such a long residence time, the OC was able to better convert the gasification products. The downside is that since the CO_2 also had a very high residence time around the reduced OC, FeO in this case, it reacted with FeO to generate carbon; this then deposited on the CO and was then gasified, as shown in Figure 5-7. From a practical operation point of view, carbon deposition would reduce the CO_2 capture efficiency of the CLC system especially when the OC with the deposited carbon enters the AR to be oxidized. As such, this should be avoided at all cost. Even when the amount of reducible material was increased by at least a factor of 16 between the first and the latter two synchrotron experiments, the generated FeO did not react with the CO_2 and this is due to the much shorter residence time that the gases spent around FeO. This shows that the carbon deposition reaction is slow at temperatures up to 950°C and requires significant contact time before it can occur. Additionally, Fe_2O_3 should not be reduced beyond Fe_3O_4 from a thermodynamic point of view as this would reduce the equilibrium concentration of CO_2; this would aid in obtaining a high CO_2 yield.

5.6 Conclusions

This chapter investigated the weight gain phenomenon which occurred during the reduction of an Fe-based OC. Additionally, synchrotron-based in-situ XRD was performed to study the reduction extent of the OC as well as the changes in the lattice parameters and crystallite sizes as a function of both temperature and the extent of reduction. The following conclusions were drawn from this study:

1. Carbon deposition is possible when using an OC containing Fe_2O_3 if the CO_2 has a long residence time around the OC particle having an oxidation state below Fe_3O_4.

2. Carbon deposition should be prevented as this would lead to a reduction in the CO_2 capture efficiency in the CLC process.

3. In terms of the fuel, coal is preferable over char because it is more reactive and the volatiles which are released can act as reducing agents for the OC. This was confirmed in the in-situ synchrotron study whereby the reduction of Fe_2O_3 was initiated 50°C earlier in the presence of coal compared to when it was reacted with char.

4. Rietveld refinement of the in-situ synchrotron XRD data showed how the lattice parameters and crystallite sizes changed with the reaction temperature and the oxidation states of the OC. This is another reason as to why Fe_2O_3 should not be reduced beyond Fe_3O_4, as the larger crystallite sizes translate to lower surface areas.

5. The results indicate that Fe_2O_3 is a suitable OC for CLC and would perform best if it is not reduced beyond Fe_3O_4 as this would yield the highest equilibrium conversion for CO.

The obtained results suggest that the reduction of Fe_2O_3 beyond Fe_3O_4 is not favourable under a CO_2 gasification environment over long residence times as it may lead to carbon deposition on the OC.

5.7 References

1. Siriwardane, R., H.J. Tian, D. Miller, G. Richards, T. Simonyi, and J. Poston, *Evaluation of reaction mechanism of coal-metal oxide interactions in chemical-looping combustion.* Combustion and Flame, 2010. **157**(11): p. 2198-2208.
2. Saha, C. and S. Bhattacharya, *Chemical looping combustion of low-ash and high-ash low rank coals using different metal oxides - A thermogravimetric analyser study.* Fuel, 2012. **97**: p. 137-150.
3. Zhang, C.-L., S. Li, T.-H. Wu, and S.-Y. Peng, *Reduction of carbon dioxide into carbon by the active wustite and the mechanism of the reaction.* Materials chemistry and physics, 1999. **58**(2): p. 139-145.
4. Hayes, P.C. and P. Grieveson, *The effects of nucleation and growth on the reduction of Fe2O3 to Fe3O4.* Metallurgical Transactions B, 1981. **12**(2): p. 319-326.
5. Pérez-Alonso, F., M. López Granados, M. Ojeda, P. Terreros, S. Rojas, T. Herranz, J. Fierro, M. Gracia, and J. Gancedo, *Chemical structures of coprecipitated Fe-Ce mixed oxides.* Chemistry of Materials, 2005. **17**(9): p. 2329-2339.
6. Wimmers, O., P. Arnoldy, and J. Moulijn, *Determination of the reduction mechanism by temperature-programmed reduction: application to small iron oxide (Fe2O3) particles.* The Journal of Physical Chemistry, 1986. **90**(7): p. 1331-1337.

Chapter 6 Kinetic Modelling and Characterization of Fe_2O_3

There have been numerous publications on modelling the reduction of different OCs in the presence of gaseous fuels such as syngas [1-3] and natural gas [4]. Since, there has been a growing interest in the field of iG-CLC in recent times, there is a need to model the reduction of an OC in the presence of a solid fuel. To date, there have not been any publications relating to modelling the reduction of an OC in the presence of a solid fuel. The benefit of a model capable of predicting the reduction of an OC is that it can be incorporated in future process and computational fluid dynamics models to assist in reactor sizing. The reduction kinetics of Fe_2O_3 in the presence of a char derived from VBC and using CO_2 as the gasification agent will be modelled using two different models. The two models used were the Shrinking Core Model (SCM) and the Modified Volume Reaction Model (MVRM). The OCs will also be characterized to understand how the different operating conditions affect its structure and morphology. A thermodynamic model was also constructed to theoretically validate a key assumption of the kinetic models.

This chapter uses two models to simulate the reduction kinetics of Fe_2O_3 in the presence of a char derived from VBC while also comparing the model's predictions to experimental results.

6.1 Experimental Conditions

The TGA was used in this study together with the commercially obtained Fe_2O_3 that was calcined alongside char produced from the devolatilization of Yallourn coal. Char was used in place of coal to simplify the processing of the weight loss data from the TGA. The OC to char ratio used was 120:1 to ensure that Fe_2O_3 was not reduced beyond Fe_3O_4. The mass of char used was 2 g in each study together with the corresponding amount of OC. An inert environment was maintained in the TGA while the temperature was increased to ensure that no reaction occurred until the temperature set point was reached. Once this was attained, CO_2 was used as the gasification agent with balance N_2. The total gas flow rate was 100 mL/min in all the experiments. To obtain sufficient data for the model, a number of experiments were done by varying either the CO_2 concentration or temperature while keeping the other constant. Firstly, the CO_2 concentration was kept constant at 10 v/v% and four temperatures were investigated: 750°C, 800°C, 850°C and 900°C. Then, the temperature was maintained at

850°C while the following CO_2 volume concentrations were used: 5%, 10%, 20% and 30%. The data from these seven experiments were used to generate the model and these are termed model data experiments. The model was validated by comparing the results from the model with experimental data obtained from the experiments that were performed with the following conditions: 850°C and 15 v/v% CO_2; 850°C and 40 v/v% CO_2; 825°C and 25 v/v% CO_2; 800°C and 20 v/v% CO_2.

The samples were also characterized using SEM, EDS, XRD and ASAP to study the changes the OC experienced as a function of CO_2 concentration and temperature.

Two different models, SCM and MVRM, were used to simulate the conversion of the OC as a function of time.

6.2 TGA Experiments

Some baseline experiments were performed to study the weight loss characteristics of the char as well as the OC-char mixture. Additionally, experiments were conducted where the temperatures and CO_2 concentrations were varied to investigate the effect of these two parameters on the reduction kinetics of the OC.

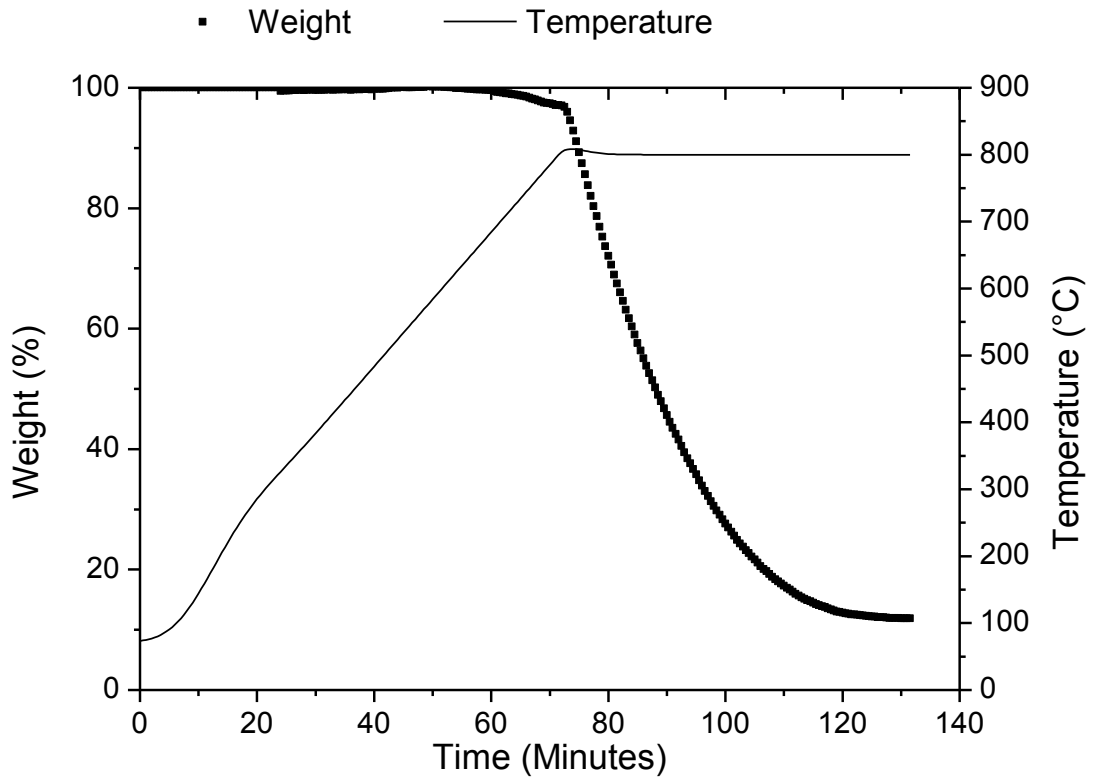

Figure 6-1 Weight loss profile of char at 800°C with 10 v/v% CO_2 as the gasification agent

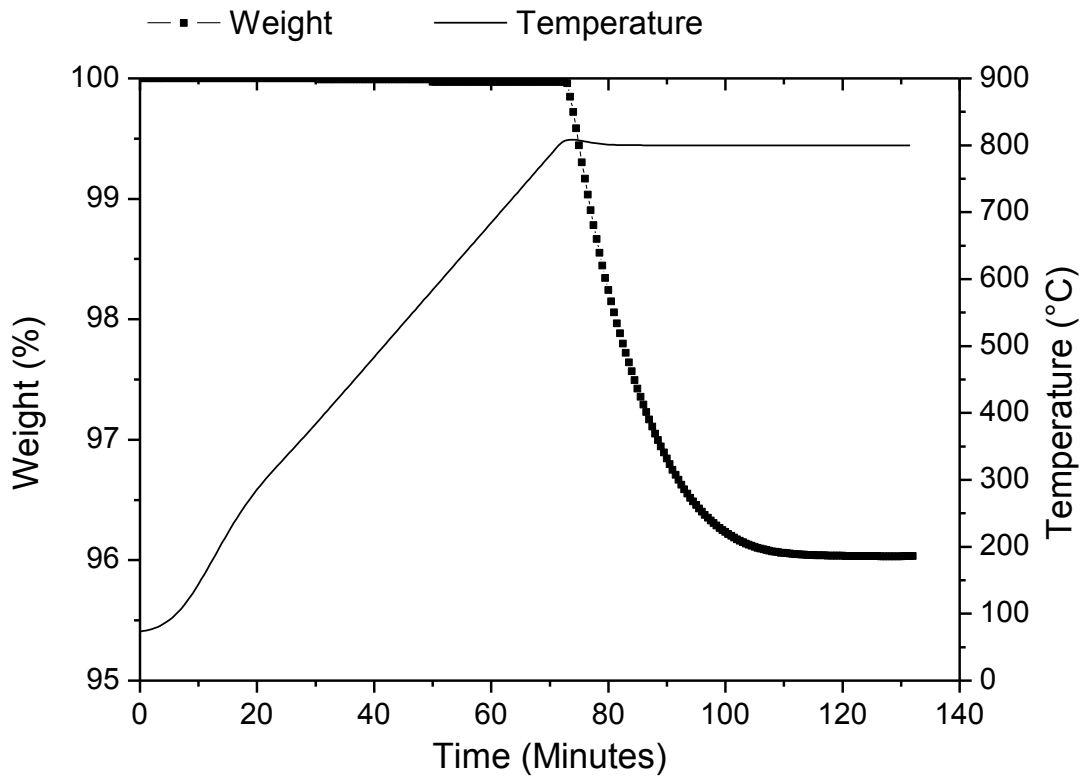

Figure 6-2 Weight loss profile of the Fe_2O_3 and char mixture at 800°C with 10 v/v% CO_2 as the gasification agent

Figure 6-1 shows the weight loss profile of the char sample used in this study while Figure 6-2 depicts the weight loss profile of the Fe_2O_3 and char mixture; both of these experiments were performed at 800°C with 10% CO_2 by volume and balance N_2. It can be seen that the weight loss profile is almost similar for both cases with the exception that the mixture containing Fe_2O_3 and char was found to complete at an earlier time. This is due to the OC removing the generated CO from char gasification, which is a known gasification inhibitor, as mentioned in Chapter 5 [5]. The sample containing char required 55 minutes to be completely reduced under these conditions, while the crucible containing both Fe_2O_3 and char only required 35 minutes to be completely reduced. This represents a 36% reduction in the time required to completely reduce the fuel, being significantly higher than the 10% reported in Chapter 4. The reason for this is that the time scale is much shorter here as the reported value in the Chapter 4 took into account the time from the start of the experiment to the end of the reduction period. In this investigation, the time taken to completely reduce the fuel started as soon as the reaction temperature was reached and not from room temperature. From a practical point of view, the value obtained here is a better estimate as the fuel would be fed

into an isothermally operated reactor at a temperature of around 800-1000°C and not at room temperature. Although the volatiles are not factored in here, the devolatilization reaction is very fast and the time taken is insignificant when compared to the time required for the gasification of char.

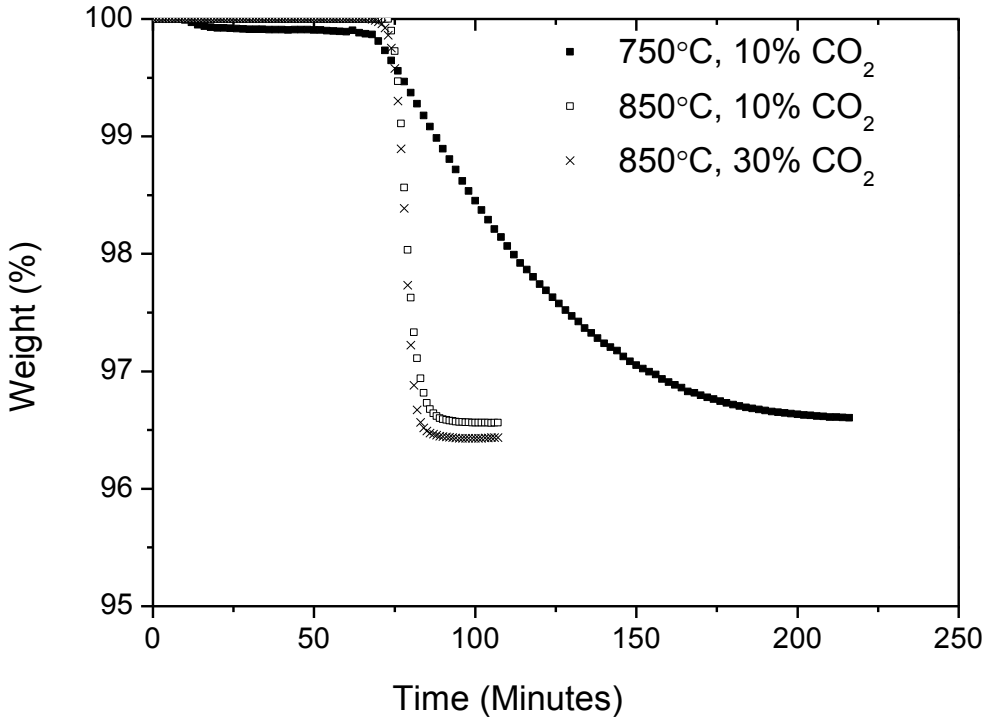

Figure 6-3 Weight loss profile of Fe_2O_3/char mixture at different temperatures and CO_2 concentrations

Figure 6-3 shows the weight loss profiles for three different investigated conditions: 750°C, 10 v/v% CO_2; 850°C, 10 v/v% CO_2 and 850°C, 30 v/v% CO_2. The final weight of the mixture at the end of the reaction is around 96.5% for all the three cases. The most obvious difference is observed when the temperature was decreased, which resulted in the time taken to complete the reaction to increase from a few minutes at 850°C to more than two hours at 750°C. This shows that a small change in temperature can have a significant effect on the kinetics of a reaction. When the concentration of CO_2 was increased while keeping the temperature constant, a slight decrease in the final weight of the sample was observed, which implies that the OC was reduced further and this could be due to the higher concentration of CO present in the vicinity of the OC. A higher concentration of CO in the CO_2 and N_2 mix would result in reduced diffusional resistance for CO from the bulk gas to the OC.

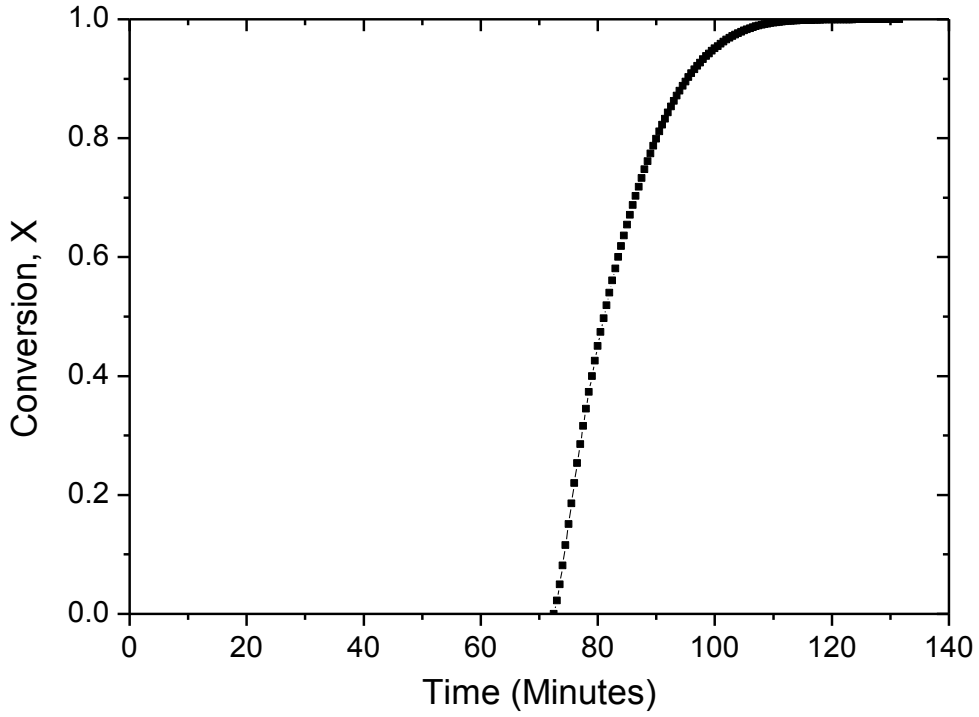

Figure 6-4 Conversion of the Fe_2O_3 and char mixture at 800°C with 10 v/v% CO_2 as the gasification agent

The weight loss data from Figure 6-2 was processed to yield the conversion of the OC and char mixture as a function of time and this is shown in Figure 6-4. It can be observed that the gradient of the curve from the start of the reduction is almost constant for the majority of the reaction and this tapers off from a conversion of 0.8 onwards. The decline in the rate towards the end is due to the reduction in the amount of available char, as this would reduce the CO generation rate and subsequent reaction rate with the OC.

Henceforth, the graphs that will be discussed with start from t=0 to allow for easier comparison between the different experimental conditions.

6.3 Shrinking Core Model (SCM) Results

This section will detail the use of the SCM model to predict the conversion of the OC and char mixture. Additionally, from the model, certain values such as the activation energy and pre-exponential factor will be calculated for comparison with values from literature.

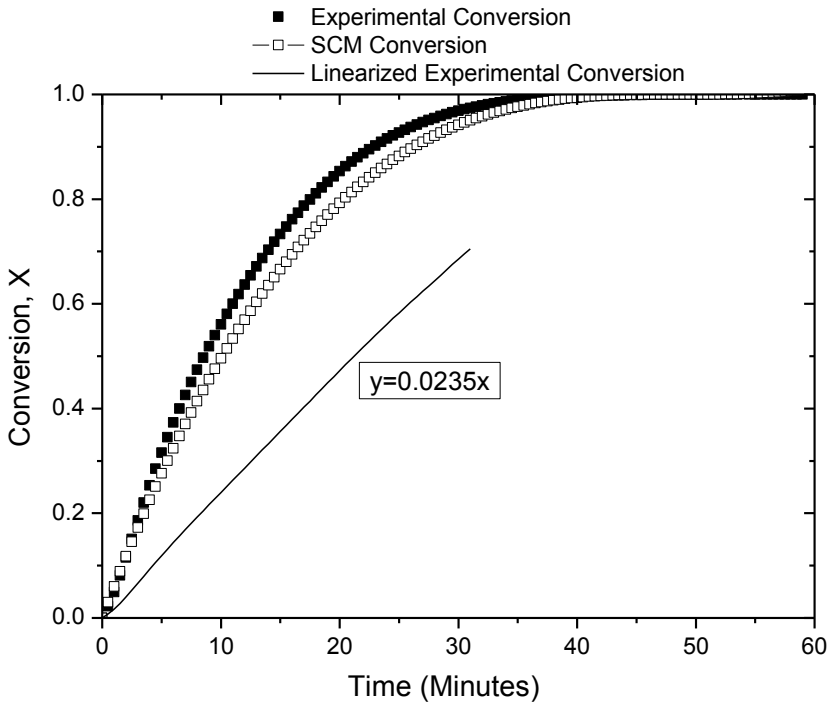

Figure 6-5 Comparison of experimental and SCM conversions for the Fe_2O_3 and char mixture at 800°C with 10 v/v% CO_2 as the gasification agent

Figure 6-5 shows the experimental and SCM conversions as well as the linearized experimental conversion as a function of time for the experimental condition at 800°C with a CO_2 concentration of 10 v/v%. The inverse gradient of the linearized plot translates to τ which yields a value of 42.55 min^{-1}.

Equation (3.17), from Chapter 3, has the following form after substituting Equation (3.19) into it:

$$\tau = \frac{\rho_m r_g}{\bar{b} C_g^n k} \tag{6.1}$$

Applying the separation of variables and taking the natural log, yields the following equation:

$$\ln\left(\frac{\rho_m r_g}{\bar{b}\tau}\right) = \ln k + n \ln C_g \tag{6.2}$$

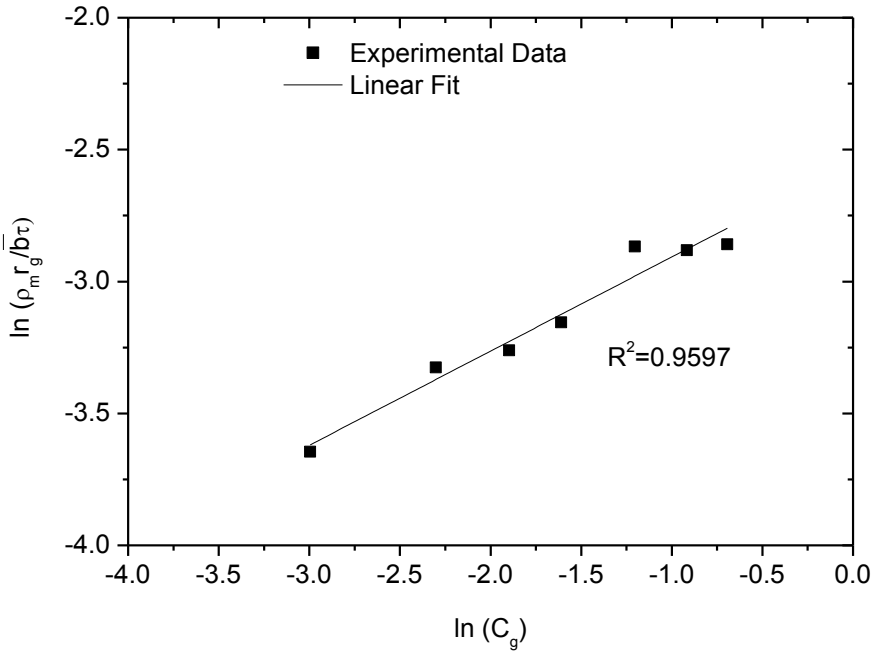

Figure 6-6 Plot to obtain the reaction order

To obtain the reaction order, ln $(\frac{\rho_m r_g}{\bar{b}\tau})$ was plotted against ln C_g. A line of best fit was then generated through the points and the reaction order was found from the gradient of this line. Figure 6-6 depicts this plot and the reaction order was found to be 0.36. Comparing this value to that of Abad *et al.* [6], the obtained value here is much lower compared to their values of 1 and 0.8 for the pre-oxidized and activated ilmenite respectively with CO as the fuel. A point to note here is that CO is not introduced directly into the TGA, rather is has to be first generated from the gasification of the char, which is a slow process; this could be a reason for the difference in the obtained order of reaction. The obtained order of reaction is similar to that reported in literature for char gasification [7]. Another point to note here is that this SCM equation uses the concentration of CO_2 and not CO as the generation of CO was found to be a function of time and the use of either an average value or a function did not yield accurate predictions.

To obtain the activation energy, E_a, a plot of ln (k_o) against T^{-1} was constructed and this can be found in Figure 6-7. The activation energy was found to be 209.1 kJ/mol, which is roughly double the value reported by Abad *et al.* [6] using CO as the fuel. On another note, this value is similar to the activation energies for the gasification of char as found by Fermoso *et al.* [7]. This serves to confirm that gasification of char is the rate limiting step in CLC, else a value similar to that reported Abad *et al.* [6] would have been obtained.

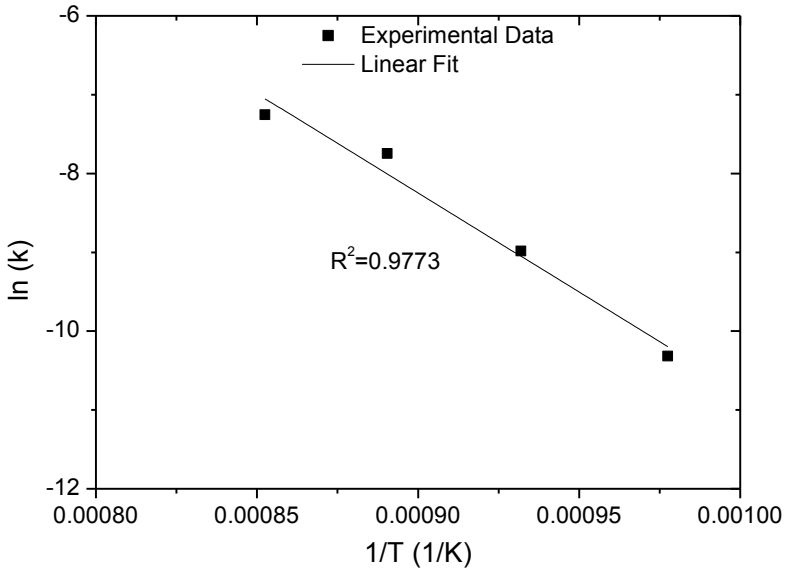

Figure 6-7 Plot to obtain the activation energy

With both the reaction order and activation energy found, the pre-exponential factor was estimated by setting both n and E_a in Equation (3.17) and using the Generalized Reduced Gradient (GRG) nonlinear method [8, 9] for the optimization of nonlinear systems. The optimization resulted in a value of 9.73×10^{-10} for c and upon substitution of ρ_m, r_g and b, k_o was found to be 3.53×10^5 $mol^{0.64} m^{-0.92} s^{-1}$. The order of magnitude of this value falls within the range reported in literature for char gasification [7].

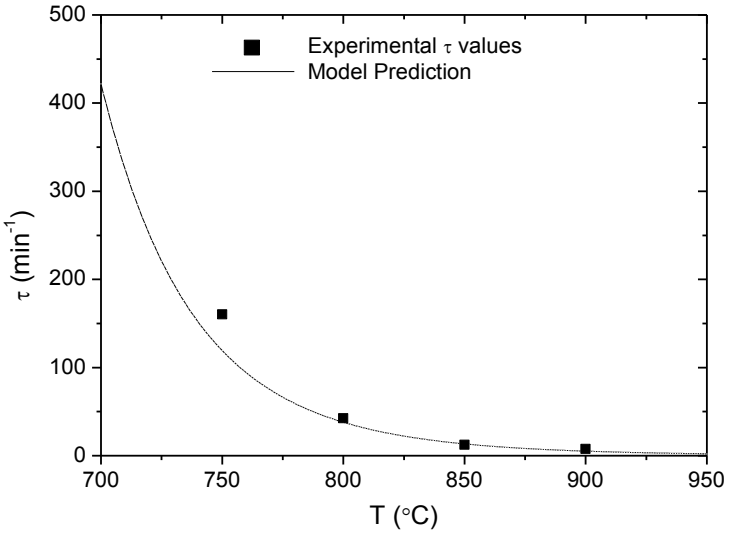

Figure 6-8 Comparison of experimental and model predictions for τ as a function of T with a constant C_g of 10 v/v% CO_2

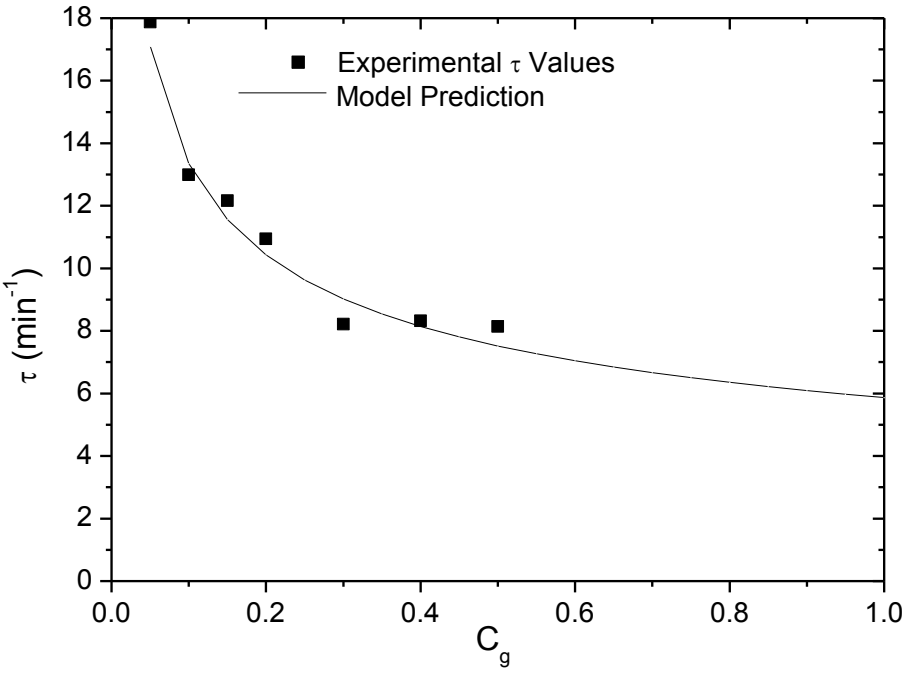

Figure 6-9 Comparison of experimental and model predictions for τ as a function of C_g with a constant T of 850°C

Based on the obtained values for c, E_a and n, a model was generated to predict τ as a function of temperature at a constant C_g of 10 v/v% CO_2 and this is shown in Figure 6-8; similarly, Figure 6-9 shows the model predictions for τ as a function of C_g at a temperature of 850°C. The former figure shows that the predictions do not do very well at low temperatures as the kinetics of both the gasification of the char and reduction of the OC are very slow, but it is capable of predicting τ for temperatures beyond 800°C within an acceptable margin of error. Figure 6-9 shows a similar trend for when C_g was varied and it can be seen that the model fits the experimental data well with the exception for when C_g had a value of 0.3, which could have been an outlier as the model fitted the rest of the data well.

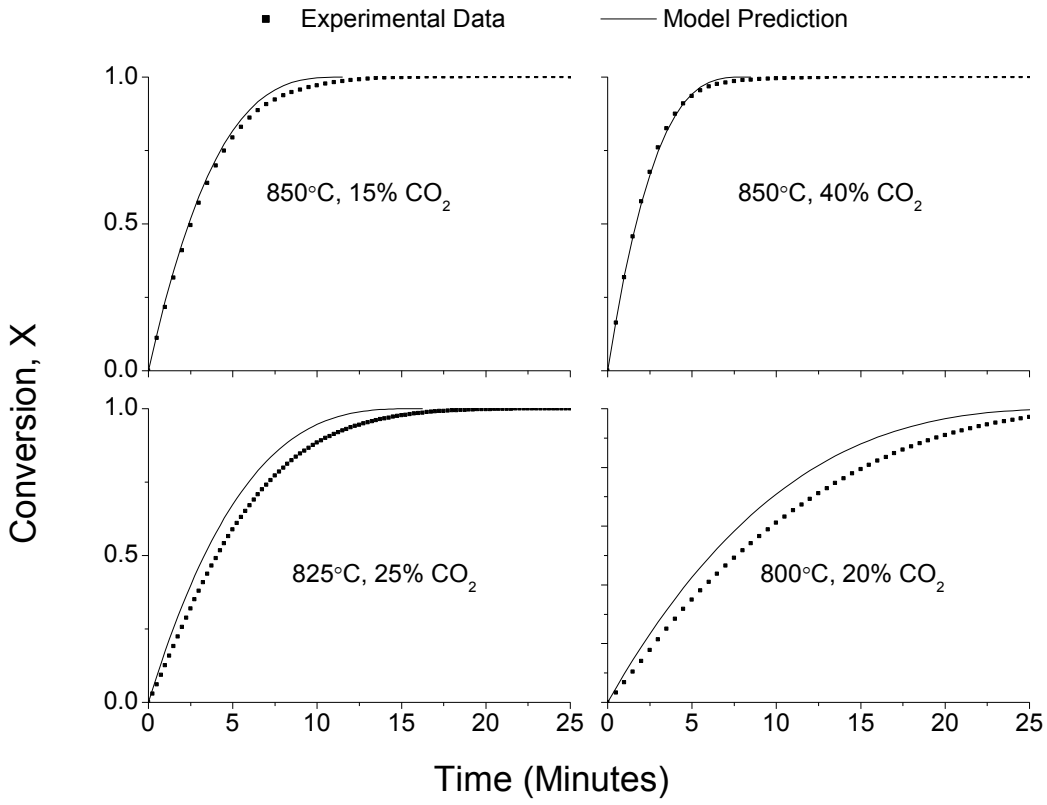

Figure 6-10 Comparison of experimental and SCM results for four different conditions

Figure 6-10 shows the data for experiments that were performed to validate the model. For the first two conditions at 850°C, it can be seen that the model and experimental data fit very well and almost perfectly when C_g was 40 v/v%. As the temperature was dropped to 825°C with a CO_2 concentration of 25 v/v%, the model was found to over predict the conversion and complete at an earlier time relative to the experimental data. When the temperature was further dropped to 800°C and with a CO_2 concentration of 20 v/v%, the disparity was found to increase even further.

In conclusion, the SCM was found to be able to sufficiently predict the reduction of the OC in the presence of char with CO_2 as the gasification agent. The predictions improved significantly at higher temperatures and CO_2 concentrations. The extent of reaction between the CO from char and the OC varies as a function of C_g and T. This could not be accurately captured and as such, a global kinetic equation was generated. As mentioned earlier, the model does not work very well at low temperatures due to a retardation in the char gasification and OC reduction kinetics. Hence, it is more applicable at higher temperatures, which is more relevant in the context of CLC.

6.4 Modified Volume Reaction Model (MVRM) Results

Unlike the SCM, the MVRM is an empirical model and as such does not require the properties of the OC to be included into the model and only relies on the conversion of the OC as a function of time.

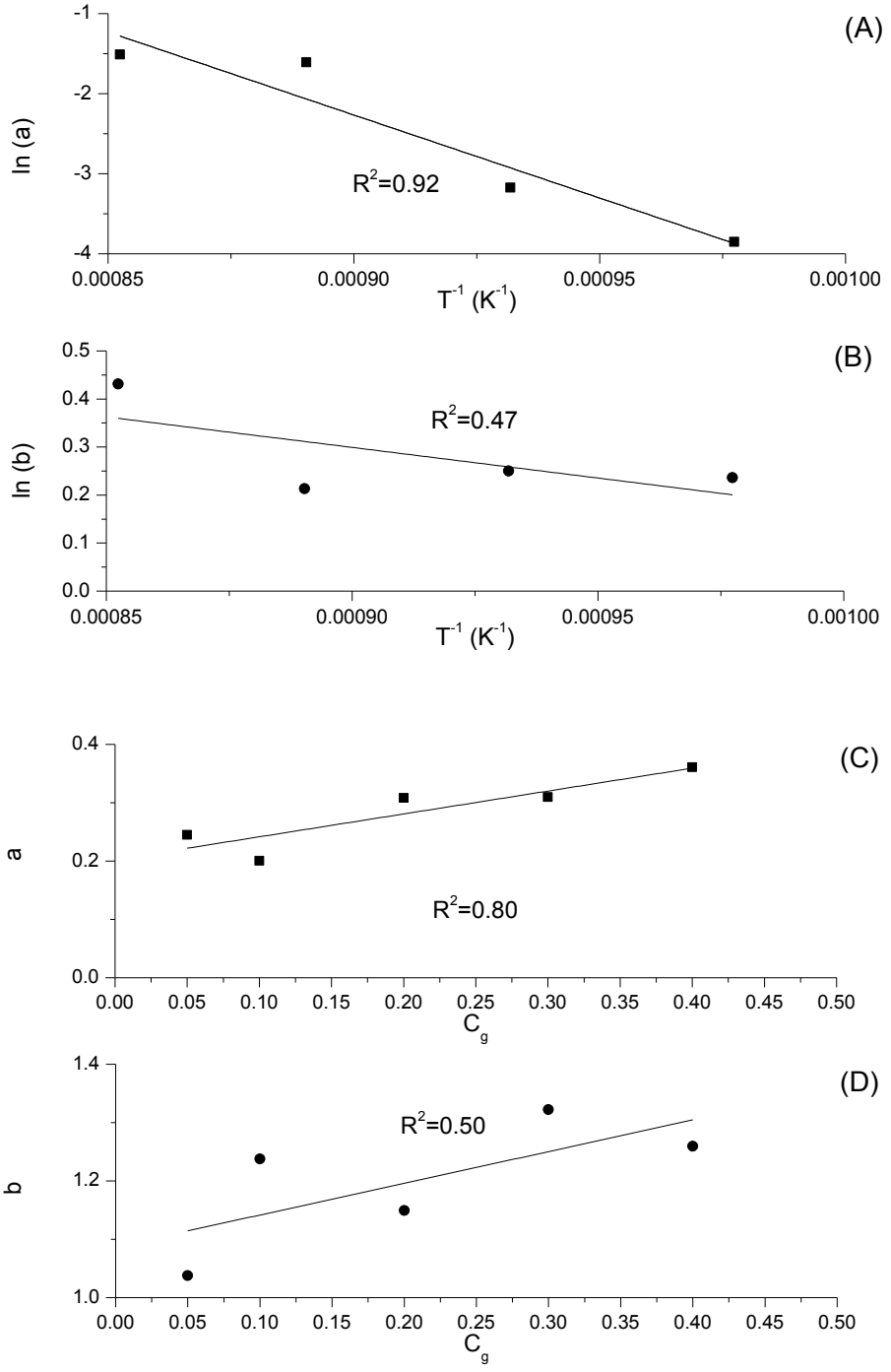

Figure 6-11 Plot of ln (a) and ln (b) against T^{-1} (A-B); plot of (a) and (b) against C_g (C-D)

From the Methodology chapter, Chapter 3, it is understood that the values of both the fitting parameters (a) and (b) are needed for the MVRM to be functional. Qualitatively, based on the observed fit with the experimental results, it was found that (a) describes the reaction rate while (b) affected the prediction of the reaction rate, resulting in it describing the shape of the conversion curve. Based on the values obtained from the model data experiments, Figure 6-11 was constructed to study the potential relationship between (a) and (b) and how they varied as a function of C_g and T. The best fit was found for the plot of ln (a) against T^{-1} with an R^2 value of 0.92. Based on this, it was predicted that the behaviour of (a) as a function of T followed an Arrhenius style relationship. The rationale behind this statement is that the reaction rate is dependent on the amount of energy available in the atoms and the Arrhenius equation predicts how many of these atoms have energies in excess of the activation energy to enable the reaction to proceed.

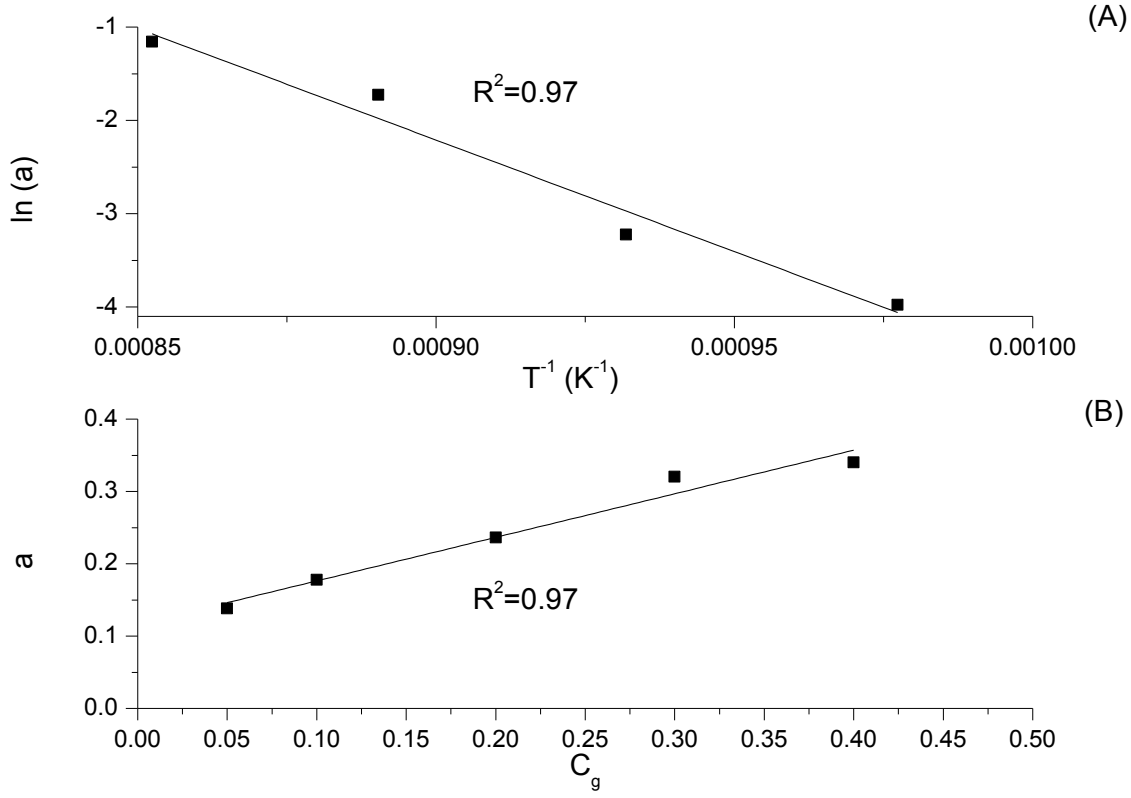

Figure 6-12 Plot of ln (a) against T^{-1} for b=1.3 (A); plot of (a) as a function of C_g for b=1.3 (B)

Since the variations in (b) were minimal, less than 15%, it was averaged out and a value of 1.3 was obtained for it. This new value of (b) was then put into the governing equation to solve for (a) and this was then plotted as a function of C_g and T^{-1}, which can be found in

Figure 6-12. A much better fit was obtained with an R^2 value of 0.97 for both the curves. This confirms that (a) follows an Arrhenius style relationship with respect to temperature and a linear relationship with C_g. Based on the aforementioned statement, the following relationship for (a) was proposed:

$$a(T) = a_0 \exp\left(\frac{-E_a}{RT}\right) \quad 6.3$$

This form assumes that (a_o) is the pre-exponential factor, while the rest of the symbols have been defined in the previous section. The activation energy was found to be 198.7 kJ/mol while the pre-exponential factor had a value of 1.45×10^{10} $s^{-1.3}$. While the activation energy is a feasible value and is similar to that obtained using Figure 6-7 above for the SCM, the pre-exponential factor is much larger than any of the values that have been reported in literature by at least three orders of magnitude [7]. One possibility for this is that while a_o represents the pre-exponential factor from a mathematical standpoint, it could be representing another constant in reality and as such requires further investigation. While it is acknowledged that there are alternate ways to interpret (a) and (b) for the MVRM, it was found that this interpretation provided a good fit for the data as well as allowed for a trend to be found for the relationship between (a) and both C_g and T.

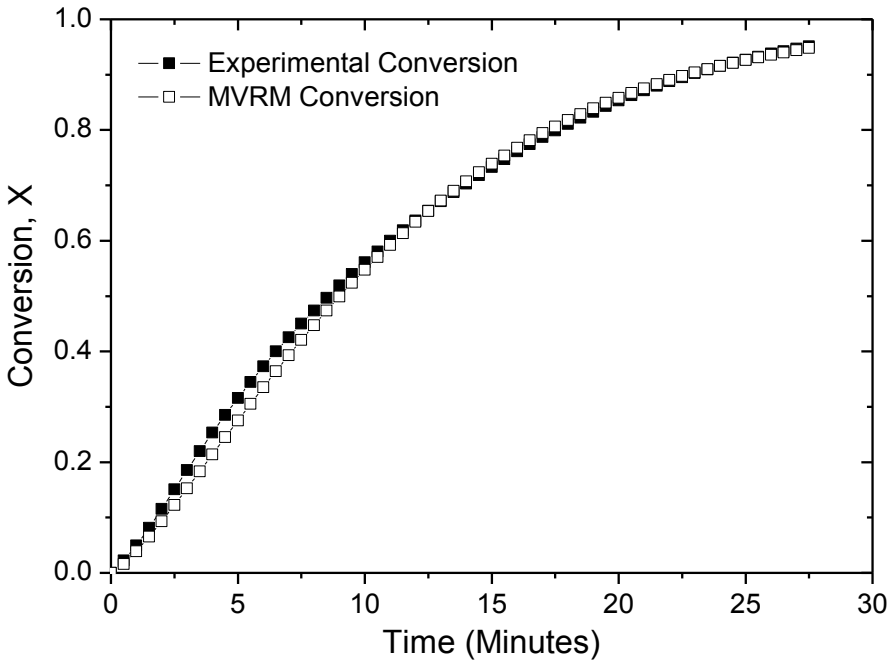

Figure 6-13 Comparison of experimental and MVRM conversions for the Fe_2O_3 and char mixture at 800°C with 10 v/v% CO_2 as the gasification agent

A similar plot to that of Figure 6-5 which was constructed for the SCM predictions was made for the MVRM predictions under the same conditions and this can be found in Figure 6-13. It can be seen that this model provides a better fit compared to SCM for this set of conditions.

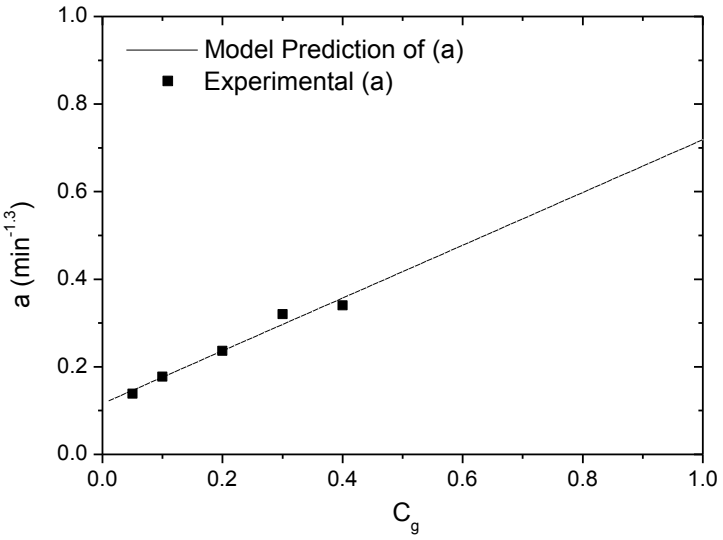

Figure 6-14 Comparison of experimental and model predictions for (a) as a function of C_g with a constant T of 850°C

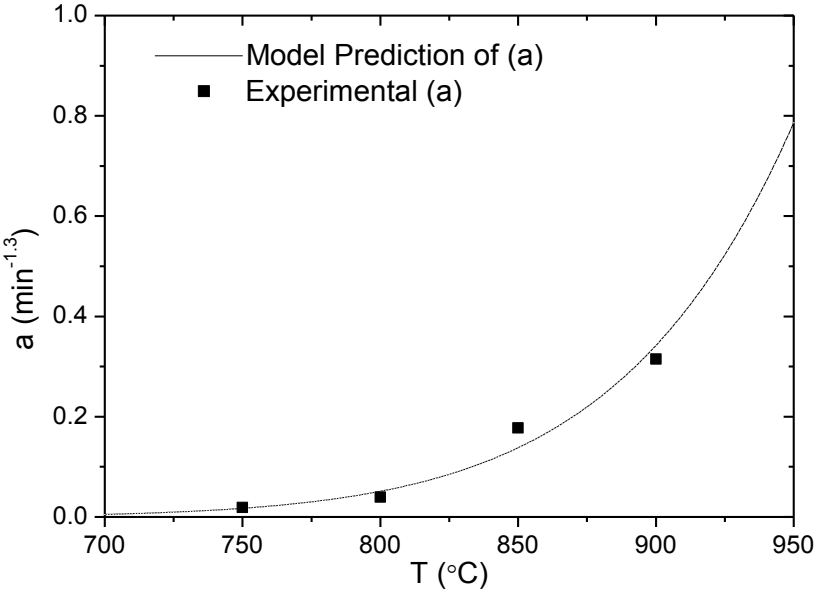

Figure 6-15 Comparison of experimental and model predictions for (a) as a function of T with a constant C_g of 10 v/v%

As the model fitted the experimental data well, Figure 6-14 and Figure 6-15 were constructed, which display the model prediction of (a) as a function of C_g and T. It can be seen that the relationship is exponential with T and linear with C_g. Using these model predictions, the value of (a) was calculated for the conditions used in the data validation experiments and plotted in Figure 6-16 below. Comparing this to Figure 6-9, it can be seen that this model appears to better predict the conversion of the OC relative to that found using the SCM. The reason for this could be due to the differences in the assumptions between the two models. The MVRM assumes negligible resistance to gas diffusion, while SCM assumes the opposite. Hence, it is possible that the diffusional resistance in this experiment was insignificant.

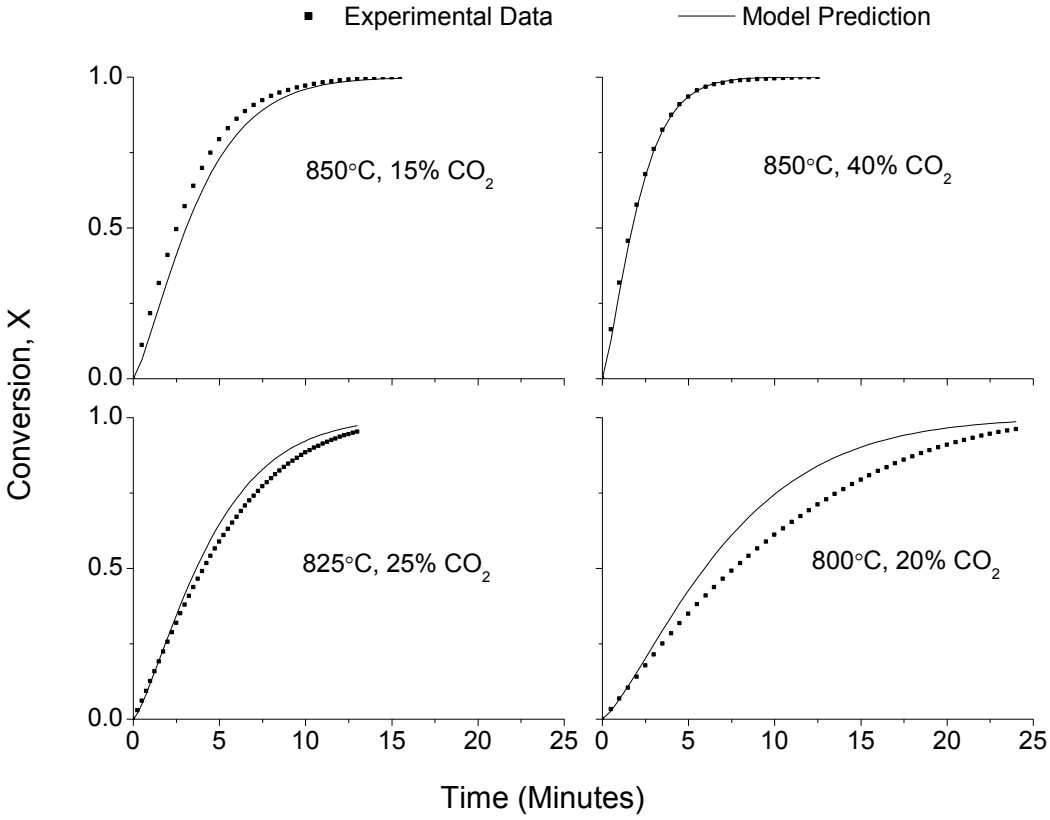

Figure 6-16 Comparison of experimental and MVRM results for four different conditions

Using FactSage 6.4, it was found that the equilibrium concentration of CO relative to the generated CO_2 was 0.002% at 750°C and this value increased to 0.004% at 900°C. These predicted values are much smaller than the experimental value of 5 v/v% CO in CO_2 found in this study. The rationale for such a high experimental value is due to the lack of intimate contact between the OC and char gasification products in the TGA. The reason the model results are so low is because the software looks at the system from a thermodynamic

equilibrium point of view and discounts aspects such as kinetics and assumes perfect contact in a closed system over an infinite time period.

6.5 Particle Characterization

Here, some of the used OC particles were characterized to study the effect of temperature and CO_2 concentration on the morphology and structure of the OC particles. A few samples were selected for this study, namely the OCs that were used in the experiments that were subjected to the following conditions: 850°C and 5 v/v% CO_2, 850°C and 50 v/v% CO_2; 725°C and 10 v/v% CO_2. These are denoted as S1, S2 and S3 respectively. The first two samples will show if the concentration of C_g has any effect on the OC while the last sample will show if operating at a low temperature has any impact on the OC.

6.5.1 Scanning Electron Microscope (SEM)

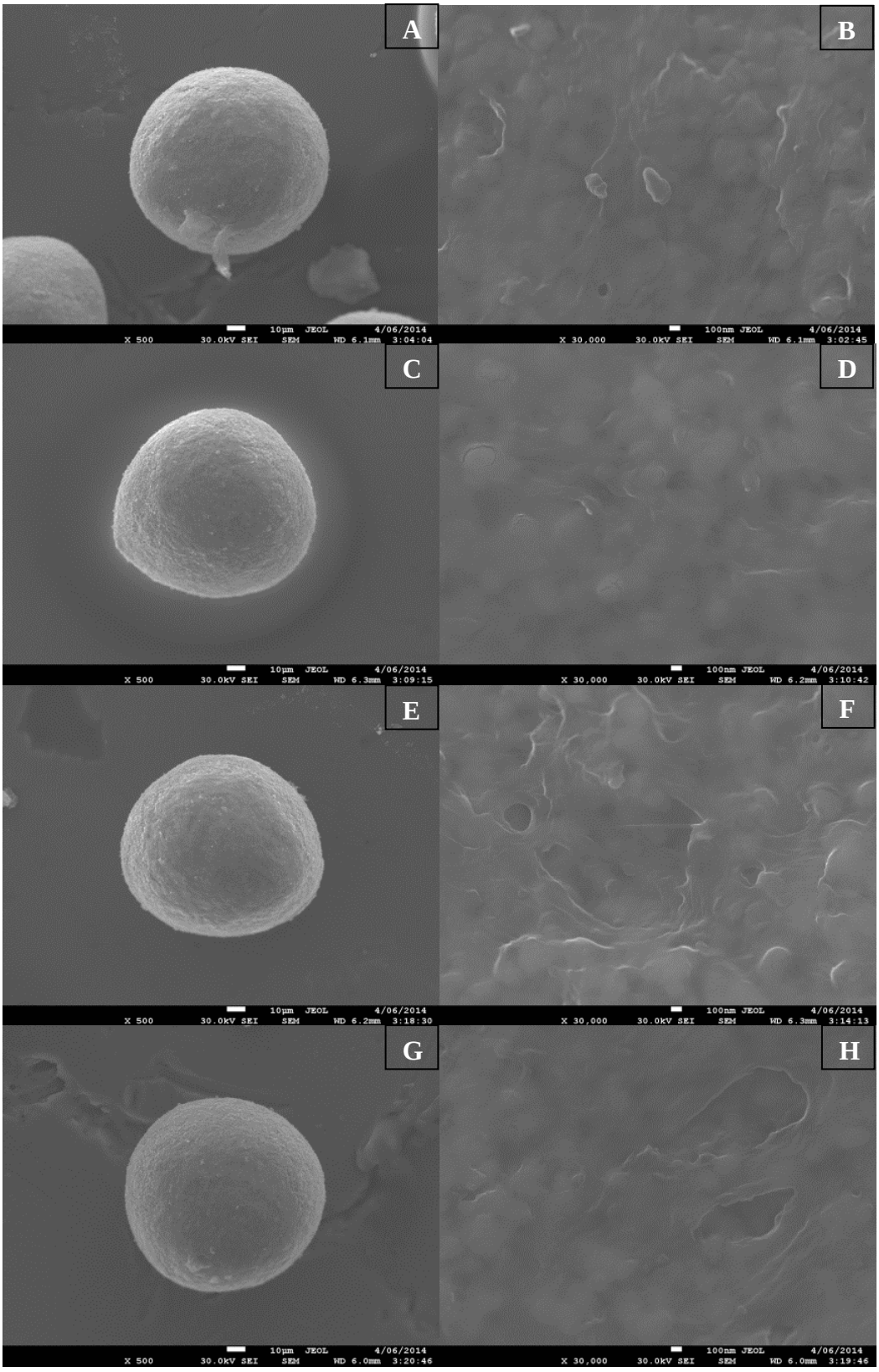

Figure 6-17 Micrographs of the fresh calcined particle (A, B); S1 (C, D); S2 (E, F); S3 (G, H)

Figure 6-17 shows the SEM images obtained for S1, S2, S3 and the fresh calcined sample. Images A, C, E and G were taken at a lower magnification of 500X while images B, D, F and G were taken at a higher magnification of 30,000X. It can be seen that the fresh and used particles appear very similar at a lower magnification. At a higher magnification, the grains of the used samples appear to be larger and having more irregularities. Typically, larger grains translate to a reduction in the surface area, but the presence of higher levels of irregularities would increase this value; this will be discussed in the following sub-sections by analysing the results from the Accelerated Surface Area and Porosimetry (ASAP) measurement. Due to the different experimental conditions that each of the OC samples were subjected to, each particle would have differing degrees of reduction as it was a heterogeneous system. Additionally, the reduction of each particle would differ depending on the local concentration of the reducing gas.

6.5.2 Energy Dispersive X-ray Spectroscope (EDS)

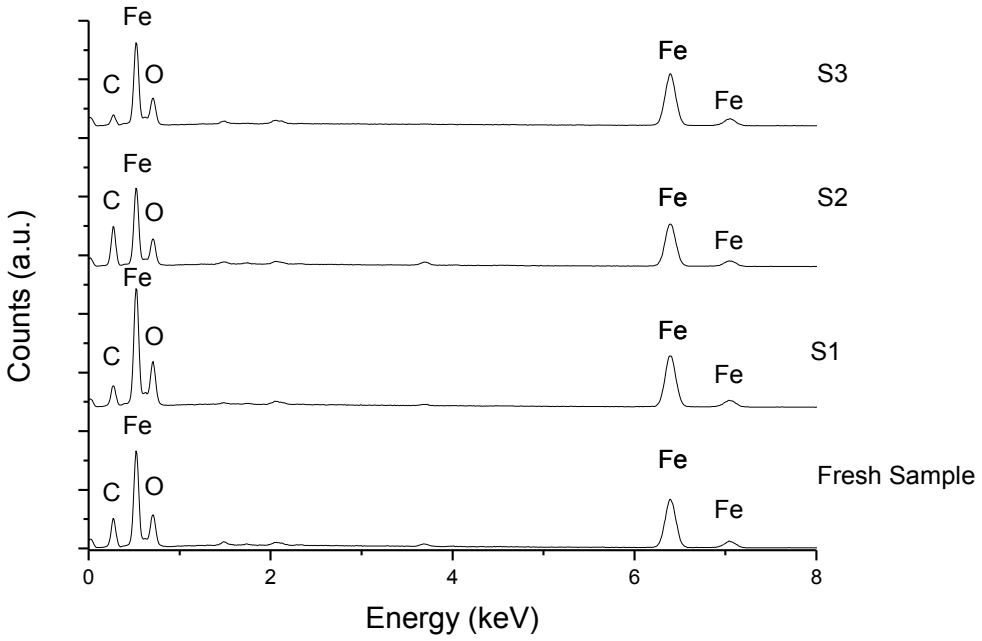

Figure 6-18 Energy dispersive X-ray spectra of S1, S2, S3 and the fresh calcined sample

The results from the EDS analyses can be found in Figure 6-18. This shows the representative results obtained over an area scan covering more than 50% of the surface of the OC. Ash was not detected due to the small amount of char used in this investigation. It is observable that all the samples contained carbon and this is not due to presence of carbon on the sample, as the fresh sample was of laboratory grade and it was calcined before use. This is due to the carbon

tape used to secure the OC to the sample stub. Besides this, the spectra of the four samples appear to be very similar to each other. Since EDS is a semi-quantitative technique, the X-ray counts can be compared in a relative sense. Compared to the fresh sample and after normalizing to exclude carbon, it was found that the used samples contained higher levels of Fe and lower amounts of O, confirming that it had been reduced.

6.5.3 Accelerated Surface Area and Porosimetry (ASAP)

Table 6-1 Pore structure analysis results for S1, S2, S3 and the fresh calcined sample

Sample	BET surface area (m^2/g)	Cumulative pore volume (cm^3/g)	Average pore width (Å)
Fresh calcined Fe_2O_3	2.7664	0.004689	54.824
S1	2.9981	0.002996	73.688
S2	3.1881	0.005116	54.046
S3	3.8484	0.006815	41.863

Table 6-1 shows the results obtained from the ASAP analysis. It can be seen that all the reduced samples have a higher BET surface area relative to the fresh particle and this is also evident from the SEM images, which was ascribed to the increase in the surface irregularities. The cumulative pore volume for all the used samples except S1 was found to be higher when compared to the fresh sample. The primary difference between S1 and S2 is the concentration of the reducing gas in the vicinity of the OC. Focussing on the average pore size, both S1 and S2 had values similar to or higher than that of the fresh sample while S3 experienced a reduction in said value. Compared to S1 and S2, S3 was subjected to a lower reaction temperature which could be the reason for this observation. Alternatively, CO_2 has a kinetic diameter of 3.9Å [10], which is larger than that of CO but much smaller than the average pore width of S3. This means that both CO and CO_2 would not have experienced difficulties entering and exiting the matrix of the OC.

6.5.4 X-ray Diffraction (XRD)

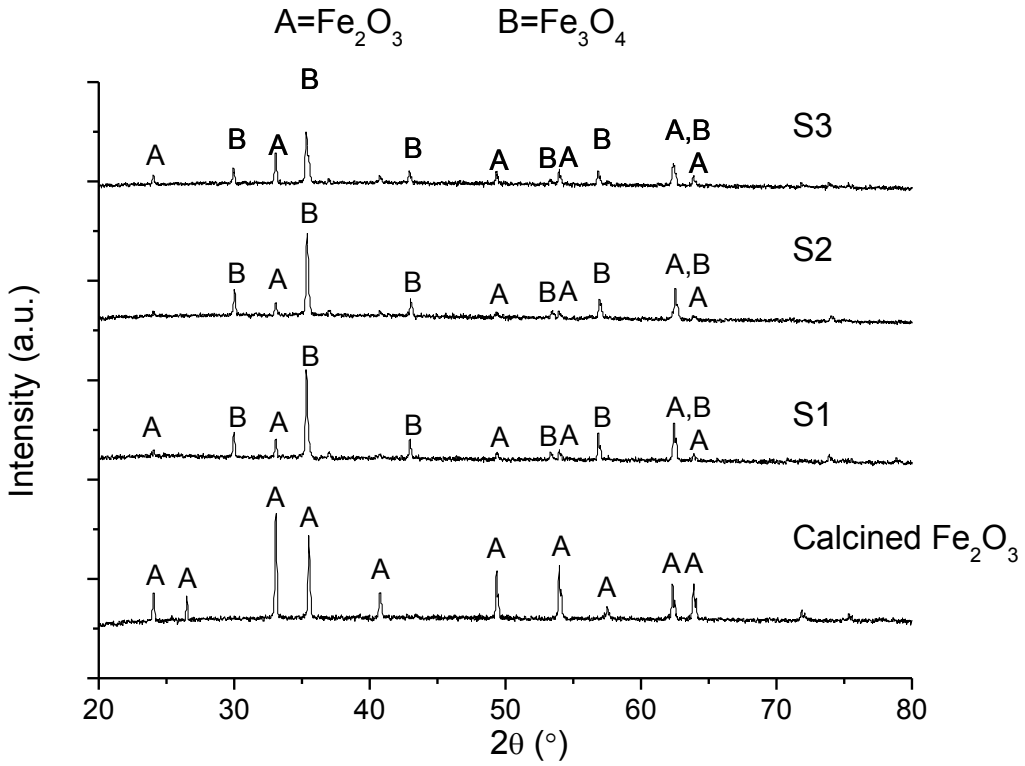

Figure 6-19 Diffractograms of S1, S2, S3 and the fresh calcined sample

Figure 6-19 shows the diffractograms of the four samples that have been discussed thus far. As expected, the fresh calcined OC only shows peaks for Fe_2O_3 due to the high purity of the sample. Samples S1 to S3 contain both Fe_2O_3 and Fe_3O_4, signifying that the OC was not fully reduced to Fe_3O_4. These results validate the statement initially made regarding the OC not being reduced beyond Fe_3O_4.

6.6 Final Comments

The SCM can predict the time it will take for the OC to be reduced by a certain amount of char at a given temperature and CO_2 concentration. Using the SCM, it was found that S1, S2 and S3 would require 17.9 minutes, 8.1 minutes and 220.8 minutes respectively to completely react with the char; S3 needs a long time to oxidize the fuel due to the slow char gasification kinetics at such a low temperature. These values were also similar, within ±5%, when predicted using the MVRM. It can be seen that the conditions that S2 were subjected to resulted in the fastest reduction time of the three; the reason behind this observation is due to both reactivity and kinetics, which are related. Since the ratio of the OC to the fuel was much higher than the stoichiometric amount, the reduction of the OC can be a measure of its

reactivity. For S2, both the temperature and concentration of CO_2 were high, which led to the char being gasified quickly while the generated CO was also quickly consumed by the OC. With respect to S3, while the reaction rate was slow, the reactivity was still adequate to allow for the conversion of CO to CO_2 by the OC. Focussing on S1, the low concentration of CO_2 led to a decrease in the rate of CO production, which in turn increased the time taken for the char to be fully consumed.

Based on the obtained results, it can be seen that the reduction of the OC is a function of the gasification rate of char. It was found that both models provided a good fit to the experimental results, enabling the prediction of the time required to fully oxidize a certain amount of fuel at a given temperatures and CO_2 concentration. This is relevant from a practical point of view as this is the first ever model to describe the reduction kinetics of Fe_2O_3 in the presence of a solid fuel.

6.7 Conclusions

This chapter modelled the reduction of Fe_2O_3 in the presence of char prepared from VBC. Two models, the SCM and the MVRM, were used. The activation energy, reaction order and pre-exponential factor were found for the SCM before it could be used to model the reduction of the OC. The fitting parameters for the MVRM, (a) and (b), were derived from the experimental data. The key conclusions from this study are as follows:

1. Two different models, SCM and MVRM, were used to model the reduction of the OC in the presence of a solid fuel, Yallourn char. The former incorporated the different physical properties of the OC while the latter was an empirical model and did not take into account the properties of the OC.

2. For the SCM, an activation energy of 209 kJ/mol, a reaction order of 0.36 and a pre-exponential factor of 3.53×10^5 $mol^{0.64}$ $m^{-0.92}$ s^{-1} were obtained. With the MVRM, the governing variables (a) and (b) were found. The variable (a) was found to be a function of temperature and concentration of CO_2 while (b) was a constant with a value of 1.3. With these values, the activation energy was found to be 198.7 kJ/mol. The difference between the two activation energies was around 5%, which is an independent confirmation of the validity of the models.

3. The obtained activation energies are higher than the values reported in literature for the reduction of Fe_2O_3 in the presence of gaseous fuels. This means that the activation energy that is required to initiate the reaction between Fe_2O_3 and syngas is smaller than when char is used as the fuel instead. The reason for this is that both the models that were used could not distinguish between the activation energies of char gasification and reduction of the OC, but were capable of extracting the higher value which corresponded to that of char gasification.

4. Using the two models, the conversion of the OC in the presence of char was predicted and a good fit was obtained for both models for temperatures above 800°C. The obtained results show that both of these models are capable of predicting the conversion of the OC in the presence of a char derived from VBC.

The obtained results showed that both the SCM and MVRM could adequately model the reduction of Fe_2O_3 in the presence of a char derived from VBC. The calculated activation energies using the two models confirm that the rate limiting step in CLC is the gasification of char.

6.8 References

1. Abad, A., F. García-Labiano, L.F. de Diego, P. Gayán, and J. Adánez, *Reduction Kinetics of Cu-, Ni-, and Fe-Based Oxygen Carriers Using Syngas (CO + H2) for Chemical-Looping Combustion.* Energy & Fuels, 2007. **21**(4): p. 1843-1853.
2. Hou, B., H. Zhang, H. Li, and Q. Zhu, *Study on Kinetics of Iron Oxide Reduction by Hydrogen.* Chinese Journal of Chemical Engineering, 2012. **20**(1): p. 10-17.
3. Xiao, R. and Q.L. Song, *Characterization and kinetics of reduction of CaSO4 with carbon monoxide for chemical-looping combustion.* Combustion and Flame, 2011. **158**(12): p. 2524-2539.
4. Monazam, E.R., R. Siriwardane, R.W. Breault, H.J. Tian, L.J. Shadle, G. Richards, and S. Carpenter, *Kinetics of the Reduction of CuO/Bentonite by Methane (CH4) during Chemical Looping Combustion.* Energy & Fuels, 2012. **26**(5): p. 2779-2785.
5. Johnson, J. and M. Elliott, *Chemistry of Coal Utilization*. Vol. 2nd Supplementary Volume. 1981: John Wiley & Sons. 1491-1598.
6. Abad, A., J. Adanez, A. Cuadrat, F. Garcia-Labiano, P. Gayan, and L.F. de Diego, *Kinetics of redox reactions of ilmenite for chemical-looping combustion.* Chemical Engineering Science, 2011. **66**(4): p. 689-702.
7. Fermoso, J., B. Arias, C. Pevida, M. Plaza, F. Rubiera, and J. Pis, *Kinetic models comparison for steam gasification of different nature fuel chars.* Journal of Thermal Analysis and Calorimetry, 2008. **91**(3): p. 779-786.
8. Lasdon, L.S., A.D. Waren, A. Jain, and M.W. Ratner, *Design and testing of a generalized reduced gradient code for nonlinear optimization*. 1975, DTIC Document.
9. Harmon, M., *Step-By-Step Optimization With Excel Solver - The Excel Statistical Master*. 2012: Excel Master Series. 250.
10. Siriwardane, R.V., M.-S. Shen, E.P. Fisher, and J.A. Poston, *Adsorption of CO2 on Molecular Sieves and Activated Carbon.* Energy & Fuels, 2001. **15**(2): p. 279-284.

Chapter 7 Effect of Reactor Operating Mode

The majority of the reported bench scale work in CLC involves the use of fluidized bed reactors [1-3] with a small amount of work reported using atmospheric and pressurized fixed bed reactors [4, 5]; the former is preferred as it provides better contact between the solids and the gases. To date, there have not been any investigations comparing these three configurations. This chapter will investigate the performance of the three setups using a multi-purpose reactor housed at Southeast University. Zhang *et al*. [6] used the same reactor to investigate the effect of pressure on the conversion of the fuel to CO_2. Hence, a comparison will be made between the results obtained in this study using Yallourn coal with those found by Zhang *et al.* [6] using a bituminous coal from Xuzhou.

This chapter compares the performance of three different reactor configurations (fluidized bed, atmospheric fixed bed and pressurized fixed bed) in CLC of VBC using an iron ore as the OC. This is the first study of its kind and will provide valuable information regarding the performance of the three different reactor configurations.

7.1 Experimental Conditions

Since the obtained results will be compared to that reported by Zhang *et al.* [6], the conditions employed in this study mimicked those which were used in their investigation. Additionally, no TGA tests were performed for this OC as it has been proven to possess sufficient reactivity based on their studies. All experiments were conducted at 970°C with a total gas flow rate of 1040 mL/min. During reduction, 74 v/v% steam was used as the gasification agent with the balance being composed of N_2. Oxidation was performed using a gas stream containing 5 v/v% O_2 and balance N_2, having a total flow rate of 1000 mL/min.

40 g of quartz sand with a size range of 600-1000 µm was placed atop the distributor after which 40 g of Companhia Vale do Rio Doce (CVRD) ore with a size range of 90-180 µm was introduced into the reactor. This was then heated to the operating temperature under oxidizing conditions to calcine the OC. Once the temperature set point was reached, 0.4 g of Yallourn coal having a size range of 125-180 µm was added into the reactor; this corresponded to an OC to coal ratio of 100:1.

It should be noted that for the three investigated configurations (fluidized bed, atmospheric fixed bed and pressurized fixed bed), the same mass of the OC and fuel were used alongside

the same fluidization gases and flow rates. This was done to ensure that the results were comparable amongst the three as well as with the results obtained by Zhang *et al.* [6].

The difference between the fluidized and two fixed bed reactors lie in the direction of gas flow. In the fluidized bed reactor the gases enter through the bottom and exit through the top. In the fixed bed reactors, the gases flow in the opposite direction. The pressurized fixed bed reactor was operated at 5 bar pressure and this was manually controlled using a pressure regulator which was installed downstream.

The gases exiting the reactor are diluted by 1000 mL/min of N_2 to satisfy the minimum gas flow rate required for the gas analyser. At the end of the tenth reduction reaction, which took approximately 10 hours, the reactor was cooled down and the samples were characterized.

A Scanning Electron Microscope (SEM), an Energy Dispersive X-ray Spectroscope (EDS), X-ray Diffraction (XRD) and Accelerated Surface Area and Porosimetry (ASAP) unit were employed to investigate if the different operating conditions affected the structure and morphology of the OC particles.

7.2 Fluidized Bed Reactor Results

The outlet gas concentration profiles, carbon conversion and gasification rate obtained using the fluidized bed reactor will be discussed in this section.

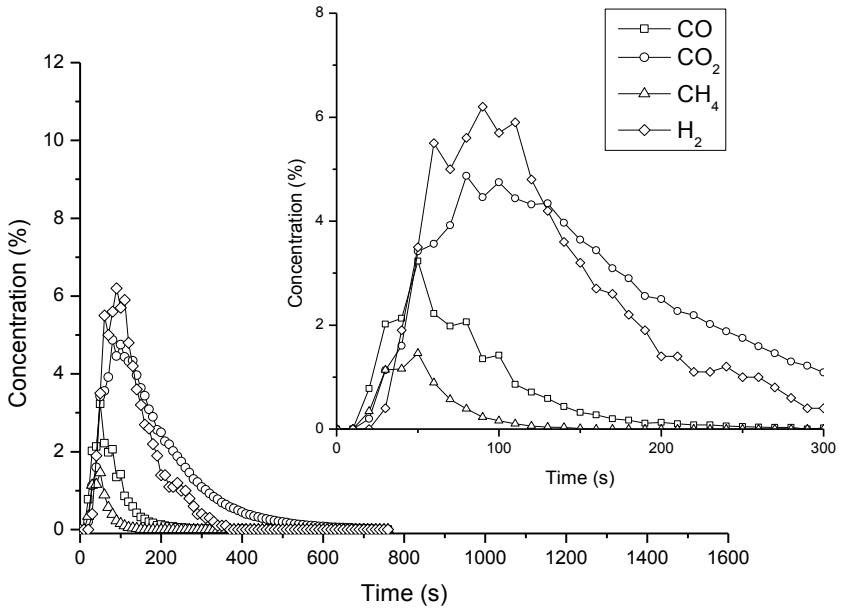

Figure 7-1 Outlet gas concentration profiles of the first reduction reaction using the fluidized bed reactor

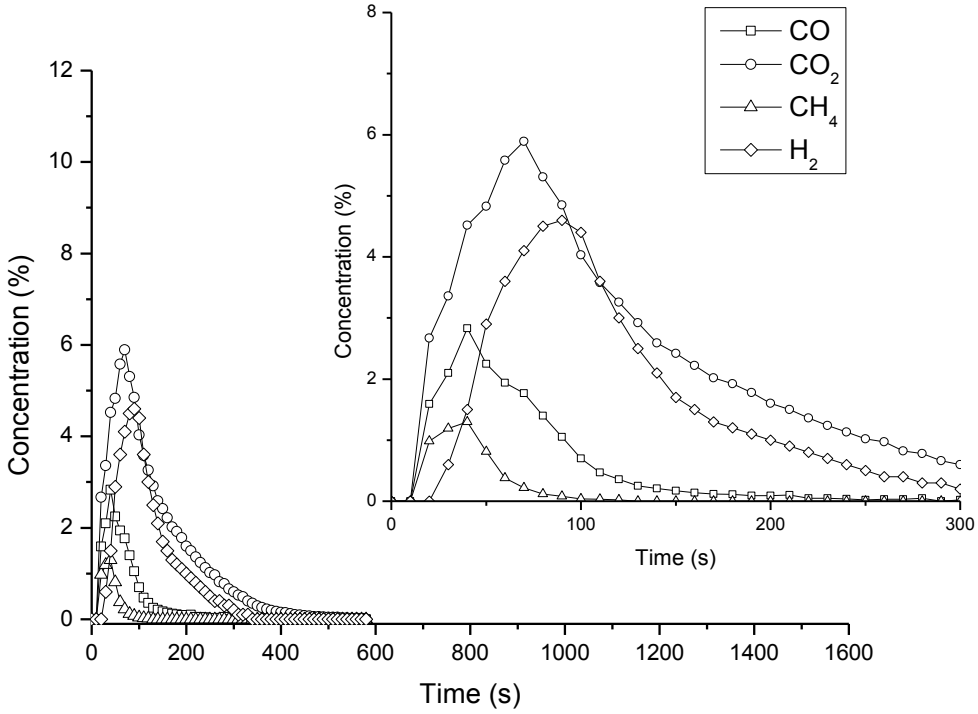

Figure 7-2 Outlet gas concentration profiles of the tenth reduction reaction using the fluidized bed reactor

The outlet gas concentration profiles for the first and tenth reduction experiments performed in the fluidized bed reactor can be found in Figure 7-1 and Figure 7-2 respectively. From Figure 7-1, it can be seen that the chronological order in which the peaks were formed are as follows: CH_4, CO, CO_2 and lastly H_2. Methane was the first gas to be detected as it is evolved during the pyrolysis of the coal, which is a very quick reaction; this occurs as soon as the coal is introduced into the isothermally operated reactor. Soon after, CO, CO_2 and H_2 were detected and these were the prevalent gases formed from both the steam gasification of coal and the combustion of these gasification intermediates by the OC. The last gas to reach the baseline value was CO_2. Both CO and H_2 are by-products of char gasification using steam and are converted into CO_2 and H_2O upon reaction with the OC. It can be seen that the amount of H_2 at any point is much higher than CO. Theoretically, the gasification of char by steam leads to the generation of an equimolar amount of CO and H_2. Additionally, it is a well-known fact that OCs are typically more reactivity with H_2 than CO [7], therefore this should have led to a lower amount of H_2 being detected by the gas analyser. This observed behaviour can be explained by the water-gas shift reaction (WGSR) in which CO reacts with the steam to form CO_2 and H_2; this explains the reason behind the low concentration of CO.

The high concentration of steam in the reactor would cause the WGSR to proceed in the direction that forms more H_2 and CO_2.

It can be observed that in the first reduction reaction, the peak outlet gas concentration was of H_2 and this changed to CO_2 in the tenth cycle. Numerically, the peak concentration of H_2 decreased from a value of 6% to around 4.5% while CO_2 increased from 5% to 6%. Based on the experimental data from the intermediate reduction reactions, this trend was found to hold true with a general increase in the concentration of CO_2 with an accompanied reduction in H_2 and CO. This variation was found to stabilize around the fifth/sixth reduction reaction and is characteristic of conditioning of the OC particles whereby the reactivity appears to increase during the initial redox cycles and then tapers off or decrease depending on the sample. The concentration of CH_4 was found to be almost constant in all the cycles and this is due to the way the fuel was introduced into the reactor. Since dried Yallourn coal is highly reactive with approximately half of its mass comprising volatile matter, a large proportion of this did not come into contact with the OC as it was dropped into the reactor. This is evident from the CH_4 peak formation in the first 30 seconds of the reaction. The other observable difference is that there is a decrease in the time taken for the reaction to complete. This reduced from around 725 seconds in the first reduction reaction to around 525 seconds in the tenth reduction reaction, which represents a 27.6% decrease in the time taken for the combustion of the fuel. This can be ascribed to the increase in the OC's reactivity, enabling it to convert the coal gasification products at a faster rate. The consumption of the gasification intermediates, which are known gasification inhibitors, results in an increase in the rate of gasification of the fuel. This in turn causes the reaction to complete at an earlier time. Additionally, this could also be due to increased attrition of the fuel particles, leading to a greater extent of particle elutriation out of the reactor and this will be discussed with the aid of the following figure.

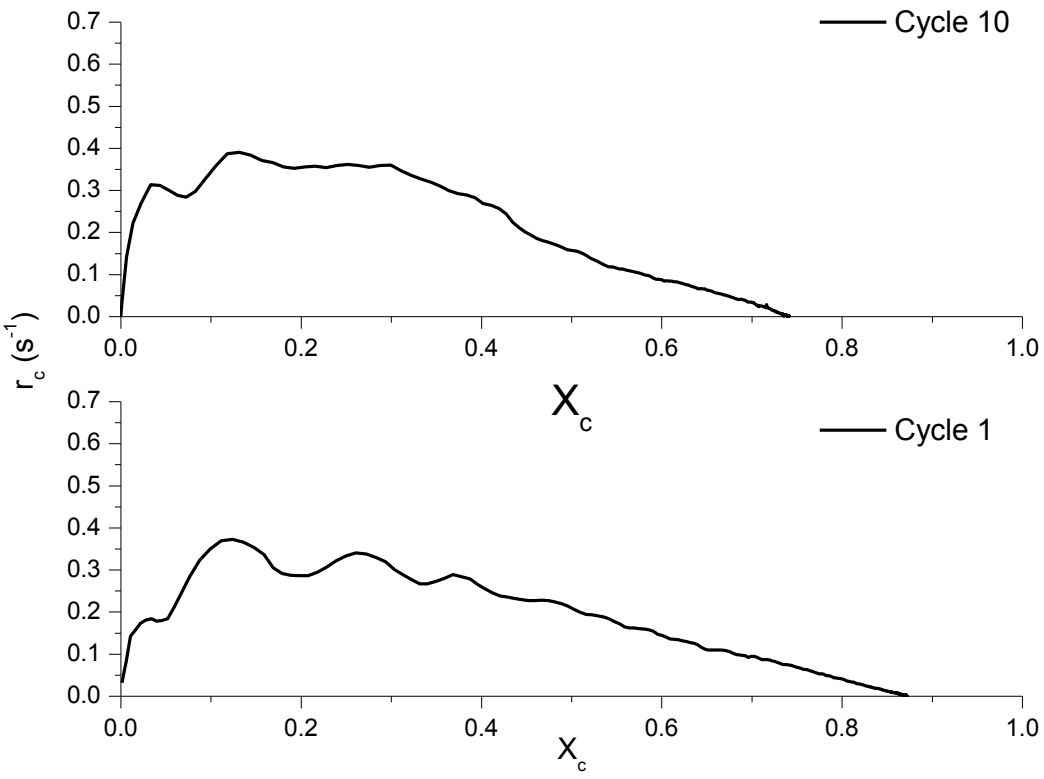

Figure 7-3 Carbon conversion rate as a function of carbon conversion for the first and tenth reduction reactions using the fluidized bed reactor

Figure 7-3 shows the plot of the carbon conversion rate against carbon conversion for the first and the tenth reduction reactions. The peak carbon conversion rate is similar for both the plots but there is a slightly higher average rate, 0.30 s^{-1} vs. 0.26 s^{-1}, during the initial stages (X=0 to X=0.4) of the tenth reduction reaction. This means that the OC is more reactive towards the reducing gases with increasing cycles. On the other hand, it can be seen that the carbon conversion experiences a decrease going from the first to the tenth reduction. The lower carbon conversion in the tenth reduction is partially due to a larger proportion of the fuel having elutriated out of the reactor. With the increasing reaction cycles, it was evident that more char was being caught in the particulate trap. Figure 7-3 shows the carbon conversion to decrease from 0.87 to 0.74 between the first and the tenth reduction reactions, confirming the observation regarding the increase in the amount of elutriated char. Alternatively, this could be due to changes in the fluidization profile in the reactor due to the degradation of the stainless steel mesh that was used over the distributor plate. At the end of the reaction, after the reactor has cooled down, it was observed that the integrity of the mesh had been compromised with gaps being formed in certain regions; this could have affected

the fluidization profile in the reactor by forming dead zones in certain regions leading to channelling of the fluidization gases.

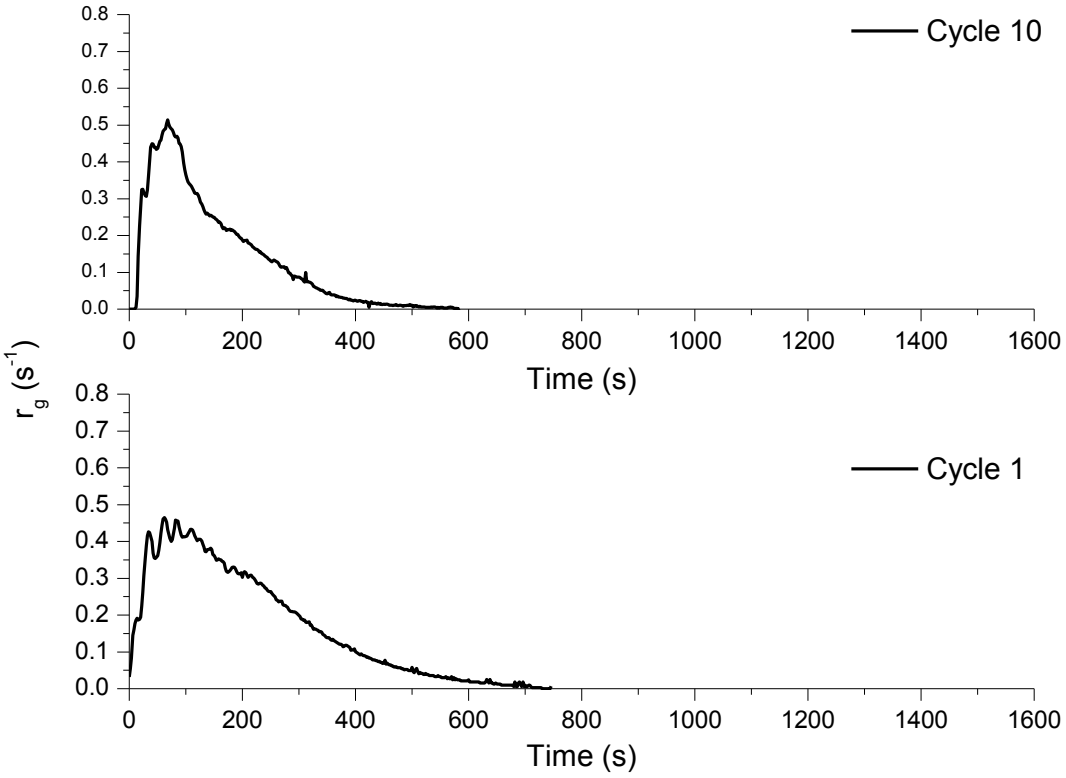

Figure 7-4 Gasification rate as a function of time for the first and tenth reduction reactions using the fluidized bed reactor

The gasification rate of the fuel as a function of time is shown in

Figure 7-4, which is an extension of the previous figure. An integration of the areas under these curves over the course of the reaction would yield the amount of carbon that has been consumed and this will be discussed in the sections to follow. It can be seen that similar to Figure 7-3, the region beneath the plot is larger in the first cycle compared to that in the tenth cycle. The main difference between the two curves is that the peak gasification rate in the tenth reduction reaction is higher by around 10% compared to that in the first cycle and the reason for this is similar to that mentioned above regarding the increased reactivity of the OC.

During the oxidation reaction, the gas concentration profiles were similar for all the cases, with the exception for minor amounts of CO_2 being found in the later cycles. This is most likely due to residual char in the dead regions of the bed. Initially, all of the available oxygen was consumed by the OC, followed by a rapid increase in the O_2 concentration at the outlet. Subsequently, this was found to stabilize to the inlet concentration of O_2.

7.3 Atmospheric Fixed Bed Results

The outlet gas concentration profiles, carbon conversion and gasification rate obtained using the atmospheric fixed bed reactor will be discussed in this section.

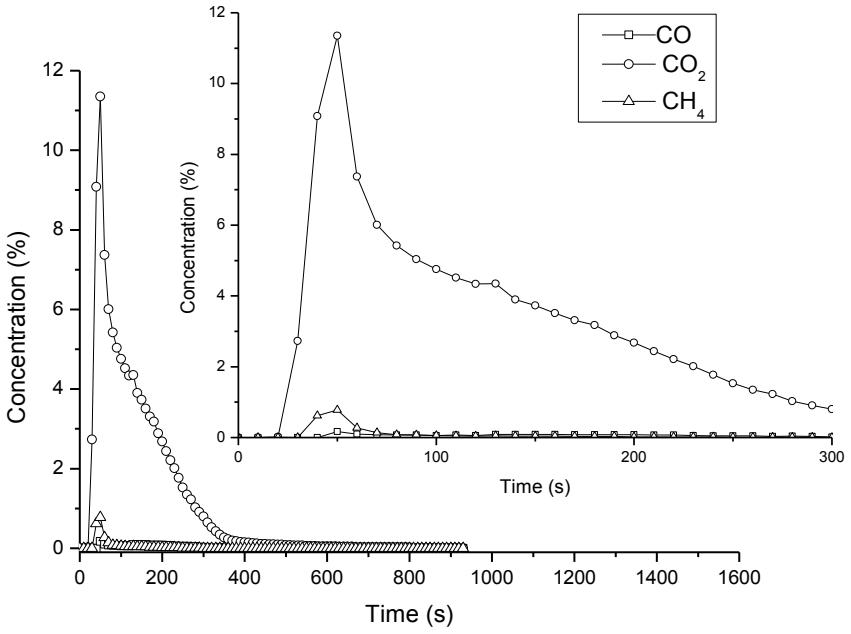

Figure 7-5 Outlet gas concentration profiles of the first reduction reaction using the atmospheric fixed bed reactor

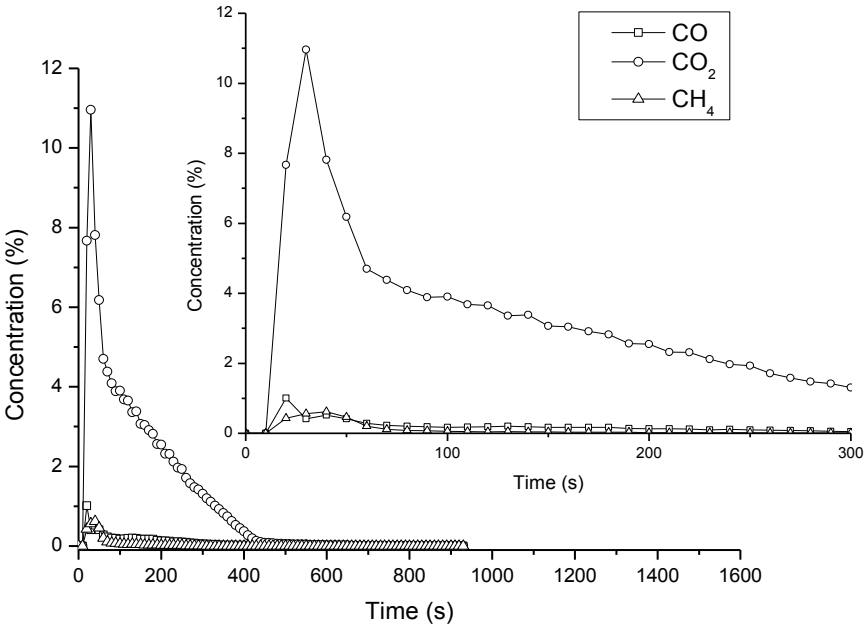

Figure 7-6 Outlet gas concentration profiles of the tenth reduction reaction using the atmospheric fixed bed reactor

The gas concentration profiles of the first and tenth reduction reactions that were undertaken using the atmospheric fixed bed reactor can be found in Figure 7-5 and Figure 7-6 respectively. The experimental conditions were similar to those used in the fluidized bed reactor except the steam and N_2 mixture was fed from the top of the reactor in this configuration. Once the reactor temperature and the gas concentrations were found to have stabilized, coal was dropped into the reactor. This configuration had the advantage of ensuring that the volatile matter passed through the OC bed. This was one of issues observed during the operation of the fluidized bed reactor whereby a large proportion of the volatile matter and coal gasification products did not contact the OC, as evidenced by the greater amounts of the unconverted gases CO, H_2 and CH_4 in Figure 7-2 relative to that in Figure 7-6.

It can be seen that both figures display a similar trend, but is significantly different from the results obtained using the fluidized bed reactor. Firstly, no H_2 was detected in the outlet gases using this setup unlike those obtained when the fluidized bed reactor was used. The reason for this is that all the generated gases had to pass through the OC. In a fluidized bed reactor, as the coal particle was fluidized and simultaneously gasified, some of the gaseous products were formed above the bed and hence did not contact the OC. Such behaviour does not occur in a fixed bed reactor and coupled with the fact that Fe_2O_3 has a higher selectivity and reactivity towards H_2 relative to CO, no H_2 was detected in the outlet gases.

The second difference is that the outlet concentrations of both CO and CH_4 are significantly lower in this setup. A 93.8% reduction in the peak CO concentration was obtained, while the peak value of CH_4 was reduced by 34.7%. An investigation by Adánez *et al.* [8] showed that ilmenite, an Fe-based OC, was most reactive with H_2, followed by CO and had the lowest reactivity when reacted with CH_4. This supports the current findings in which the concentration of CO was significantly reduced compared to that of CH_4 between the two configurations as the OC has a higher reactivity towards CO relative to CH_4.

Thirdly, the peak CO_2 concentration obtained using this reactor configuration increased by 151.1% relative that obtained using the fluidized bed reactor. Numerically, this increased from 4.87% to 12.23%. The reason behind this increase is due to the increased conversion of CO and CH_4 into CO_2.

The next difference lies in the CO_2 concentration profile. In the fluidized bed experiment, the distribution of the gases appears to be positively skewed, which means that the distribution is heavier to the left of the mean. While the gas concentration profile here is similar to that

obtained using the fluidized bed experiment, it is more positively skewed. There is also an obvious distinction with respect to the combustion of the volatiles relative to the combustion of the char gasification products. It can be seen here that the combustion of the volatiles occurs primarily in the first minute, as the level of CH_4 and CO_2 can be seen to drop after this period, due to the slower rate of char gasification.

The last difference lies in the time taken to completely combust the coal. Here, complete combustion was achieved at around the 600 second mark which is 14.3% slower compared to the time taken by the 10^{th} reduction using the fluidized bed reactor. This observation is to be expected as the reaction time in a fluidized bed reactor would be much shorter due to better mixing and contact between the fuel and the gasification agent.

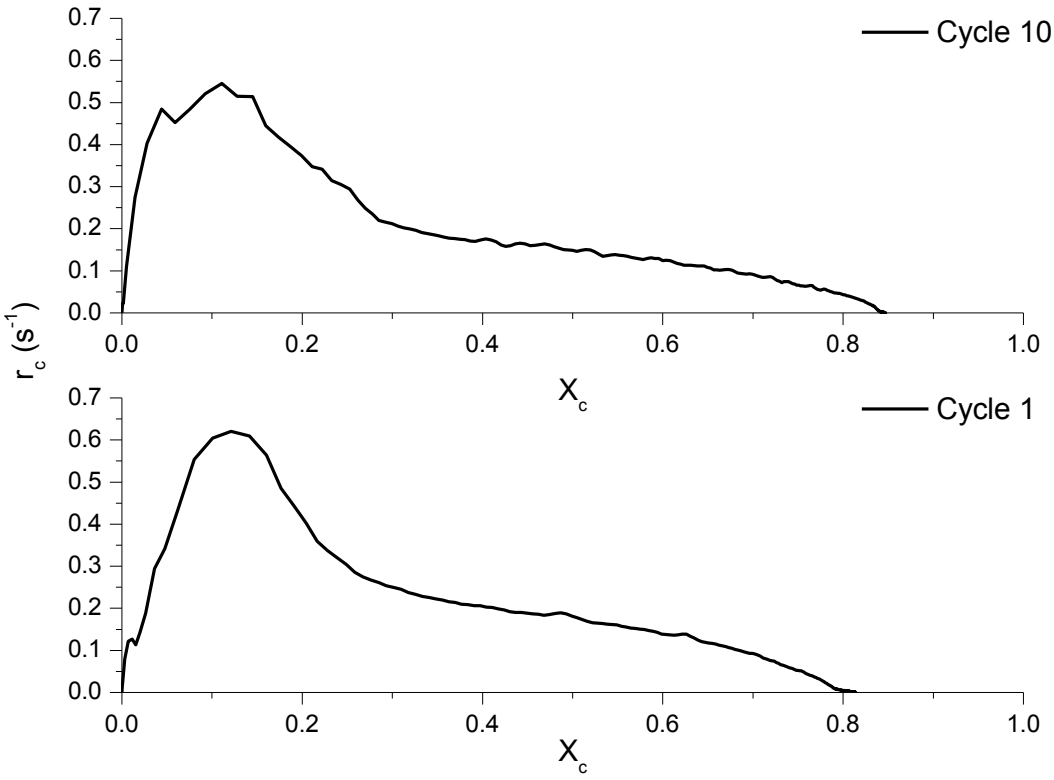

Figure 7-7 Carbon conversion rate as a function of carbon conversion for the first and tenth reduction reactions using the atmospheric fixed bed reactor

Figure 7-7 shows the carbon conversion rate as a function of carbon conversion for the first and tenth reduction reactions and it can be seen that these two profiles are similar with a few minor differences. The peak value appears to have dropped slightly going from the first to the tenth reduction reaction. At the tenth reduction reaction, it can be seen that the carbon conversion rate during the initial reaction stage rose faster compared to that in the first

reduction reaction. Additionally, the extent of carbon conversion appears to be higher in the tenth cycle when compared to that of the first cycle. When comparing this to

Figure 7-4, the main difference lies in the peak value of r_c, which is approximately 50% higher here compared to that obtained using the fluidized bed reactor. The reason behind this is due to the improved contact between the combustible gases and the OC. The proof for this statement is the significantly reduced levels of incompletely combusted gases such as CO, CH_4 and H_2 in the atmospheric fixed bed reactor relative to that obtained using the fluidized bed reactor.

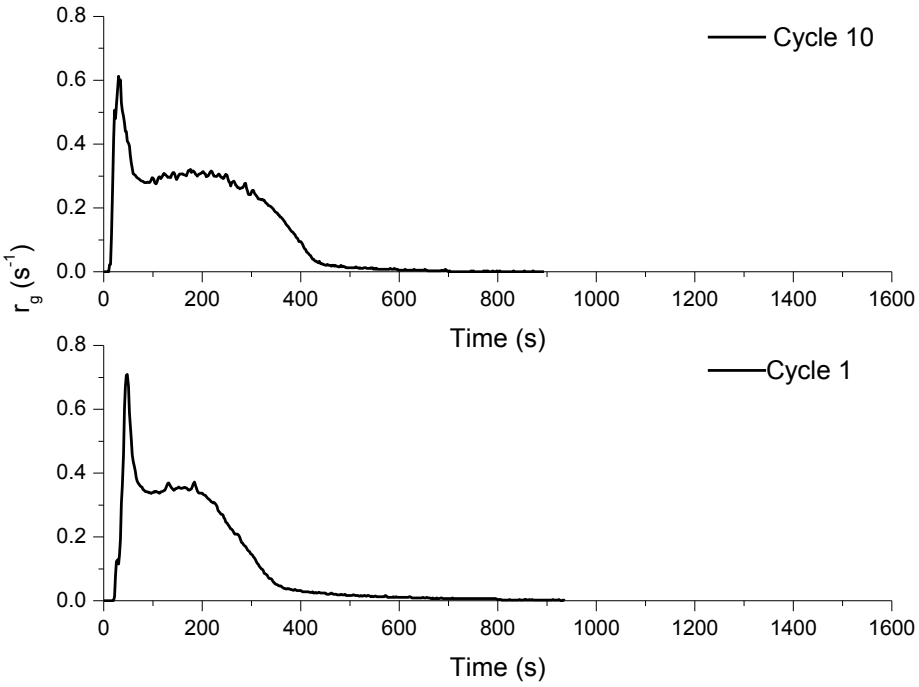

Figure 7-8 Gasification rate as a function of time for the first and tenth reduction reactions using the atmospheric fixed bed reactor

The plot of the gasification rate as a function of time for the first and tenth reduction reactions in the atmospheric fixed bed reactor can be found in Figure 7-8. Once again, it can be observed that the time required for complete fuel conversion is higher using this configuration relative to using the fluidized bed reactor. This profile is similar to the CO_2 concentration profile with the presence of a sharp initial peak corresponding to the conversion of the volatiles. Going from the first to the tenth reduction reaction, there is a slight reduction in the peak gasification rate accompanied by a broadening of the curve, which signifies a greater extent of gasification of the fuel. On the other hand, the reduction times are similar for both the first and tenth reactions.

7.4 Pressurized Fixed Bed Results

The outlet gas concentration profiles, carbon conversion and gasification rate obtained using the pressurized fixed bed reactor operated at 5 bar will be discussed in this section.

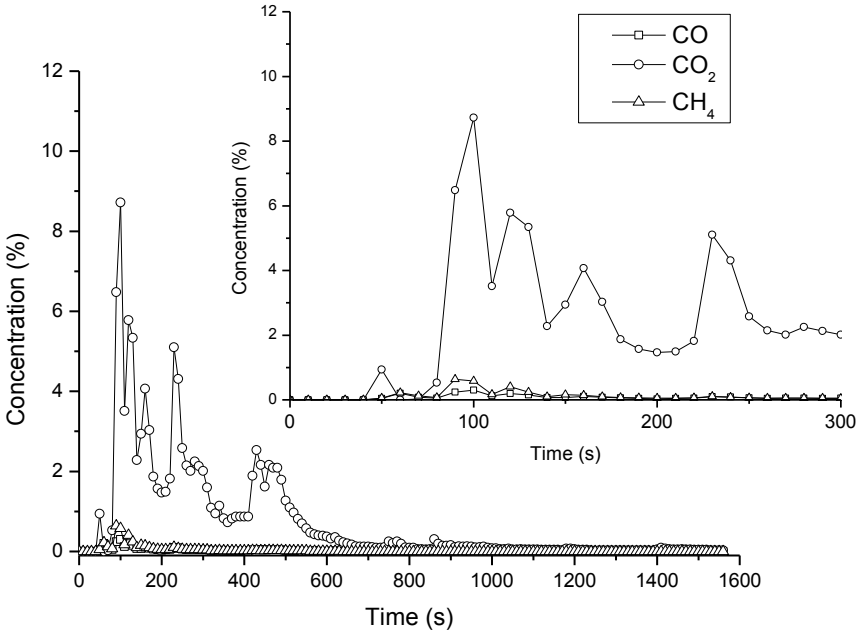

Figure 7-9 Outlet gas concentration profiles of the first reduction reaction using the pressurized fixed bed reactor

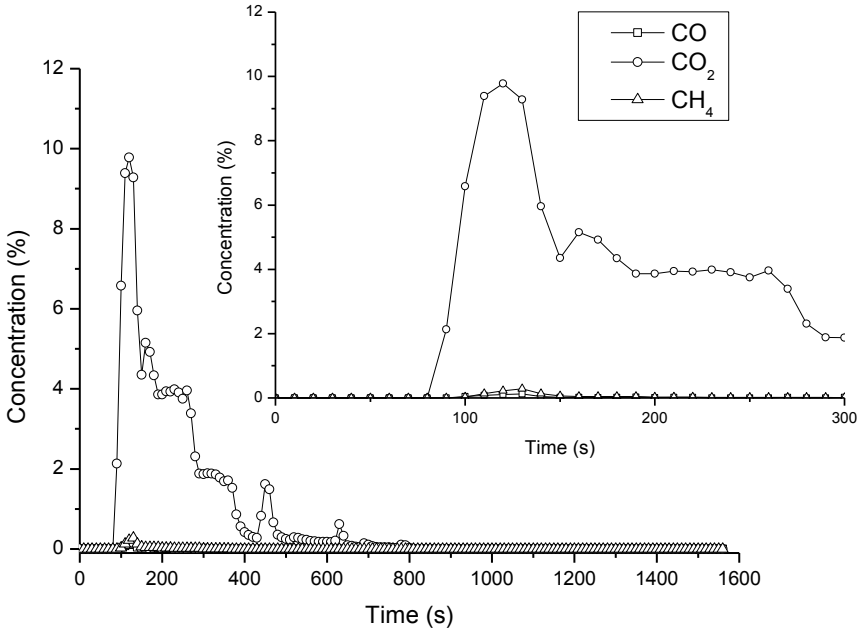

Figure 7-10 Outlet gas concentration profiles of the tenth reduction reaction using the pressurized fixed bed reactor

The outlet gas concentration profiles for the first and tenth reduction reactions in the pressurized fixed bed setup can be found in Figure 7-9 and Figure 7-10 respectively. Again, no H_2 was detected in this setup, similar to that found using the atmospheric fixed bed reactor. The first noticeable difference compared to the previous two setups is that the first concentration reading occurs around the 50 to 70 second mark for the first and tenth reduction reactions respectively. This is significantly higher compared to the 10 to 20 seconds time frame observed using the other two reactor configurations and this phenomenon can be attributed to the longer residence time of the gases in the reactor. Moreover, Chen *et al.* [9] found that at a higher pressure, the evolution of gases were delayed due to the suppression of the coal devolatilization rate.

Secondly, the CO_2 concentration profile shown in Figure 7-9 appears unstable compared to that shown in Figure 7-10. This was due to pressure variation in the reactor, which was caused by the generation of gases from the gasification and combustion of the fuel. As mentioned in the experimental summary section of this chapter, as the pressure increased during the reaction, the downstream pressure regulator was opened to release the pressure build-up. The pressure variation in this setup was between 4.5-6 bar. Each peak represents the point at which the regulator was opened to relieve the pressure.

With regards to the other carbonaceous gases, CO and CH_4, there was an observable amount in the first reduction reaction but this almost completely disappeared in the tenth reduction reaction. Comparatively, the amounts measured using this configuration were much lesser relative to that obtained using the earlier two configurations. This reason behind this observation is a function of the increased residence time and higher concentration of the combustible gases around the OC; these conditions are more favourable for the conversion of the OC as the latter reduces the gas phase diffusional resistance.

The other major difference lies is the time taken for the fuel to be completely consumed. This value ranged from around 1500 seconds in the first reduction reaction to around 825 seconds in the tenth reduction reaction. This is slower than that obtained when using the atmospheric fixed bed reactor and even more so when compared to when the fluidized bed reactor was used; this is due to the higher pressure in the reactor, which led to an increased in the residence time of the gases.

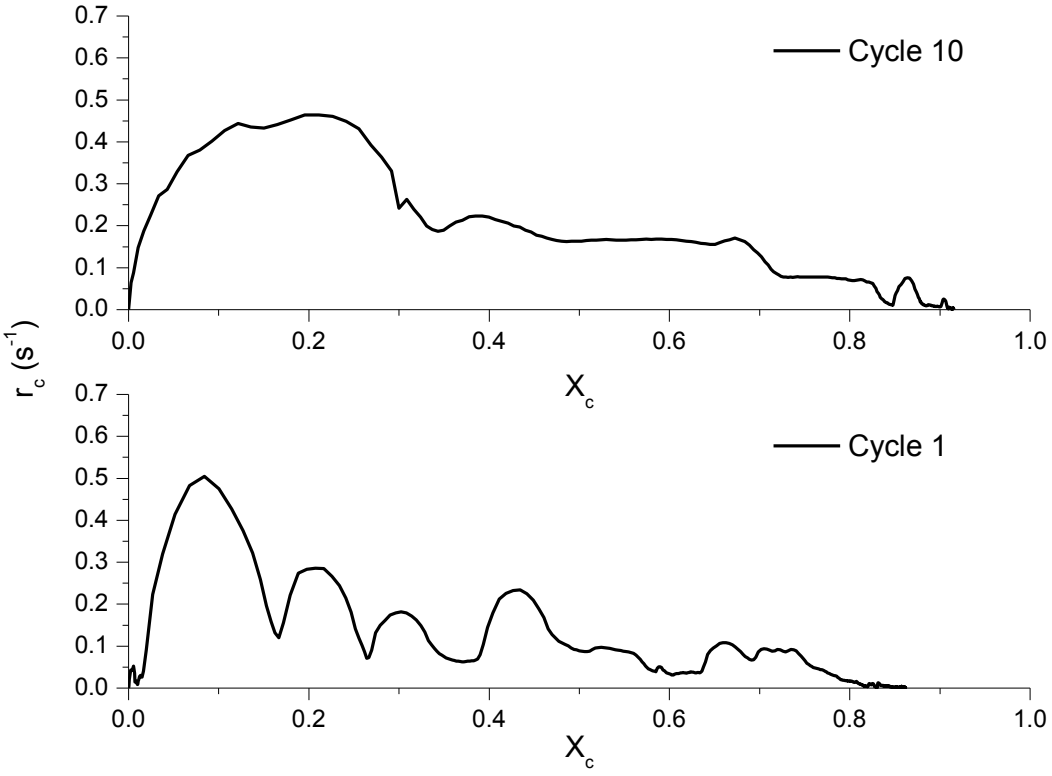

Figure 7-11 Carbon conversion rate as a function of carbon conversion for the first and tenth reduction reactions using the pressurized fixed bed reactor

The plot of the carbon conversion rate against the carbon conversion for the first and tenth reduction reactions undertaken using this reactor configuration can be found in Figure 7-11. The peak carbon conversion rate is higher than that obtained when using the fluidized bed reactor setup but still lower than that obtained through the use of the atmospheric fixed bed reactor. The other difference lies is the higher extent of carbon conversion observed here relative to when the other two reactor configurations were. A study by Xiao *et al.* [4] using a bituminous coal concluded that higher residence times and steam pressures led to an increase in char gasification reactivity. Furthermore, Roberts and Harris [10] investigated the effect of pressure on char gasification and found that there was a positive correlation between pressure and the gasification rate. The authors ascribed this to the increasing level of surface complexes formed on the char particle with increasing pressures.

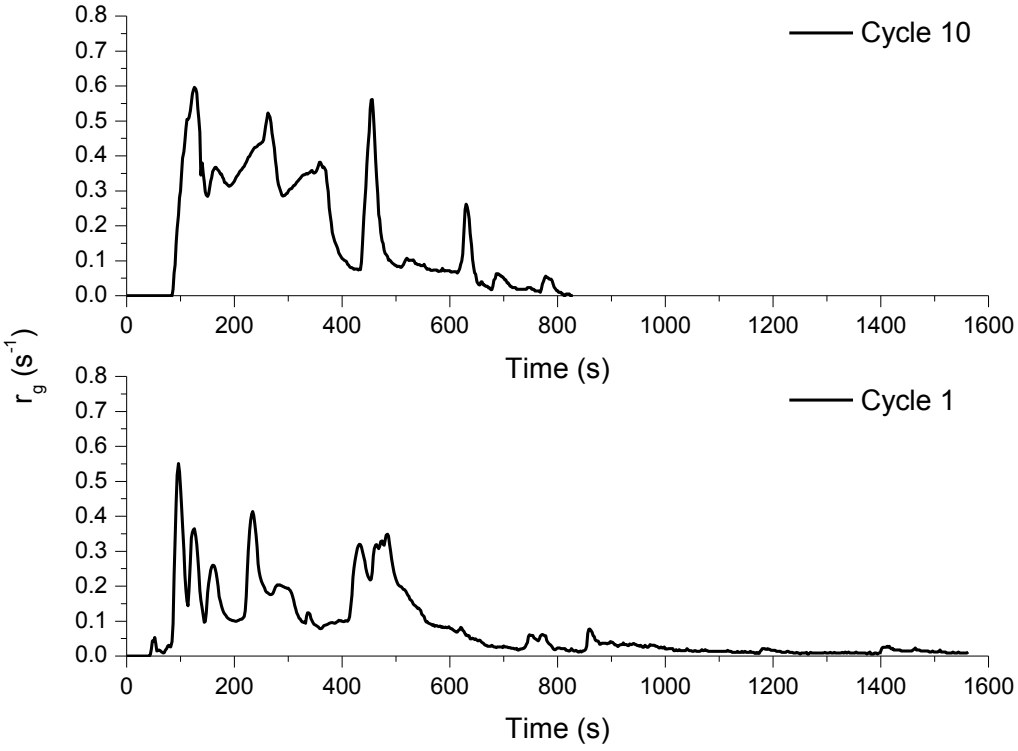

Figure 7-12 Gasification rate as a function of time for the first and tenth reduction reactions using the pressurized fixed bed reactor

Figure 7-12 shows a plot of the gasification rate as a function of time for the first and tenth reduction reaction and it can be seen that there are many peaks here similar to the obtained CO_2 profiles; this has been explained to be due to the use of the pressure regulator to maintain a pressure of 5 bar. The peak gasification rate at the tenth reduction reaction is comparable to that obtained when using the atmospheric fixed bed reactor. Additionally, the average gasification rate from the operation of the atmospheric fixed bed reactor is lower compared to the value obtained here using the pressurized fixed bed reactor.

The next section will aim to objectively compare the three reactor configurations to highlight the advantages and disadvantages of each of the setups.

7.5 Comparison Study

Two of the main criteria used to judge the performance of a CLC system is the carbon conversion and the CO_2 yield. Since the OC and the experimental conditions used in this study are the same between the three reactors, is it therefore valid to use the aforementioned parameters to gauge the relative performance of the different setups. Additionally, the outlet gas fractions from the three reactor configurations will also be discussed.

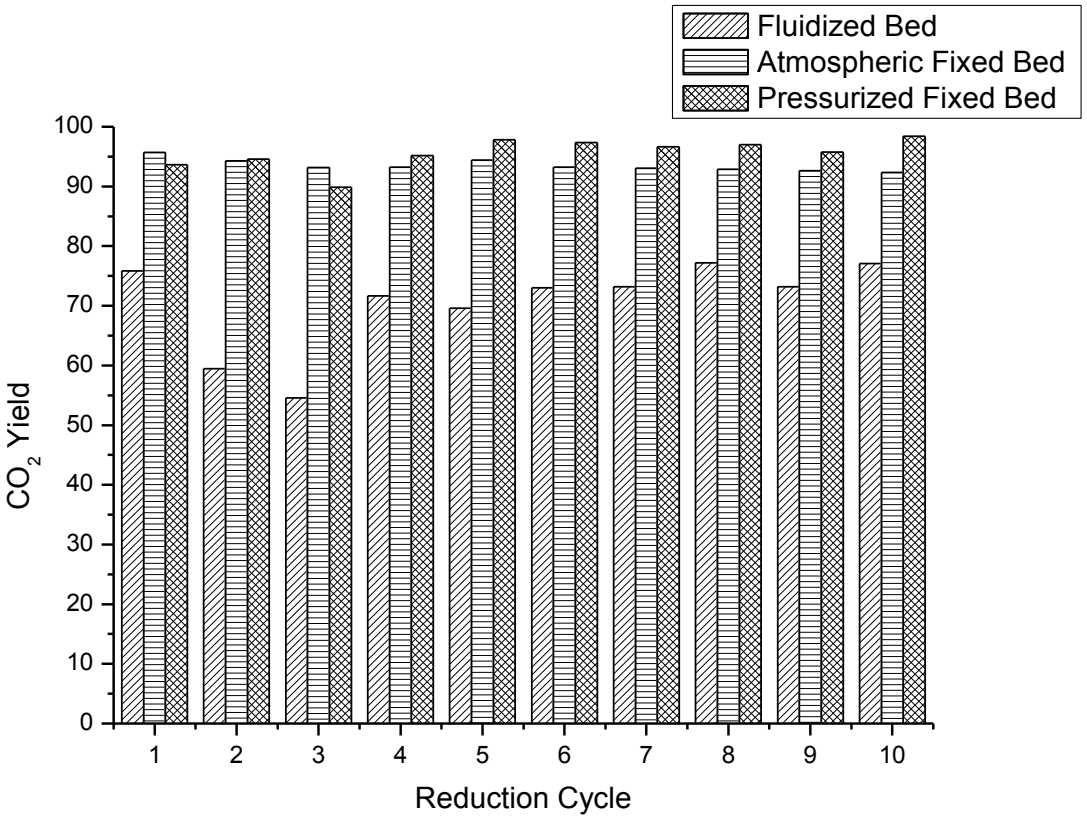

Figure 7-13 CO_2 yield over ten reduction reactions for the three investigated reactor configurations

Figure 7-13 depicts the variation in the CO_2 yield over the course of the ten reduction reactions using the three reactor configurations. The general trend that can be observed from this figure is that the CO_2 yield is the lowest with the fluidized bed configuration and highest when the pressurized fixed bed reactor was used. Secondly, there is also a general increasing trend in these values with increasing redox cycles and this is attributed to the changes in the OC's structure over the multiple redox reactions. Cuadrat *et al*. [11] found that the OC in their study, ilmenite, underwent activation; this resulted in an increased in its reactivity, which they attributed to the changes in its morphology. This translates to more CO and CH_4 being converted into CO_2 on account of the increase in the OC's reactivity. Focussing on the last five cycles, where the CO_2 yield had stabilized, the average values are 74.74%, 92.83% and 97.03% for the fluidized, atmospheric and pressurized reactor configurations. This represents approximately an increase of 18 and 22 percentage points going from the fluidized bed reactor to the atmospheric and pressurized fixed bed reactors respectively. The reason for this increased CO_2 yield is because all of the combustible gases that were generated in the fixed bed reactor configurations were able to pass through the OC bed, ensuring that more gases had the opportunity to be oxidized by the OC. This was not the case when the fluidized

bed reactor was used as some of the char particles would have been gasified above the OC bed and these gasification intermediates would not have come into contact with the OC, reducing the CO_2 yield.

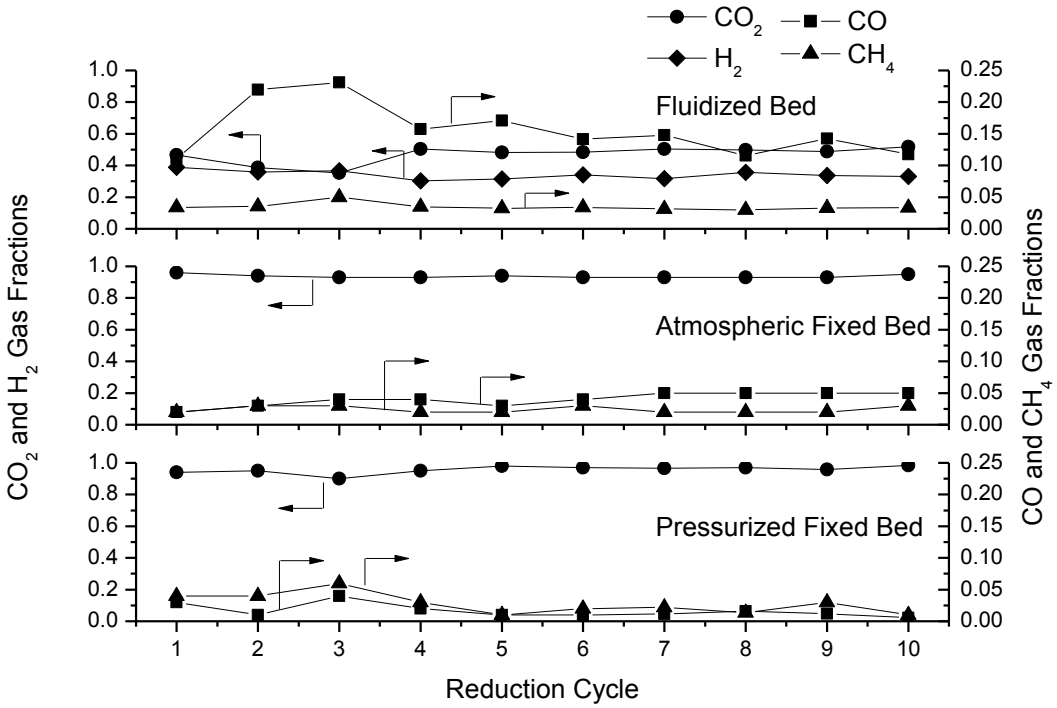

Figure 7-14 Outlet gas fractions over ten reduction reactions for the three investigated reactor configurations

To complement Figure 7-13, Figure 7-14 was constructed and this shows the fraction of the outlet gases for the different reactor configurations over ten reduction reactions. Since this figure is in terms of fractions, the evolved H_2 was also included when calculating the fractions of the outlet gases from the fluidized bed reactor. Stable operation was observed from the sixth cycle onwards for all three cases. Analysing the results obtained using the fluidized bed reactor, there appears to be a decrease of around 50% in the concentration of CO between the first few cycles and the last few cycles. As expected, this was accompanied by an increase in the CO_2 concentration. The concentrations of CH_4 and H_2 were relatively unchanged from the start to the end. With respect to CH_4, this was possibly due to an almost constant amount of volatile matter escaping the reactor as soon as the coal was dropped into the reactor, which prevented it from coming in contact with the OC. The high and almost constant concentration of H_2 was due to the high levels of steam present, which generated H_2 through the WGSR.

With respect to the operation of the atmospheric fixed bed reactor, a slight decrease in the CO_2 fraction is observed with progressive cycles but this was found to stabilize at around the sixth cycle as previously mentioned. On the other hand, using the pressurized fixed bed reactor resulted in a slight increase in the CO_2 fraction accompanied by reductions in both CO and CH_4. The absence of H_2 using both of these configurations proves that the reactivity of Fe_2O_3 is indeed higher with H_2 relative to CO. The CO_2 fraction in the atmospheric fixed bed configuration ranged between 0.93-0.95 and this increased to 0.95-0.99 in the pressurized fixed bed reactor. A similar finding was reported by Zhang *et al.* [6] whereby they found that the concentrations of CO and CH_4 decreased with increasing pressures, highlighting the beneficial effect of pressure in the CLC process. The explanation for this has been mentioned above whereby a higher pressure leads to longer residence times and higher concentrations of combustible gases around the OC particle, which in turn causes an increase in the conversion of the gasification intermediates. Additionally, another possible explanation for this observation is due to the differences in the structure and morphology of the OCs that were used in the three reactor configurations and this will be discussed in the following subsections.

Based on calculations which were performed, the residence times of the gases through the OC bed material are 0.2 s, 0.3 s and 1.1 s for the atmospheric fixed bed, fluidized bed and pressurized fluidized bed reactors respectively. Although the residence time of the gases through the OC bed in the fluidized bed reactor is larger than that in the fixed bed reactor, the reason the CO_2 fraction from the operation of the fluidized bed reactor is the lowest relative to the other two fixed bed reactor setups is due to the lack of contact between the combustible gases and the OC.

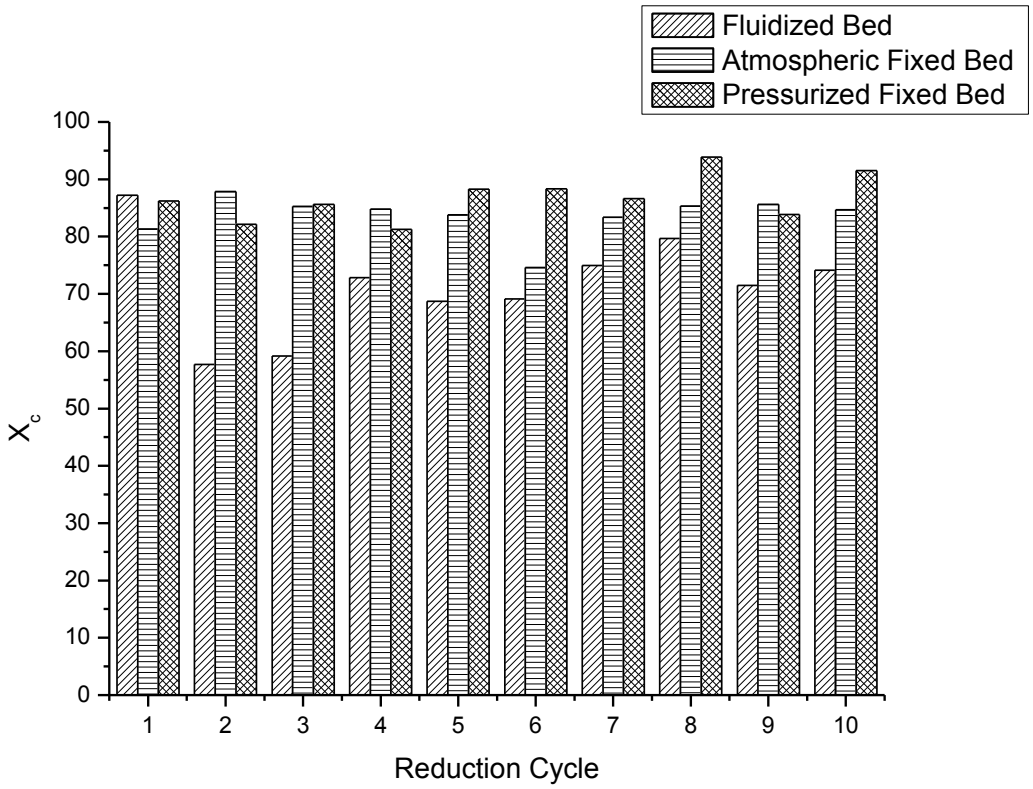

Figure 7-15 Carbon conversion over ten reduction reactions for the three investigated reactor configurations

A plot of the carbon conversion over the ten reduction reactions can be found in Figure 7-15. While there is a variation in these values over the ten redox cycles, the general trend follows the CO_2 yield results shown in Figure 7-13 whereby the lowest carbon conversion is obtained using the fluidized bed reactor, with a subsequent increase when using the atmospheric fixed bed reactor and is highest when the pressurized fluidized bed reactor was used. Focussing on the average values of the last five cycles, the carbon conversions are 73.88%, 82.72% and 88.84% for the fluidized bed, atmospheric fixed bed and pressurized fluidized bed reactors respectively. The lowest value, as obtained when using the fluidized bed reactor, is due to the elutriation of the fines generated through the attrition and shrinkage of the coal particles over the course of the reaction.

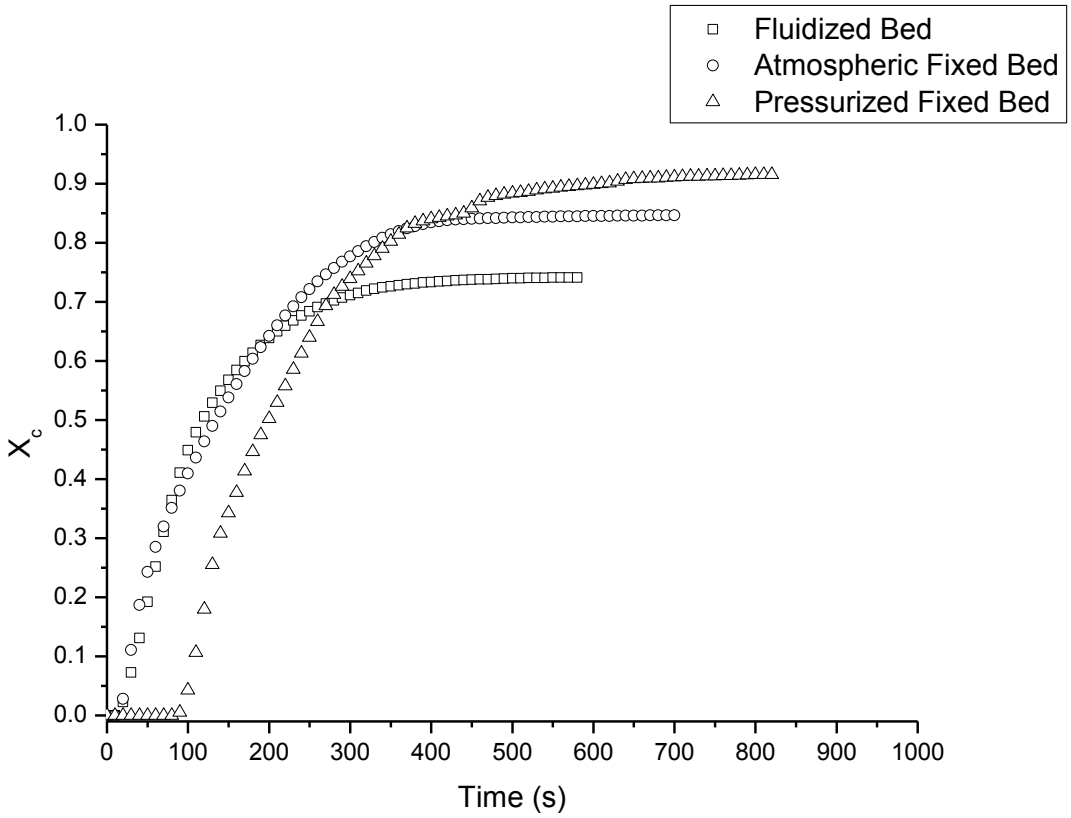

Figure 7-16 Carbon conversion as a function of time during the tenth reduction reaction for the three investigated reactor configurations

To further explain the differences in the carbon conversion of the fuel in the different setups, a plot of the carbon conversion as a function of time at the tenth reduction reaction was generated and can be found in Figure 7-16. Here, the time taken for complete reaction can be clearly seen, with the fastest time obtained when the fluidized bed reactor was used followed by the atmospheric and pressurized fixed bed reactors. Analysing the pressurized fixed bed reactor results, there is approximately a 100 second lag between when the fuel was fed and the generated gases were detected. This proves that the combustion of the volatiles and char gasification products is improved at higher pressures due to an increase in the residence time. Discounting the lag, the time taken to complete the reaction using both the atmospheric and pressurized fixed bed reactors is similar with the exception of a seven percentage point increase in the carbon conversion when using the latter. Another observable feature is that the carbon conversion rate for the first 100 s is similar for three reactor configurations; this is due to the volatiles that were evolved during the initial stages of the reaction.

Practically, this means that the contact between the volatile matter and the OC is very important to ensure improved CO_2 yields for coals with high volatile matter, such as VBC.

As can be clearly seen, the time for complete conversion of the fuel is much lower in a fluidized bed reactor and this is an important engineering design consideration as a shorter gasification time would mean that more coal can be fed into a given reactor volume, translating to an increase in the power output.

7.6 Characterization

The fresh and used OC samples from the termination of the tenth reduction reaction were analysed using SEM, EDS, XRD and ASAP to characterize the particles. This was done to understand the structural, chemical and morphological changes that the OC had underwent and how these affected the obtained results using the three different setups.

7.6.1 Scanning Electron Microscope (SEM)

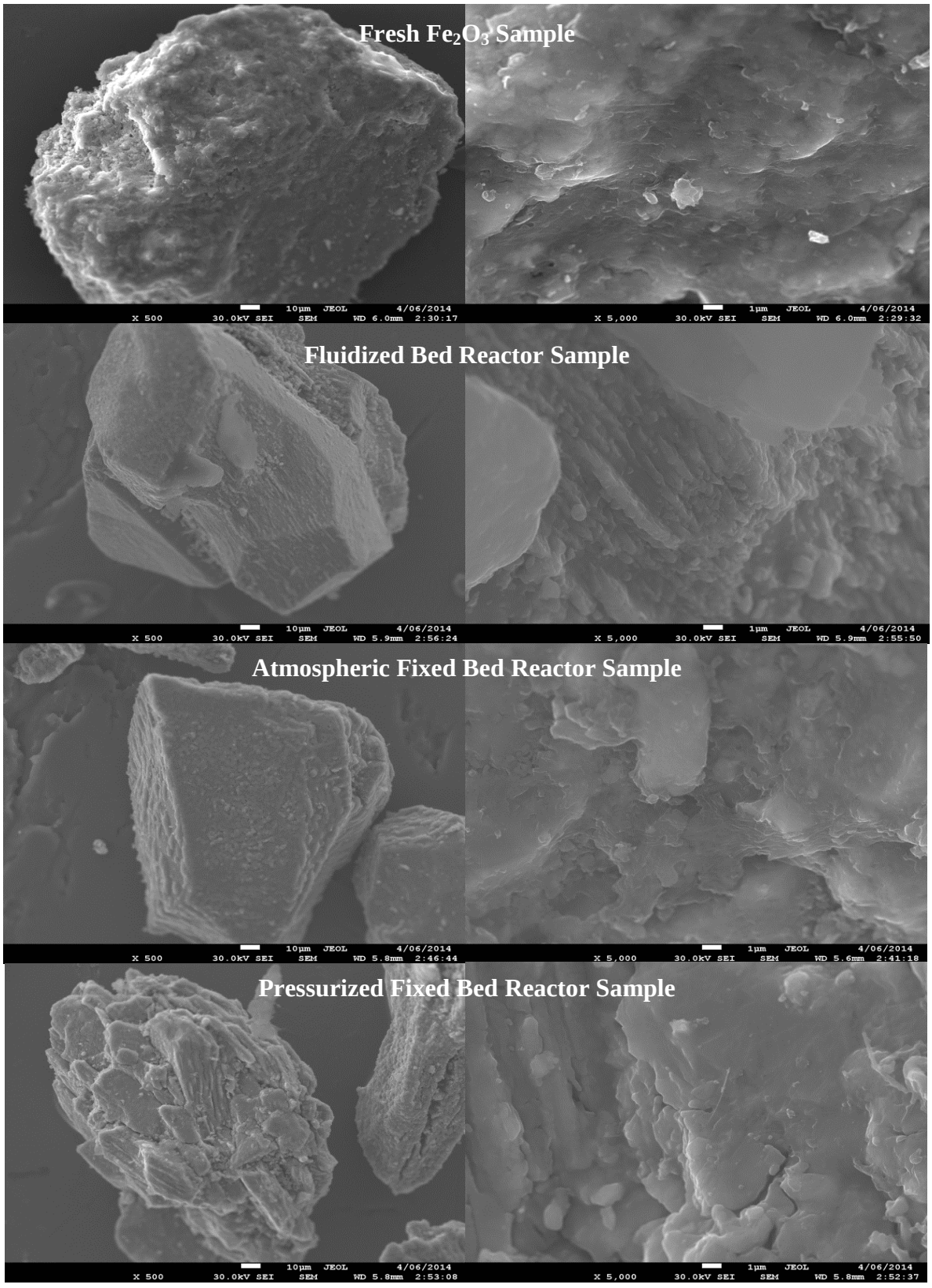

Figure 7-17 Micrographs of the fresh and used OC samples at lower (LHS) and higher magnifications (RHS)

Figure 7-17 shows the SEM images taken of the fresh and used samples at two different magnification levels. The images on the left hand side were taken at a lower magnification of 500X while the ones on the right were obtained at a higher magnification of 5000X. The fresh sample can be seen to have a rough appearance with a high degree of irregularities. In contrast, the used samples appear to have a smoother surface. All of the used samples appear to have undergone grain coalescence due to thermal and chemical stresses over the ten redox cycles. This process inevitably results in the lowering of the surface area of the OC and will be discussed in the subsections to follow. The term coalescence is used here as agglomeration and excessive sintering is not expected of Fe_2O_3 at the experimental temperatures used in this study, even when localized heating during the oxidation reaction is taken into account. Additionally, an investigation by Thaler *et al.* [12] showed that the presence of SiO_2 in Fe_2O_3 could aid in increasing the latter's thermal stability and mechanical strength while increasing its porosity. The presence of SiO_2 in the CVRD ore would have improved the aforementioned properties in this OC. From a practical application point of view, the use of Fe_2O_3 in a CLC system is beneficial as its exceptional thermal stability would allow for higher temperatures to be used in the reactor, resulting in an increased inlet temperature to the turbine yielding higher efficiencies. Although all of the used samples experienced grain coalescence, the degree of coalescence of the samples varied depending on which reactor configuration was used. The OC that was used in the fluidized bed reactor appears to have smaller grains on its surface compared to the OCs from both the fixed bed reactor configurations. This could be due to the fact that since the carbon conversion and CO_2 yield were the lowest when the fluidized bed reactor was used, the extent of reduction and oxidation of the OC would have been lower. The OCs that were used in the fluidized bed reactor appear to have experienced a small degree of attrition and this was evident from the presence of fragmented particles as observed in some of the other micrographs. Comparing the samples that were used in the atmospheric and pressurized fixed bed reactors, one major difference is observable whereby the samples from the latter appear to have developed cracks. This is most likely due to the effect of pressure on the samples coupled with increased thermal and chemical stresses over the ten redox cycles. While fragmentation may not be a big issue in a fixed bed reactor, excessive fragmentation could lead to channelling of these fragments through the distributor; these would then need to be replaced, incurring OC make-up costs.

7.6.2 Energy Dispersive X-ray Spectroscope (EDS)

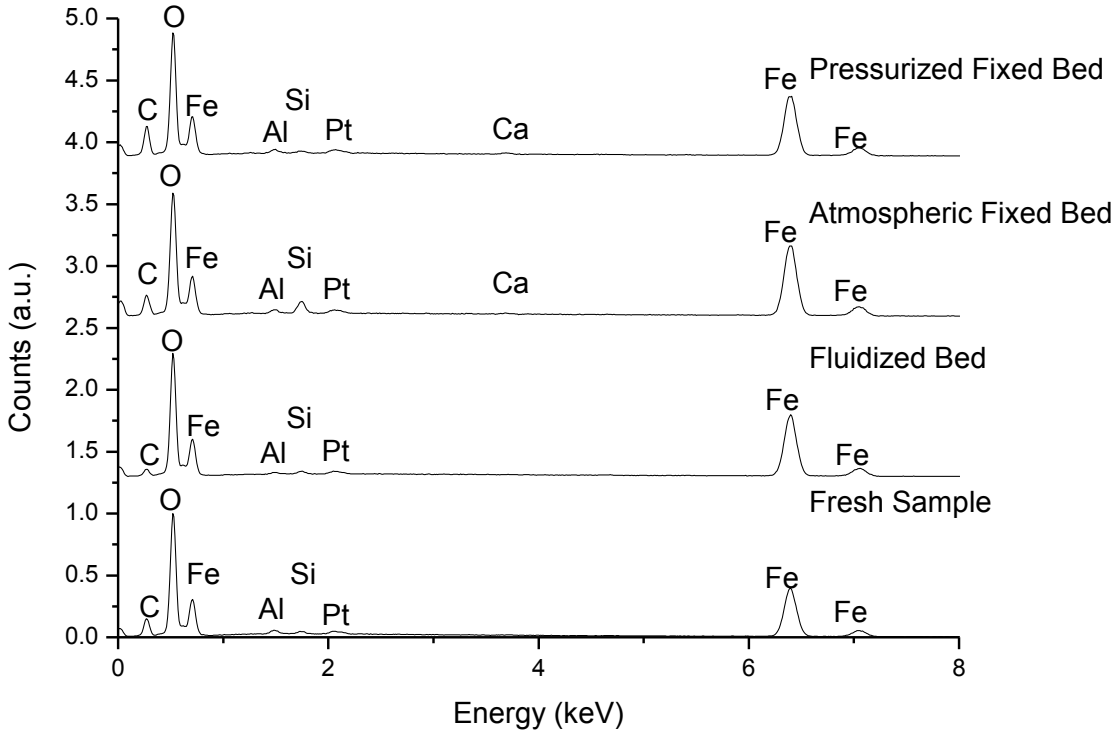

Figure 7-18 Energy dispersive X-ray spectra of the fresh and used samples

Figure 7-18 shows the energy dispersive X-ray spectra obtained for the OCs used in the three different reactor configurations. This figure shows the representative elemental composition on the surface of the OC particles. Firstly, the major elements that were identified were C, Fe, Al, Si and Ca. The presence of carbon is due to both the carbon tape that was used as well as char and this will be discussed towards the end of this section. The next three elements are predominantly from the OC, while the last, Ca, is from the ash of the coal. The amount of carbon in the fresh sample was approximated to be the baseline amount as it would have only contained carbon from the carbon tape. Based on the amount of carbon on the OC sample that was used in the fluidized bed reactor, it can be seen that it is slightly lower than the baseline value but within instrumental errors. The OC samples that were used in the atmospheric and pressurized fixed bed reactors appear to have a higher level of carbon compared to the baseline value; this disparity is due to the amount of residual carbon at the end of the reaction. Since the OC samples were analysed after the tenth reduction reaction, without having been oxidized, residual carbon due to incomplete gasification of the fuel remained in the reactor. This was not the case with the fluidized bed reactor as most, if not all, of the remaining

carbon would have elutriated out of the reactor. Since coal is highly heterogeneous, a fraction of it may have been highly resistant to gasification; as such, it would have had a very long residence time in both the fixed bed reactors. Depending on the oxidation state of Fe in the OC, this could lead to the formation of iron carbide (Fe_3C), which is very brittle [13]; this would then lead to the formation of cracks over multiple redox cycles. Therefore, the cracks that were observed on the surface of the OCs that were used in the pressurized fixed bed reactor could be due to the aforementioned reason.

The next observable difference comes from the presence of Ca on the OC samples that were used in both the fixed bed reactors. Typically, in a fluidized bed reactor, the generated ash compounds would be elutriated out of the reactor on account of its small particle size. Therefore, the separation of the ash compounds from the OCs that are used in fixed bed reactors would be a significant issue. If left unseparated, these would lead to the build-up of ash in the OC bed as well as propagate the formation of inert and unreactive compounds with the OC, which should be avoided at all costs. Since Yallourn coal has a low ash content, with a large proportion being iron, other compounds were not observed in the energy dispersive X-ray spectra. Even with such a low amount of Ca, totalling 7.5 mg over the ten redox cycles, it was detected by the EDS. As Ca has a low melting point, this would pose operational issues, particularly in the fixed bed reactor configurations as it may melt over the OC particles and form agglomerates; this would affect the reactivity of the OC, while also increasing the operating costs. The presence of SiO_2 and Al_2O_3 in the OC is not expected to be an issue as thermodynamic simulations performed by Siriwardane *et al.* [14] has shown that there are negligible interactions between these two compounds and Fe_2O_3.

7.6.3 X-ray Diffraction (XRD)

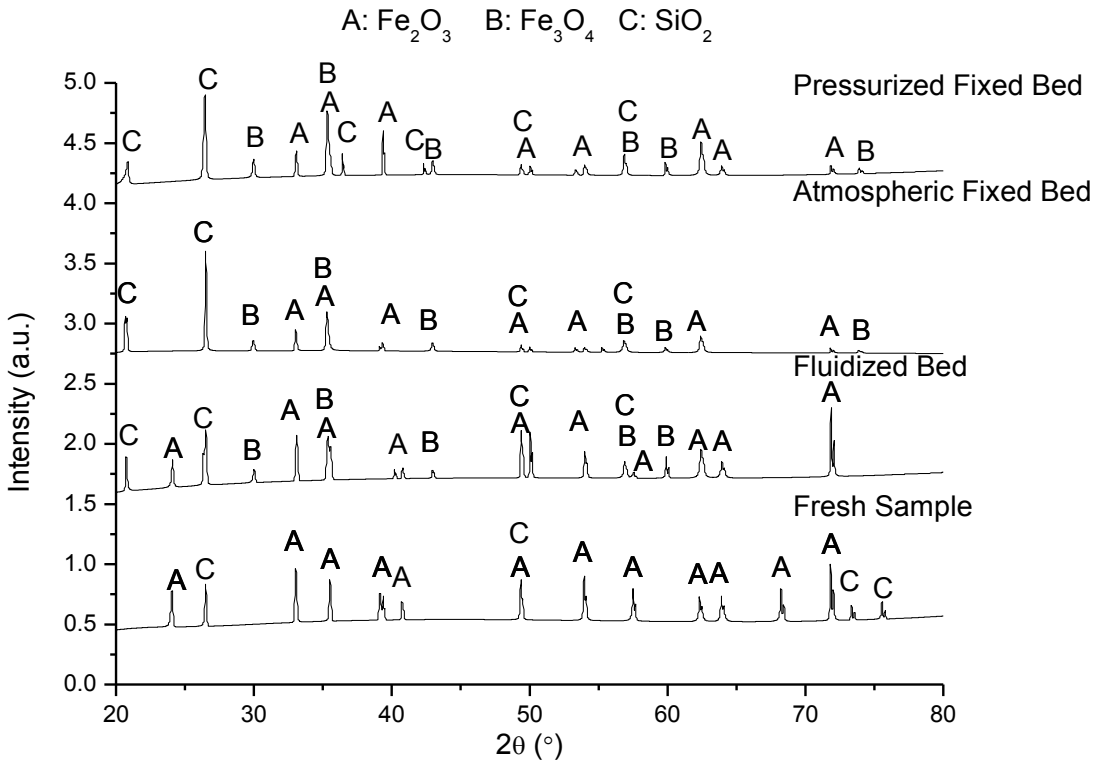

Figure 7-19 Diffractograms of the fresh and used samples

The diffractograms of the fresh and used samples can be found in Figure 7-19. The only crystalline compounds that were identified were Fe_2O_3, Fe_3O_4 and SiO_2. Since the amount of Al in the OC sample was very low, it was not identified by the XRD unit but it was detected through the use of the EDS. It can be seen here that the fresh sample consisted only of Fe_2O_3 and SiO_2 while the all of the used samples contained a mixture of the three phases. The main observable feature from this figure is that the OC sample that was used in the fluidized bed reactor had much higher intensities for the reflections of Fe_2O_3, while the OC samples that were used in both the fixed bed reactors had lower amounts of Fe_2O_3 with higher intensities for Fe_3O_4. These findings support the low CO_2 yield obtained when the fluidized bed reactor was used.

7.6.4 Accelerated Surface Area and Porosimetry (ASAP)

Table 7-1 Pore structure analysis results for the fresh and used OC samples

OC sample	BET surface area (m^2/g)	Cumulative pore volume (cm^3/g)
Fresh	6.2073	0.00469
Fluidized bed reactor	0.8408	0.00134
Atmospheric fixed bed reactor	0.5902	0.00006
Pressurized fixed bed reactor	0.6815	0.00095

The pore structure analysis which includes the BET surface area and cumulative pore volume can be found in Table 7-1. From the BET surface area, it can be seen that the fresh CVRD particles have a much higher surface area compared to the used particles. This is in line with the findings obtained using the SEM, whereby grain coalescence was observed to have occurred in all of the used particles irrespective of the reactor configuration that was used. Comparing the results obtained for the used OC particles, the sample from the fluidized bed reactor appears to have the highest BET surface area and cumulative pore volume, followed by the OCs that were used in the pressurized and atmospheric fixed bed reactors. As previously mentioned, the OC samples that were used in the fluidized bed reactor did not appear to have undergone significant grain coalescence on account of the lower extent of reduction and oxidation that the OC experienced. The higher surface area of the OC sample that was used in the pressurized fixed bed reactor is likely due to the formation of cracks, which would invariably lead to an increase in the surface area. Comparing the OC samples that were used in the atmospheric and pressurized fixed bed reactors, the OCs that were used in the latter had a higher surface area and pore volume. This could also be part of the reason as to why the CO_2 yield was higher when the pressurized fixed bed reactor was used relative to when the atmospheric fixed bed reactor was used. These results are in accordance with the findings of Xiao *et al.* [15]; the authors proposed that the elevated pressure may have positively impacted the OC's morphology, leading to increased reactivity and improved results.

7.7 Final Comments

Based on the aforementioned information and discussion, it can be seen that the fluidized bed reactor is the favourable configuration, relative to both the fixed bed reactors, with respect to reaction kinetics as the gasification rate of the fuel was enhanced due to increased contact with the gasification agent. This is a very important aspect, as it is been shown that the rate limiting step in the CLC process is that of coal gasification and not the reaction with the OC. While it is noted that the carbon conversion and CO_2 yield were not exceptionally good when the fluidized bed reactor was used, it is expected that the use of the same fuel and OC in a circulating fluidized bed (CFB) reactor would improve said values. Additionally, Ca was found on the surface of the OCs that were used in both of the fixed bed reactors, which poses a significant issue from an operational perspective. Hence, such a configuration should be avoided, particularly with fuels containing high amounts of low melting point ash compounds.

Comparing the results obtained here with those obtained by Zhang *et al.* [6] and Xiao *et al.* [4, 5] using a bituminous Chinese coal in both atmospheric and pressurized fixed bed reactors, a few differences come to light even after taking into account the slightly higher steam concentration that was used in their studies. Firstly, the time taken to completely convert the same amount of Xuzhou coal in the presence of the same OC at the tenth reduction reaction is between 65-70 minutes with the shorter time obtained using the pressurized unit. When Yallourn coal was used, this value ranged from 11-14 minutes, keeping in mind the lower steam concentration used here. Secondly, the reported carbon conversions using the Xuzhou coal are lower and ranged between 73-87%, with the higher values obtained using the pressurized unit operated at 5 bar; in this study, these values were between 81-91%.

This highlights that low rank coals such as VBC are better suited for use in CLC on account of its higher reactivity.

7.8 Conclusions

The effect of reactor configuration on the performance of CLC was investigated. Three different configurations were examined including a fluidized bed reactor, atmospheric fixed bed reactor and a pressurized fixed bed reactor operated at 5 bar. Steam was used as the gasification agent with N_2 as a diluent. Coal totalling 0.4 g was used together with 40 g of the Fe-based OC. The particle size range of the coal and OC were 600-1000 µm and 90-180 µm respectively. The amount of fuel and OC used was kept constant in all of the investigations. A total of ten redox reactions were completed using each of the reactor configurations. The

product gas compositions, CO_2 yields and carbon conversions were then obtained and compared. The OC particles were characterized using SEM, EDS, XRD and ASAP. The following are the main conclusions from this study:

1. The best performance in terms of the CO_2 yield and carbon conversion was obtained using the pressurized fixed bed reactor followed by the atmospheric fixed bed unit and lastly the fluidized bed reactor. The average CO_2 yields from the last five cycles were found to be 74.74%, 92.83% and 97.03% for the fluidized bed reactor, atmospheric fixed bed reactor and pressurized fixed bed reactors respectively. The carbon conversions were found to be 73.88% followed by 82.72% and 88.84% for the same reactor order as above.

2. A larger amount of fuel was found to elutriate out of the fluidized bed reactor, as evidenced by the accumulation of char in the particulate trap, which led to a reduction in the carbon conversion. The CO_2 yield was also low as a large amount of the volatiles and a sizeable amount of the coal gasification products did not come into contact with the OC. This was not the case with both of the fixed bed reactors as all the generated gases passed through the OC bed, resulting in excellent CO_2 yields and carbon conversion efficiencies. The issue that was faced when using this fluidized bed reactor can be solved by having a longer expanded freeboard together with cyclones and a carbon stripper.

3. The SEM images showed differences in the morphologies of the OCs that were used in each of the three setups. The samples that were used in the both of the fixed bed reactors experienced a greater degree of grain coalescence. Also, the OC samples there were used in the pressurized fixed bed reactor were found to develop cracks. Additionally, EDS analyses showed that the OCs that were used in both of the fixed bed reactors had Ca on their surface due to ash deposition but this was not detected on the OCs that were used in the fluidized bed reactor; this was due to the elutriation of the ash particles out of the reactor as well as lower residence time of the ash particles around the OC. Based on the diffractogram intensities, the OC samples that were used in the pressurized fixed bed reactor experienced the greatest extent of reduction followed by the samples that were used in the atmospheric fixed bed reactor and fluidized bed reactor. ASAP analysis showed that the fresh sample had the highest BET surface area followed by the used samples and this was due to grain coalescence.

4. Comparing the results from this study with a study that was done using a bituminous coal under similar conditions, it is evident that VBC is the stronger candidate due to its high reactivity and low ash content. The former results in quicker gasification of the fuel while the latter reduces the amount of interaction between the ash and the OC.

5. Fluidized bed reactors are favourable for use in CLC as they provide improved contact between the solids and the gases, resulting in shorter reaction times. Practically, this means that for a given desired electrical output, a smaller reactor can be designed using the fluidized bed reactor configuration. Also, the use of a CFB reactor is expected to generate significantly improved results over those obtained using a fluidized bed reactor.

This chapter showed that although the CO_2 yield and carbon conversion efficiency obtained using the fluidized bed reactor was lower relative to those obtained using the atmospheric and pressurized fixed bed reactors, it had the shortest reaction time due to better contact between the fuel and the gasification agent. It is expected that the use of a CFB reactor alongside a longer expanded freeboard, cyclones and a carbon stripper, would yield significantly improved results.

7.9 References

1. Leion, H., T. Mattisson, and A. Lyngfelt, *Use of Ores and Industrial Products As Oxygen Carriers in Chemical-Looping Combustion.* Energy & Fuels, 2009. **23**: p. 2307-2315.
2. Teyssie, G., H. Leion, G.L. Schwebel, A. Lyngfelt, and T. Mattisson, *Influence of Lime Addition to Ilmenite in Chemical-Looping Combustion (CLC) with Solid Fuels.* Energy & Fuels, 2011. **25**(8): p. 3843-3853.
3. Gao, Z.P., L.H. Shen, J. Xiao, C.J. Qing, and Q.L. Song, *Use of Coal as Fuel for Chemical-Looping Combustion with Ni-Based Oxygen Carrier.* Industrial & Engineering Chemistry Research, 2008. **47**(23): p. 9279-9287.
4. Xiao, R., Q.L. Song, M. Song, Z.J. Lu, S.A. Zhang, and L.H. Shen, *Pressurized chemical-looping combustion of coal with an iron ore-based oxygen carrier.* Combustion and Flame, 2010. **157**(6): p. 1140-1153.
5. Xiao, R., Q.L. Song, S.A. Zhang, W.G. Zheng, and Y.C. Yang, *Pressurized Chemical-Looping Combustion of Chinese Bituminous Coal: Cyclic Performance and Characterization of Iron Ore-Based Oxygen Carrier.* Energy & Fuels, 2010. **24**: p. 1449-1463.
6. Zhang, S., C. Saha, Y.C. Yang, S. Bhattacharya, and R. Xiao, *Use of Fe2O3-Containing Industrial Wastes As the Oxygen Carrier for Chemical-Looping Combustion of Coal: Effects of Pressure and Cycles.* Energy & Fuels, 2011. **25**(10): p. 4357-4366.
7. Abad, A., J. Adanez, F. Garcia-Labiano, L.F. de Diego, P. Gayan, and J. Celaya, *Mapping of the range of operational conditions for Cu-, Fe-, and Ni-based oxygen carriers in chemical-looping combustion.* Chemical Engineering Science, 2007. **62**(1-2): p. 533-549.
8. Adanez, J., A. Cuadrat, A. Abad, P. Gayan, L.F. de Diego, and F. Garcia-Labiano, *Ilmenite Activation during Consecutive Redox Cycles in Chemical-Looping Combustion.* Energy & Fuels, 2010. **24**: p. 1402-1413.
9. Chen, H., Z. Luo, H. Yang, F. Ju, and S. Zhang, *Pressurized pyrolysis and gasification of Chinese typical coal samples.* Energy & Fuels, 2008. **22**(2): p. 1136-1141.
10. Roberts, D. and D. Harris, *A kinetic analysis of coal char gasification reactions at high pressures.* Energy & fuels, 2006. **20**(6): p. 2314-2320.
11. Cuadrat, A., A. Abad, J. Adánez, L.F. de Diego, F. García-Labiano, and P. Gayán, *Behavior of ilmenite as oxygen carrier in chemical-looping combustion.* Fuel Processing Technology, 2012. **94**(1): p. 101-112.
12. Thaler, M., V. Hacker, M. Anilkumar, J. Albering, J. Besenhard, H. Schröttner, and M. Schmied, *Investigations of cycle behaviour of the contact mass in the RESC process for hydrogen production.* International journal of hydrogen energy, 2006. **31**(14): p. 2025-2031.
13. McMahon Jr, C. and M. Cohen, *Initiation of cleavage in polycrystalline iron.* Acta Metallurgica, 1965. **13**(6): p. 591-604.
14. Siriwardane, R., H.J. Tian, G. Richards, T. Simonyi, and J. Poston, *Chemical-Looping Combustion of Coal with Metal Oxide Oxygen Carriers.* Energy & Fuels, 2009. **23**(8): p. 3885-3892.
15. Xiao, R., L.Y. Chen, C. Saha, S. Zhang, and S. Bhattacharya, *Pressurized chemical-looping combustion of coal using an iron ore as oxygen carrier in a pilot-scale unit.* International Journal of Greenhouse Gas Control, 2012. **10**: p. 363-373.

Chapter 8 Performance of Synthetic Oxygen Carriers

One of the main research focuses in recent times is the fabrication of highly reactive OCs for use in CLC. This is being actively pursued as most of the reported results in literature show that the experimental outlet CO_2 concentration has not reached its thermodynamic equilibrium concentration, with differences of up to 40 percentage points [1]. Hence, many researchers [2-5] are focussing their efforts to synthetically generated highly reactive OCs. To date, there have been numerous publications on supporting metal oxides such as Fe_2O_3, CuO, Mn_2O_3 and NiO on inert materials such as SiO_2 [6, 7], TiO_2 [8, 9], Al_2O_3 [10, 11] and ZrO_2 [12, 13]. The purpose of such investigations is to generate OCs with improved reactivity and mechanical strength. While synthetic OCs have shown promise, the issue lies in the fact that a larger quantity of these synthetic OCs will be required as the active metal oxide content is lower in such OCs when compared to unsupported OCs. Up until now, there has been very limited research into the use of bimetallic OCs with solid fuels. Johansson *et al.* [14] found that the use of a small amount of NiO, 3 wt%, in Fe_2O_3 resulted in significant reductions in the outlet concentration of CH_4. Therefore, this chapter will build on this concept of synergy between two metal oxides by supporting NiO, CuO and Mn_2O_3 on Fe_2O_3. Here, Fe_2O_3 will function as an active support by providing better dispersion for the secondary metal oxides on itself while also contributing as an OC.

This chapter will investigate the potential synergistic effect of bimetallic OCs on improving the reactivity of Fe_2O_3. The impact of the bimetallic OC preparation method will also be investigated.

8.1 Experimental Conditions

Synthetic OCs were fabricated using both mechanical mixing and wet impregnation. The mass fractions of the secondary metal oxides (NiO, CuO and Mn_2O_3) were 5, 10 and 20 wt% with the balance comprising Fe_2O_3. The samples are denoted by the preparation method, followed by the loading of the secondary metal oxide and terminated with the primary metal oxide. The sample I-20Mn-Fe represents an OC having 20 wt% of Mn_2O_3 impregnated onto Fe_2O_3.

Firstly, the samples were investigated using a TGA. OC to fuel ratios of 60, 40 and 20 were investigated with a total gas flow rate of 60 mL/min comprising 10 mL/min of CO_2 and balance N_2. The mass of the OC was maintained at 900 mg, while the mass of the coal sample

was varied depending on the desired OC to coal ratio. The experiments were performed at temperatures of 800°C, 850°C and 900°C. The purpose of these experiments was to perform a sensitivity analysis on the OC's reactivity as a function of the amount of fuel, temperature and loading content of the secondary metal oxide.

Next, the OCs were used in a bench scale fluidized bed reactor as shown in Section 3.2.2 of Chapter 3. 50 g of sand was introduced into the reactor followed by 60 g of the synthetic OC. The experiments were conducted at 900°C and the reactor was fluidized with 6 L/min of 20 v/v% CO_2 with balance N_2. Once the temperature set point was reached, 0.6 g of Yallourn coal was added into the reactor. The outlet gases were measured using the online gas analyser described in Section 3.3.1 of Chapter 3. Once the gas concentrations returned to their baseline values, the CO_2 gas stream was changed to air to oxidize the OC. Upon completion of the oxidation reaction, the next reduction reaction was initiated in the presence of CO_2; a total of ten redox cycles were performed and the run was terminated at the end of the tenth reduction.

The samples were characterized using a Scanning Electron Microscope (SEM), an Energy Dispersive X-ray Spectroscope (EDS), X-ray Diffraction (XRD) and Accelerated Surface Area and Porosimetry (ASAP) unit to study the changes in the structure and morphology of the used OC relative to the fresh OC.

8.2 TGA Experiments

Preliminary tests were first conducted using the TGA to study the effect of the OC to fuel ratio as well as the effect of the type and loading content of the secondary metal oxide.

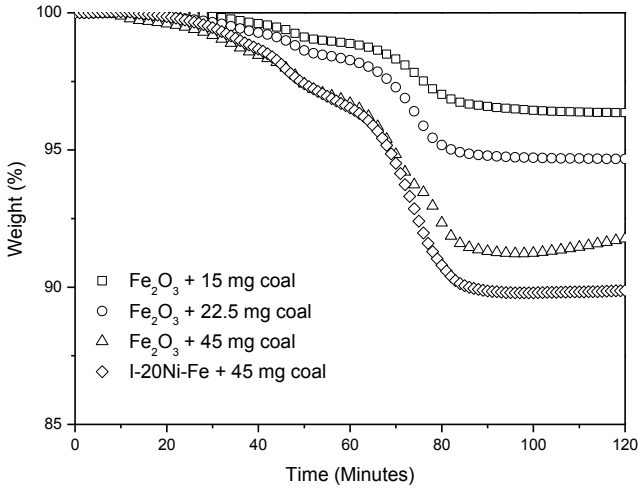

Figure 8-1 Effect of OC to coal ratio on the weight loss

Using Fe_2O_3 as the OC, it can be seen that the final weight loss increased with increasing mass of the coal. It should be noted here that the Fe_2O_3 used in this study was also subjected to the same processes experienced by the synthetic OCs to ensure that all of the OCs had undergone the same chemical and physical treatment. The increasing weight loss trend can be ascribed to two characteristics. Firstly, the increasing weight loss is due to the increasing amount of coal used in the experiments, which upon gasification would result in an increase in the weight loss. Secondly, with a higher amount of fuel present, the OC was reduced to a greater extent as it oxidized the combustible gases, resulting in a greater weight loss as observed. In essence, this means that a smaller OC to coal ratio would result in a greater reduction of the OC. When the mass of the coal sample was either 15 or 22.5 mg, both weight loss curves were similar wherein the weight loss reached a maximum and remained stable thereafter. However, this was not the case for the test which used 45 mg of coal as this sample was found to experience a weight gain after the weight loss curve had reached a maximum; the reason for this has been detailed in Chapter 5 and is due to oxidation of FeO to Fe_3O_4 by CO_2.

As mentioned in Chapter 5, the reduction of Fe_2O_3 beyond Fe_3O_4 is unfavourable. This is due to thermodynamic limitations which reduce the equilibrium concentration of CO_2 when Fe_2O_3 is reduced beyond Fe_3O_4. Additionally, reducing Fe_2O_3 beyond Fe_3O_4 could lead to the deposition of carbon in environments with high CO_2 residence times. Therefore, the equation below shows the reaction between Yallourn coal and Fe_2O_3 using CO_2 as gasification agent and only considering the reduction of Fe_2O_3 to Fe_3O_4.

$$CH_{0.782}O_{0.257} + 6.402\ Fe_2O_3 + xCO_2 \rightarrow 4.268\ Fe_3O_4 + (1+x)\ CO_2 + 0.391\ H_2O \qquad 8.1$$

Using Fe_2O_3, 15 mg of Yallourn coal would reduce about 910 mg of Fe_2O_3 to Fe_3O_4. Therefore, a coal mass that is higher than 15 mg would further reduce Fe_3O_4 to a lower oxidation state such as FeO or even metallic Fe, depending on the exact amount of fuel. Here, even when 22.5 mg of coal was used, the OC was not reduced beyond Fe_3O_4. The only time the OC was reduced beyond Fe_3O_4 was when 45 mg of coal was used. The reason behind this is that the above equation assumes that all of the introduced fuel reacts with the OC. Two occurrences disprove this assumption. Firstly, a large proportion of the fuel, in the form of volatile matter, does not react with the OC as the temperature is not sufficient for the reaction to proceed at an appreciable rate. Secondly, a small amount of the combustible gases do not come into contact with the OC and exits the TGA unreacted. Based on these two facts, the disproportionate weight loss of the OC can be explained. However, to avoid the reduction of

Fe_2O_3 beyond Fe_3O_4 in subsequent TGA based experiments in this study, an OC to coal ratio of 60 was adopted.

Figure 8-1 also shows the results obtained using the I-20Ni-Fe OC to allow for a comparison between the reactivity of this sample and the Fe_2O_3 OC. 45 mg of coal was used and the mass of the I-20Ni-Fe OC was the same as that of Fe_2O_3, i.e., 900 mg. Two main differences can be observed immediately. Firstly, the weight increase phenomenon was not observed when the I-20Ni-Fe sample was used, unlike when Fe_2O_3 was used. Also, a higher weight loss was obtained when the I-20Ni-Fe sample was used. These two observations indicate that the I-20Ni-Fe sample converted more fuel relative to when Fe_2O_3 was used, implying a higher outlet CO_2 concentration. One interesting feature here is that although the I-20Ni-Fe sample underwent a greater degree of reduction, more so then when the Fe_2O_3 sample was used, it did not experience any weight gain unlike that of the Fe_2O_3 sample. The reason for this is that the weight gain only occurs when Fe_2O_3 is reduced beyond Fe_3O_4 and the amount of available oxygen between these two oxidation states is 3.3%. Beyond this, it is reduced to FeO, which causes it to be oxidized by CO_2. With the I-20Ni-Fe sample, 20 wt% of the OC consisted of NiO; there is 21% O_2 available when reducing NiO to Ni. Therefore, although the oxygen carrying capacity of Fe_2O_3 is higher than NiO, the latter had more oxygen to give off compared to the 3.3% from the reduction of Fe_2O_3 to Fe_3O_4. It is for of this reason that the I-20Ni-Fe sample did not experience any weight gain. The lower weight loss of Fe_2O_3 relative to that observed using the I-20Ni-Fe OC is due to the low reactivity of the Fe_2O_3 sample towards the combustible gases. This preliminary study shows that the inclusion of a more reactive secondary metal oxide has the capability of increasing the conversion of the fuel on account of the increased reactivity of the bimetallic OC.

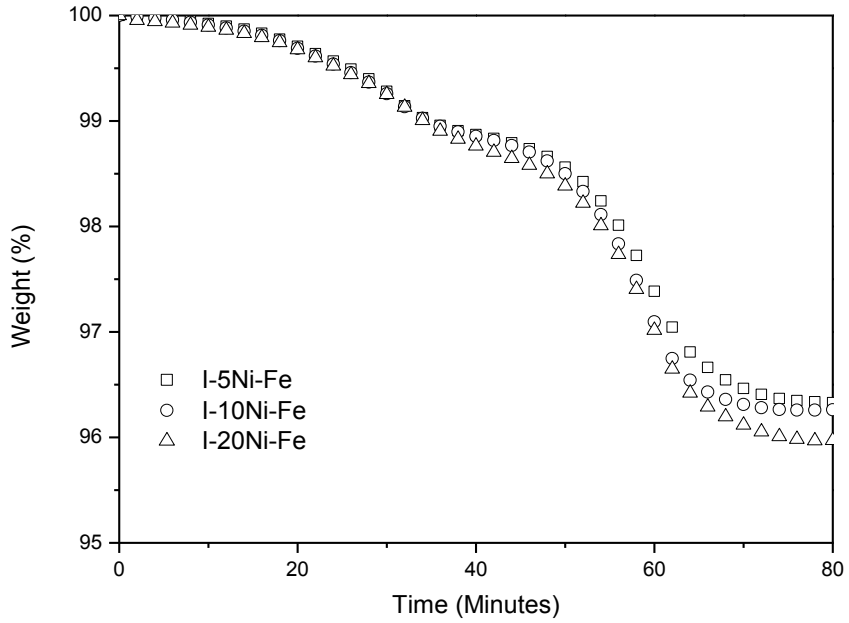

Figure 8-2 Effect of NiO content on the weight loss using the impregnated OCs

The effect of the NiO content on the reactivity of the bimetallic OC was investigated here. The impregnated Ni-Fe samples loaded with different amounts of NiO were investigated using 15 mg of Yallourn coal and the results are shown in Figure 8-2; as mentioned above, an OC to coal ratio of 60:1 was used. It can be seen that a higher weight loss was obtained when a higher amount of NiO was used in the I-Ni-Fe OCs. The weight readings of the TGA thermobalance changed from 96.4% when 5 wt% of NiO was used to a value of 96.0% with the use of the I-20Ni-Fe sample. Also, a greater extent of reduction was observed going from the I-10Ni-Fe sample to the I-20Ni-Fe sample. This is due to the higher reactivity of NiO relative to that of Fe_2O_3; as such, a greater amount of NiO would lead to a greater reduction of the OC as it is more reactive than Fe_2O_3 towards the combustible gases. Bhavsar and Veser [15] found that alloying a less reactive metal such as Fe with one that is more reactive such as Ni, can significantly improve the reactivity of the bimetallic OC.

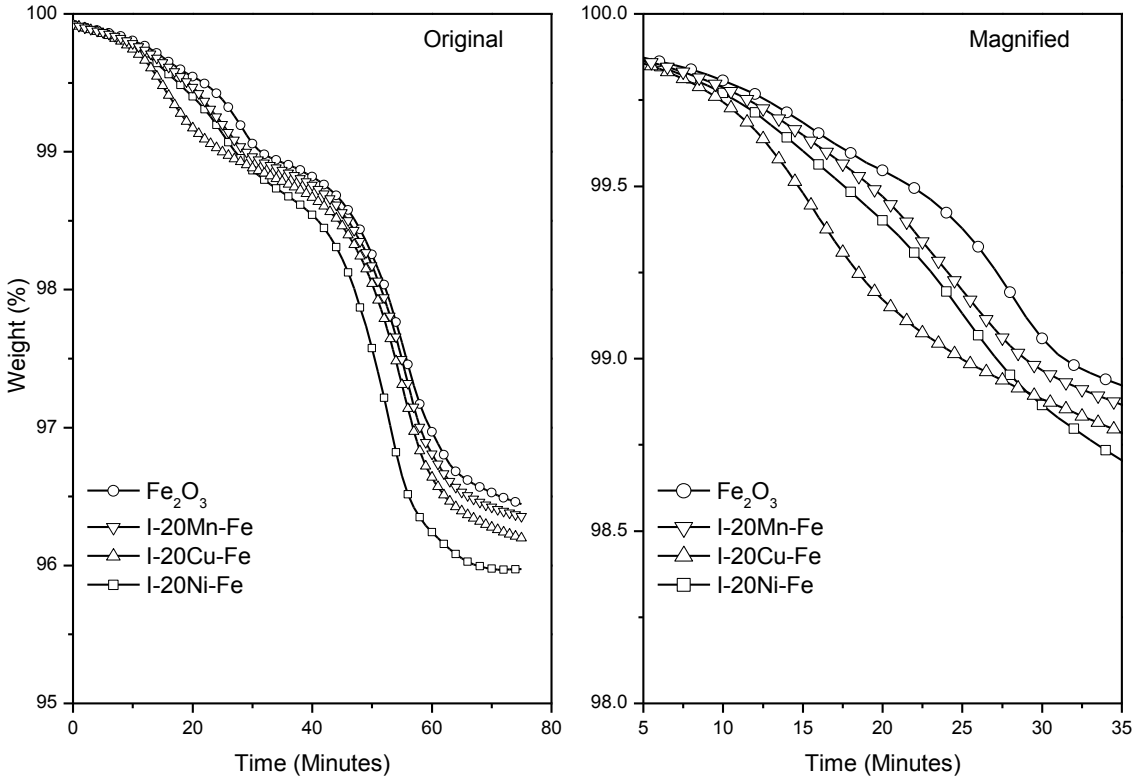

Figure 8-3 Effect of the impregnated secondary metal oxide species on the weight loss

The plot on the left hand side of Figure 8-3 shows the weight loss curves for iron oxide and the synthesized bimetallic impregnated OCs with 20 wt% of the three different secondary metal oxides. It is immediately noticeable that the final weight loss was significantly higher when the I-20Ni-Fe sample was used. As for the I-20-Cu-Fe and I-20Mn-Fe samples, these also displayed a greater final weight loss relative to the monometallic Fe_2O_3 OC; however, the improvement these two OCs exhibited was much lesser when compared to that displayed by the I-20Ni-Fe sample. The final weight loss of the OC and coal mixture in descending order is: I-20Ni-Fe, I-20Cu-Fe, I-20Mn-Fe and lastly Fe_2O_3. The reactivity of these four samples are consistent with the reactivity of the secondary metal oxide i.e., comparing the four, NiO has been shown to be the more reactive OC, followed by CuO, Mn_2O_3 and lastly Fe_2O_3. These results are in line with the findings of Zafar *et al.*[16] in which they found this same trend using these metal oxides supported on SiO_2 with CH_4 as the fuel.

In the magnified plot of Figure 8-3, an interesting phenomenon can be observed; the highest weight loss during the initial stages of the reaction was obtained using the I-20Cu-Fe sample. CuO is known to dissociate to Cu_2O accompanied by the release of oxygen in an environment with a low oxygen partial pressure, as it is here in an environment consisting of CO_2 and N_2

[17]. Although CuO exhibited the property of releasing gaseous oxygen, having been extensively applied in the Chemical Looping Oxygen Uncoupling (CLOU) process, it was expected that the relatively small amount of CuO would have reacted with Fe_2O_3 to form the $CuFe_2O_4$ solid solution, which has been identified and confirmed by other researchers [18]. Additionally, $CuFe_2O_4$ does not possess the ability to release gaseous oxygen unlike CuO. Therefore, it is deduced that there was an appreciable amount of free CuO in the OC matrix which allowed it to release its oxygen. This will be confirmed in the subsections to follow through the use of XRD, which enables the detection of crystalline phases on the OC.

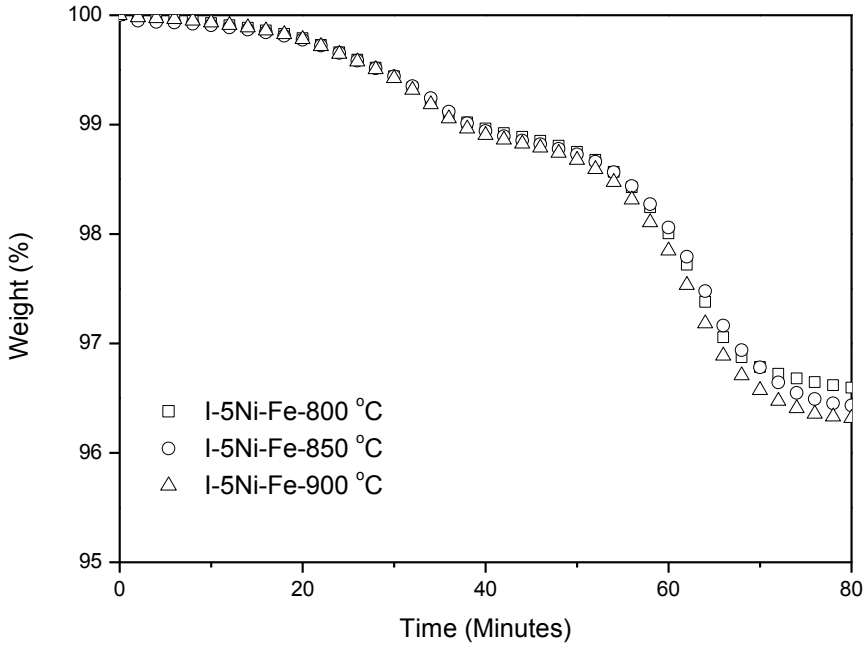

Figure 8-4 Effect of temperature on the weight loss using the I-5Ni-Fe OC

Figure 8-4 shows the results from a TGA study in which the effect of temperature was investigated using the I-5Ni-Fe OC. It can be seen that the operating temperature showed a positive effect on the reactivity of the OC towards the combustible gases derived from coal. A higher temperature was found to accelerate the reaction rate and resulted in a higher weight loss. The reason behind this observation is that at a higher temperature, the reaction kinetics between the combustible gases and the OC increases. This allows for more reactions to occur resulting in a smaller amount of unconverted combustible gases at the outlet of the TGA. This means that a higher temperature is beneficial not only from an experimental point of view, but also from a practical perspective as a higher reaction temperature would increase the energetic efficiency of the system. This is only true given that the mechanical, chemical and

structural integrity of the OC is not adversely affected by the increase in temperature, leading to the formation of agglomerates when the operating temperature is close to the melting point of the OC.

8.3 Bench Scale Fluidized Bed Reactor Results

Experiments were performed in a fluidized bed reactor to simulate the operation of a CLC system under practical operating conditions. In terms of reactor scale, this is the next step after small scale TGA work. Here, the factors influencing the reactivity and cyclic performance of the synthetic bimetallic OCs will be investigated.

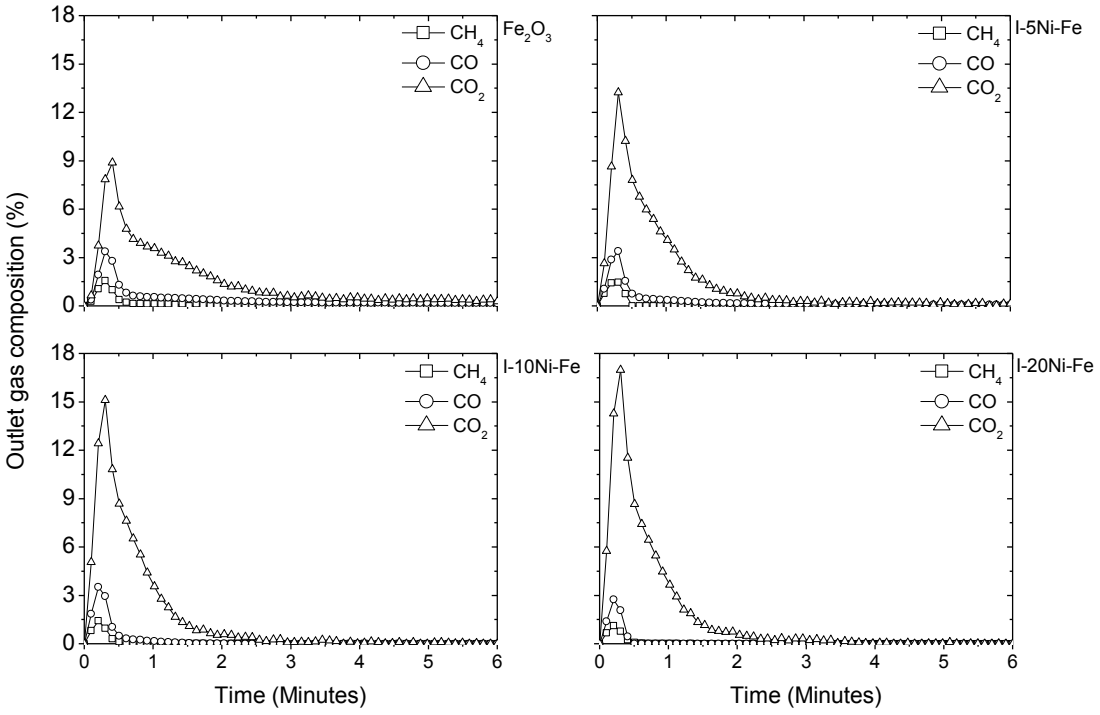

Figure 8-5 Outlet gas concentrations as a function of time obtained using the Fe_2O_3 and I-Ni-Fe OC samples

Figure 8-5 shows the outlet gas concentrations as a function of time for when the Fe_2O_3 and three I-Ni-Fe OC samples were used. The CO_2 concentration shown in this figure represents the CO_2 that was generated from the oxidation of the fuel pyrolysis and gasification products by the OC. It can be observed that all the gases exhibited the same trend, whereby there was a sharp initial increase in these concentrations followed by a slower decrease until the concentrations became zero. The initial CO_2 peak is due to the reaction between the OC and both the volatile matter and coal gasification products, albeit to a lesser extent with the latter.

The initial peaks of the combustible gases, CO and CH_4, are a result of the fast pyrolysis of VBC. As soon as the fuel was introduced into the reactor, the volatiles were quickly evolved due to the high temperature in the reactor; this resulted in a lack of contact between the combustible gases and the OC, as a portion of the volatile matter exited the reactor without contacting the OC. Practically, the incomplete combustion of the volatiles by the OC could be solved by changing the coal feeding position from the top of the reactor to a location in the OC bed, allowing for increased contact between the volatiles and the OC.

Comparing these four OCs in terms of the initial CO_2 peak shows that the presence of NiO in the bimetallic OC significantly enhances the peak CO_2 concentration. Additionally, the peak CO_2 concentration increased with increasing NiO loading contents, from a value of 8.89% obtained using the pure Fe_2O_3 to 16.99% when the I-20Ni-Fe sample was utilized. Also, a detectable amount of CO was observed at the outlet of the reactor after six minutes of reaction using Fe_2O_3, whereas negligible amounts of CO were detected when the I-Ni-Fe OC samples were used. These results confirm the synergistic effect of NiO on the reactivity of Fe_2O_3 and are consistent with the TGA results in Section 8.2.

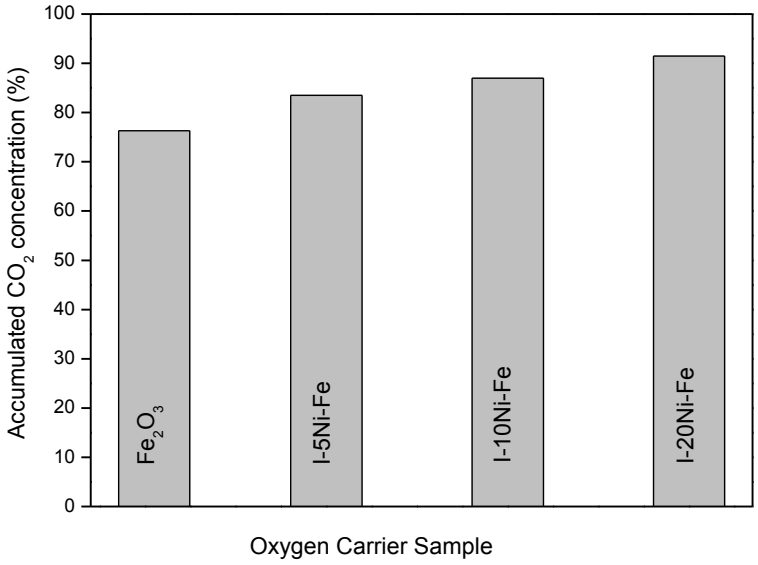

Figure 8-6 Average accumulated CO_2 concentration over five redox cycles obtained using the Fe_2O_3 and I-Ni-Fe OC samples

Figure 8-6 shows the accumulated CO_2 concentration produced from the reaction between the Yallourn coal and the four OCs; this is the averaged value over five consecutive redox reactions, which took a total of 75 minutes. It is clear that the higher the NiO content in the I-

Ni-Fe OC samples, the higher the accumulated concentration of CO_2; this concentration was found to increase from 83.5% when using the I-5Ni-Fe sample to 91.5% for when the I-20Ni-Fe sample was used. For comparison purposes, using the monometallic Fe_2O_3 OC yielded only 71.5% accumulated CO_2, which is much lower compared to the values obtained using the samples loaded with NiO. This represents an improvement of 12 and 20 percentage points in the accumulated CO_2 concentrations using the I-5Ni-Fe and I-20Ni-Fe samples respectively over Fe_2O_3. These results imply that significant enhancements in the reactivity of the synthetic OCs were achieved by impregnating NiO on Fe_2O_3.

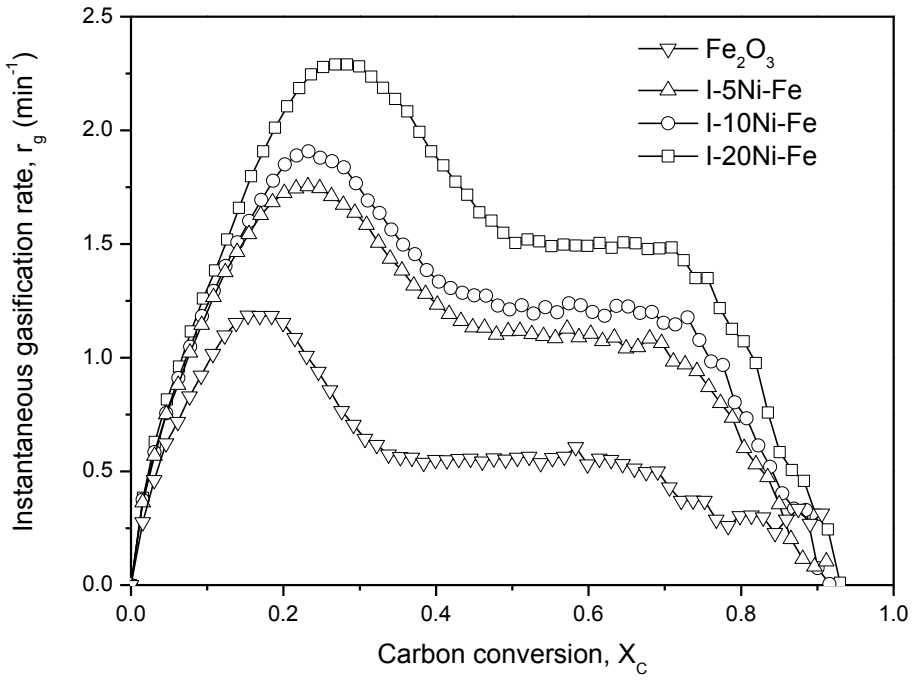

Figure 8-7 Instantaneous gasification rate as a function of carbon conversion obtained using the Fe_2O_3 and I-Ni-Fe OC samples

Figure 8-7 shows the instantaneous gasification rate as a function of carbon conversion when the Fe_2O_3 and the I-Ni-Fe OC samples were used. The instantaneous gasification rate can be seen to quickly reach its maximum between a carbon conversion of 0.2 and 0.3. This then slowly decreased with increasing carbon conversion, irrespective of which OC was used. The initial peak instantaneous gasification rate can be seen to occur during the coal pyrolysis stage; the subsequent rate can be ascribed to the char gasification reaction. It was found that the higher the NiO loading content in the bimetallic OCs, the higher the instantaneous gasification rate and this holds true at every value of carbon conversion here.

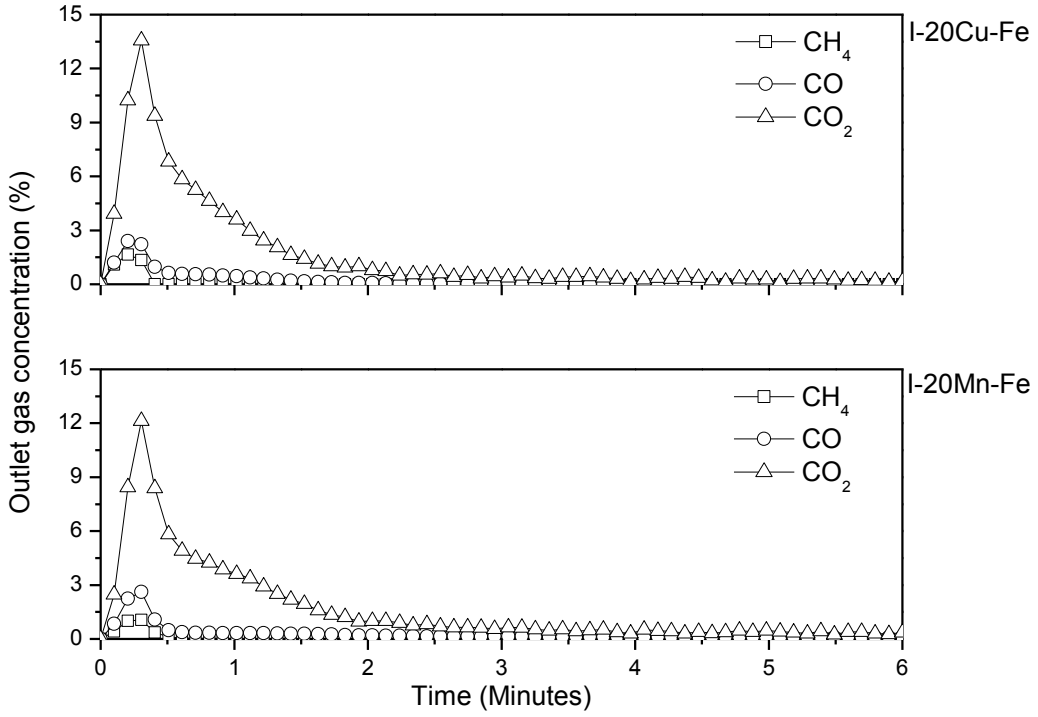

Figure 8-8 Outlet gas concentrations as a function of time obtained using the I-20Cu-Fe and I-20Mn-Fe OC samples

Figure 8-8 shows the outlet gas concentrations as a function of time obtained using the I-20Cu-Fe and I-20Mn-Fe OC samples. This was done to complement the results shown in Figure 8-5, allowing for the performance of the three synthetically impregnated OCs having 20 wt% of the secondary metal oxide to be compared to one another. It can be seen that similar to the I-20Ni-Fe OC sample, both the I-20Cu-Fe and I-20Mn-Fe OC samples were found to be more reactive relative to the monometallic Fe_2O_3 OC; the bimetallic OCs were able to convert a greater amount of fuel, yielding higher CO_2 concentrations during the reduction reaction. Although the results obtained using these two OCs are good, the reactivity enhancement by these two metal oxides are inferior compared to that of Ni in the I-20Ni-Fe OC sample on the basis of the peak CO_2 concentration. Comparing the I-20Cu-Fe and I-20Mn-Fe OC samples, it can be seen that the former sample outperforms the latter, with peak CO_2 concentrations of 13.56% and 12.13% respectively. Hence, the reactivity of the three bimetallic OC samples in descending order is I-20Ni-Fe, I-20Cu-Fe and I-20Mn-Fe. This conclusion is also confirmed by the results shown in Figure 8-9. This figure shows the average accumulated CO_2 concentrations obtained using the three bimetallic OC samples over five redox reactions in the fluidized bed reactor with Yallourn coal as the fuel. The use of the I-20Ni-Fe sample yielded the highest amount of CO_2, followed by that obtained using

the I-20Cu-Fe sample; the lowest amount of CO_2 was obtained using the I-20Mn-Fe OC sample. It should be noted that the CO_2 concentration obtained from using the I-20Cu-Fe sample was taken from the first reduction reaction due to defluidization beyond the first reduction reaction; this will be discussed in the subsequent subsections.

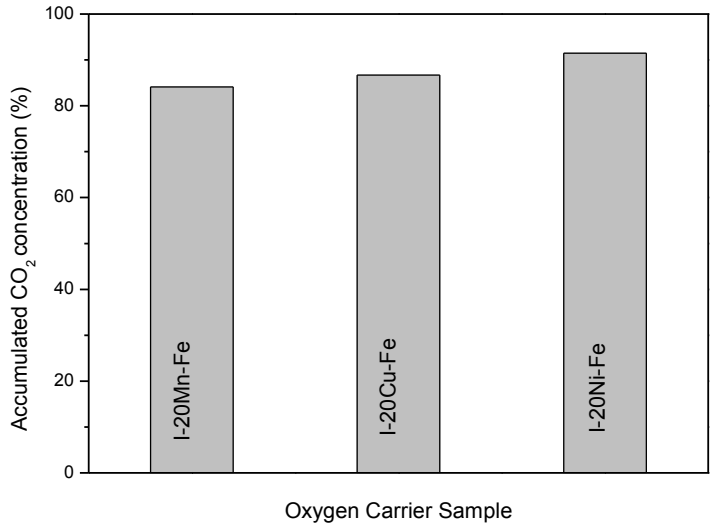

Figure 8-9 Average accumulated CO_2 concentration over five redox cycles obtained using the impregnated OCs containing 20 wt% of the secondary metal oxide

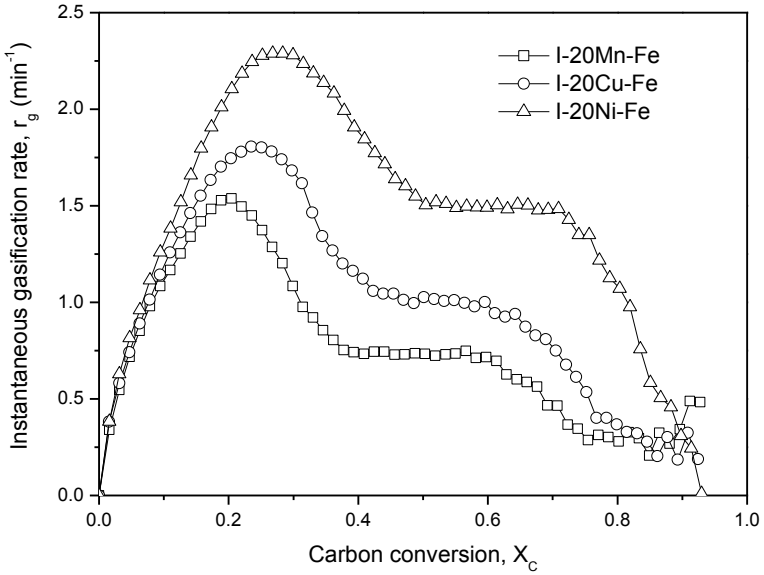

Figure 8-10 Instantaneous gasification rate as a function of carbon conversion obtained using the impregnated OCs containing 20 wt% of the secondary metal oxide

Figure 8-10 was constructed to investigate the effect of the secondary metal oxide on the instantaneous gasification rate; this plot was constructed for the three impregnated OCs containing 20 wt% of the secondary metal oxide. It is apparent that the sample containing 20 wt% of NiO showed the best performance, achieving a significantly higher instantaneous gasification rate relative to that obtained using the other two OC samples. This suggests that the incorporation of NiO in the bimetallic OC has a more pronounced effect on the physicochemical properties of the synthetic OC than incorporating either CuO or Mn_2O_3.

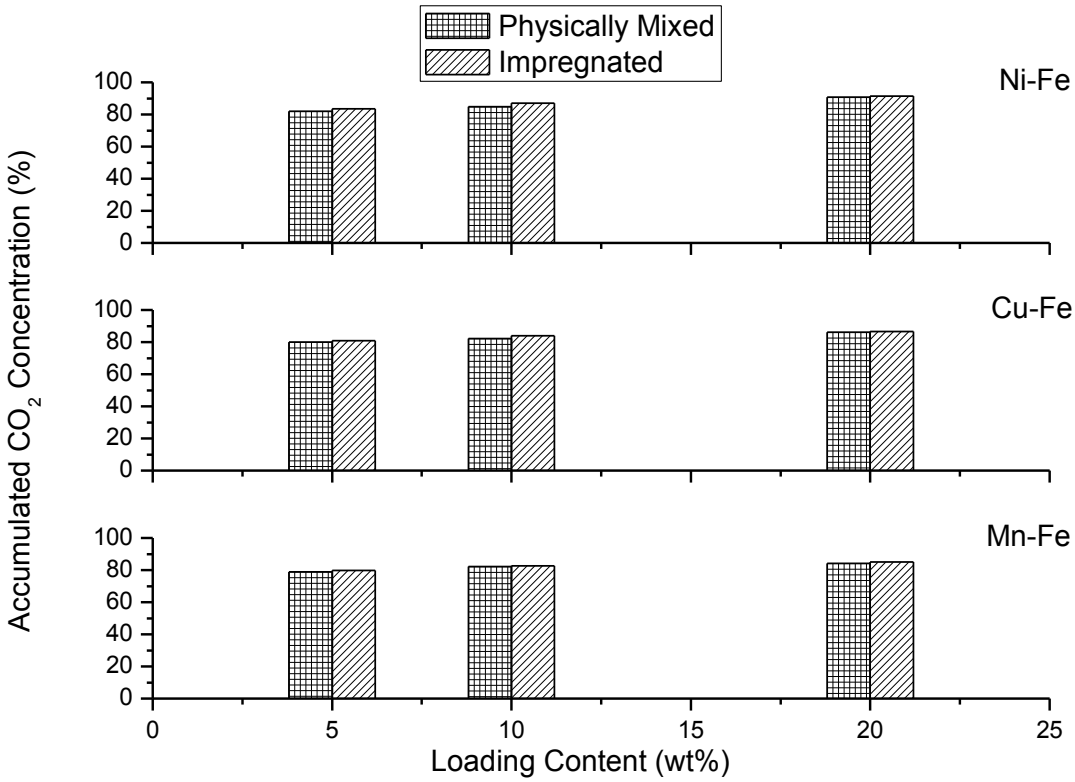

Figure 8-11 Average accumulated CO_2 concentration over five redox cycles obtained using the physically mixed and impregnated OCs.

The reactivity enhancement of Fe_2O_3 by a secondary metal oxide has been shown in literature to be largely associated with the physical structure of OC [18]. Generally, the physical and chemical properties of an OC such as the surface morphology, elemental distribution and pore structure are affected by the method used to prepare the OC. Therefore, investigations to better understand the implications that the synthesis method has on the reactivity of the OC is necessary. Figure 8-11 was constructed to show the effect of the preparation method on the accumulated CO_2 concentration. It can be seen that all the samples prepared via impregnation exhibited better performance over their physically mixed counterparts. This is evident based

on the higher accumulated CO_2 concentrations obtained through the use of the impregnated OC samples, irrespective of the amount and type of the secondary metal oxide. The accumulated CO_2 concentrations obtained using the impregnated samples were always higher than those obtained using the physically mixed samples, up to a maximum of two percentage points; this confirms that the OC preparation method is indeed an important criteria to consider when fabricating synthetic OCs as it has an impact on the OC's reactivity.

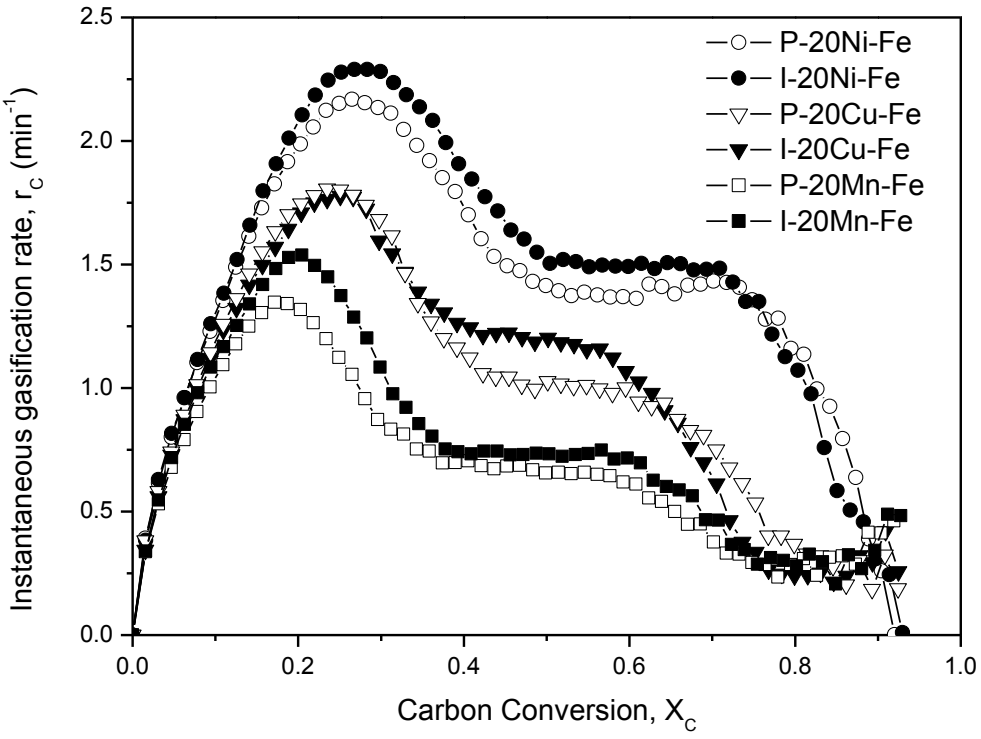

Figure 8-12 Instantaneous gasification rate as a function of carbon conversion obtained using the impregnated and physically mixed OCs containing 20 wt% of the secondary metal oxide

Figure 8-12 shows the effect of the preparation method on the instantaneous gasification rate using both the physically mixed and impregnated OC samples containing 20 wt% of the secondary metal oxide. It can be seen that the samples prepared using the impregnation method performed better, in terms of enhancing the instantaneous gasification rates of the fuel, than the physically mixed samples; the findings here are consistent with those shown in Figure 8-11. As the OC's reactivity was affected by the synthesis method, it is a fair conclusion that the physicochemical properties of an OC are altered by the preparation method.

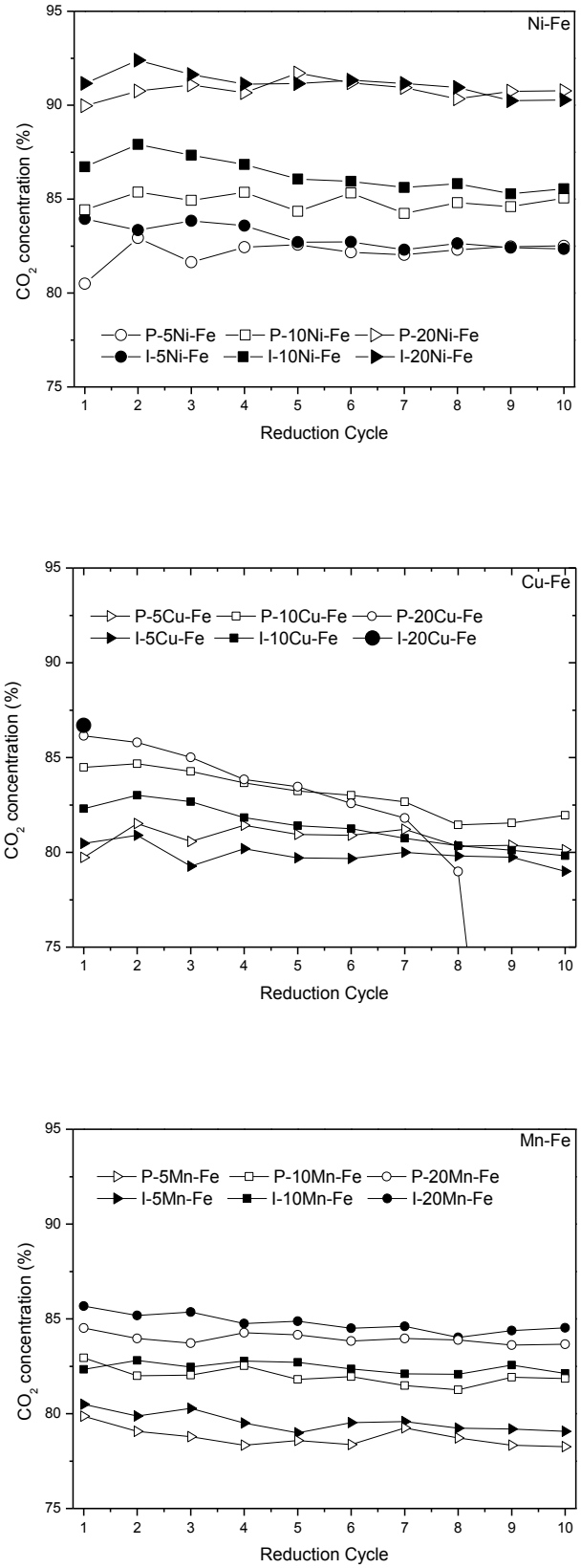

Figure 8-13 Accumulated CO_2 concentrations over ten reduction reactions obtained using the physically mixed and impregnated OCs.

Figure 8-13 shows the cyclic performance of the 18 bimetallic OC samples in terms of the CO_2 concentration accumulated from the combustion of the coal-derived gases. Ten redox cycles were performed at a temperature of 900°C using each of these OC samples. Comparing the two Ni-Fe samples, it is apparent that the I-Ni-Fe samples performed better than the P-Ni-Fe samples in terms of the outlet CO_2 concentrations, but their cyclic performance was not as impressive. It can be seen that all three I-Ni-Fe samples showed different degrees of reactivity deterioration, whereas the P-Ni-Fe samples showed relatively better cyclic performance; similar results were also observed for the Mn-Fe impregnated and physically mixed OC pairs. With respect to the Cu-Fe composite OCs, all of the synthesized samples experienced a decrease in their accumulated CO_2 concentrations with progressive reduction reactions. It can be seen that the P-5Cu-Fe and P-10Cu-Fe samples were capable of completing the 10 reduction reactions but this was accompanied by a reduction in the CO_2 outlet concentrations by around two percentage points after 10 cycles. On the other hand, the P-20Cu-Fe OC showed a significant deterioration in its recyclability and failed to complete the 10 redox reactions. The I-20Cu-Fe OC sample performed well during the first cycle but then defluidization was found to occur in the reactor. Therefore, the experiment had to be stopped and as such the result from the first reduction reaction is presented in Figure 8-13. Although the P-20Cu-Fe OC performed better than I-20Cu-Fe sample, the accumulated CO_2 concentration was found to quickly decrease going from the first cycle to the 8^{th} cycle. Beyond this, a significant decrease was observed due to defluidization; this indicates that synthetic OCs containing Fe_2O_3 and large amounts of CuO are undesirable as these would have poor thermal and mechanical stabilities leading to a deterioration in their reactivity or even defluidization of the bed.

8.4 Characterization

As previously mentioned, the fresh and used OC particles obtained at the end of the reaction in the fluidized bed reactor were characterized using SEM, EDS, XRD and ASAP to help shed some light on the experimental results.

8.4.1 Scanning Electron Microscope (SEM)

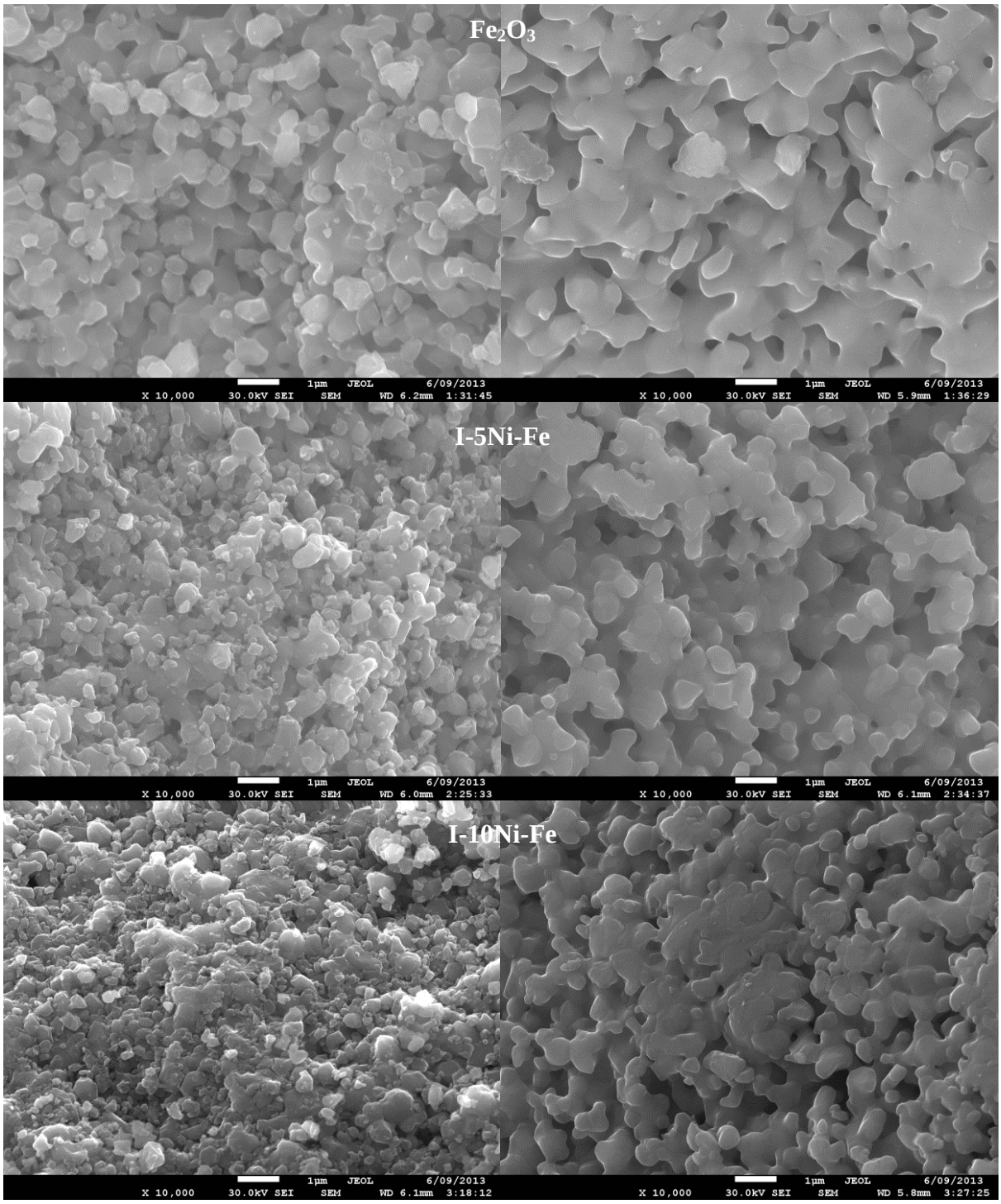

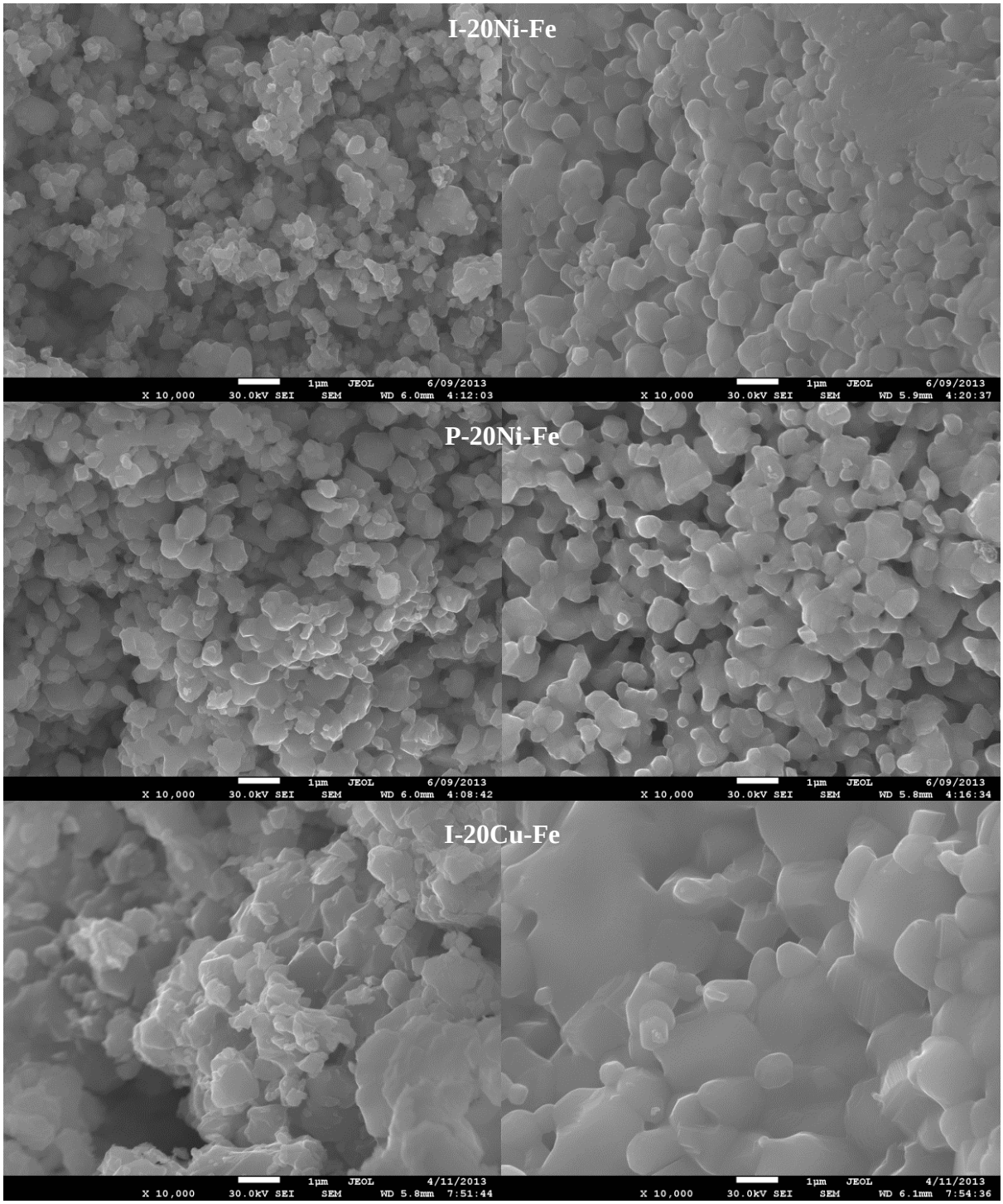
I-20Ni-Fe
1μm JEOL 6/09/2013
X 10,000 30.0kV SEI SEM WD 6.0mm 4:12:03
1μm JEOL 6/09/2013
X 10,000 30.0kV SEI SEM WD 5.9mm 4:20:37
P-20Ni-Fe
1μm JEOL 6/09/2013
X 10,000 30.0kV SEI SEM WD 6.0mm 4:08:42
1μm JEOL 6/09/2013
X 10,000 30.0kV SEI SEM WD 5.8mm 4:16:34
I-20Cu-Fe
1μm JEOL 4/11/2013
X 10,000 30.0kV SEI SEM WD 5.8mm 7:51:44
1μm JEOL 4/11/2013
X 10,000 30.0kV SEI SEM WD 6.1mm 7:54:36

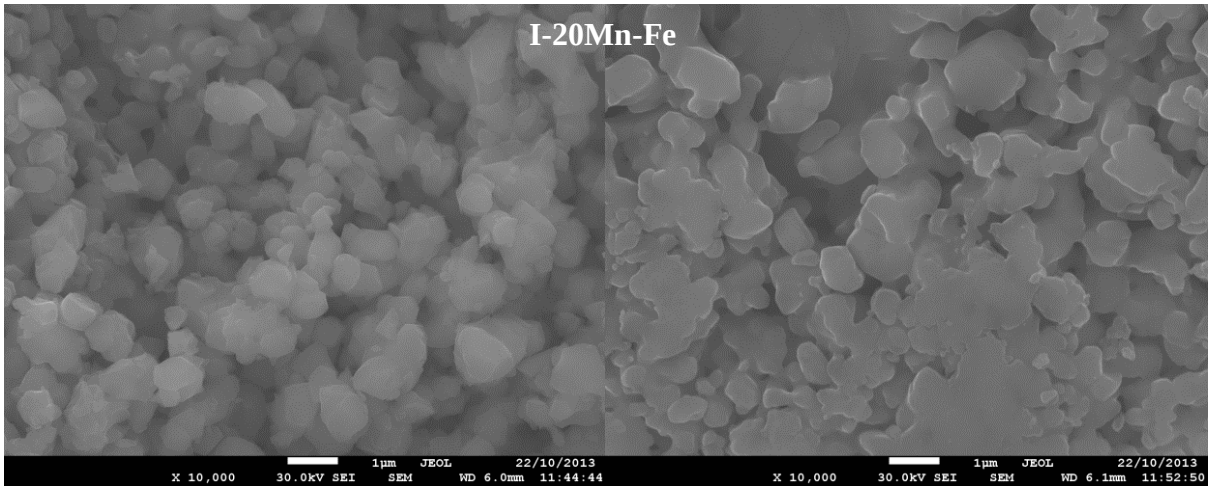

Figure 8-14 Micrographs of the fresh (LHS) and used (RHS) OC samples

Figure 8-14 shows the SEM images of some of the fresh and used Fe_2O_3, Ni-Fe, Cu-Fe and Mn-Fe OC samples. It can be observed that the grains of the fresh Fe_2O_3 particle are larger compared to those in the bimetallic OCs. This is one of the advantages of fabricating synthetic OCs as the synthesis process allows for the physicochemical characteristics of the OC to be engineered to obtain certain desired characteristics. While the surface areas of these OCs can be qualitative compared using these micrographs, the surface area analysis in the subsections to follow will allow for quantitative comparisons to be done. On the other hand, the grains of the used Fe_2O_3 particle appear to have undergone coalescence; this phenomenon can also be observed in each of the used OCs. All the fresh Ni-Fe samples were found to have a porous structure with small grains on the surface of the particle. The I-20Ni-Fe sample appears to have the best surface structure when compared to all of the other Ni-Fe OCs, including even the P-20Ni-Fe sample. This indicates that the impregnation method was better than physical mixing in terms of the development of the OC's pore structure. After 10 redox cycles, however, differing degrees of grain coalescence was observed for the used Ni-Fe samples, as evidenced by the formation of larger grains and a reduction in the amount of pores. Such an observation is typical of OCs that have been subjected to repeated physical and chemical stresses, as present in multicycle redox reactions. This explains the slight decrease in the reactivity of the synthetic OCs with progressing redox cycles, as shown in Figure 8-13. An interesting observation here is that although the P-20Ni-Fe sample also underwent grain coalescence, its performance was not as adversely affected as its impregnated counterpart. This reason behind this observation could be due to the chemical treatment that the impregnated OC was subjected to, resulting in it having poorer stability.

Comparing the impregnated samples containing 20 wt% of the secondary metal oxides, the fresh I-20Ni-Fe sample was still found to have the best morphology, while the other two bimetallic OC samples had rougher surface structures with larger grains and fewer pores. The used I-20Cu-Fe OC sample appears to have undergone severe grain coalescence, due to the presence of very large grains, as well as agglomeration; this explains the defluidization which occurred when this sample was used and could be due to the low melting point of Cu. While the reaction temperatures would not have caused it to melt, the temperatures were sufficiently high for it to soften and agglomerate. Although severe grain coalescence was observed for the used Cu-Fe samples, these still performed better than the Mn-Fe samples. This indicates that the reactivity of the bimetallic OC is not only dependent on the physical structure of the secondary metal oxide, but also its reactivity.

8.4.2 Energy Dispersive X-ray Spectroscope (EDS)

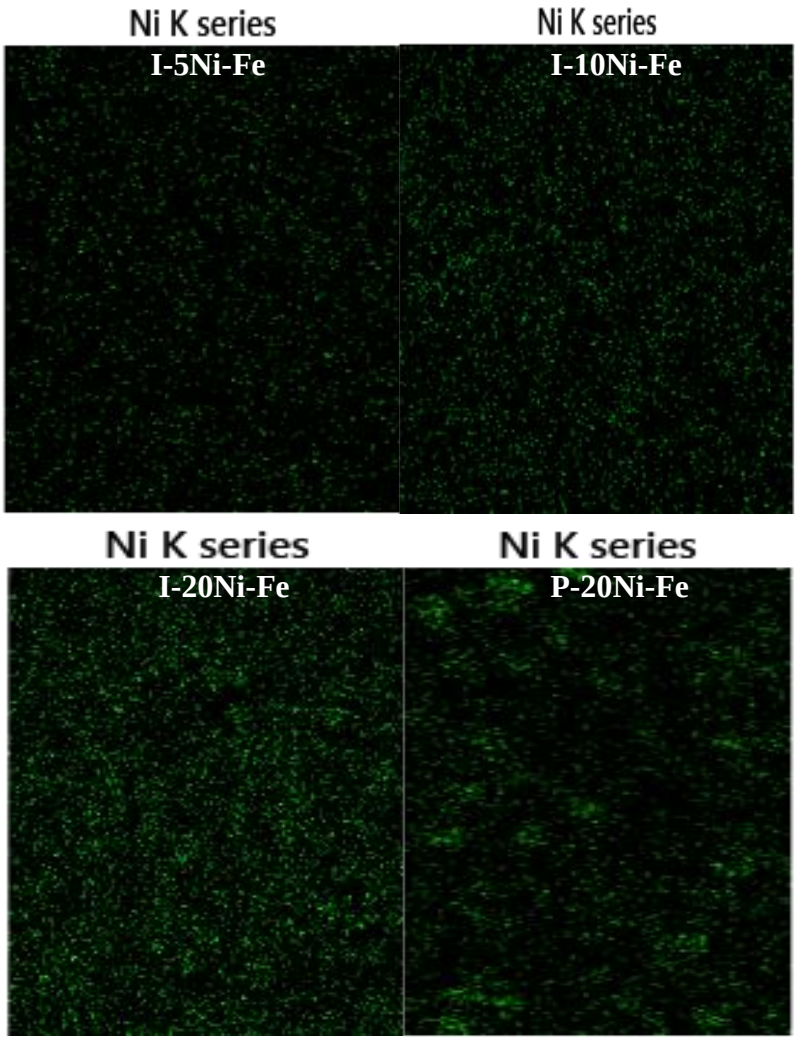

Figure 8-15 Distribution of the element Ni on the surface of the Ni-Fe OC particles

Figure 8-15 shows the distribution of Ni on the surface of the Ni-Fe OC particles. It can be seen that the higher the loading content of NiO, the higher the concentration of green deposits. This translates to the availability of a larger area and amount of NiO to combust the coal-derived combustible gases when a higher amount of NiO was added. Thus, a higher amount of CO_2 could be obtained using Ni-Fe OCs containing higher amounts of NiO, as confirmed by the results obtained from the TGA and fluidized bed reactor experiments. From this figure, it is also clear that there is a better distribution of Ni on the surface of the I-Ni-Fe OC particles. Since the physical mixing method involved the combination of two solid metal oxides, the dispersion of Ni on the surface of the P-Ni-Fe samples were found to be quite poor relative to that found on the surface of the I-Ni-Fe samples. This is most likely the reason for the poorer performance of the physically mixed OCs relative to their impregnated counterparts. Similarly, a superior dispersion of the secondary metal oxides was found on the impregnated Mn-Fe and Cu-Fe samples relative to their physically mixed counterparts. This proves that the dispersion of the secondary metal oxide plays an important role in the reactivity of the synthesized OCs.

8.4.3 X-ray Diffraction (XRD)

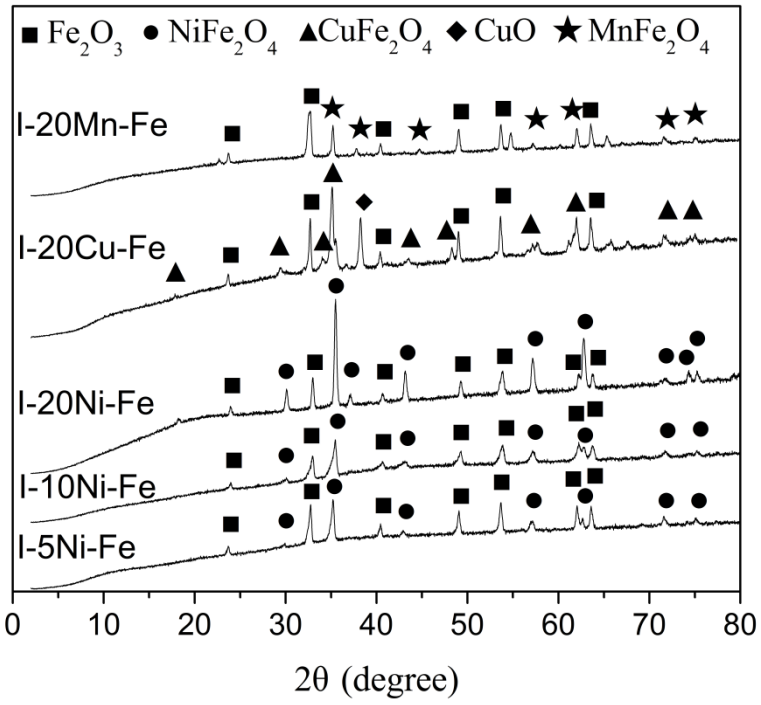

Figure 8-16 Diffractograms of the fresh bimetallic OC samples

Figure 8-16 shows the diffractograms of the fresh Ni-Fe, Cu-Fe and Mn-Fe bimetallic OCs. As expected, the diffractogram of the fresh Fe_2O_3 sample was found to only contain Fe_2O_3, due to it being of reagent grade and as such it was not included in this figure. The diffractograms of the Ni-Fe samples show that two crystalline phases consisting of Fe_2O_3 and $NiFe_2O_4$ were detected in all three Ni-Fe samples. This means that the added NiO completely combined with Fe_2O_3 to form a solid solution. It can also be seen that with the increase in the NiO loading content in the I-Ni-Fe OC samples, the intensity of the $NiFe_2O_4$ reflections was intensified. This is especially noticeable with the I-20Ni-Fe sample as there is a significant increase in the intensity of the $NiFe_2O_4$ reflection relative to the other two I-Ni-Fe OC samples. A similar pattern was observed for the other two OC samples impregnated with CuO and Mn_2O_3, whereby a solid solution was found to form between Fe_2O_3 and the secondary metal oxides. However, one significant difference was found to be present when comparing the diffractograms of the Cu-Fe sample with the other bimetallic OC samples; the reflection corresponding to CuO was detected in the I-20Cu-Fe sample. The low degree of interaction between CuO and Fe_2O_3 could be ascribed to the low melting point of CuO. This may have resulted in the coating of the Fe_2O_3 particles by the softened CuO, making the reaction between CuO and Fe_2O_3 much harder. The presence of CuO in the Cu-Fe sample confirms the findings shown in Figure 8-3, wherein a noticeable weight loss was observed during the initial stages of the reaction due to the release of oxygen from the dissociation of CuO to Cu_2O.

8.4.4 Accelerated Surface Area and Porosimetry (ASAP)

Table 8-1 Pore structure analysis results for the fresh and used OC samples

Sample	BET surface area (m^2/g)	
	Fresh	Used
Fe_2O_3	0.75	0.55
I-5Ni-Fe	1.01	0.44
I-10Ni-Fe	1.44	0.17
I-20Ni-Fe	1.86	0.55
P-20Ni-Fe	1.01	0.79
I-20Cu-Fe	0.37	0.08
P-20Cu-Fe	0.31	0.09
I-20Mn-Fe	0.56	0.51
P-20Mn-Fe	0.42	0.35

Table 8-1 lists the BET surface areas of the fresh and used Fe_2O_3, Ni-Fe, Cu-Fe and Mn-Fe samples. It can be seen that there is an appreciable decrease in the surface area of the Fe_2O_3 OC after 10 redox cycles, confirming the qualitative analysis of the SEM images in Figure 8-14. This is also supported by similar results in literature regarding the decrease of an OC's surface area after being utilized in multiple redox reactions [19]. The surface areas of the fresh Ni-Fe samples were found to increase as the loading content of NiO was increased. Additionally, the I-20Ni-Fe sample was found to possess a greater surface area compared to the P-20Ni-Fe sample and this is in agreement with the qualitative analysis performed on the SEM images in Figure 8-14. A similar trend was also observed with the fresh impregnated Cu-Fe and Mn-Fe samples, whereby the impregnated samples always had higher surface areas relative to their physically mixed counterparts. After 10 consecutive redox reactions, the impregnated and physically mixed Ni-Fe, Cu-Fe and Mn-Fe samples showed different degrees of reduction in their BET surface areas. It was found that the Cu-Fe samples experienced the most significant decrease in their BET surface areas which is due to severe sintering and agglomeration of the OCs. The ASAP analysis of the fresh and used samples confirms the experimental findings pertaining to the deterioration in the reactivity of the

bimetallic OCs, which has been explained to be due to coalescence of the grains in the OC. An interesting observation is that while most of the OC samples experienced a significant reduction in their BET surface areas after ten redox reactions, the physically mixed and impregnated bimetallic OCs containing Mn showed only a very slight reduction in this value. This is an important observation, as the use of Mn_2O_3 was found to allow the bimetallic OCs to better maintain their physical structure and reactivity after multiple redox reactions. Additionally, while the use of an inert support is likely to reduce the extent of grain coalescence in the metal oxide, a larger OC mass would be required to compensate for the weight of the support material; this is because the inert support material would not be able to contribute to the oxidation of the fuel.

8.5 Conclusions

Synthetic bimetallic OCs were fabricated by supporting secondary metal oxides such as NiO, CuO and Mn_2O_3 on Fe_2O_3; these OCs were synthesized via wet impregnation and physical mixing. The secondary metal oxide loading contents were varied and included 5, 10 and 20 wt%. Experiments were performed using both a TGA and a fluidized bed reactor. The following conclusions were drawn based on this study:

1. The incorporation of secondary metal oxides can significantly increase the reactivity of Fe_2O_3 in the bimetallic OCs. Both the synthesis techniques, impregnation and physical mixing, were found to yield significantly more reactive OCs compared to Fe_2O_3.

2. It was found that the higher the loading content of the secondary metal oxide, the greater the reactivity of the resultant bimetallic OC in most cases. The obtained results imply that the addition of a secondary metal oxide can lead to synergies between the two metal oxides, improving the reactivity of the bimetallic OC. Additionally, the Mn-Fe OC samples experienced the smallest reduction in their BET surface areas compared to the Ni-Fe and Cu-Fe OC samples; this means that the physical and chemical stabilities of these OCs were superior relative to the Ni-Fe and Cu-Fe OC samples.

3. The impregnated samples performed better than their physically mixed counterparts. The accumulated CO_2 concentrations obtained using the impregnated samples were always higher than those obtained using their physically mixed counterparts, up to a maximum of two percentage points. The reason behind this was found using the EDS; there was better dispersion of the secondary metal oxides on Fe_2O_3 when the bimetallic OC was synthesized

via impregnation instead of being physically mixed. The synthesis technique also affected the BET surface areas of the bimetallic OCs, with the impregnated samples having higher surface areas relative to their physically mixed counterparts.

4. Multicycle redox reactions using a fluidized bed reactor showed that both the Ni-Fe and Mn-Fe samples experienced a slight decrease in their reactivity; this was made worse when the Cu-Fe samples containing 20 wt% of CuO were used as these underwent sintering and agglomeration, resulting in the defluidization of the bed. This was ascribed to the low melting point of CuO, which was found to be present on the Cu-Fe OC particles based on the characterization of these particles using XRD.

This chapter showed that the use of a secondary metal oxide, even in small amounts, can lead to an increase in the reactivity of Fe_2O_3 in the bimetallic OC. However, high levels of CuO in these OCs should be avoided as this could lead to operational issues such as agglomeration of the OCs and defluidization of the bed. On the other hand, the use of NiO may not be suitable due to its toxicity. The use of Mn_2O_3 as the secondary metal oxide is recommended as it results not only in a synergy with Fe_2O_3, but the resultant bimetallic OC has more stable physical characteristics.

8.6 References

1. Berguerand, N. and A. Lyngfelt, *The use of petroleum coke as fuel in a 10kWth chemical-looping combustor.* International Journal of Greenhouse Gas Control, 2008. **2**(2): p. 169-179.
2. Adanez, J., F. Garcia-Labiano, L.F. de Diego, P. Gayan, J. Celaya, and A. Abad, *Nickel-copper oxygen carriers to reach zero CO and H-2 emissions in chemical-looping combustion.* Industrial & Engineering Chemistry Research, 2006. **45**(8): p. 2617-2625.
3. Abad, A., T. Mattisson, A. Lyngfelt, and M. Johansson, *The use of iron oxide as oxygen carrier in a chemical-looping reactor.* Fuel, 2007. **86**(7–8): p. 1021-1035.
4. Ryu, H.J., D.H. Bae, K.H. Han, S.Y. Lee, G.T. Jin, and J.H. Choi, *Oxidation and reduction characteristics of oxygen carrier particles and reaction kinetics by unreacted core model.* Korean Journal of Chemical Engineering, 2001. **18**(6): p. 831-837.
5. Roux, S., A. Bensakhria, and G. Antonini, *Study and improvement of the regeneration of metallic oxides used as oxygen carriers for a new combustion process.* International Journal of Chemical Reactor Engineering, 2006. **4**.
6. Johansson, M., T. Mattisson, and A. Lyngfelt, *Comparison of oxygen carriers for chemical-looping combustion.* Thermal Science, 2006. **10**(3): p. 93-107.
7. Zafar, Q., T. Mattisson, and B. Gevert, *Redox investigation of some oxides of transition-state metals Ni, Cu, Fe, and Mn supported on SiO2 and MgAl2O4.* Energy & Fuels, 2006. **20**(1): p. 34-44.
8. Corbella, B.M. and J.M. Palacios, *Titania-supported iron oxide as oxygen carrier for chemical-looping combustion of methane.* Fuel, 2007. **86**(1–2): p. 113-122.
9. Corbella, B.M., L.F. de Diego, F. García-Labiano, J. Adánez, and J.M. Palacios, *Characterization Study and Five-Cycle Tests in a Fixed-Bed Reactor of Titania-Supported Nickel Oxide as Oxygen Carriers for the Chemical-Looping Combustion of Methane.* Environmental Science & Technology, 2005. **39**(15): p. 5796-5803.
10. Kidambi, P.R., J.P.E. Cleeton, S.A. Scott, J.S. Dennis, and C.D. Bohn, *Interaction of Iron Oxide with Alumina in a Composite Oxygen Carrier during the Production of Hydrogen by Chemical Looping.* Energy & Fuels, 2012. **26**(1): p. 603-617.
11. Dueso, C., A. Abad, F. Garcia-Labiano, L.F. de Diego, P. Gayan, J. Adanez, and A. Lyngfelt, *Reactivity of a NiO/Al2O3 oxygen carrier prepared by impregnation for chemical-looping combustion.* Fuel, 2010. **89**(11): p. 3399-3409.
12. Ryden, M., E. Cleverstam, M. Johansson, A. Lyngfelt, and T. Mattisson, *Fe2O3 on Ce-, Ca-, or Mg-Stabilized ZrO2 as Oxygen Carrier for Chemical-Looping Combustion Using NiO as Additive.* Aiche Journal, 2010. **56**(8): p. 2211-2220.
13. Johansson, M., T. Mattisson, and A. Lyngfelt, *Investigation of Mn3O4 with stabilized ZrO2 for chemical-looping combustion.* Chemical Engineering Research & Design, 2006. **84**(A9): p. 807-818.
14. Johansson, M., T. Mattisson, and A. Lyngfelt, *Creating a synergy effect by using mixed oxides of iron-and nickel oxides in the combustion of methane in a chemical-looping combustion reactor.* Energy & Fuels, 2006. **20**(6): p. 2399-2407.
15. Bhavsar, S. and G. Veser, *Bimetallic Fe–Ni Oxygen Carriers for Chemical Looping Combustion.* Industrial & Engineering Chemistry Research, 2013. **52**(44): p. 15342-15352.
16. Zafar, Q., T. Mattisson, and B. Gevert, *Integrated Hydrogen and Power Production with CO2 Capture Using Chemical-Looping ReformingRedox Reactivity of Particles*

of CuO, Mn2O3, NiO, and Fe2O3 Using SiO2 as a Support. Industrial & Engineering Chemistry Research, 2005. **44**(10): p. 3485-3496.

17. Eyring, E.M., G. Konya, J.S. Lighty, A.H. Sahir, A.F. Sarofim, and K. Whitty, *Chemical Looping with Copper Oxide as Carrier and Coal as Fuel.* Oil & Gas Science and Technology-Revue D Ifp Energies Nouvelles, 2011. **66**(2): p. 209-221.
18. Hu, Y., W. Wang, S. Wang, and J. Zhu, *Effect of Copper Addition on Reduction Properties of the Iron-Based Oxygen Carriers in the Chemical-Looping Process for Hydrogen Production.*
19. Bhavsar, S. and G.t. Veser, *Reducible supports for Ni-based oxygen carriers in chemical looping combustion.* Energy & Fuels, 2013. **27**(4): p. 2073-2084.

Chapter 9 Operational Experience with a 10kW_{th} Alternating Fluidized Bed Reactor

The previous result chapters have investigated the performance of Yallourn coal using a TGA, a bench scale fluidized bed reactor and a multipurpose reactor. The results obtained thus far suggest that VBC is a suitable candidate for use in the CLC process because of its high reactivity and low ash content. Additionally, there is no information in literature regarding the operation of a VBC-fuelled CLC system over an extended period of time. Here, a 10kW_{th} fluidized bed reactor capable of continuous fuel feeding was used to investigate the effect of scaling-up the CLC system.

This chapter aims to identify any potential issues of using VBC in a large scale CLC setup over an extended period of time.

9.1 Summary of Experimental Conditions

The iron ore from Western Australia was used as the OC in this study. Initially, an experiment was conducted in the bench scale fluidized bed reactor, as described in Section 3.2.2 in Chapter 3. This was done to enable the performance of this OC to be compared to the OCs which have been used in the earlier studies. 50 g of sand was introduced into the reactor after which 100 g of the OC was added. The reactor was operated at 900°C, while a fluidization gas comprising 20 v/v% CO_2 with balance N_2 was introduced into the reactor at a flow rate of 6 L/min. Oxidation of the reduced OC sample was achieved by switching CO_2 to air, while maintaining the same flow rates. An OC to coal ratio of 100:1 was used; hence, 1 g of coal was used in each reduction reaction. A total of 10 redox reactions were performed and the product gases were analysed using an online gas analyser.

Next, the 10kW_{th} fluidized bed reactor was used and a few different investigations were performed using this setup. Detailed description of the experimental setup can be found in Section 3.2.4 of Chapter 3. Initially, 1 kg of sand was introduced into the reactor to function as an inert bed over the distributor. Then, 5 kg of the OC was added atop the sand bed. The fluidization gas, totalling 25 L/min, consisted of 20 v/v% CO_2 with balance N_2. During oxidation, 80 v/v% air with balance N_2 was used. The same OC to fuel ratio as above was used; hence, 50 g of coal was added into the reactor at the start of each reduction reaction. The gases that were analysed were CO_2, CO, CH_4, H_2, O_2, NO, N_2O and NO_2. Most of the

tests were terminated at the 6th reduction reaction, as operational experience has shown the results to stabilize around the 5th reduction reaction.

The influence of temperature on the performance of the CLC system was investigated by conducting tests at 100°C intervals between 700-1000°C. Tests were also conducted using both Yallourn coal and char derived from Yallourn coal to study the effect of the fuel type. In another test, the particle size range of the OC was varied from 106-150 µm to 150-350 µm to study the effect of the OC particle size. The final investigation involved performing a 35 cycle test to study the performance of the OC over an extended period of time.

The OCs were characterized using a Scanning Electron Microscope (SEM), an Energy Dispersive X-ray Spectroscope (EDS), X-ray Diffraction (XRD) and Accelerated Surface Area and Porosimetry (ASAP) unit to study changes in the structure, composition and morphology of the OC particles. The particle size distribution of the OC particles used in the 35 cycle test was also determined.

9.2 Bench Scale Fluidized Bed Reactor Results

This experiment was done to determine the reactivity of the iron ore from Western Australia while allowing it to be compared to the synthetic OCs that were used in this reactor at the same operating conditions. This will allow the CO_2 yield and carbon conversion obtained using this OC to be compared to those obtained using the bimetallic OCs.

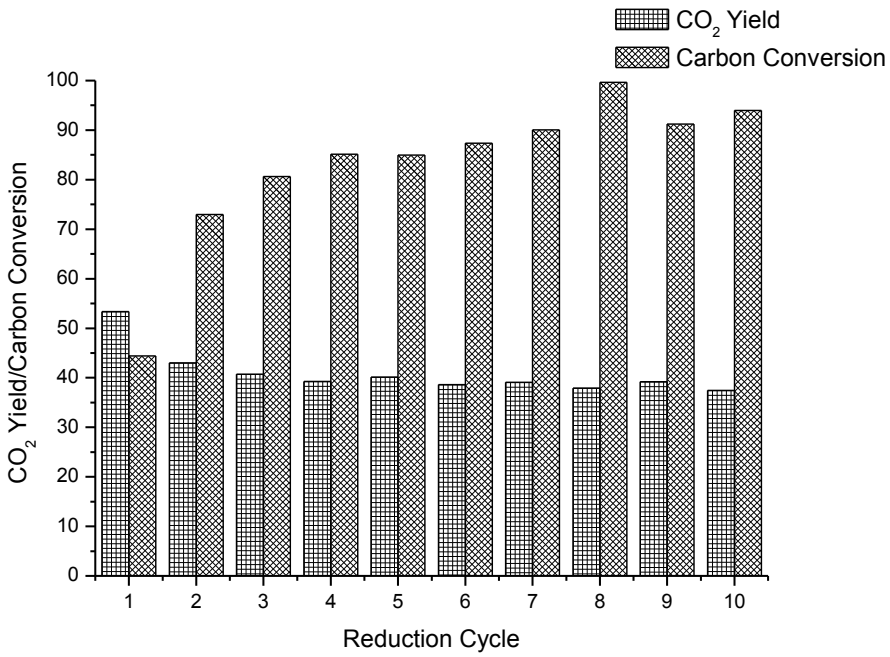

Figure 9-1 CO_2 yield and carbon conversion over ten reduction reactions

Figure 9-1 shows the results obtained using Yallourn coal and the iron ore from Western Australia over ten redox cycles. Based on the CO_2 yield, it can be seen that this iron ore performed poorly relative to the synthetic OCs that were used in Chapter 8. Using the synthetic OCs resulted in CO_2 yields between 75-90%, while the use of this iron ore yielded a value of around 40%. This represents approximately a 50% decrease in the outlet CO_2 concentration when this iron ore was used relative to the synthetic OCs. On the other hand, the carbon conversion obtained here is comparable to that achieved using the synthetic OCs. This shows that the behaviour of the fluidized bed reactor was similar in both the studies. The conclusion from these preliminary results is that the iron ore from Western Australia is not very reactive but is capable of maintaining its reactivity over 10 redox reactions unlike most of the synthetic OCs, which experienced reductions in their reactivity with progressing redox reactions. This shows that the current iron ore has both the chemical and physical stability to withstand the stresses from being used in a fluidized bed reactor over 10 redox cycles. Hence, this OC was used in the subsequent experiments that were performed in the 10 kW_{th} reactor.

9.3 10 kW_{th} Fluidized Bed Reactor Results

Since the iron ore from Western Australia was selected as the OC for use in all of the studies performed in the 10 kW_{th} fluidized bed reactor, this section will detail the results obtained for the various investigations that were performed.

9.3.1 Baseline Experiment at 900°C

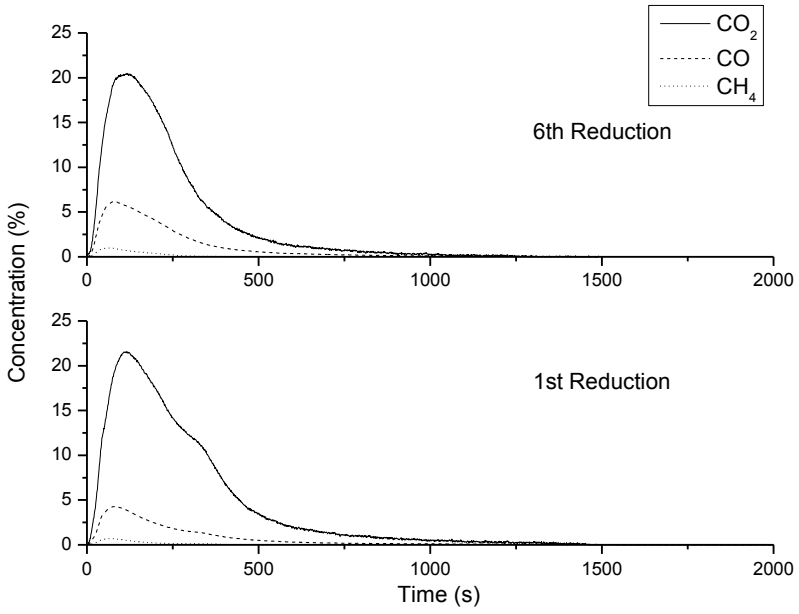

Figure 9-2 Outlet gas concentration profiles of the 1st and 6th reduction reactions

Figure 9-2 shows the outlet gas concentration profiles of the first and sixth reduction reactions for the experiment conducted at 900°C and this will be denoted as the baseline experiment henceforth. The first noticeable feature is that the concentration of CH_4 is very low in both reduction reactions even though Yallourn coal contains approximately 50% volatile matter on a dry basis. The concentration of CH_4 obtained in the preliminary investigation using the bench scale fluidized bed reactor was much higher than that which was obtained using the current reactor; this was due to insufficient contact between the volatiles and the OC. In the bench scale fluidized bed reactor, the fuel was dropped from the top of the reactor and as it fell through the length of the reactor to enter the OC bed, it underwent pyrolysis releasing significant amounts of volatile matter. A large proportion of these gases did not get the opportunity to come into contact with the OC; these were subsequently driven out of the reactor by the fluidizing gas, resulting in a large amount of CH_4 to be detected at the outlet hence reducing the CO_2 yield. There is a reduction in the CH_4 concentration by a factor of five when the current setup was used instead of the bench scale fluidized bed reactor. The reason for this significant improvement is due to the way the fuel was introduced into the $10kW_{th}$ fluidized bed reactor. The outlet of the fuel feeding tube was constructed to terminate at the bottom of the OC bed, which ensured that most of the evolved volatiles would come into contact with the OC as soon as it entered the reactor.

There are minor variations in the CO and CO_2 concentration profiles of the first and sixth reduction reactions. The peak CO_2 values were slightly higher while the peak CO values were lower in the first reduction reaction compared to those in the sixth reduction; this observation is in agreement with the results obtained using the bench scale reactor. Typically upon calcination, the OC particles experience a reduction in their surface areas [1]; this is a consequence of the structural and morphological changes that the OC particles undergo. The initial surface areas of the OC particles are typically reduced due to coalescence of the grains, which normally stabilizes after a few redox cycles. This reduction in the OC's surface area will be confirmed through surface area measurements in Section 9.3.1.4 below.

9.3.1.1 CO_2/CO Ratio and Oxygen Demand

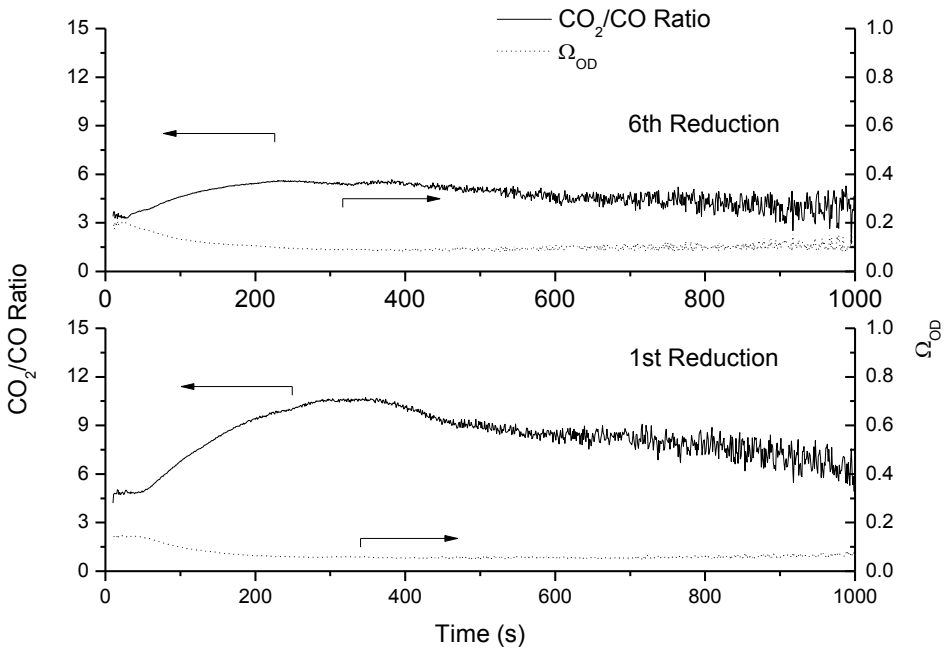

Figure 9-3 CO_2/CO ratio and oxygen demand as a function of time for the 1st and 6th reduction reactions

Figure 9-3 depicts the ratio of CO_2 to CO on the primary y-axis while the oxygen demand (Ω_{OD}) is shown on the secondary y-axis with both plotted as a function of time. The equation used to calculate the oxygen demand can be found in Section 3.6.2 of Chapter 3. The oxygen demand denotes the fraction of oxygen that is required to completely oxidize the remaining combustible gases, namely CO and CH_4. The plots were terminated at 1000 s as noise was found to dominate towards the end of the reaction due to the low concentrations of the gases. The CO_2/CO ratio shows the volume ratio of the predominant gas to the second most abundant gas. The peak CO_2/CO ratio in the first reduction reaction was found to be around 10.7 as opposed to 5.7 in the sixth reduction; this represents a significant reduction albeit an unobservable difference between the peak CO_2 concentrations of the first and last reduction reactions as shown in Figure 9-2. The significant reduction of this ratio is due to the increase in the concentration of CO in the sixth reduction reaction, which plays a major role in the CO_2/CO ratio; this is a result of the reduced reactivity of the OC over the course of the multicycle reactions, leading to an increase in the concentration of CO. The second part of this figure shows the oxygen demand for the two reduction reactions. The initially high oxygen demand was due to the volatiles that did not react with the OC. As expected, the oxygen demand of the sixth reduction reaction was higher for the reasons that were

mentioned above. The average oxygen demand values during the stable period between the 400 and 500 second mark was found to be 0.055 and 0.090 for the first and sixth reduction reaction respectively; this translates to an increase of roughly 64% in the oxygen demand due to the reduction in the OC's reactivity.

9.3.1.2 Carbon Conversion Rate and Carbon Conversion

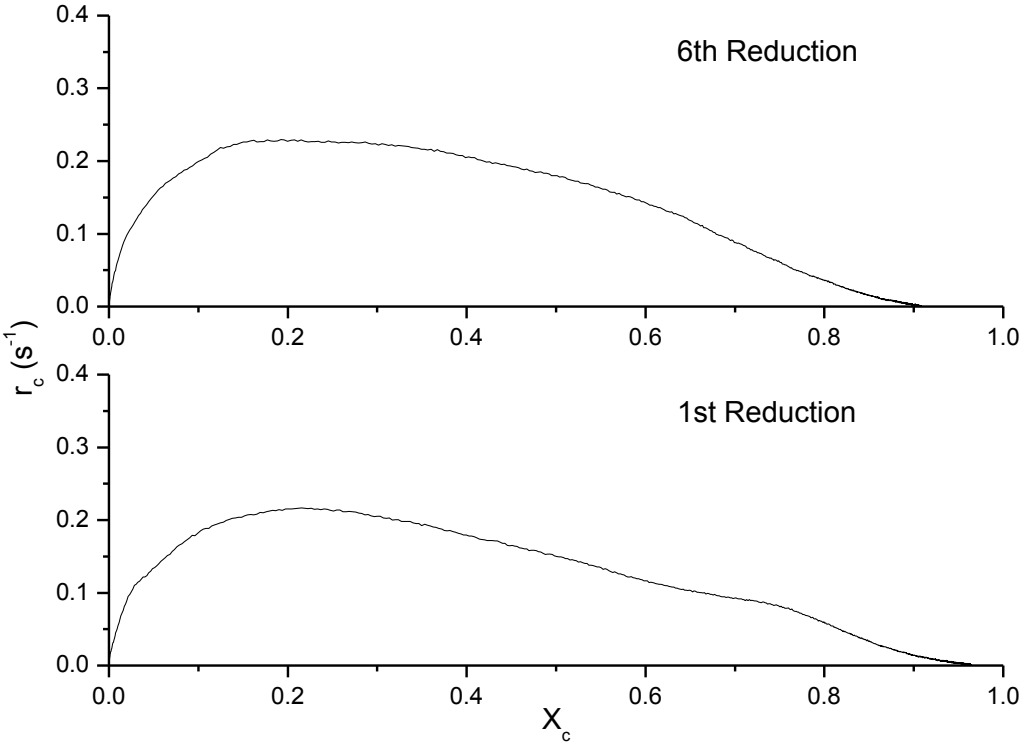

Figure 9-4 Carbon conversion rate as a function of carbon conversion for the 1st and 6th reduction reactions

Figure 9-4 shows the carbon conversion rate plotted as a function of carbon conversion and these equations used to obtain these two parameters can be found in Section 3.6.2 of Chapter 3. The carbon conversion obtained during the first reduction reaction is higher compared to that of the sixth reduction reaction. Numerically, this is 0.96 and 0.91 for the first and sixth reduction reactions respectively. While it has been explained that the differences in the results of the first and sixth reduction reactions in the previous figures were due to the reduction in the OC's reactivity, the difference here is due to other reasons. These reasons include variations in the bulk coal composition between one cycle and the next due to the heterogeneity of coal as well as the possibility that the entire 50 g of coal may not have entered the reactor as some of these may have adhered to the walls of the hopper or the screw

feeder tube. Additionally, since Yallourn coal is highly friable, it is possible that some coal particles may have undergone attrition in the screw feeder as it was fed into the reactor. This would have led to increased elutriation of these particles out of the reactor. Therefore, it is important to look at the performance of a reactor system over an extended period of time to minimize the effect of operational variations; such a study was performed and will be discussed in the sections to follow.

9.3.1.3 Gasification Rate

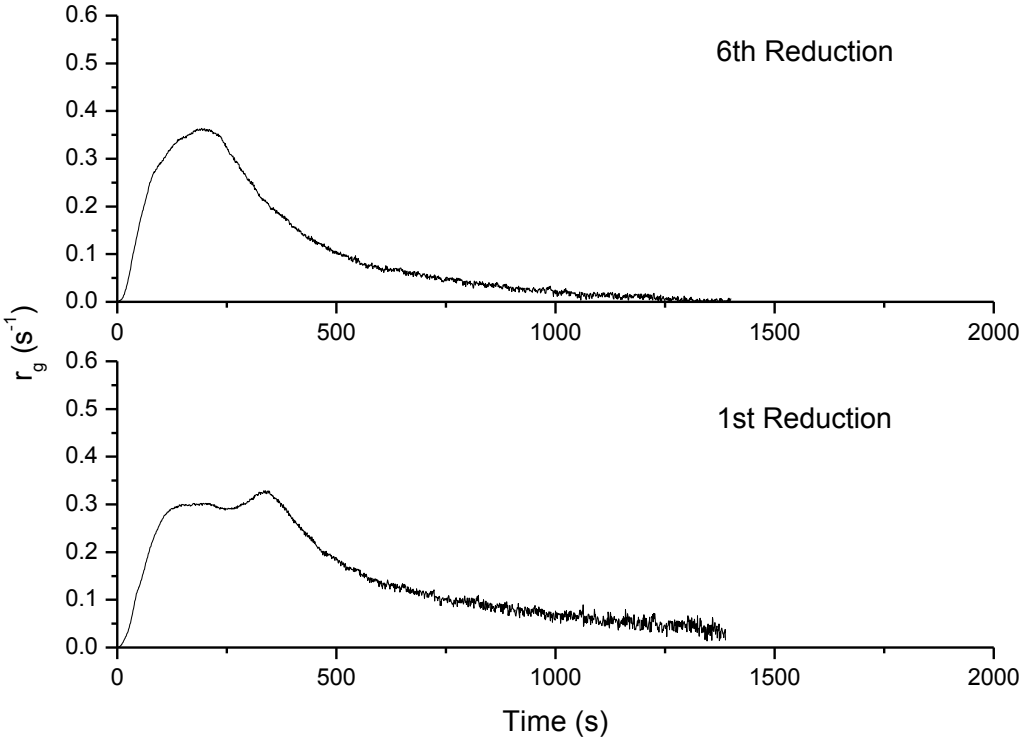

Figure 9-5 Gasification rate as a function of time for the 1st and 6th reduction reactions

Next, the gasification rate was plotted as a function of time and this can be found in Figure 9-5. This result differs from those shown in the previous figures as the peak rate here was slightly higher in the sixth reduction reaction compared to that in the first reduction reaction. The peak values were $0.33s^{-1}$ and $0.36s^{-1}$ in the first and sixth reduction reactions respectively. Additionally, the formation of a second peak can be observed in the first reduction reaction and this could be due to issues associated with the fuel feeding system whereby an amount of fuel larger than the average amount was fed into the reactor towards the end resulting in a greater instantaneous gasification rate at that point in time. This also explains why the peak gasification rate in the sixth reduction reaction was marginally higher than that in the first.

Additionally, this explanation supports the slight shifting of the peaks to the right as observed in Figure 9-2. Besides this observation, the rest of the profile appears to be similar between the two reduction reactions. Therefore, in conclusion, the findings from this baseline study show that the OC had the highest reactivity in the first reduction reaction which subsequently decreased over the course of the multicycle reaction.

9.3.1.4 NO_x Emission

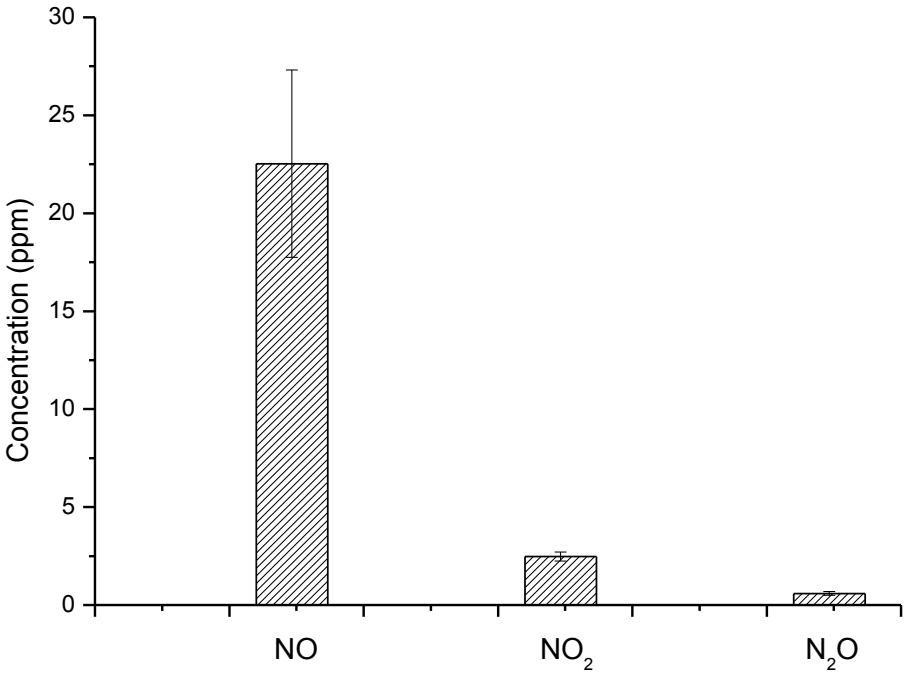

Figure 9-6 NO_x emissions from the baseline experiment

Figure 9-6 was constructed to investigate the NO_x emissions from the baseline experiment which was conducted at 900°C. The results reported in this figure were obtained from the 4th and 5th reduction reactions; these values were averaged over the course of the 4th and 5th reduction reactions. The concentrations were found to be 22.5 ppm, 2.48 ppm and 0.59 ppm for NO, NO_2 and N_2O respectively, corresponding to 8.79%, 1.49% and 0.34% of the inlet fuel nitrogen; the ratio of the concentrations of NO: NO_2: N_2O was found to be 38:4.2:1 using VBC as the fuel. The remaining fuel nitrogen would be released in the form of gaseous N_2, as found by Linderholm *et al.* [2].

9.3.1.5 Carbon Balance

Table 9-1 Carbon balance of the baseline experiment

Source		Mass of C in Source (g)	Fraction of Inbound C (%)
In	Coal	166.87	100.00
Out	Solid Carbon		
	Filters/Catch pots	0.96	0.57
	Gaseous Carbon		
	Flue Gas	153.83	92.18
	Air Reactor	0.68	0.41
	Total	155.52	93.19
Balance = In - Out		11.36	6.81

A carbon balance was done for the baseline experiment over six redox cycles and this can be found in Table 9-1. It can be seen that a large proportion of the carbon that was fed into the reactor was converted to CO, CO_2 and CH_4 in the flue gas; this is in agreement with the high carbon conversion obtained in the baseline experiment. In terms of percentages, around 92% of the introduced carbon was detected in the flue gas during the reduction period. As previously mentioned, since the reduction reaction was terminated after 30 minutes, there would have been some residual fuel in the bed when air was introduced into the reactor to initiate the oxidation reaction. Approximately 0.4% of the introduced carbon was detected in the flue gas as CO_2 during the oxidation reaction. Furthermore, around 0.6% of the introduced carbon was found in the catch pots, which also contained a small amount of fragmented OC particles. This mass of carbon was measured by combusting the samples in the catch pots and measuring the weight loss. Therefore, of the introduced carbon, 93.19% has been accounted for, leaving behind an unaccounted amount of 6.81%; this could be due to the low cyclone separation efficiency which caused a large proportion of the elutriated carbon to exit through the stack uncaptured. Additionally, this could have also been due to the low reactor height. Linderholm *et al.* [2] pointed out that the use of utility-scale boilers and higher efficiency cyclones would lead to an increase in the particle residence time. Hence, the appreciable loss of carbon that was observed in this investigation is not expected to occur during the operation of an industrial scale system.

9.3.1.6 Scanning Electron Microscope (SEM)

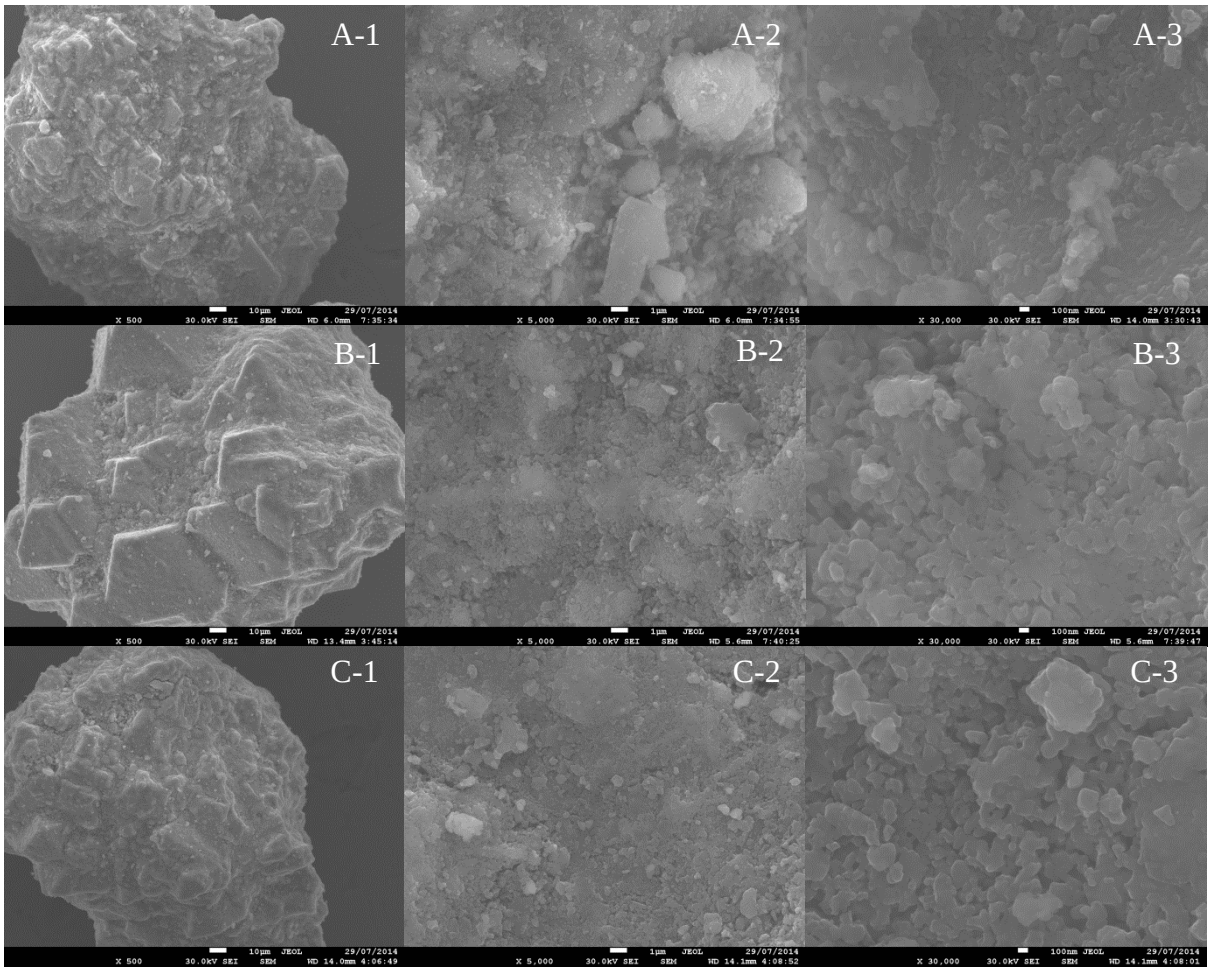

Figure 9-7 Micrographs for the fresh (A), reduced (B) and oxidized (C) OC samples at three different magnification levels (1:500X; 2:5000X; 3:30,000X)

Figure 9-7 shows the micrographs which were obtained for the fresh, reduced and oxidized OC particles at three different magnification levels. No significant differences between the fresh and used samples were observed at the lowest magnification; all of the OC particles appear highly irregular without any defining characteristics. The micrographs of the OC particles that were taken at higher magnifications, denoted by the numbers 2 and 3, show some differences. The fresh sample had many loose particles and small grains on its surface. Comparing both the reduced and oxidized OC particles, the grains initially present on the surface of the fresh OC particles appear to have undergone coalescence to form larger grains. Qualitatively, this would lead to a reduction in the available surface area for reaction with the combustible gases; this explains the reduction in the reactivity of the OC beyond the first reduction reaction, as observed in the above figures. Practically, since a reduction in the OC's surface area would lead to a reduction in its reactivity, make-up OC would need to be added

into the reactor to compensate for this loss in reactivity to enable the same amount of fuel to be combusted.

9.3.1.7 Energy Dispersive X-ray Spectroscope (EDS)

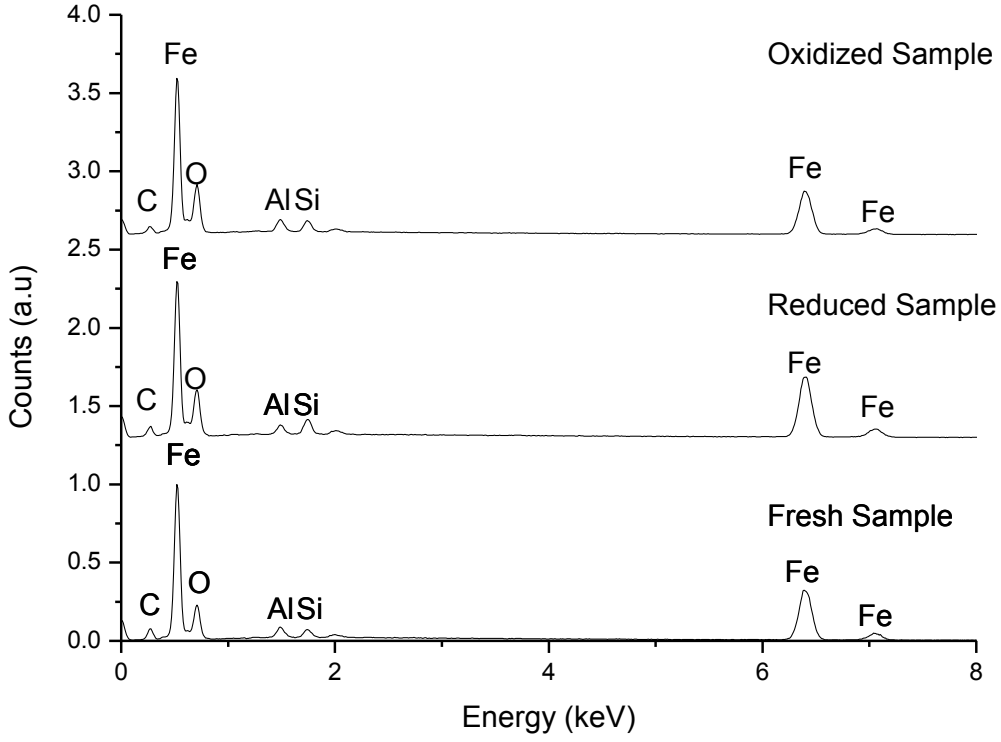

Figure 9-8 Energy dispersive X-ray spectra of the fresh, reduced and oxidized samples

These OC samples were subjected to EDS analyses and Figure 9-8 shows these results. Besides the elements present in the OC, no other elements were detected. The predominant elements in Yallourn ash is iron, silicon and magnesium. The OC contained Fe and Si; as such, these would not have resulted in the generation of additional peaks. The Mg in the coal ash was not detected even after the OC was reacted with 300 g of the coal. The presence of carbon was detected in all of the samples due to the use of cyanoacrylate as an adhesive to secure the OC particles on the sample stub. Additionally, a higher level of carbon was detected in the reduced sample, which was due to the residual carbon present at the end of the reduction reaction. The unlabelled peaks belong to the Iridium that was used to coat the OC particles.

9.3.1.8 X-ray Diffraction (XRD)

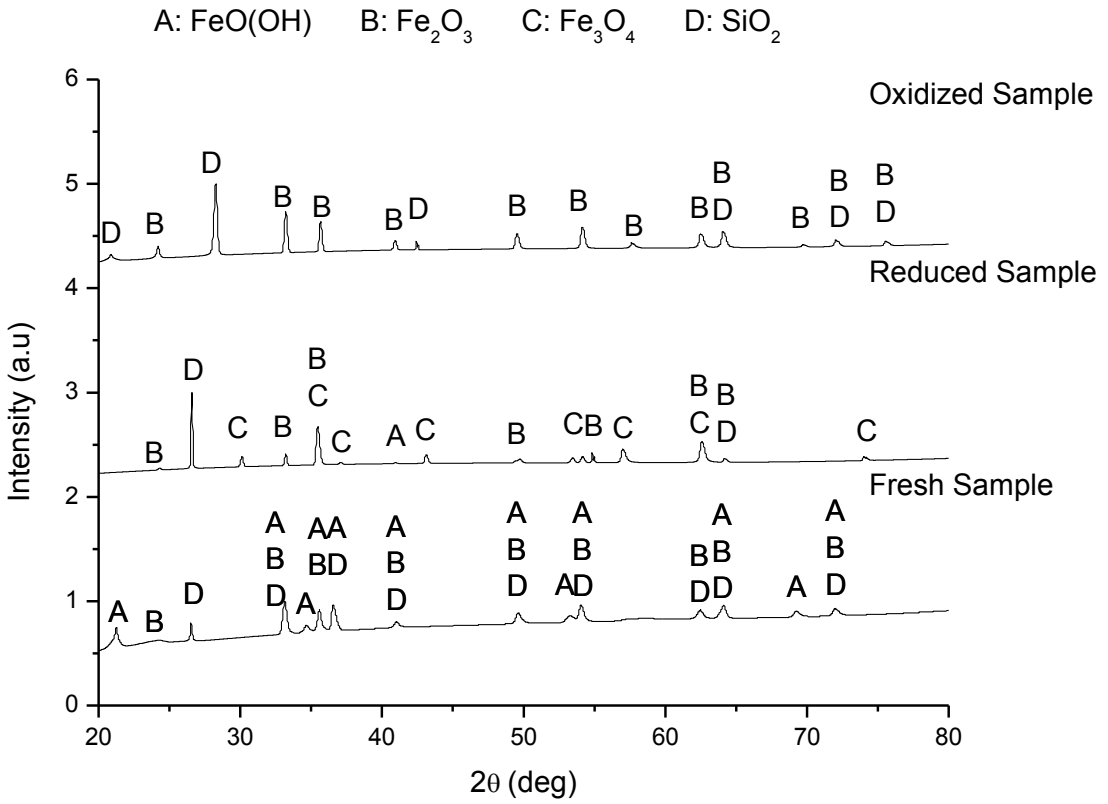

Figure 9-9 Diffractograms the fresh, reduced and oxidized samples

XRD was used to detect the presence of crystalline compounds on the surface of the fresh, reduced and oxidized OC particles. As mentioned in the methodology section, the fresh particle is primarily composed of SiO_2, FeO(OH) and Fe_2O_3, all of which can be seen to be present in the diffractogram; this OC also contains a small amount of Al_2O_3, but this was not detected by the XRD unit. The reduced and oxidized samples were found to not contain any FeO(OH) because it was irreversibly oxidized to Fe_2O_3 during the initial oxidation stage. The reduced sample contained Fe_2O_3, SiO_2 and Fe_3O_4 but the amount of Fe_2O_3 was very small as evidenced by the height of its reflections. The oxidized sample contained only Fe_2O_3 and had more pronounced reflections, which shows that the sample was fully reoxidized. Also, the peak widths of the used samples appear to be narrower, which indicates that its surface area has reduced. Based on the diffractograms, ash deposition on the OC particles was not observed and the reason for this has been mentioned in the preceding subsections.

9.3.1.9 Accelerated Surface Area and Porosimetry (ASAP)

Table 9-2 Pore structure analysis results for the fresh, reduced and oxidized samples

Sample	BET surface area (m^2/g)	Cumulative pore volume (cm^3/g)
Fresh	40.69	0.0173
Reduced	2.20	0.0042
Oxidized	1.87	0.0035

Table 9-2 shows the BET surface areas and cumulative pore volumes of the fresh, reduced and oxidized OC particles. The BET surface area of the fresh OC sample was significantly higher, about 20 times, compared to the used samples. This confirms the qualitative results obtained using the micrographs, which showed that the grains of the used OC particles had coalesced. Additionally, the surface area of the oxidized sample appears to be lower than that of the reduced sample. Since this difference is around 0.3 m^2/g, it could be due to instrumental errors. The cumulative pore volume was found to follow the trends exhibited by the surface area; the cumulative pore volumes of the used samples were lower than that of the fresh sample.

9.3.2 Effect of Reaction Temperature

This section will discuss the effect of temperature on the performance of the CLC system. As mentioned in the methodology section, the four temperatures that were investigated were 700°C, 800°C, 900°C and 1000°C. These temperatures were maintained using an electrically heated furnace. With the exception of temperature, the rest of the operation conditions were kept constant; this was done to ensure that the effect of temperature was accurately captured.

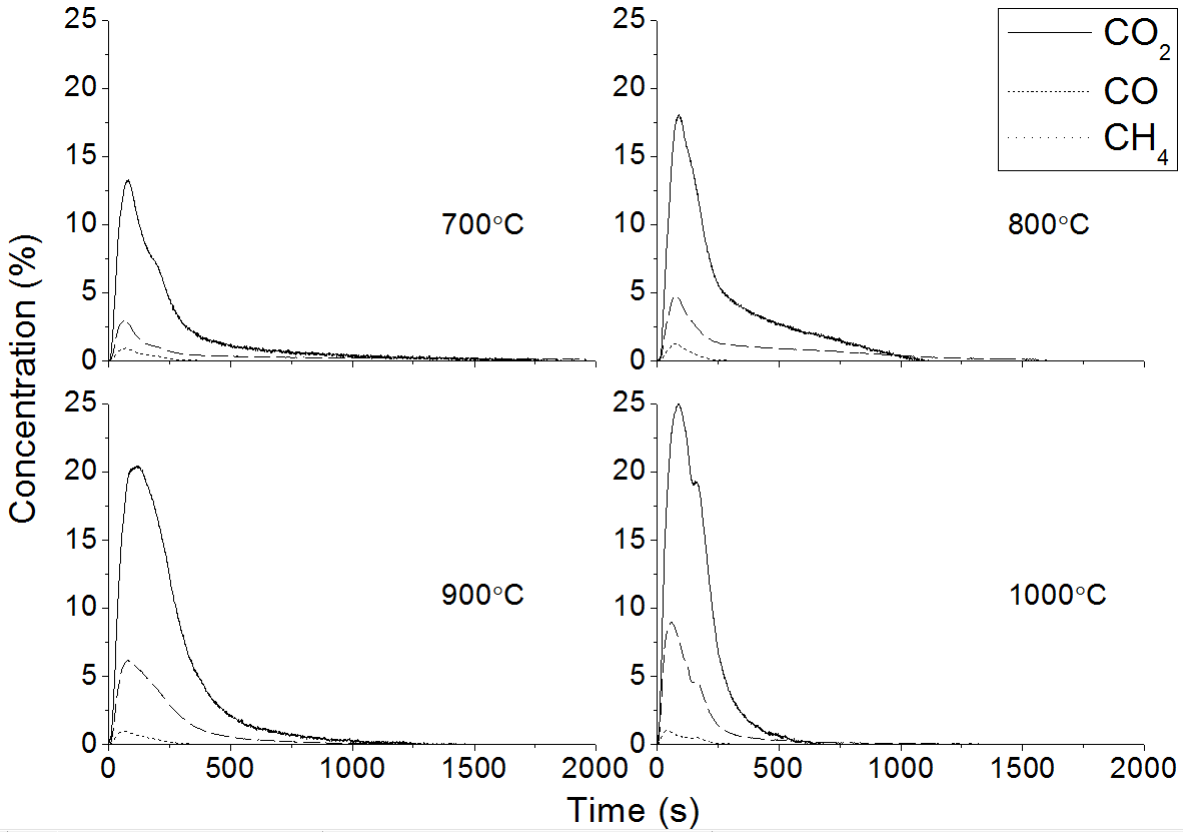

Figure 9-10 Outlet gas concentration profiles of the 5th/6th reduction reactions at different reaction temperatures

Figure 9-10 shows the outlet gas concentration profiles of either the fifth or sixth reduction reactions at four different reaction temperatures. Operational issues were encountered when carrying out some of the sixth reduction reactions and therefore the results from the fifth reduction reactions were used instead. It should be noted that the results of the fifth and sixth reduction reactions were similar for all of the investigated conditions and hence it is justifiable to use one in place of the other. It can be seen that there is a steady increase in the concentrations of CO_2 with increasing temperatures. This increased from around 13% at 700°C to around 25% at 1000°C. This represents approximately a doubling of the outlet CO_2 concentration when the temperature was increased by 300°C. The reason behind this is that a higher temperature causes an increase in both the gasification rate of the solid fuel and the rate of oxidation of the combustible gases by the OC. With respect to CO, the generated amount was also found to increase with temperature but at a greater rate relative to that of CO_2. The concentration of CO was found to be around 3% at 700°C and this increased to around 9% at 1000°C; this represents a 200% increase which is significantly higher than the 92% increase in the CO_2 concentration between the lowest and highest investigated reaction

temperatures. The concentrations of CH_4 appeared to be relatively constant for the four investigated temperatures, but the generated volumes would have been larger at higher reaction temperatures due to a greater volume of gases being evolved. Calculating the flow rate of CH_4, there is approximately a 40% increase in the peak rate at the highest temperature relative to that at 700°C. This was because the OC was unable to convert such a large volume of CH_4 over the short duration that this gas spent in the vicinity of the OC. Unlike the gasification of char, pyrolysis occurs at a much quicker rate. At higher reaction temperatures, the devolatilization rates were much higher and when coupled with the shorter residence times due to the higher temperatures, the OC was unable to convert some of these volatiles; this was most likely due to the low reaction kinetics of the OCs, meaning that its reaction rate was not quick enough to oxidize all of the evolved CH_4. As a comparison, the peak outlet flow rate of the generated gases was around 6 L/min at 700°C and this increased to 18.6 L/min at 1000°C. This confirms that the increase in the gasification rate of the fuel caused a decrease in the time needed to complete the reduction reaction from 29 minutes at 700°C to 12.5 minutes at 1000°C. In addition to faster reaction times, a higher temperature is beneficial from an operational point of view as a higher inlet temperature to the turbine would increase the overall efficiency of the power station.

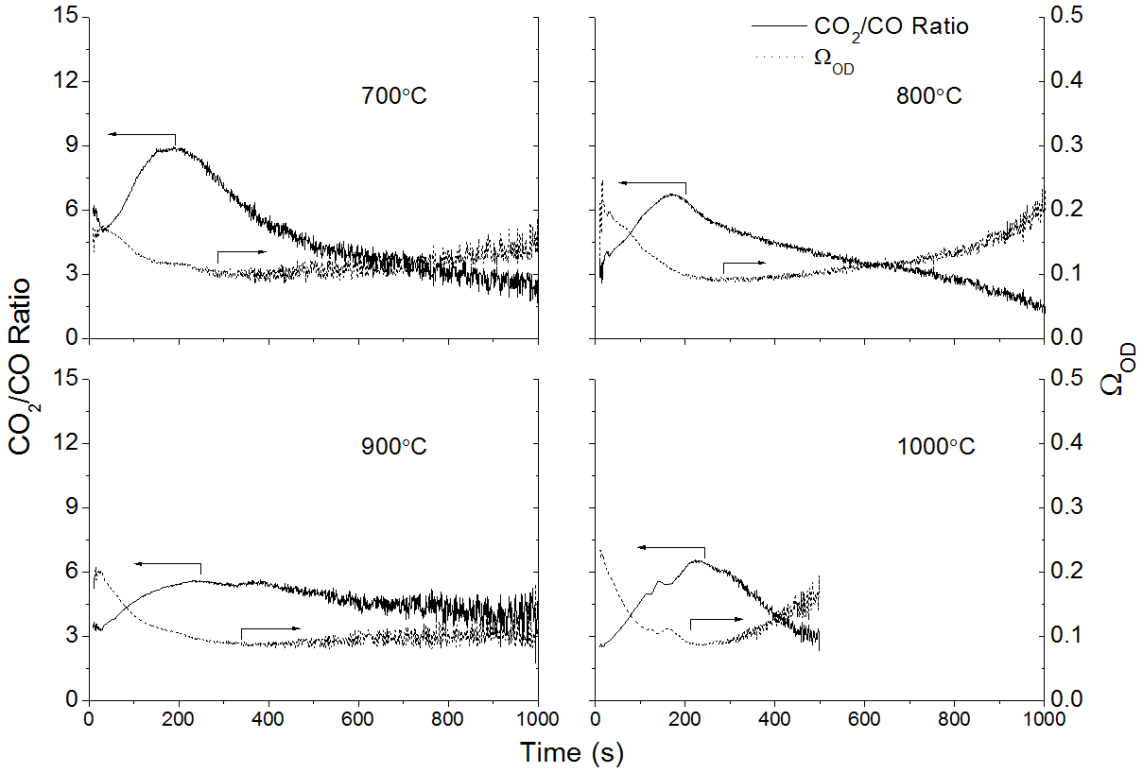

Figure 9-11 CO_2/CO ratio and oxygen demand as a function of time for the 5^{th}/6^{th} reduction reactions at different reaction temperatures

Figure 9-11 shows the ratio of CO_2 to CO as well as the oxygen demand for either the fifth or sixth reduction reactions at the four investigated reaction temperatures. In all of the investigated conditions, the CO_2/CO ratios started at a low initial value, followed by a rapid increase to the peak value after which there was a slower reduction in this value, except for the investigation at 1000°C. The highest CO_2/CO ratio was obtained at 700°C, which was due to the very small amount of CO that was generated. For the remaining three experimental conditions, the peak ratios appear to be around six; this value increased to 9 for the experiment that was performed at 700°C. At 800°C, once the peak CO_2/CO ratio was reached, it experienced a steep drop with time while an almost stable trend throughout the experiment was observed for the investigation at 900°C. At 1000°C, the obtained trend mimicked that of the 800°C investigation except with a quick drop around the 200 second mark. This shows that stable operation with consistent results can be obtained at 900°C. It should be noted that the CO_2/CO ratio is not the best performance indicator when comparing experiments conducted at different reaction conditions as it is very sensitive to variations in the CO concentration; a small change in the concentration of CO can significantly alter the CO_2/CO ratio. The oxygen demand is a better indicator of the extent of combustion in a system as it translates to the amount of oxygen that is needed to oxidize the remaining combustible gases. Most of oxygen demands started at an initial value of 0.2 due to the large amount of unreacted CH_4 in the outlet gas; this value was then found to reduce with time and stabilized around the 200 second mark. Subsequently, for all of the investigated conditions except for the one at 900°C, the oxygen demand averaged at around 0.12 and then slowly increased with time to around 0.2 towards the end of the reduction reaction. This was not so with the 900°C experiment whereby the oxygen demand was consistently below 0.1 most of the time, except for fluctuations towards the end due to noise. The reason behind this revolves around the balance between the OC's reactivity and the gasification rate of the fuel as a function of temperature. It can be seen that using the current experimental setup, the optimum reaction temperature is 900°C as a good balance between these two rates was found.

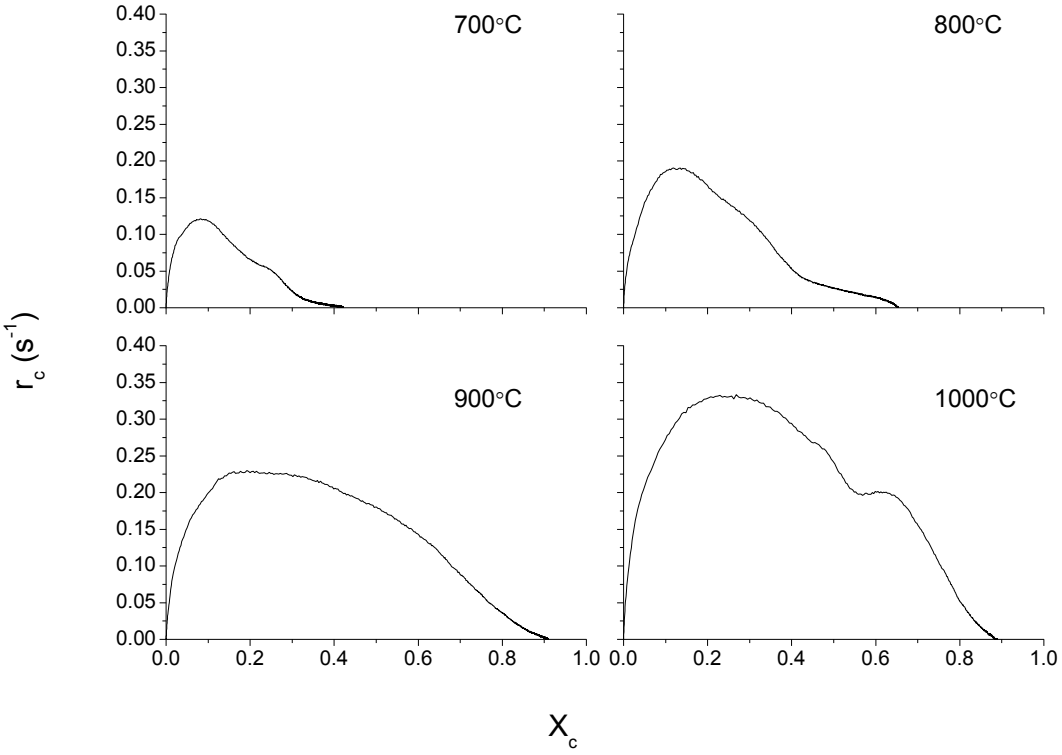

Figure 9-12 Carbon conversion rate as a function of carbon conversion for the $5^{th}/6^{th}$ reduction reactions at different reaction temperatures

The carbon conversion rate was plotted as a function of carbon conversion for the four investigated temperatures and this can be found in Figure 9-12. A trend in the extent of carbon conversion, as shown on the abscissa, can be observed here. These values were found to be 0.42, 0.51, 0.91 and 0.89 going from 700°C to 1000°C. The carbon conversion was found to increase by more than a factor of two from the lowest obtained value at 700°C to the highest at 900°C; this shows that the greatest extent of carbon conversion was obtained when the reaction temperature was 900°C. The peak carbon conversion rates were found to shift to the left at lower reaction temperatures and this was more pronounced for the experiments that were conducted at 700°C and 800°C. What this means is that the peak carbon conversion rates were found at higher carbon conversions as the reaction temperatures were increased; the reason for this will be explained in the next paragraph.

At the lower reaction temperatures of 700°C and 800°C, there was residual carbon in the reactor at the end of the reduction period. This was subsequently combusted during the oxidation stage, resulting in the lowering of the carbon conversion; this occurrence was minimal for the other two investigated reaction temperatures. The reason carbon was still

present at the end of the reduction reaction is that within a batch of coal, different lithotypes may be present; some of these lithotypes would have a greater resistance towards gasification but this resistance diminishes with increasing reaction temperatures. At 1000°C, the extent of carbon conversion was seen to reduce relative to that obtained at 900°C; this could be due to a greater degree of attrition and fragmentation of the fuel particles at higher temperatures, leading to a larger amount of fines elutriating out of the reactor. It is expected that the use of reaction temperatures in excess of 1000°C in this reactor setup would lead to further reductions in the extent of carbon conversion and this will be discussed in the paragraphs to follow. The ordinate shows the carbon conversion rate and the value of this rate at a given carbon conversion can be seen to increase as a function of temperature. The peak rate at 700°C was around 0.12 s^{-1} and this increased to 0.33 s^{-1} at 1000°C. The areas under the curves can also be seen to increase as a function of temperature and these observations will be explained with the aid of Figure 9-13.

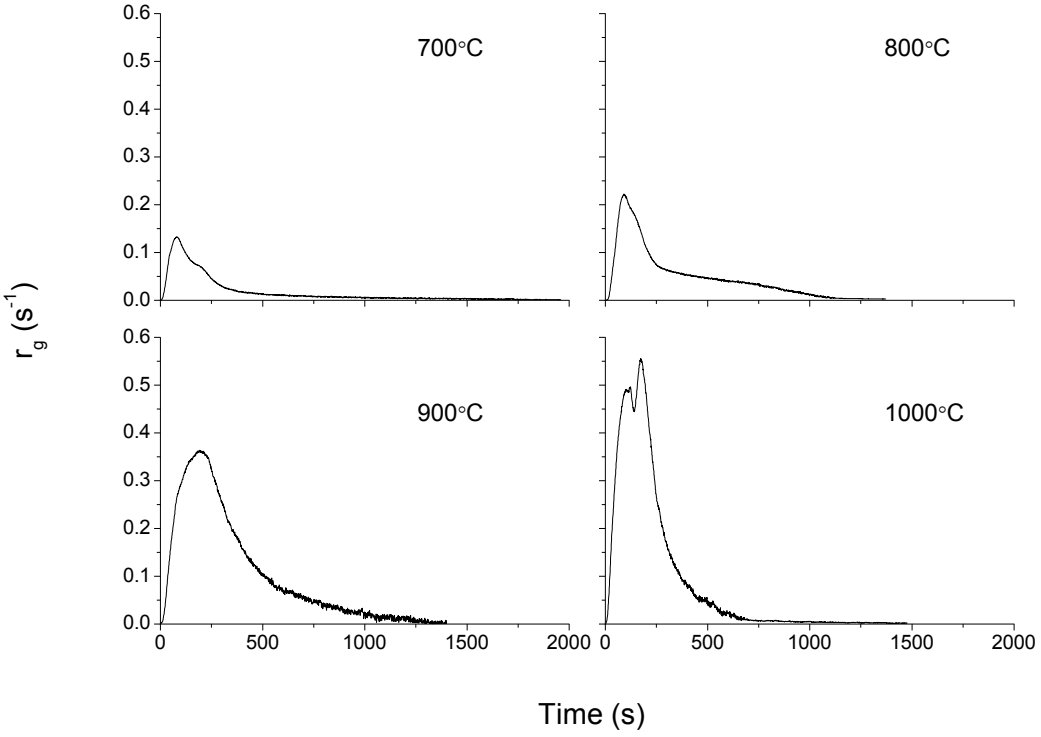

Figure 9-13 Gasification rate as a function of time for the 5th / 6th reduction reactions at different reaction temperatures

Figure 9-13 shows the gasification rate as a function of time for the four investigated reaction temperatures. The peak gasification rate was approximately 0.55s^{-1} at 1000°C while the

lowest was $0.13s^{-1}$ at 700°C; these values are to be expected based on the results and discussion above. Between these two reaction temperatures, a quadrupling in the peak gasification rate can be seen to occur. As the amount of char in the reactor reduces along the course of the reduction reaction, the gasification rate can also be seen to reduce. Focussing on experiment that was conducted at 700°C, it can be seen that the fuel had not completely gasified by the end of the reduction reaction. The reason for this is that at low temperatures, gasification is slow and this explains the results obtained between 0-1000 seconds. Beyond this time, the rate appears to gradually diminish. Low temperatures provide favourable thermal annealing conditions by graphitization while low temperature devolatilization leads to increased tar deposition on the char and lower char porosity [3]. Additionally, Schmal *et al.* [4] described the processes leading to the formation of low reactivity chars. They found that the reaction initially occurs at the external surface and the front gradually moves in, leaving behind a layer of ash; this reaction sequence is the same as that in the Shrinking Core Model (SCM). Such a process causes additional diffusional resistance for the gasification agent through the stagnant gas film around the fuel particle as well as through the ash layer, which becomes thicker with time. Therefore, as the conversion of the fuel increases, the thickness of the ash layer also increases which in turn heightens the diffusional resistance for the gasification agent through the ash layer. Additionally, the ash layer may potentially prevent certain regions of the char particle from being gasified. Hence, this results in the formation of unreactive char particles. With respect to the shift in the peak carbon conversion rates, as observed in Figure 9-12, this is possibly due to the aforementioned reason. At lower temperatures, the kinetic energy of the gasification agent is lower and this makes penetrating the ash layer more difficult. This causes the peak rate to occur earlier, corresponding to the gasification of the char particle before the ash layer becomes difficult to penetrate; this effect is not as pronounced at higher temperatures due to the higher kinetic energies of CO_2. Alternatively, tar deposition and re-polymerization alongside the lower porosity of the chars at low temperatures may contribute to this result with a greater extent of these effects being observed at lower temperatures due to lower reaction kinetics and gas velocities [5]. The deposition of tar on the surface of the char particle would lead to a reduction in the carbon conversion rate, resulting in the peak rate being shifted to the left at lower temperatures prior to the point at which tar deposition becomes significant enough to reduce the carbon conversion rate. Also, the decrease in the carbon conversion rate beyond the peak rate can be attributed to the aforementioned mechanisms. The area under the plot in Figure 9-13

represents the total amount of fuel that has been gasified; this area is the largest for the investigation that was performed at 900°C, followed by those performed at 1000°C, 800°C and lastly 700°C. The trend in this observation is similar to that which was exhibited by carbon conversion as shown in Figure 9-12.

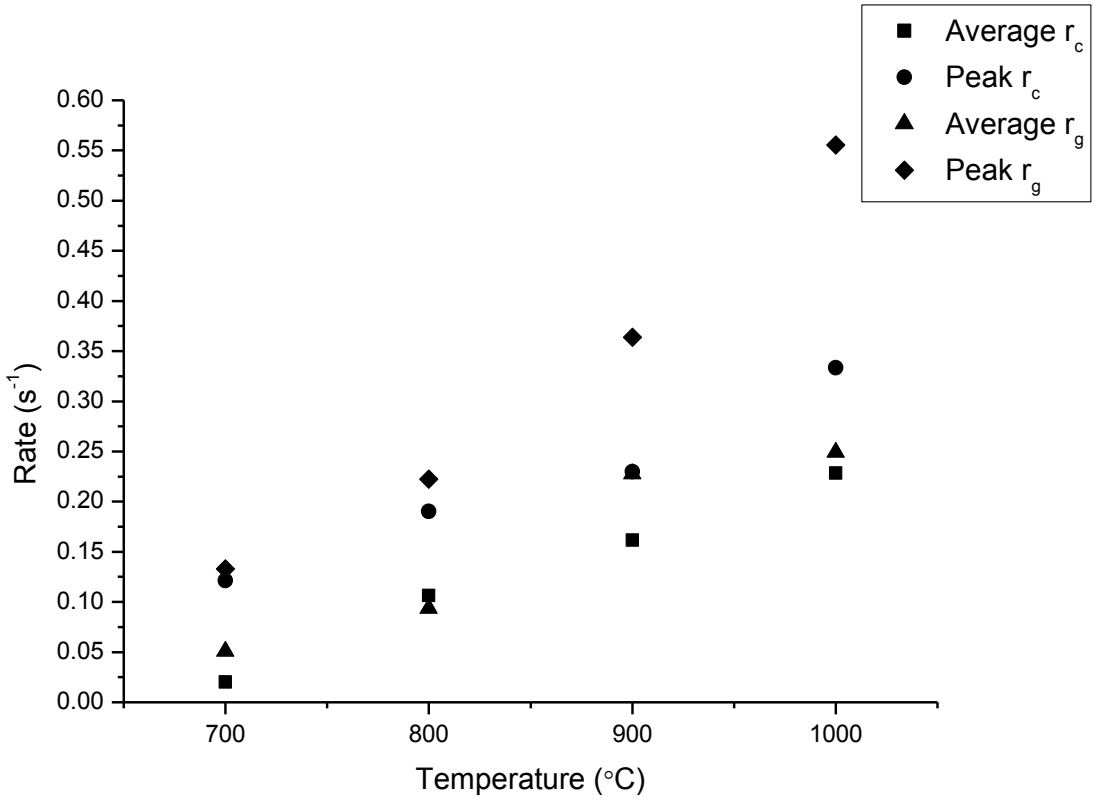

Figure 9-14 Average and peak carbon conversion and gasification rates as a function of temperature for the $5^{th}/6^{th}$ reduction reactions

Figure 9-14 shows a plot of the peak and average carbon conversion rates (r_c) and gasification rates (r_g) as a function of temperature for either the 5^{th} or 6^{th} reduction reactions. This was done to complement the results that were shown in Figure 9-12 and Figure 9-13. The peak and average carbon conversion rates were calculated for X_c values between 0 and 0.4; the peak and average gasification rates were calculated using the first 500 seconds of the gasification rate data. Most of these calculated values can be seen to vary linearly with respect to temperature, except for the peak gasification rate values, which appear to follow an exponential function. It is a well-known fact that the rate of a reaction, such as the gasification rate, increases exponentially with temperature and this can be observed here with the peak gasification rate values [6]. The reason the average rate did not exhibit the same behaviour is due to the fact that the fuel was not continuously fed over the entire course of the

reduction reaction but only over three minutes at the start of the reaction. While an increase in the reaction temperature results in an increase in the gasification rate of the fuel, the OC must have sufficient reactivity and contact with the gasification products to convert these into CO_2, increasing the CO_2 yield. Therefore, the use of a CFB reactor will allow for greater CO_2 yields to be obtained by providing increased contact between the OC and the coal-derived combustible gases.

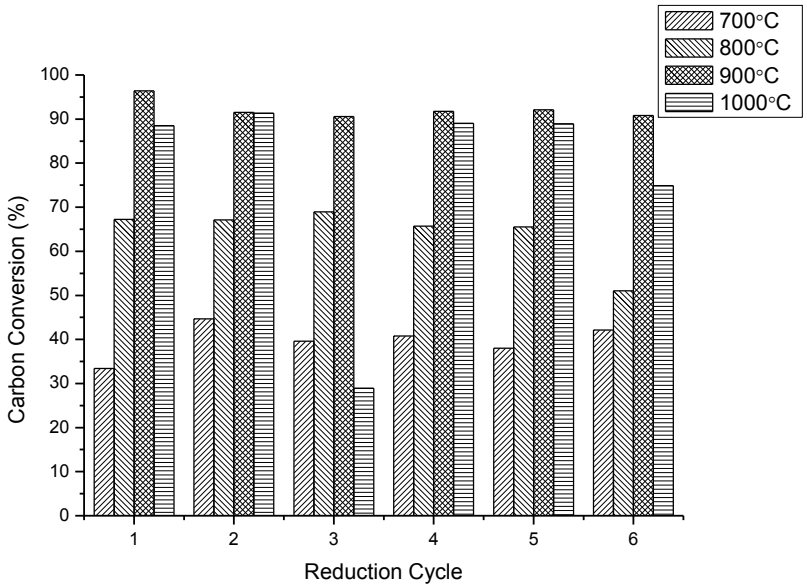

Figure 9-15 Carbon conversion over six reduction reactions for the four investigated reaction temperatures

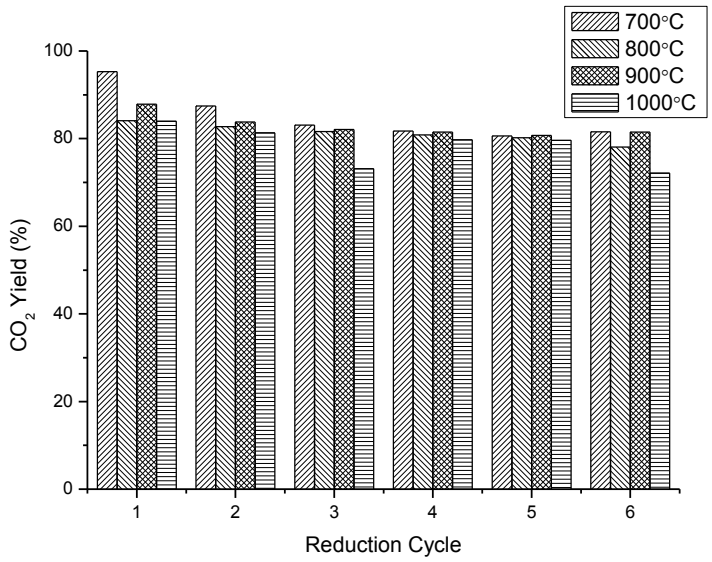

Figure 9-16 CO_2 yield over six reduction reactions for the four investigated reaction temperatures

The carbon conversions and CO_2 yields over the six reduction reactions for the four investigated reaction temperatures are shown in Figure 9-15 and Figure 9-16 respectively. As previously mentioned, operational issues were encountered at different reduction reactions due to issues with the fuel feeding or gases running out during the course of the reduction reaction. This led to the acquisition of results that did not conform to a trend. Discounting these results, the general trend will be discussed here. Focussing on the carbon conversion results as shown in Figure 9-15, it can be seen that for a given temperature the variation in these values were minimal over the six reduction reactions. Peak values were obtained for the investigation that was conducted at 900°C and these values were consistently higher than those obtained at both 800°C and 1000°C. The lower carbon conversion obtained at 700°C and 800°C is understandable as the gasification rate of the fuel was slow and therefore there would have been residual carbon in the reactor at the end of the reduction reaction, reducing the carbon conversion. As mentioned previously, it is expected that at temperatures in excess of 1000°C, the carbon conversion would reduce. The reason behind this is that as soon as the coal is introduced into the reactor, it experiences a sharp and rapid heating resulting in an almost instantaneous and violent release of the volatiles; this results in the fragmentation of the friable coal particles as vast amounts of gases quickly exit the coal particle's matrix. This fragmentation causes a greater amount of fines to be generated, which would then elutriate out of the reactor; this would invariably lead to a reduction in the carbon conversion as a portion of the carbon in the fuel would elutriate out the system in the form of coal/char fragments. What these results show is that the carbon conversion is affected by both the gasification rate and degree of fragmentation of the fuel, both of which are a function of the reaction temperature. The next figure, Figure 9-16, shows the obtained CO_2 yields. With the exception of the runs that encountered operational issues, the average CO_2 yield can be seen to be approximately the same for all of the reduction reactions at the four investigated temperatures. While minor fluctuations exist, the general observation is that the CO_2 yield is independent of temperature. This statement is justified as the CO_2 yield relates to the conversion of the coal-derived combustible gases, which is a function of the contact between the gasification agent and the OC. Therefore, for the temperature range investigated in this study, the contact between the combustible gases and the OC was the limiting factor. As such, a conversion of about 85% was obtained using this reactor setup. The other theory that this finding proves is that the oxidation of the combustible gases by the OC is not kinetically

limited and this supports the findings in literature regarding the gasification of the fuel being the rate limiting step in CLC [7].

Therefore, one of the most important aspects relating to the operation of a CLC system is to ensure that there is sufficient contact between the combustible gases and the OC. Here, the feeding of the fuel into the OC bed led to almost a doubling of the CO_2 yield compared to that obtained using the bench scale fluidized bed reactor and this serves to show the importance of the reactor configuration on the performance of a CLC system. It is expected that further performance improvements would come through the use of a CFB reactor in place of an alternating fluidized bed reactor. The conclusion of this subsection is that 900°C is the optimum temperature for use with this setup when VBC is used as the fuel.

9.3.3 Effect of Oxygen Carrier Particle Size

This subsection will discuss the effect that the OC particle size has on the performance of the CLC system; a reaction temperature of 900°C was used while all other conditions were kept constant. The smaller particle size range had a value of 106-150 μm while the larger particle size range, 150-350 μm, was the same as the one that was used in the baseline study.

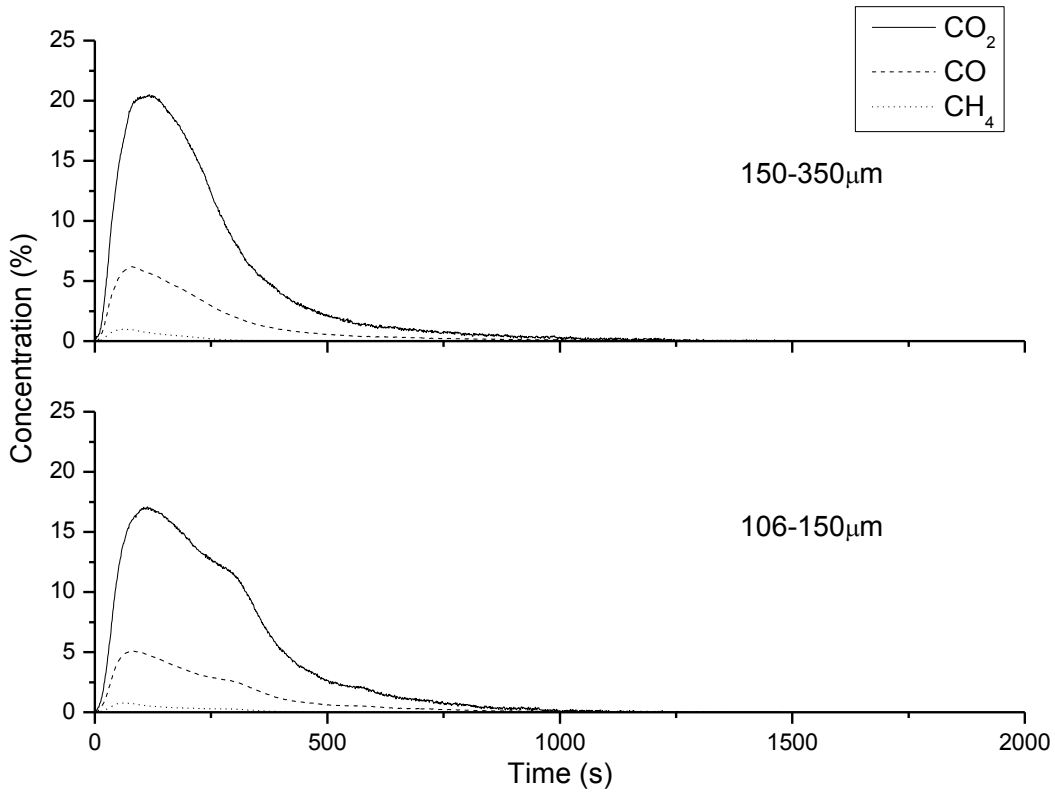

Figure 9-17 Outlet gas concentration profiles of the 6th reduction reaction using the two OC particle size ranges

The outlet gas concentration profiles at the 6th reduction reaction obtained using the two OC particle size ranges are shown in Figure 9-17. Examining the time taken for the fuel to be completely reduced, it can be seen that this value is almost similar for both the investigated cases, completing at around the 1000 s mark. The peak CO_2 and CO concentrations were found to be higher when the larger OC particle size range was used while the peak CH_4 concentrations appear to be the same for both cases. The peak CO_2 concentration obtained using the smaller OC particle size range was 17.1% and this value increased to 20.5% when the larger OC particles were used; this signifies a 20% increase in the peak CO_2 concentration between the two investigated conditions. This was most likely due to differences in the hydrodynamics in the reactor, particularly the way in which the particles in the two size ranges were fluidized, as all other parameters were kept constant; this will be discussed in the subsequent paragraphs.

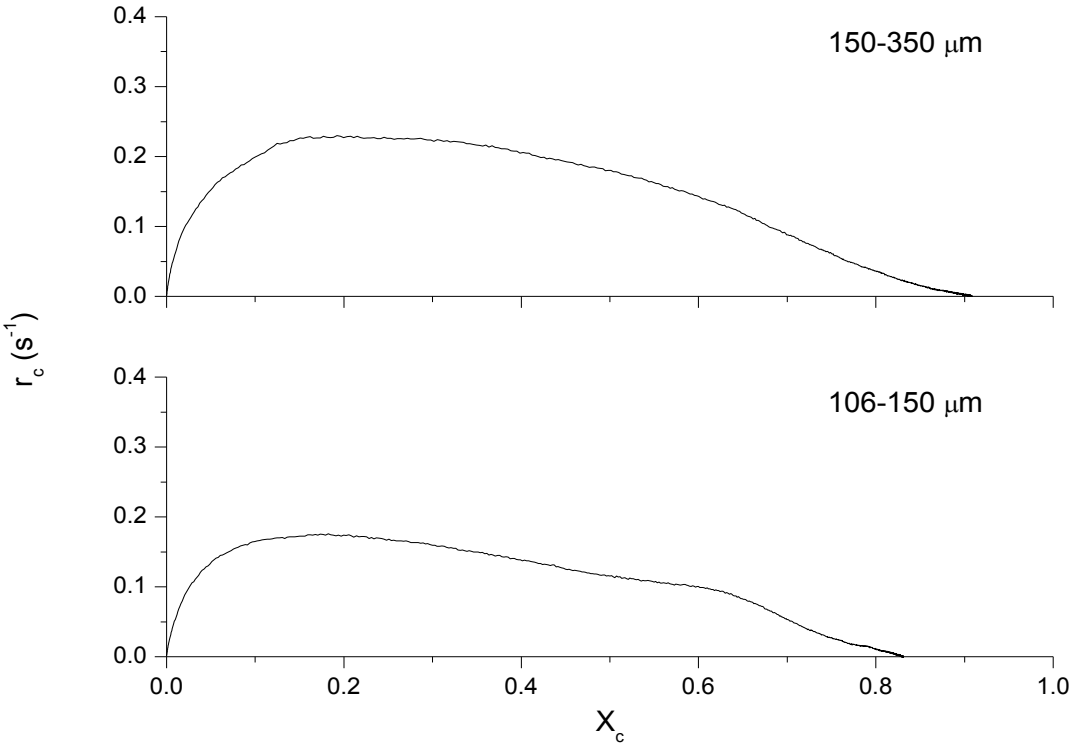

Figure 9-18 Carbon conversion rate as a function of carbon conversion for the 6th reduction reaction using the two OC particle size ranges

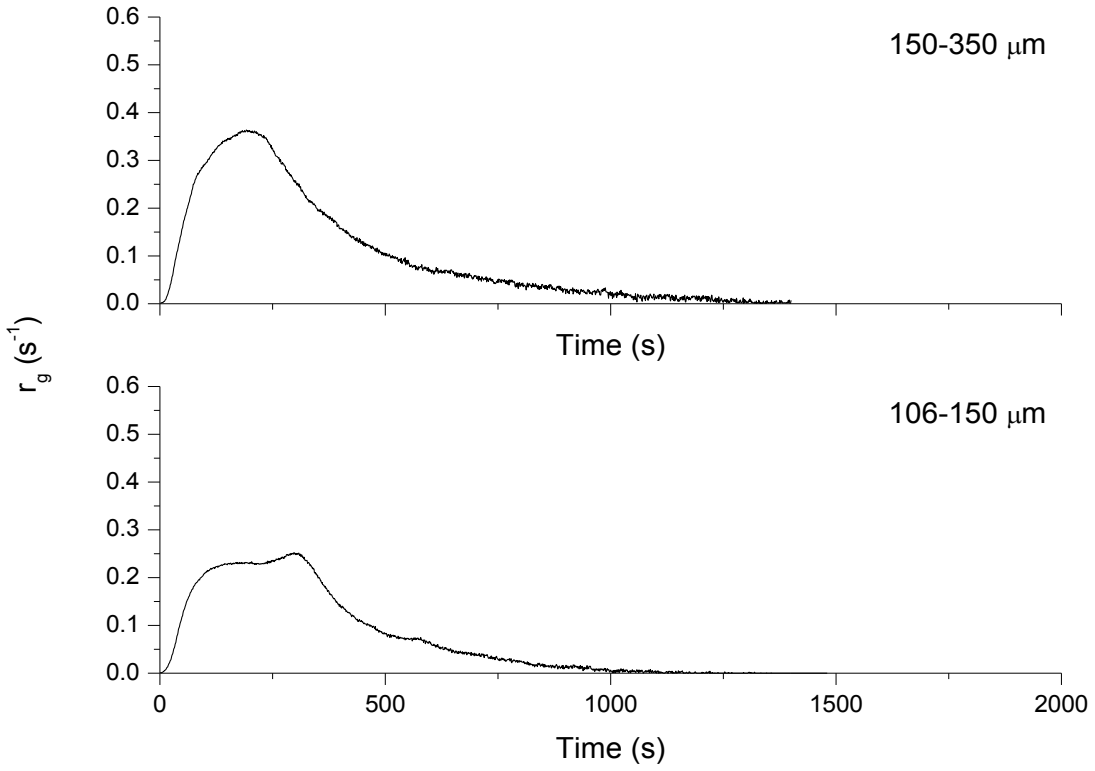

Figure 9-19 Gasification rate as a function of time for the 6th reduction reaction using the two OC particle size ranges

The plot of the carbon conversion rate as a function of carbon conversion and the gasification rate as a function of time for the 6th reduction reaction using the two OC particle size ranges can be found in Figure 9-18 and Figure 9-19 respectively. The peak carbon conversion rates were found to be 0.18 s^{-1} and 0.23 s^{-1} for the smaller and larger OC particle size ranges respectively; this represents a 28% increase in the peak rate between the two investigated conditions. Additionally, the extent of carbon conversion at the sixth reduction reaction was approximately 0.91 and 0.83 for the smaller and larger OC particle size ranges respectively.

The OC particles in the smaller particle size range would form a larger expanded bed upon fluidization relative to that obtained using the larger particle size range. Additionally, the smaller OC particles would have higher average instantaneous velocities on account of their smaller diameters as the fluidization gas flow rate was kept constant. The higher average instantaneous particle velocities coupled with the increased number of OC particles using the smaller OC particle size range could have led to increased attrition of the fuel particles; this would subsequently result in a greater extent of elutriation of the fuel particles out of the reactor. Additionally, Figure 9-19 also shows a disparity in the peak gasification rates which increased from 0.25 s^{-1} to 0.36 s^{-1} when the larger OC particle size range was used, signifying

an increase of about 44% between these two conditions. As previously mentioned, the reason the peak rate is discussed instead of the average rate is because the investigations performed using current experimental setup involved the fuel being fed in batches instead of being continuously fed. Discussing the average rates would not allow for the performance of the various investigated conditions to be adequately compared.

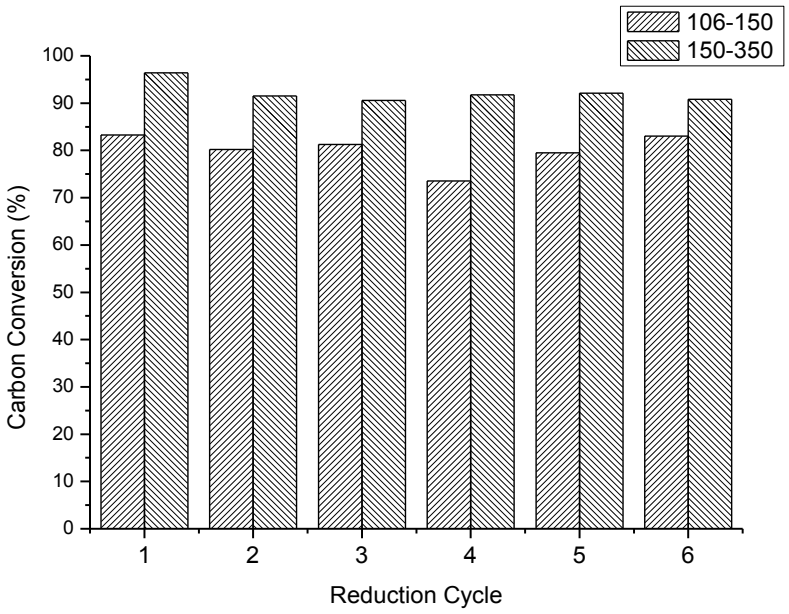

Figure 9-20 Carbon conversion over six reduction reactions using the two OC particle size ranges

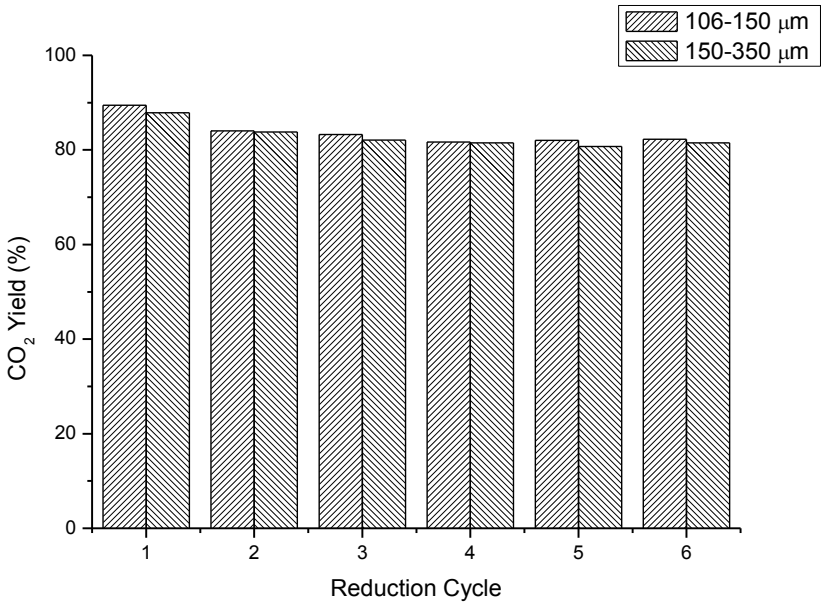

Figure 9-21 CO_2 yield over six reduction reactions using the two OC particle size ranges

The carbon conversions and CO_2 yields over the six reduction reactions for the two investigated OC particle size ranges are shown in Figure 9-20 and Figure 9-21 respectively. The obtained results from the former figure shows the carbon conversion of the fuel in the presence of the smaller OC particle size range to be consistently lower when compared to that obtained using the large particle size range; the differences in the carbon conversions between the two investigated OC particle size ranges were typically around ten percentage points. This figure shows that the larger OC particle size range is favourable from a carbon conversion point of view.

On the other hand, Figure 9-21 shows the obtained CO_2 yields to be very similar for the two OC particle size ranges that were investigated. Therefore, based on the abovementioned discussions, the larger OC particle size range appears to be a better candidate relative to the smaller OC particle size range on account of the higher extent of carbon conversion obtained using the former; additionally, the average and peak carbon conversion and gasification rates were found to be higher when the larger OC particle size range was used.

9.3.4 Effect of Fuel Type

This subsection will detail how the use of different fuel types affects the CLC process. The first fuel that was used in this investigation was Yallourn coal while the second was a char generated from Yallourn coal. In essence, this investigation studies the effect of coal rank as the char can be taken to be a high rank coal due to its negligible volatile content. All the investigations were performed at the same experimental conditions to allow the results obtained using the different fuels to be accurately compared.

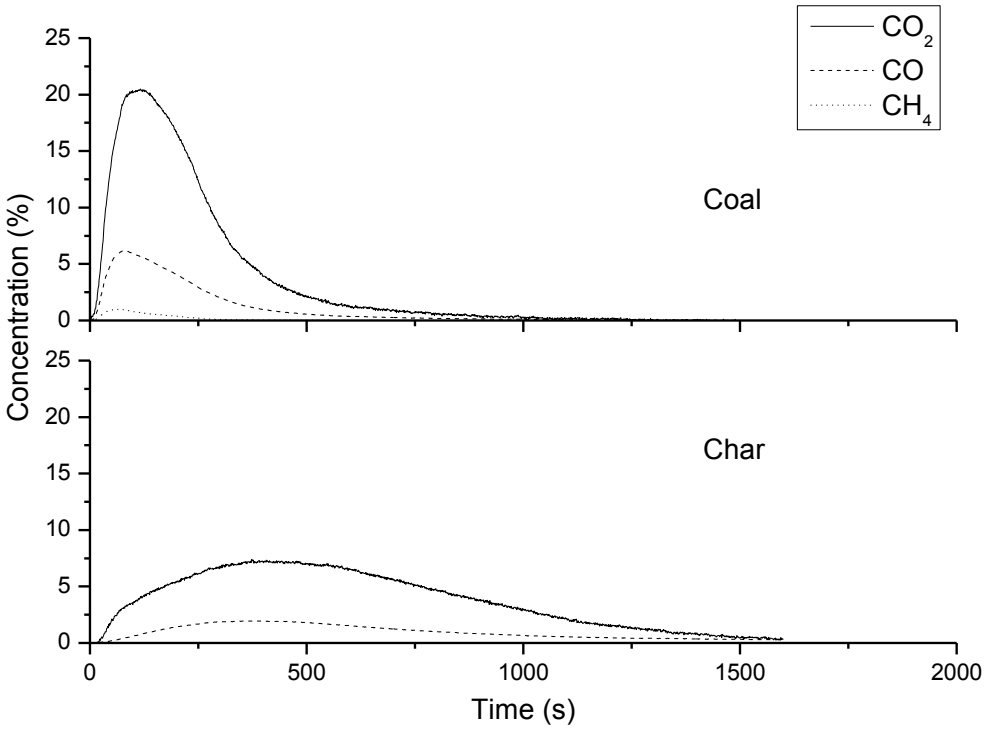

Figure 9-22 Outlet gas concentration profiles of the 6th reduction reaction using coal and char

The outlet gas concentration profiles at the 6th reduction reaction obtained using the two fuels are shown in Figure 9-22. The outlet gas concentration profile for the study employing coal has been delineated in an earlier subsection and will be used here to compare with results obtained using char. Firstly, no CH_4 was detected during the course of the reaction in which char was used and this proves that the char was mostly devolatilized; only CO_2 and CO were detected in the outlet gases when char was used as the fuel. Examining the abscissa in the plot that was constructed for when char was used as the fuel, there is a slight lag in the time taken for the gases to be detected by the online gas analyser; this is due to the low reactivity of the char, which is supported by the low peak CO_2 concentration that was obtained. The peak CO_2 concentration obtained for when coal was used was approximately 200% higher relative to that which was obtained using char. The structural and chemical changes that the char had undergone during the reaction that was used to generate it resulted in a reduction in its reactivity compared to that of coal. This subsequently caused an increase in the time needed to convert the same amount of char relative to the time required by coal. It has been said that the reactivity of a char sample can be attributed to its inorganic constituents and porosity [8]. Also, it is a well-known fact that the reactivity of a char increases with a decrease in the rank of the parent coal. Additionally, some researchers have found that with an increase in the

temperature used to prepare the char, the influence of the rank of the parent coal decreases and this leads to the formation of low reactivity chars [9, 10]; this reduces the intrinsic reactivity of the char, which could explain the behaviour observed here as the char was prepared at 1000°C.

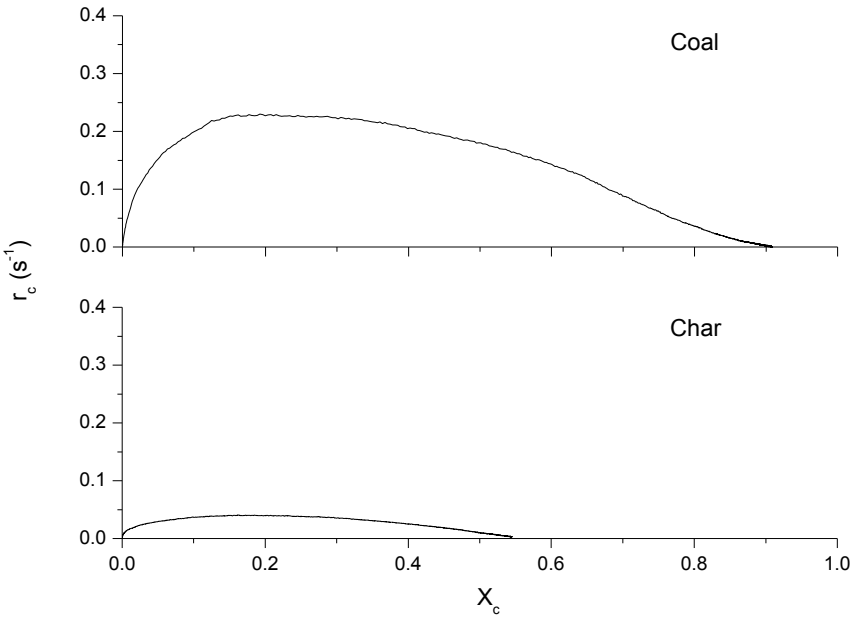

Figure 9-23 Carbon conversion rate as a function of carbon conversion for the 6th reduction reaction using coal and char

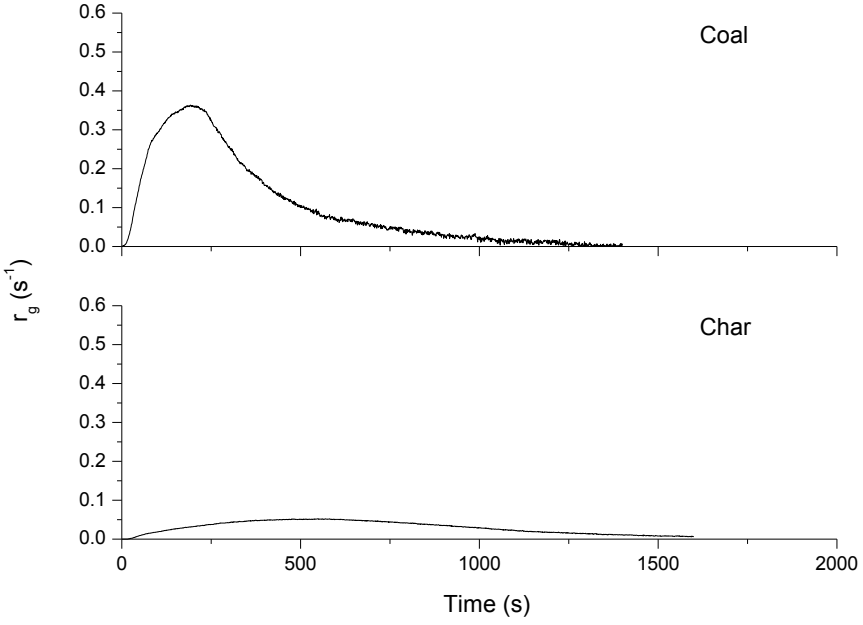

Figure 9-24 Gasification rate as a function of time for the 6th reduction reaction using coal and char

The plot of the carbon conversion rate as a function of carbon conversion can be found in Figure 9-23 while Figure 9-24 shows the plot of the gasification rate as a function of time. Based on the results shown in Figure 9-23, there is a very large difference in the calculated carbon conversion rates that were obtained for the two fuels that were used. When coal was used as the fuel, the peak carbon conversion rate was approximately five times higher than that obtained using char; this shows the significance of the rank of the fuel on its reactivity. When coal was used as the fuel instead of char, a 70% increase in the extent of carbon conversion was observed. This observation is supported by the reasons mentioned above with respect to the formation of low reactivity chars due to the use of high char preparation temperatures. It is also worth noting that the ash content of the char is approximately twice that of the coal. The long residence time that was used to prepare the char sample could have potentially led to the formation of a layer of ash which in turn increased the diffusional resistance for CO_2 and reduced the gasification rate of the char, as mentioned in Section 9.3.2 above. As the char was gasified, the physical front of the particle was consumed and this caused the reaction front to move towards the core of the char particle; as this reaction front progressed towards the core, the effect of the ash layer became more significant, resulting in a reduction in the reactivity of the char. Similarly, Figure 9-24 shows that the peak gasification rate achieved using coal was approximately 600% higher than that obtained using char; this factor is similar to that found when the peak carbon conversion rates obtained using the two fuels were compared. Additionally, the coal sample was found to have been completely consumed by 1400 s but char was still found to be present in the reactor at the 1600 s mark; this difference is due to the fact that the coal sample is more reactive than the char sample.

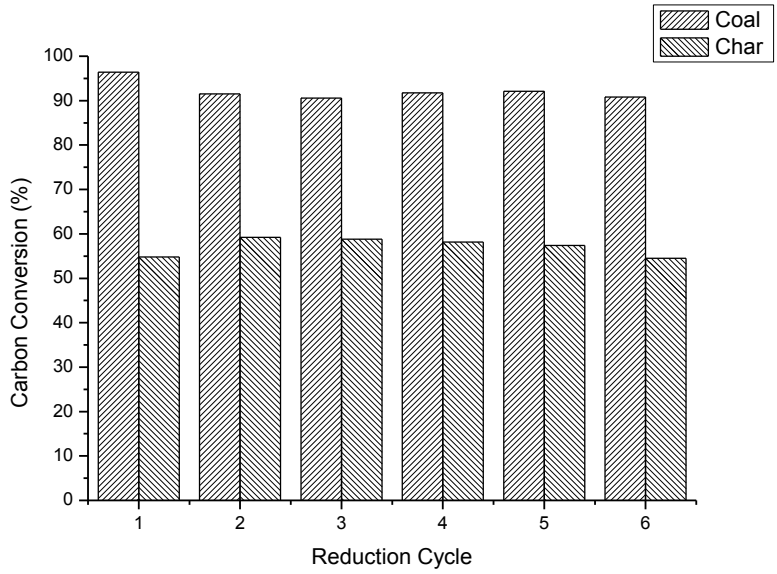

Figure 9-25 Carbon conversion over six reduction reactions using coal and char

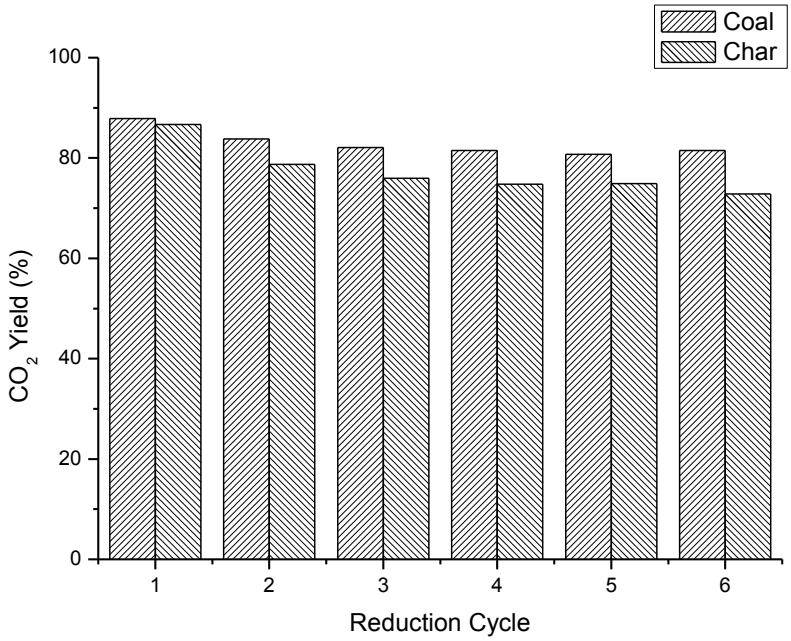

Figure 9-26 CO_2 yield over six reduction reactions using coal and char

The carbon conversions and CO_2 yields over the six reduction reactions using the two fuels are shown in Figure 9-25 and Figure 9-26 respectively. It can be seen that the carbon conversion obtained using char was much lower than that obtained with coal; this is the same as that which has been previously observed in Figure 9-23. The average extent of carbon conversion was 57% and 91% for when the char and coal were used respectively; this result is relatively consistent between the different runs. The low carbon conversion obtained using

char was due to the fact that a large portion of this char remained in the reactor at the end of the reduction reaction with a sizeable quantity also found in the catch pots.

In Figure 9-26, the CO_2 yield over multiple reduction reactions can be observed to be relatively stable. Numerically, the average CO_2 yields were found to be 77% and 81% for when the char and coal were used respectively. Again, the variation in the CO_2 yield was not significant, similar to that observed in Figure 9-16 and this was ascribed to be due to the contact between the OC and the coal-derived combustible gases; this contact should not vary with the fuel type and the obtained results confirm this.

9.3.5 Effect of Longer Duration Operation (35 Redox Cycles)

This subsection will study and discuss the potential changes in the performance of the CLC system over 35 redox reactions at 900°C using VBC as the fuel and an OC particle size range of 150-350 µm. The attrition rate and reactivity of the OC will also be discussed here. The 35 redox reactions were performed over 40 hours and this took a total of 6 days to complete. The following shows the breakdown of the runs that were performed for each of the days: 1-6, 7-12, 13-18, 19-24, 25-30 and 31-35. The results obtained from the 1st, 12th, 24th and 35th reduction reactions will be discussed here.

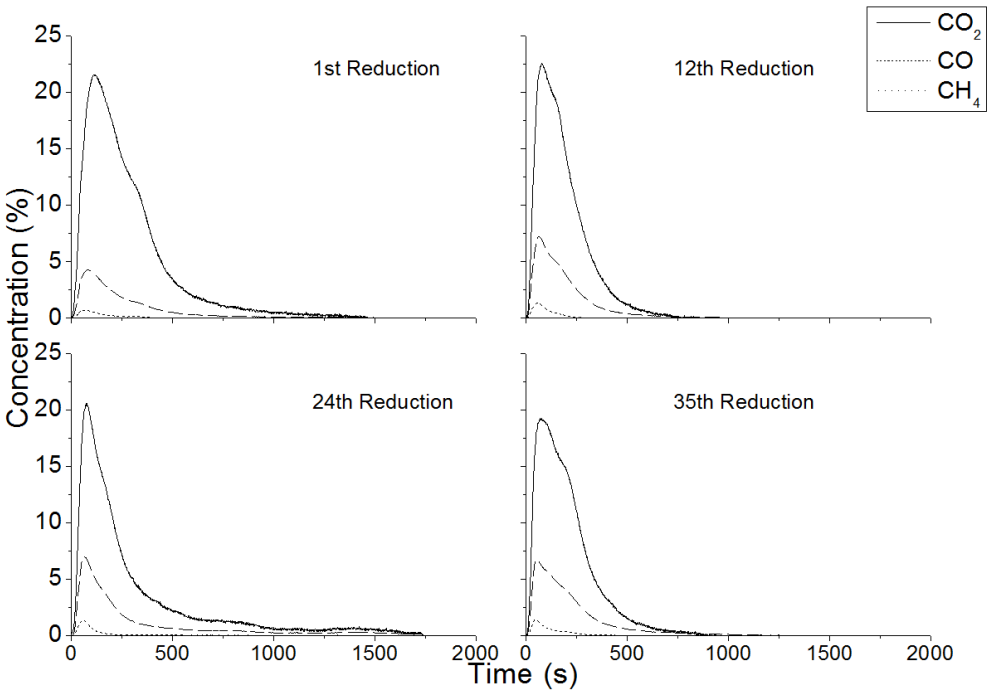

Figure 9-27 Outlet gas concentration profiles of the 1st, 12th, 24th and 35th reduction reactions

Figure 9-27 shows the outlet gas concentration profiles for the four reduction reactions that will be the focus of this subsection. Going from the 1st reduction reaction to the 12th, there is

a slight increase in the peak CO_2 concentration, but beyond this point a decrease in the peak CO_2 concentrations was observed in the 24th and 35th reduction reactions. Also, in the first reduction reaction, the peak CO concentration had a value of less than 5% but this increased to between 6.5-7.5% in the other three reduction reactions; this same behaviour is observed for CH_4 as well. It can be seen that the best performance was obtained in the first reduction reaction but beyond this the decrease in the concentration of CO_2 coupled with the increase in the concentration of CO signify that the performance was relatively similar in the other three reduction reactions. With respect to the 24th reduction reaction, the time taken for the reaction to complete was longer compared to the other reduction reactions as an operational issue relating to fluidization was experienced. The reduction in the peak CO_2 values with the corresponding increase in concentrations of CO and CH_4 as the reduction cycles progressed could be due to coalescence of the grains in the OC particles beyond the first reduction reaction as well as a reduction in the bed mass over the multiple cycles due to attrition and subsequent elutriation of the OC particles. It is worthwhile noting that no make-up OC was added into the reactor over the course of the 35 redox cycles. Taking the representative values of the time taken to complete these four reduction reactions, it can be seen that this is less than 1000 seconds, which is about 17 minutes; typically, this period is dictated by the duration required by the coal to be completely gasified, which is the rate limiting step.

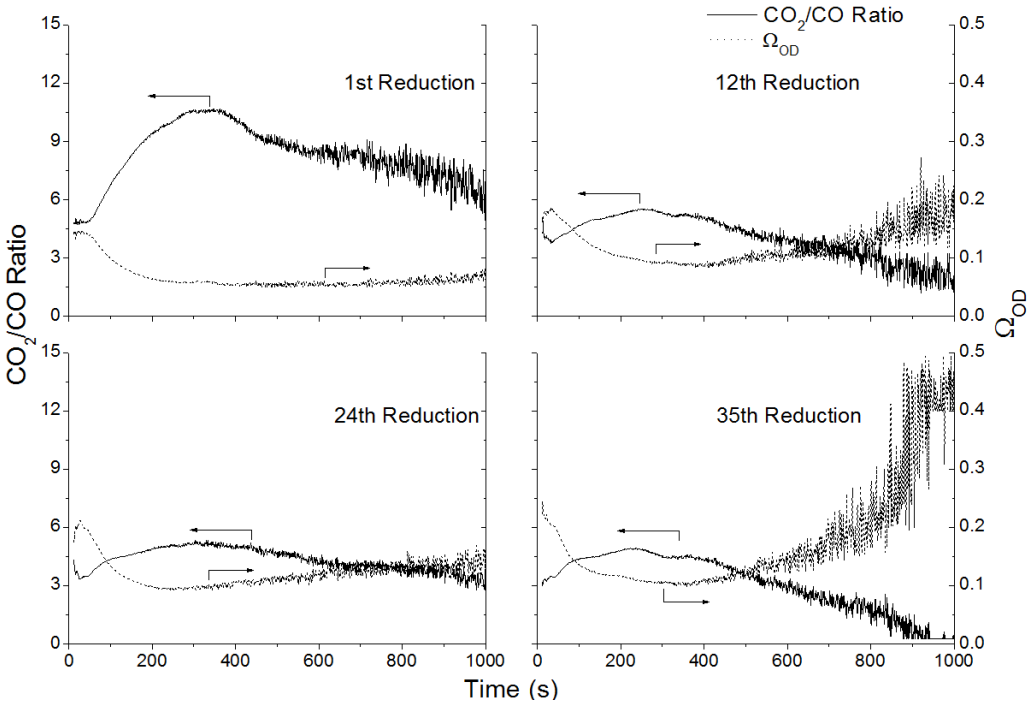

Figure 9-28 CO_2/CO ratio and oxygen demand as a function of time for the 1st, 12th, 24th and 35th reduction reactions

The plot of the CO_2/CO ratio and oxygen demand as a function of time over the four investigated reduction reactions is shown in Figure 9-28. There is an appreciable reduction in the former parameter going from the first reduction reaction to the rest. Although the peak CO_2 concentration at the 12th reduction reaction was higher than that at the 1st reduction reaction, as shown in Figure 9-27, its peak CO_2/CO ratio was significantly lower and similar to those of the 24th and 35th reduction reactions; this is due to the higher concentrations of CO that was generated in the three reduction reactions other than the first. Additionally, it can be seen from the above figure that the oxygen demand is virtually a mirror image of the CO_2/CO ratio for most parts of the four reduction reactions. This is because the oxygen demand is a function of the concentrations of CO_2, CO and CH_4, but the concentration of CH_4 does not affect the oxygen demand beyond the first part of the reduction reaction i.e., after the coal has undergone pyrolysis. The small CO_2/CO ratio and large oxygen demand towards the end of the 35th reduction reaction is due to noise. The char particles become smaller over the course of the gasification reaction, resulting in the generation of fines. As these fines elutriate, it may also be gasified, producing CO that does not contact the OC, leading to the observed small CO_2/CO ratio and large oxygen demand. Alternatively, this phenomenon could be explained by the attrition that the OC particles progressively experience over the course of the 35 redox reactions and this will be discussed in the subsequent paragraphs.

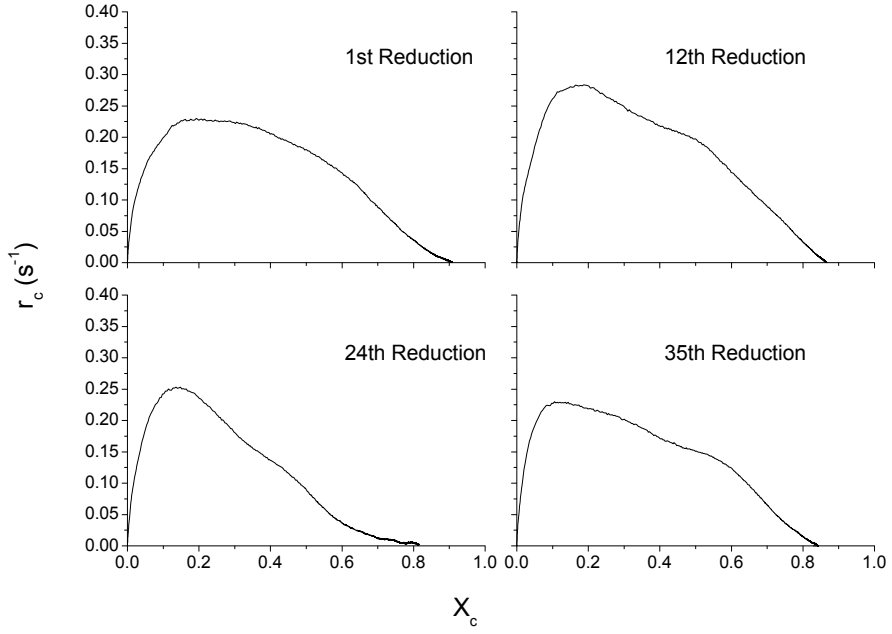

Figure 9-29 Carbon conversion rate as a function of carbon conversion for the 1st, 12th, 24th and 35th reduction reactions

The plot of the carbon conversion rate as a function of carbon conversion is shown in Figure 9-29. This figure shows that the peak carbon conversion rate is slightly lower than $0.25s^{-1}$ at the 1st, 24th and 35th reduction reactions, but it increases to $0.28s^{-1}$ at the 12th reduction reaction. As previously mentioned, this could have been due to an issue with the fuel feeding that was experienced during the 12th reduction reaction; the fuel may have been introduced into the reactor at a rate faster than 16.7 g/min. This would explain the higher peak rate that was obtained as more fuel was available to be gasified. Besides this, the extent of carbon conversion was lowered beyond the first reduction reaction to the other three reduction reactions. Initially, this value was found to be approximately 0.9 and reduced to around 0.83 at the 35th reduction reaction. As mentioned previously, the extent of carbon conversion should not vary significantly from one reduction reaction to another as it is a function of the gasification of the fuel. Therefore, one aspect could have played a role in this observed phenomenon; the progressive attrition of the OC particles over the course of the 35 redox cycles would have led to the generation of smaller OC particles which may have caused a greater degree of attrition in the coal particles. This would lead to a larger amount of fragmented fuel particles being elutriated out of the reactor, reducing the extent of carbon conversion, similar to that observed when using the smaller OC particles; this will be confirmed in the paragraphs to follow using results obtained from the particle size analysis of the OC particles that were collected at the end of each run.

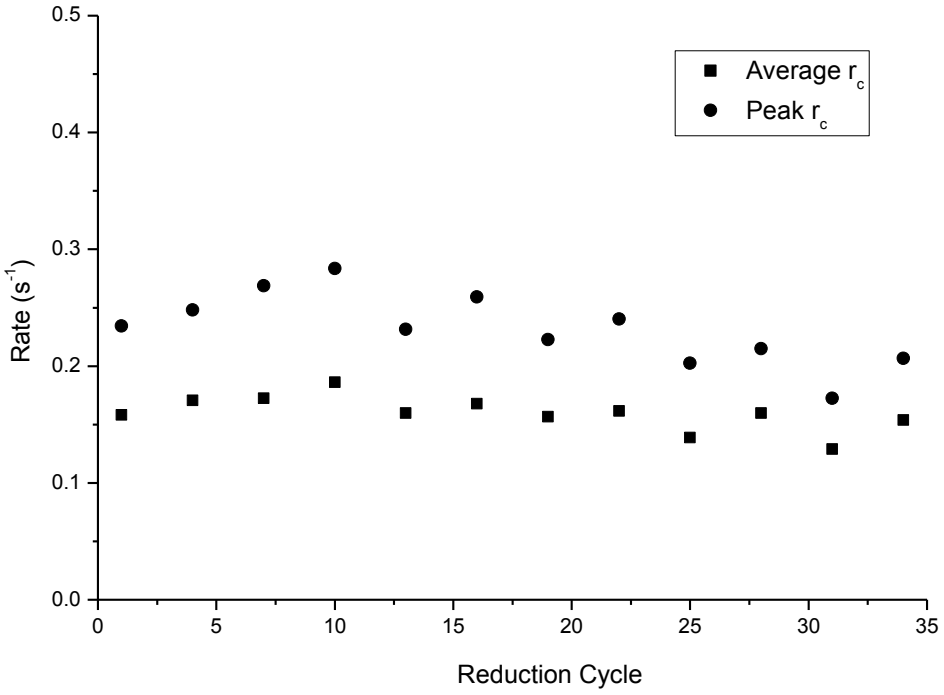

Figure 9-30 Average and peak carbon conversion rates over 35 reduction reactions

Figure 9-30 shows the peak and average carbon conversion rates obtained over 35 reduction reactions. While minor fluctuations exist, due to operational issues which were encountered, both the peak and average rates can be seen to decrease going from the 1st cycle to the 35th cycle. This is most likely a direct consequence of the attrition of the OC particles which affects these rates either due to a reduction in the OC bed mass or increased fragmentation of the fuel particles due to heightened collisions with the OC particles. Attrition of the fuel particles could have been accelerated by the fragmented OC particles, the extent of which would have increased with progressive redox cycles.

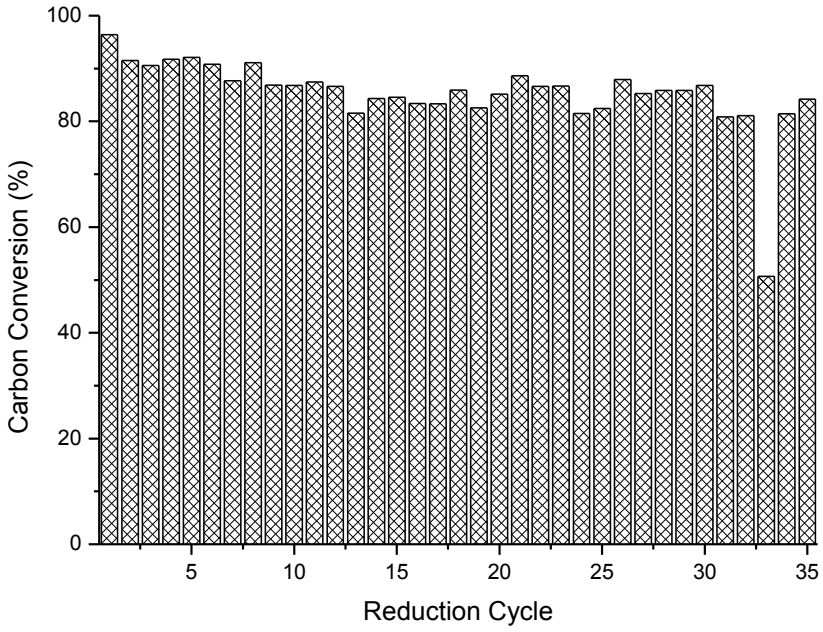

Figure 9-31 Carbon conversion over 35 reduction reactions

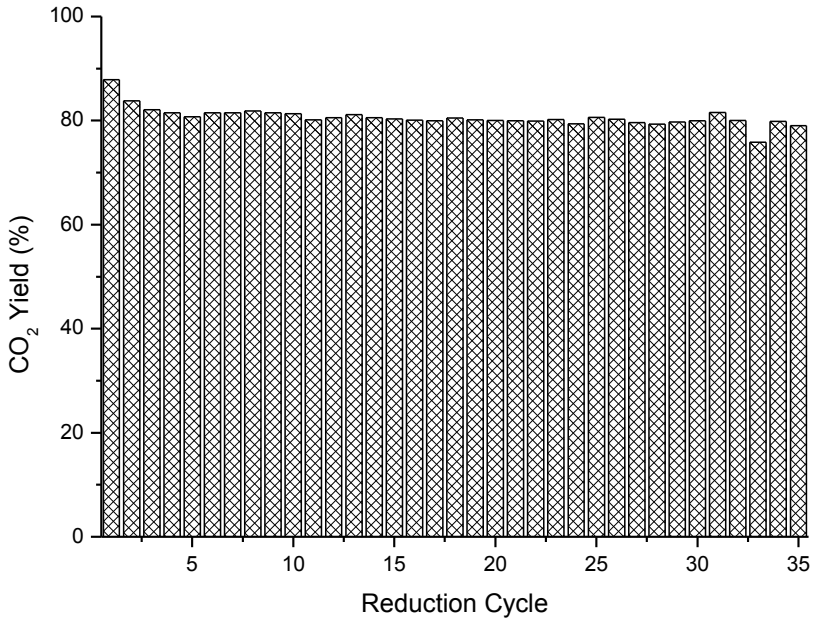

Figure 9-32 CO_2 yield over 35 reduction reactions

The carbon conversion and CO_2 yield over the 35 reduction reactions are shown in Figure 9-31 and Figure 9-32 respectively. The average carbon conversion was found to be 86.3% with a standard deviation of 3.7% when disregarding the results from the 33rd reduction reaction and the reason for this will be discussed below. There is also a slight drop in the carbon conversion between the 1st and 6th reduction reactions, but beyond this the carbon conversions can be seen to be relatively similar. There was a large drop in the carbon conversion at the 33rd reduction reaction which was due to issues with the fuel feeding. It was an isolated issue and the carbon conversion was found to return to the normal value at the 34th reduction reaction. The CO_2 yield on the other hand can be seen to be exceptionally stable, with an average value of around 81%; this is similar to the values found in the preceding subsections for the different investigated conditions. This result confirms that the CO_2 yield is dependent on the contact between the coal-derived combustible gases and the OC, which should not change with increasing redox cycles. Therefore, to ensure higher CO_2 yields and carbon conversions, two aspects need to be considered. Firstly, the use of a CFB reactor would serve to increase both of these values. In CLC, the residence time of the combustible gases and the contact between these gases and the OC are both very important parameters, both of which can be increased by using a CFB reactor. Secondly, periodic introduction of make-up OC particles into the reactor would also help to compensate for the fragmented and elutriated OC particles.

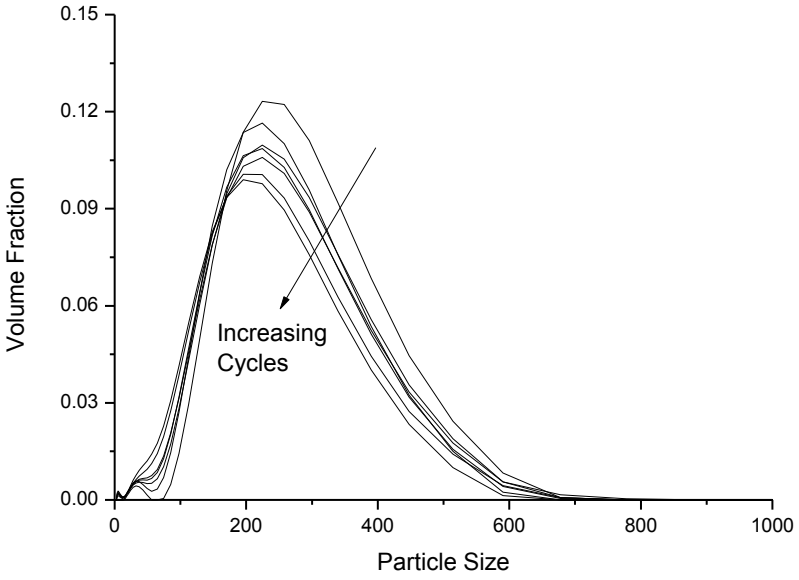

Figure 9-33 Volume fraction as a function of particle size for the fresh OC sample and the used OC samples after the 6th, 12th, 18th, 24th, 30th and 35th reduction reactions

Figure 9-33 shows the results obtained from the particle size analysis that was conducted for the fresh OC sample as well as the used OC samples from the 6th, 12th, 18th, 24th, 30th and 35th reduction reactions. This figure shows that with increasing redox cycles, the average OC particle size decreases; this is due to particle attrition, which typically occurs in a fluidized bed combustor. The fresh OC sample had the highest volume fraction at a mean particle size of 224 µm. This value dropped to 195 µm at the 35th reduction reaction, representing a 13% decrease in this value relative to that obtained using the fresh OC particles. Upon closer examination of the 224 µm mean particle size, it can be see that the volume fraction for this size drops from 12.3% in the fresh sample to 10.1% in the used sample from the 35th reduction reaction. Additionally, the volume weighted mean diameter, D[4, 3], was calculated. The fresh OC particles had a volume weighted mean diameter of 249 µm, which decreased to 204 µm for the used OC particles that were collected at the end of the 35th reduction reaction. This represents an 18% reduction in the volume weighted mean diameter over a course of 35 redox cycles as attrition of the OC particles would also occur during the oxidation reaction. The other observable feature is that with progressing redox cycles, the volume fraction in the size range of 10-60 µm was found to increase. This is characteristic of attrition, with some amount of the fragmented particles remaining in the bed at the end of the reaction. As such, this means that make-up OC particles would be needed to replace the generated fines. What

these results show is that attrition did indeed occur and was responsible for the reduction in the carbon conversion of the fuel with progressive reduction reactions due to the generation of a larger amount of fuel fines from the collision between the fragmented OC particles and fuel particles.

9.4 Conclusions

The effects of temperature, OC particle size range and fuel type on the performance of a CLC system were investigated using a 10kW_{th} alternating fluidized bed reactor. Additionally, a long term investigation was performed over 35 redox cycles. The degree of attrition of the OC particles over the 35 cycles was determined using particle size analysis. NO_x emissions were quantified for the baseline experiment at 900°C, while a carbon balance was also performed. The following conclusions were drawn based on the results obtained in this study:

1. With respect to temperature, while the peak CO_2 concentration was found to be the highest at 1000°C, the carbon conversion at this temperature was low due to a higher amount of fuel being fragmented and subsequently elutriated. The highest carbon conversion and CO_2 yield was obtained at a temperature of 900°C. At lower reaction temperatures, such as at 700°C, the gasification rate was found to be very slow with complete consumption of the fuel requiring 1750 s relative to 750 s at 1000°C.

2. The investigation of the OC particle size showed that the larger size range, 150-350 µm, performed better than the sample having a smaller size range of 106-150 µm. This was evidenced by the higher peak CO_2 concentration, faster carbon conversion rate and greater extent of carbon conversion when the larger OC particle size range was used.

3. For the 35 redox cycle investigation, the OC was found to perform sufficiently well over the multicycle reaction with minor loss in reactivity as evident from the reduction in the average carbon conversion rates. The carbon conversion was found to stabilize after the first few reduction reactions while the CO_2 yield remained almost constant throughout the 35 reduction reactions. With progressing redox cycles, the peak volume fractions and particle sizes of the OC samples were found to decrease due to attrition.

4. The NO_x emissions were found to be minimal with averaged values of 22.5 ppm for NO, 2.48 ppm for NO_2 and 0.59 ppm for N_2O. The carbon balance showed that the vast majority of the carbon in the fuel, 92.2%, was found in the outlet gas in the form of CO_2, CO and CH_4. Minor amounts (~1%) of carbon were found in the catch pots and the OC bed in the

reactor. This left around 7% unaccounted for, which most likely elutriated out of the reactor due to the low cyclone separation efficiency and short reactor length.

This chapter showed that attrition and deactivation of the OC particles would invariably occur immaterial of the experimental conditions and therefore it is favourable to use low cost OCs having acceptable reactivity such as ore-based OCs. Defluidization was not observed to occur in any of the investigations. The average carbon conversion and CO_2 yield was found to be 86% and 81% respectively over 35 redox reactions and it is proposed that the use of a CFB reactor would lead to an improvement in these values.

9.5 References

1. Rajendran, S., S. Zhang, R. Xiao, and S. Bhattacharya, *Use of synthetic oxygen carriers for Chemical Looping Combustion of Victorian brown coal.* Proceedings of the Combustion Institute, 2014.
2. Linderholm, C., P. Knutsson, M. Schmitz, P. Markström, and A. Lyngfelt, *Material balances of carbon, sulfur, nitrogen and ilmenite in a 100kW CLC reactor system.* International Journal of Greenhouse Gas Control, 2014. **27**: p. 188-202.
3. Orenbakh, M., *Reaction Surface in Heterogeneous Combustion*. 1973, Nauka, Novosibirsk.
4. Schmal, M., J.L.F. Monteiro, and J.L. Castellan, *Kinetics of coal gasification.* Industrial & engineering chemistry process design and development, 1982. **21**(2): p. 256-266.
5. Messenböck, R.C., D.R. Dugwell, and R. Kandiyoti, *CO2 and steam-gasification in a high-pressure wire-mesh reactor: the reactivity of Daw Mill coal and combustion reactivity of its chars.* Fuel, 1999. **78**(7): p. 781-793.
6. Tremel, A., T. Haselsteiner, C. Kunze, and H. Spliethoff, *Experimental investigation of high temperature and high pressure coal gasification.* Applied Energy, 2012. **92**: p. 279-285.
7. Dennis, J.S., S.A. Scott, and A.N. Hayhurst, *In situ gasification of coal using steam with chemical looping: a technique for isolating CO_2 from burning a solid fuel.* Journal of the Energy Institute, 2006. **79**(3): p. 187-190.
8. Laurendeau, N.M., *Heterogeneous kinetics of coal char gasification and combustion.* Progress in Energy and Combustion Science, 1978. **4**(4): p. 221-270.
9. Jenkins, R.G., S.P. Nandi, and P.L. Walker Jr, *Reactivity of heat-treated coals in air at 500 °C.* Fuel, 1973. **52**(4): p. 288-293.
10. Hippo, E. and P.L. Walker Jr, *Reactivity of heat-treated coals in carbon dioxide at 900 °C.* Fuel, 1975. **54**(4): p. 245-248.

Chapter 10 Conclusions and Recommendations for Future Work

CLC has grown from a paper concept to being demonstrated in pilot scale reactors. This technology has attracted a vast amount of funding from both governmental bodies as well as utility companies such as ALSTOM due to the promising results that have been reported. CLC first started with gaseous fuels such as syngas and natural gas due to the ease of the gas-solid reaction with the OC. This then shifted towards the use of solid fuels such as coal and biomass due to their widespread abundance and lower cost; this process is called in-situ Gasification Chemical Looping Combustion (iG-CLC) as the solid fuel is first gasified in the reactor and these gases then react with the OC. While about 10% of the results in literature encompass the utilization of solid fuels in CLC, the vast majority of research has been done with gaseous fuels as this was the initial focus. In regards to the solid fuels that have been researched with iG-CLC, most of these investigations have been focussed on high rank fuels such as bituminous coal and petroleum coke. Around 15-20% of the investigations that have been undertaken with iG-CLC involved the use of low rank coals, one of which is VBC. There have only been a handful of investigations involving the use of VBC in a CLC system, all of which were performed using small scale laboratory equipment. Since VBC is a unique fuel and does not share its properties with any other coal around the world, more work needs to be done to determine the applicability of this fuel in the CLC process.

10.1 Conclusions

The preliminary work [1] that set the ground for this thesis found Fe_2O_3 to be a suitable OC for use with VBC and this was determined using small scale laboratory equipment. It is for this reason that all of the studies reported in this thesis involved the use of Fe-based OCs. Since this thesis aims to determine the applicability of using VBC in the CLC process, a number of investigations were done in both small and large scale fluidized bed reactor systems while some others were done in a thermogravimetric analyzer (TGA). The fresh and used OC particles were characterized using instruments such as a Scanning Electron Microscope (SEM), an Energy Dispersive X-ray Spectroscope (EDS), X-ray Diffraction (XRD) unit and Accelerated Surface Area and Porosimetry (ASAP) unit to study any changes that the OC may have undergone over the course of its reaction with VBC.

10.1.1 Chapter 4: Effect of Inherent Coal Minerals on the Performance of CLC

The first results chapter, Chapter 4, investigated the role of the minerals present in coal and how this affected its reaction rate. It has been reported in literature that one of the potential issues with iG-CLC is the interaction between the OC and the ash as this may affect the performance of the OC over time. As such, a comparative study was done between a low ash Victorian brown coal and a high ash Canadian lignite. Next, the interaction between the ash that was formed from the thermal processing of the fuel and the OC was studied.

The ash formed from the thermal processing of coal minerals had an adverse effect on the OC's oxygen carrying capacity by either preventing the OC from being reoxidized or forming unreactive compounds with the OC. This effect would be worsened in the presence of high ash coals having low melting point compounds as this could lead to agglomeration of the OC particles. VBC is advantageous from this point of view as it has a low ash content with high levels of Fe in it.

The obtained results suggest that VBC is better suited for use in the CLC process relative to the high ash Canadian coal as the former is more reactive and contains a very low amount of ash which translates to less potential interactions between the ash and the OC.

10.1.2 Chapter 5: In-situ Synchrotron Study of Fe_2O_3 Reduction with Victorian Brown Coal

Chapter 5 investigated the phenomenon of carbon deposition, which has been reported in literature with the use of gaseous fuels. Also, a study on the reduction of the OC in the presence of VBC was done using in-situ XRD powered by synchrotron radiation.

Since VBC contains a high level of volatiles, this aided in reducing the OC at a quicker rate as pyrolysis is a faster process relative to gasification. Rietveld refinement of the synchrotron data showed that the crystallite size of the OC decreased with an increase in the extent of the reduction of the OC. Carbon deposition was a possibility when using Fe-based OCs given that CO_2 had a long residence time around the OC that had been reduced beyond Fe_3O_4. Hence, it is best to prevent the reduction of Fe_2O_3 beyond Fe_3O_4 when using CO_2 as the gasification agent in environments with high gas residence times.

The obtained results suggest that the reduction of Fe_2O_3 beyond Fe_3O_4 is not favourable using CO_2 as the gasification agent in an environment with long gas residence times as this leads to carbon deposition, which causes a reduction in the CO_2 yield.

10.1.3 Chapter 6: Reduction Kinetics and Characterization of Fe_2O_3 with Victorian Brown Coal

Chapter 6 studied the reduction kinetics of Fe_2O_3 in the presence of a solid fuel, which was a first-of-its-kind investigation. A number of studies have been performed in literature with respect to modelling the reduction of OCs in the presence of gaseous fuels. The significance of this study is that the obtained kinetic parameters can be used in CFD and process simulations to model iG-CLC processes employing VBC as the fuel.

The reduction of Fe_2O_3 was modelled using the Shrinking Core Model (SCM) and the Modified Volume Reaction Model (MVRM) with similar results obtained using both the models. The former incorporates the physical properties of the OC while the latter is purely an empirical model. The activation energy was found to be 209 kJ/mol, which is similar to that of char gasification. This served to confirm that the gasification of char is the rate limiting step in CLC as the activation energy for the reaction of Fe_2O_3 with gaseous fuels is much lower based on the values reported in literature. The models were found to perform better at higher reaction temperatures and CO_2 concentrations, both of which are more relevant from a practical point of view.

The obtained results show that both the SCM and MVRM can adequately model the reduction of the Fe_2O_3 OC in the presence of a char derived from VBC. The calculated activation energies confirm that the rate limiting step in CLC is the gasification of char.

10.1.4 Chapter 7: Effect of Reactor Operating Mode

Chapter 7 investigated how the use of different reactor configurations affected the performance of the CLC system. This involved the use of a fluidized bed reactor, which is the configuration that is typically used in most of the studies reported in literature, together with atmospheric and pressurized fixed bed reactors. The advantages and disadvantages of using the three reactor configurations were then discussed.

It was found that both of the fixed bed reactors outperformed the fluidized bed reactor in terms of the CO_2 yield and carbon conversion, with improvements of around 20 and 10 percentage points respectively. The reason for this was two-fold, there was insufficient contact between the volatile matter and the OC in the fluidized bed reactor due to the way the fuel was introduced into the reactor as well as the fact that some of the fuel underwent attrition and elutriated out of the reactor. Ash deposition was found to occur on the OCs that were used in the fixed bed reactors but not for those that were used in the fluidized bed

reactor due to the low residence time of the ash in the reactor and the low degree of contact between the OC and the ash. In terms of the reaction rate, the fastest fuel consumption was observed when using the fluidized bed reactor which took around 550 seconds relative to over 700 seconds when using both of the fixed bed reactors due to better contact between the fuel and the gasification agent. It is expected that the use a circulating fluidized bed (CFB) reactor which incorporates a longer expanded freeboard together with cyclones and a carbon stripper would vastly improve the results.

The obtained results show that the use of a fluidized bed reactor allows for faster gasification of the fuel relative to that obtained using both the atmospheric and pressurized fixed bed reactors due to better contact between the gasification agent and the fuel in the fluidized bed reactor.

10.1.5 Chapter 8: Performance of Synthetic Oxygen Carriers

Chapter 8 investigated the reactivity and performance of 18 different synthetic OCs which were fabricated in-house. Most of the investigations in literature involve supporting different metal oxides on inert materials. One downside of such a combination is that a larger amount of the OC would be needed to compensate for the weight of the inert support, which does not function as an oxygen donor. Additionally, Fe_2O_3 has a lower reactivity relative to metal oxides such as CuO, NiO and Mn_2O_3. Therefore, this study focussed on synthesizing bimetallic OCs, via two pathways, and investigated how the different metal oxides, loading contents and synthesis methods affected the performance of the synthetic OCs.

Most of the synthetic OCs were found to outperform the monometallic Fe_2O_3 OC. It was also found that the OCs prepared via impregnation performed slightly better relative to their physically mixed counterparts. This was due to the better distribution of the secondary metal oxides on the impregnated OCs. Also, with increasing concentrations of CuO, NiO and Mn_2O_3, the resultant OCs were found to be more reactive with the exception of the samples containing 20 wt% of CuO as the use of these led to agglomeration of the OC particles followed by defluidization of the bed. The OCs containing Mn_2O_3 were found to have the least affected surface characteristics and the most stable performance. This was potentially due to synergistic effects between the two metal oxides.

The obtained results show that the use of a secondary metal oxide, even in small amounts, can lead to an increase in the reactivity of the synthetic OC. However, high levels of CuO should be avoided as this could lead to operational issues such as defluidization while NiO

may not be suitable for handling due to its toxicity. The use of Mn_2O_3 as the secondary metal oxide is recommended as it results in not only a synergistic effect with Fe_2O_3, but also more stable physical characteristics.

10.1.6 Operational Experience with a 10 kW_{th} Alternating Fluidized Bed Reactor

Chapter 9 investigated the use of an iron ore in a 10 kW_{th} alternating fluidized bed reactor with VBC as the fuel. In this chapter, the effects of the temperature, OC particle size range and fuel type on the performance of the CLC system were also investigated. The NO_x emissions were also quantified and a carbon balance on the entire process was also performed. A multicycle test was undertaken to determine the performance of the OC over an extended period of time, totalling 40 hours. Here, the attrition of the OC was also investigated.

The operation of the 10 kW_{th} fluidized bed reactor yielded favourable results compared to the results obtained using the bench scale fluidized bed reactor under the same operating conditions. Highly similar carbon conversions were obtained using both the setups but the CO_2 yield was improved by a factor of two when using the 10 kW_{th} reactor. The reason for this was that with the 10 kW_{th} reactor, the fuel was fed through the OC bed enabling a higher proportion of the volatile matter to react with the OC. It was found that the use of coal resulted in a faster reaction time and higher carbon conversion relative to those obtained using char. The optimum reaction temperature was found to be 900°C as the use of a lower temperature led to a reduction in the reaction kinetics while the use of a higher temperature resulted in the generation and elutriation of more fines due to the rapid release of the volatiles from the coal. NO_x emissions were found to be minimal at 25 ppm over the course of the reduction reaction. On the other hand, the carbon balance showed that around 6.8% of the introduced carbon was unaccounted for and this was most likely due to the low capture efficiencies of the cyclones. Long term experiments did not show ash deposition or agglomeration to be an issue but it was found that the OC particles underwent attrition.

The obtained results show that attrition and deactivation of the OC will invariably occur in a fluidized bed reactor and therefore it is favourable to use low cost OCs such as ores. Defluidization was did not occur in any of the investigations here. The average carbon conversion and CO_2 yield was found to be 86% and 81% respectively over 35 redox reactions. It is proposed that the use of a CFB reactor would lead to an improvement in these two parameters.

10.1.7 Summary

In summary, the various investigations that have been performed in this thesis show that the low ash content and the high reactivity of VBC makes it a highly suitable fuel for use in CLC. Nevertheless, more work still needs to be done before VBC can be utilized in an industrial scale CLC system. The following section will provide recommendations for future work based on the findings in this thesis.

10.2 Recommendations for Future Work

This thesis has investigated the applicability of using VBC in a CLC setup. The focus of the follow-up work in this field should be on the use of a CFB reactor as well as the generation of more in-depth models before trialling it in a pilot scale power station. This will be detailed in the following subsections.

10.2.1 Experimental Work

Although this study utilized a 10 kW_{th} alternating fluidized bed reactor, the use of such a configuration is not feasible on an industrial scale due to it being operated in a batch mode and as such it is not capable of auto thermal operation. Therefore, the use of a CFB reactor is required to study both the heat and mass balances of the system. Additionally, this will enable the continuous operation of the CLC system.

This study investigated at the emissions of NO_x but could not quantify SO_x and trace element emissions due to the small amount of fuel used, even in the 10 kW_{th} reactor. This information is important as the use of a CLC system may lead to a reduction in these emissions relative those emitted in a conventional power station. Such information may help to propagate and advance the development of CLC from an environmental impact point of view.

The last recommendation revolves around the OC. It was found that although the synthetic OCs were more reactive compared to the natural ores, most of the synthetic OCs suffered a deterioration in their reactivity with progressing time. It is also expected that the use of synthetic OCs would not be highly viable as the costs of these OCs may outweigh the performance improvements. Therefore, it is recommended that different Fe-based ores such as ilmenite and limonite are trialled as low cost OCs.

10.2.2 Modelling Work

To date, there has not been a techno-economic analysis of the CLC process using VBC as the fuel. This information is important for both governmental bodies and utility providers to prove the viability of a VBC-fuelled CLC system. This will then enable pilot scale investigations to be undertaken before the process can be scaled-up to demonstration and commercial scales. This model should also incorporate different OCs and how the use of these OCs affects the operating cost of the CLC system.

The modelling of the reduction of the OC in the presence of VBC using a fluidized bed reactor should be done as a follow-up to the TGA investigations that were performed. This would provide more relevant information as a fluidized bed reactor is the most likely reactor choice for CLC. Additionally, this information could be used in scale-up studies using CFD models to investigate the hydrodynamics of the process in a larger reactor.

10.3 References

1. Saha, C., *Chemical-looping combustion of Victorian brown coal*. 2012

Appendix A – Summary of Literature Review

Note: TGA – thermogravimetric analyzer; FzB – fluidized bed; FxB – fixed bed; CFB – circulating fluidized bed; MB – moving bed; SFB – spout fluid bed

No.	Reactor system	Oxygen Carrier (OC)	Fuel	Key findings	Ref.
1	FzB	Fe_2O_3 Mixed with: Lignite ash Bituminous coal ash	CO	Most coal ash decreased the OC's reactivity, except for ash mainly composed of $CaSO_4$. Most coal ash caused sintering and agglomeration of the OC. These were caused by ash deposition and the formation of new OC-ash compounds (such as Fe_2SiO_4). Larger ash particles size had less effect on the OC's reactivity than smaller particles.	[1]
2	TGA	$CoFe_2O_4$	Chinese Liuzhi coal (5.23 wt% S, air dried basis)	TGA results showed $CoFe_2O_4$ had higher reactivity compared to monometallic OCs like CoO and Fe_2O_3. Most of the sulphur present in the coal was converted to solid Co_3S_4 during the reaction between the coal and $CoFe_2O_4$. However, attention should be paid to the other side products, which inhibited the regeneration of $CoFe_2O_4$.	[2]
3	FzB	Mn ores Ilmenite Mn_3O_4/ MgO stabilized ZrO_2	Mexican petroleum coke Swedish wood char	Higher conversion obtained using Mn-based ores and oxides compared to ilmenite. The increased rate of char conversion was mainly due to the presence of Na and K in the Mn ores. When the Mn-based OCs were used, the alkali impurities were uniformly distributed and formed cavities and channels on the surface of the fuel particles, resulting in alkali-catalysed steam gasification of char. Increased rate of char gasification and the potentially low OC costs imply that Mn-based OCs are	[3]

				highly suitable for use in a CLC system.	
4	FzB	Synthetic Fe-based OC Fe_2O_3 Ilmenite	Lignite char (generated from a lignite having 43.05% volatile matter on an air dried basis)	Char segregation was found to occur in the FR. Larger particles yielded higher conversions than smaller particles. Hence, these particles are advantageous from a hydrodynamic point of view. Larger fluidizing gas velocity, over 1.6 U_{mf}, can reduce the effect of char segregation. OCs with high reactivity could still convert CO amidst particle segregation.	[4]
5	CFB	Ilmenite	Mexican petroleum coke Cerrejón bituminous coal	6 experiments successfully conducted with stable operation over 6-32 minute time periods of continuous fuel feeding in a CLC unit. At around 950°C, 90% CO_2 capture efficiency was achieved in the FR. Unconverted CO, H_2 and CH_4 present in the exhaust gases corresponded to an oxygen demand of around 20%.	[5]
6	MB	Fe_2O_3	Asbury Carbons #4072-C metallurgical coke Powder River Basin sub-bituminous coal Illinois #6 bituminous coal	The rate determining step for the Coal Direct Chemical Looping (CDCL) process was found to be the char gasification step. Almost complete coal conversion achieved without any problems. Higher reactor temperature, OC to char ratio, enhancer gas flow rate and OC flow rate resulted in higher conversion of char, with reactor temperature having the most significant impact. The authors suggested that the MB configuration is favourable due to the successfully obtained operational results.	[6]
7	TGA	Poland sewage sludge	3% H_2 with 97% Ar	Sewage sludge ash was an effective and low-cost OC with a reasonable oxygen carrying	[7]

		ashes containing Fe_2O_3	Janina hard coal	capacity of 3.5% by mass. At 900°C, an OC to fuel ratio of 100:1 yielded complete fuel combustion. Complete combustion at an appreciable rate required an operating temperature of 750-800°C for the sewage sludge ash and coal system. This was lower when compared to the pure Fe_2O_3 and coal system which required an operating temperature of 950°C. A low attrition index of 1%, a high melting temperature of 1170°C, a low tendency to agglomerate and prevention of deposition in the FR make this a favourable OC.	
8	FzB	Iron ore and Na-loaded iron ore	Coal	78.6% CO_2 capture efficiency and 80.54% carbon capture efficiency for Na-loaded OC. 40.27% and 45.65% CO_2 and carbon capture efficiencies respectively for iron ore OC. Na-loaded OC experienced sintering and agglomeration which was potentially due to the low melting point of Na.	[8]
9	TGA	Fe_2O_3	Coal and straw mixture	Reaction rate at lower temperature improved by increasing the OC to fuel ratio. Addition of straw increased both the combustion and oxidation rates of the OC.	[9]
10	CFB model	Ilmenite	Cerrejón bituminous coal	First mathematical model validated against experimental results for a continuously operated iG-CLC unit. The operating conditions which had significant impacts on the oxygen demand in the FR were the reactor temperature, solids circulation flow rate and the solids inventory. The model predicted a 98.5% CO_2 capture efficiency and a total	[10]

				oxygen demand of 9.6% for operating conditions of 1000°C and 1500kg OC/MW_{th} in the FR.	
11	CFB	Iron ore containing 76% Fe_2O_3	Spain pine sawdust	More than 95% carbon capture achieved in the temperature interval of 880-915°C using CO_2 and steam as gasification agents. The main combustion products were CO_2 and steam with CO, H_2 and CH_4 detected as unburned compounds. Tars, mostly naphthalene, were detected but these amounts decreased with increasing FR temperatures. No changes in the physical and chemical properties of the OC, such as alkali deposition from biomass ash, after 78 hours of continuous operation.	[11]
12	FxB	CaO and $CaCO_3$ with added $CaSO_4$	Xuzhou bituminous coal	Favourable CLC setup to achieve both desulphurisation and CO_2 capture. At optimum conditions (950°C and 0.5 MPa), 83% carbon conversion and 94% CO_2 outlet concentration achieved. Higher desulphurisation efficiencies obtained when using CaO and $CaCO_3$ at elevated temperatures and pressures. CaO performed better than $CaCO_3$ due to an optimum Ca/S ratio with CaO.	[12]
13	FzB	Ilmenite mixed with ash from: German lignite Chinese coal	CH_4 German lignite Chinese bituminous coal Mexican petroleum coke	CO conversion decreased with the initial loading of both ashes, but then increased with higher ash loading. Using the German lignite ash, the CO conversion with maximum ash loading (50%) surpassed the results obtained with 0% ash loading. The increase was most likely due to the effect of Ca and Fe in the ash which acted as catalysts or as OCs. The added ash did not affect	[13]

			Wood char	fluidization.	
14	TGA	$CuFe_2O_4$	Jinshan petroleum coke	$CuFe_2O_4$ showed superiority reactivity over Fe_2O_3, having a reactivity similar to CuO, although the dopant fraction of CuO in the OC was deduced to be around 33 wt%. Formation of side products (Cu_2S and Fe_2SiO_4) are detrimental to the reactivity of the OC, affecting its ability to fully regenerate.	[14]
15	FzB	Fe_2O_3	Hambach lignite	The apparent gasification rate of the lignite was enhanced in the presence of Fe_2O_3, especially at temperatures above 850°C. The ability of Fe_2O_3 to rapidly convert CO to CO_2 within the mass transfer boundary layer surrounding the particle significantly improved the observed rate of gasification, particularly at a conversion of 20%. The gasification rates observed experimentally agreed with the rates predicted by the developed numerical model.	[15]
16	FzB	Fe_2O_3-$Ca_2Al_2SiO_7$	Chinese traditional anthracite	The Fe_2O_3-$Ca_2Al_2SiO_7$ OC demonstrated a higher carbon conversion rate, gasification rate and oxygen usage compared to hematite. The addition of Ni and K, particularly K, during the OC synthesis improved the reactivity of the OC. When K was added, a CO_2 conversion in excess of 97% was achieved due to the formation of catalytic active phases of $K_2Fe_{22}O_{34}$ and/or $KFeO_2$ in the OC.	[16]
17	FzB	K_2CO_3 loaded Fe_2O_3	Coal	Addition of potassium increased reaction rate and CO_2 conversion. Maximum CO_2 conversion obtained with OC having 6% K_2CO_3.	[17]

				Sintering occurred with the addition of K_2CO_3.	
18	FzB	K_2CO_3 loaded iron ore Iron ore containing 86.27% Fe_2O_3	Huaibei anthracite	For the iron ore loaded with 6% K_2CO_3, the carbon conversion and CO_2 yield reached maximum values at 920°C having values higher than that of the original iron ore. At 920°C, increasing the K_2CO_3 loading (within the range of 0-20%) increased the rate of reaction resulting in a decrease in the reaction time. Addition of K_2CO_3 to the iron ore caused sintering on the surface of the OC particle and hence, it was proposed that the K_2CO_3 loading should not be too high. The future work included investigating the catalytic effect and mechanism of K_2CO_3 loading on iron ore.	[18]
19	TGA	Fe_2O_3 NiO	Loy Yang brown coal Santa Catarina lignite	Fe_2O_3 performed well over multiple redox cycles but NiO showed decreasing reactivity with increasing redox cycles. After 5 redox cycles, 87% coal combustion was obtained using Fe_2O_3 but only 67% using NiO. No agglomeration between the OCs and coal ash was observed within the experimental timeframe.	[19]
20	TGA	Fe_2O_3-Al_2O_3 CuO-Al_2O_3	Yang Quan anthracite	Using CuO resulted in a higher mixture conversion index and higher maximum weight loss rate (2.8 wt%/min) relative to Fe_2O_3. Hence, CuO was found to be a more suitable OC for used with the Yang Quan coal. The formation of Al_2SiO_5 from the reaction between the Al_2O_3 support and SiO_2 in the ash resulted in the loss of the Al_2O_3 support. This lowered the CuO-Al_2O_3 OC's resistance to sintering	[20]

				and reactivity degradation.	
21	TGA	Fe_2O_3-Al_2O_3 CuO-Al_2O_3	Liu Pan Shui sub-bituminous coal	Introduction of Al_2O_3 made the OCs more porous and promoted the reaction between the fuel and OC.	[21]
22	CFB	Ilmenite	Cerrejón bituminous coal	The gasification and combustion reactions were promoted at higher FR temperatures. Char conversion and combustion efficiencies were 15% and 70% at 870°C but increased to 82% and 95% at 950°C. The unburnt gases detected at the outlet of the FR predominantly came from the volatile matter in the coal that did not react with the OC. Ilmenite reacted faster with H_2 but slower with CH_4. The presence of the OC promoted char gasification, since it reacted with CO and H_2, which are gasification inhibitors.	[22]
23	FzB	Cement decorated iron ore	Coal	Addition of cement decreased the outlet CO gas fraction. Volume fraction of CO_2 increased greatly over the 20 reaction cycles.	[23]
24	CFB	Ilmenite	Biomass	CO and NO concentrations decreased by as much as 80% and 30% respectively when 40 wt% of the silica sand bed in the boiler was replaced with ilmenite.	[24]
25	FzB	K_2CO_3 and NiO decorated Fe_2O_3	Coal	Composite OCs were found to completely regenerate after 6 cycles. The Fe4Al6K1 particles performed well.	[25]
26	FzB	Fe_2O_3-$Ca_2Al_2SiO_7$	Huabei anthracite	Addition of $Ca_2Al_2SiO_7$ improved the overall mechanical strength of the OC and prevented sintering during the multicycle operation. The addition of $Ca_2Al_2SiO_7$ nearly doubled the coal gasification rate during the initial reduction	[26]

				process.	
27	CFB	$NiO-Al_2O_3$	Coal	Increased reaction temperatures as well as air and steam flow rates resulted in increased carbon conversions.	[27]
28	FzB CFB	Iron ore	Anthracite	Anthracite conversion accelerated in the presence of the OCs with nearly 90% conversion at 950°C.	[28]
29	TGA	CuO	Yimin coal Candlenut wood Rice hull	The synergetic effect observed during the combustion of coal and candlenut wood was not found when coal and rice hull were used. This was possibly due to the higher content of alkali and alkali earth metals in the candlenut wood relative to rice hull. Adding 80 wt% candlenut wood ash provided a similar theoretical coal conversion as adding 50 wt% K_2CO_3. Negligible interaction was found to exist between the biomass ash and CuO. Addition of biomass and biomass ash with high alkali/alkali earth content, to function as inexpensive catalysts, can improve coal conversion efficiencies at a given temperature while also reducing the gasification temperature.	[29]
30	TGA	Fe_2O_3-K_2CO_3 CuO-K_2CO_3	Shenmu bituminous char	The addition of K_2CO_3 increased the reduction rate by enhancing the gasification rate of char. The addition of K_2CO_3 did not affect the oxygen carrying capacity of the OCs but promoted sintering of both OCs.	[30]
31	FzB	Fe_2O_3	Coal	High conversion efficiency of coal was obtained. Significant sintering of the OCs in the later period of the experiment sharply decreased the OC's reactivity.	[31]
32	MB	Fe_2O_3	Metallurgical	A sub-pilot plant was successfully	[32]

			coke Sub-bituminous coal	operated for over 230 hours. 81% and 97% carbon conversion achieved using coke and coal respectively. The MB configuration for the reducer displayed superior performance in terms of CO_2 yield, producing a steady stream consisting of more than 99% CO_2.	
33	TGA FxB	$CuO-Fe_2O_3$	Coal Methane	The combination having >40% CuO, <45% Fe_2O_3 with <30% Al_2O_3 as the support showed the best performance, having the highest reaction rates, combustion performance and oxygen utilization while keeping agglomeration to a minimum. The synergistic effect of the bimetallic $CuO-Fe_2O_3$ OC was attributed to the micropore and crack formation during the reduction of Cu, which facilitate gas diffusion. The formation of $CuFe_2O_4$ contributed to oxygen release at lower temperatures due to the lower bond energy of $CuFe_2O_4$.	[33]
34	MB	Fe_2O_3	Wyoming Powder River Basin sub-bituminous coal North Dakota Powder River Basin lignite	Successful continuous operation of a sub-pilot plant for 200 hours with steady solid circulation and steady OC reactivity and recyclability. Achieved over 90% coal conversion and 99.5% CO_2 purity in the reducer. By avoiding thermal NO_x formation, this process can reduce NO_x emissions.	[34]
35	FzB	$CaSO_4$ $CaSO_4$-Fe_2O_3	Shenhua bituminous coal	Adding Fe_2O_3 to $CaSO_4$ (up to 7%) increased the carbon conversion and CO_2 capture efficiency of the OC relative to that with only $CaSO_4$. The carbon conversion efficiency increased from 79% to 90% while the CO_2 capture efficiency increased from	[35]

				88% to 91%. The addition of Fe_2O_3 to $CaSO_4$ supressed the release of sulphur containing compounds such as SO_2 and H_2S from $CaSO_4$. The suppression mechanism was not due to the desulphurisation capacity of Fe_2O_3, but due to the suppression of the $CaSO_4$ decomposition side reactions during both the reduction and oxidation periods.	
36	TGA	CuO	Loy Yang brown coal Morwell brown coal	Due to the relatively low melting point of CuO, it underwent severe sintering at 950°C. Hence, a temperature of 800°C was used. Strong interaction between Morwell coal minerals and CuO was observed.	[36]
37	FzB	$Ca(NO_3)_2$ loaded iron ore	Coal	91.2% carbon conversion and 95% CO_2 yield obtained at 920°C.	[37]
38	TGA FzB	Fe-based bauxite waste	El Bierzo anthracite Columbian bituminous coal South Africa bituminous coal Spanish lignite	Using the TGA, the results suggested that the char was being directly combusted by the O_2 in the bauxite waste. However in the FzB, gasification was found to be a necessary step for char conversion. The bauxite waste was able to combust the gases generated from the gasification of char. Using steam over CO_2 gave higher fuel gasification rates. Comparing the lignite and anthracite at an operating temperature of 980°C, the use of the lignite with CO_2 as the gasification agent resulted in a doubling of the gasification rate over the use of the anthracite with steam.	[38]
39	FzB	Ilmenite Bauxite waste	Spanish anthracite coal and char	Bauxite waste and the Fe-based materials performed the best. For all the investigated OCs, an estimated OC inventory of 1600	[39]

		Fe-based OC Fe_2O_3 synthetic OC	South African bituminous coal and char Spanish lignite and char	kg/MW_{th} was required to achieve a 93% carbon capture and 99% combustion efficiency at 1000°C.	
40	TGA FzB	Ilmenite Bauxite waste Fe-based OCs Copper ferrite	South African bituminous char	For high combustion efficiencies, a low concentration of CO and H_2 in the reactor was necessary as it reduced the char gasification inhibition effect. Fe-based OCs yielded the highest combustion efficiencies with the lowest OC bed inventories.	[40]
41	FzB	Fe_2O_3-coal ash	Coal	84.9% conversion was obtained and it was found that high operating temperatures caused sintering of the OC particles.	[41]
42	FzB	Ilmenite Oxide scales NiO-$NiAl_2O_4$ Quartz sand	Swedish wood char El Cerrejon bituminous coal	The oxygen exchange model was found to be a good model to describe the behaviour of steam gasification and fuel conversion in CLC. Higher steam concentration increased the rate of char conversion but a higher H_2 concentration decreased this rate due to char gasification inhibition by the H_2.	[42]
43	TGA FxB FzB	$CaSO_4$	CO H_2 CH_4 Coal Biomass	Performance of the OC was affected by the OC preparation method and was improved by fabricating mixed oxides. Supports such as Al_2O_3 or SiO_2 increased the reactivity of the OC by providing a higher surface area for reaction. $CaSO_4$ was found to be a promising OC for CLC. However, thermodynamic limitations of the OC could cause sulphur release, incomplete fuel combustion and poor mechanical properties.	[43]

44	CFB FzB	Ilmenite	Coal	Unexpected release of approximately 0.1 v/v% O_2 from ilmenite at 950°C. Possibilities for the O_2 release were due to the presence of Mn-impurities in the OC or the interaction between the Mn-impurities and the iron oxides.	[44]
45	FzB	Fe_2O_3 loaded with Na or Ni	Coal	Reaction rate increased with increased loading of secondary metal oxide. 6% Ni loading resulted in a carbon conversion of 92.7%.	[45]
46	CFB	Iron ore	Shenhua bituminous coal	Increasing the pressure improved the carbon conversion, CO_2 concentration and combustion efficiency. 97.2% carbon conversion, 84.7% CO_2 concentration and 95.5% combustion efficiency achieved at an operating pressure of 0.5 MPa. Elutriation of fines increased with pressure.	[46]
47	FzB	K promoted iron ore	Coal	Outlet CO_2 concentration increased significantly with K addition. Significant sintering observed during first 11 reaction cycles.	[47]
48	TGA	Fe_2O_3-Al_2O_3 mixed with: Bulgaria sub-bituminous fly ash China bituminous fly ash Texas lignite ash Powder River Basin	Beneficiated coal char from gasification	The OC mixed with the lignite ash was found to be beneficial to the oxidation of carbon in the char while the other ashes were detrimental to the OC's performance. Low concentration of ash increased the reduction rates but high concentrations of around 75% significantly decreased this rate.	[48]

		sub-bituminous ash			
49	TGA	CuO-TiO_2 Fe_2O_3-TiO_2	Shenhua bituminous coal	OC mixed with the TiO_2 support had better reactivity with coal. When TiO_2 was used as a support, a decrease in the onset of the reduction reaction temperature was observed. Smaller OC particle size improved coal conversion but would make separation of the OC from the ash and unburned carbon difficult.	[49]
50	TGA	CuO	Loy Yang brown coal Morwell brown coal	After 5 redox cycles, 97% coal conversion was achieved with Loy Yang coal and 91% with Morwell coal. It was found that using the experimental results, 1400-2100 hours of continuous operation would be possible for the reaction between CuO and Loy Yang coal but only 170-260 hours using CuO with Morwell coal. No deterioration or sintering was observed for the CuO OC after 5 redox cycles.	[50]
51	FzB	Manganese ore Ilmenite	Mexican petroleum coke	Compared to ilmenite, the use of manganese ore showed an increase in the gasification rate by a factor of 5. This was possibly due to gas phase O_2 release, suppression of H_2 inhibition and catalytic effects of the minerals present in the ore.	[51]
52	TGA	Fe_2O_3 loaded with: K_2CO_3 Na_2CO_3 Li_2CO_3	Shenmu bituminous char	Higher C to Fe_2O_3 ratios resulted in faster reduction rates and better oxygen carrying capacities due to increased contact between the OC and fuel. Addition of alkali carbonates improved the reduction rates, with decreasing catalytic activities in the following order: K_2CO_3, Na_2CO_3 and Li_2CO_3.	[52]

53	CFB	Fe_2O_3 with NiO	Shenhua bituminous coal Huaibei anthracite	At 970°C, CO_2 capture efficiency was found to be 81.7% using Shenhua bituminous coal but only 65% with the Huaibei anthracite. Hence, CO_2 capture efficiency was found to be greatly impacted by the coal rank. Addition of NiO to Fe_2O_3 improved its reactivity and CO_2 capture efficiency but negatively affected its microstructure.	[53]
54	FzB	Fe_2O_3 CuO	Hambach lignite and char Activated carbon Taldinski bituminous coal US bituminous coal	After 20 redox cycles, both OCs were found to reoxidized back to their original state but contained lower concentrations of the metallic oxides. There was also a 50% decrease in the BET surface area and a decrease in the pore volume even though the pore size was found to increase. Fe_2O_3 particles were found to contain trace amounts of SiO_2 and underwent severe attrition. CuO particles were found to have trace amounts of Cu complexes such as copper aluminate and showed signs of agglomeration.	[54]
55	CFB	Ilmenite	Columbian bituminous coal	It was found that the reactor could operate with a lower flow rate of the gasification agent relative to stoichiometric requirements. A portion of the steam could be replaced by recirculating CO_2 from the outlet of the FR. Coal conversion improved with lower solid circulation rates.	[55]
56	FxB	Steel industrial waste containing Fe_2O_3 Australian MAC iron ore	Xuzhou bituminous coal	Using the industrial waste containing Fe_2O_3, carbon conversion, gas conversion and reaction rate improved with higher pressures and higher number of redox cycles. Steel industrial waste containing Fe_2O_3 performed better compared to the other two iron ores.	[56]

		Brazilian CVRD iron ore			
57	FzB	Ilmenite with: calcined limestone sulphated limestone	Petroleum coke	Addition of calcined limestone to ilmenite improved the gas conversion by reducing the fraction of unconverted CO by half. CaO acted as a catalyst for the water-gas shift reaction, converting CO to H_2, which is a more reactive gas. Addition of sulphated limestone resulted in the release of large amounts of SO_2.	[57]
58	TGA	$CuFe_2O_4$	Liu Pan Shui sub-bituminous coal Yang Quang anthracite	Two distinct reaction stages for the reduction reaction was found, 300-600°C and 600-850°C, when $CuFe_2O_4$ was reacted with Liu Pan Shui sub-bituminous coal. Only one reaction stage, above 600°C, was found for when $CuFe_2O_4$ was used with the Yang Quang anthracite.	[58]
59	TGA	$CuFe_2O_4$	Liu Pan Shui sub-bituminous coal	The amount of lattice oxygen transferred from $CuFe_2O_4$ was the same as that of a mixture containing CuO and Fe_2O_3, but at a faster rate. Overall activation energy was estimated to be 83.16 kJ/mol.	[59]
60	TGA	Fe_2O_3	Ping Ding Shan bituminous coal Liu Pan Shui sub-bituminous coal Yang Quang anthracite	At just over 200°C, reaction of pyrolysis products with Fe_2O_3 was detected during the primary and secondary pyrolysis stages. Low rank coals with high volatile contents were found to be preferable for full coal conversion to CO_2. Fe_2O_3 reduced to Fe_3O_4 with the formation of some inert compounds such as Fe_2SiO_4 and $FeAl_2O_4$.	[60]
61	TGA	Fe_2O_3-Al_2O_3	Ping Ding Shan bituminous coal	It was found that having an excess of either coal or OC was not economical as a full conversion of coal was not achieved.	[61]

62	FzB	CuO	Graphite	Novel H_2 production method using a dual chemical looping setup with lithium silicate and copper oxide. CuO is more favourable than Fe_2O_3 and NiO because the reduction of CuO is exothermic, unlike the other two.	[62]
63	FzB	Fe_2O_3 Ilmenite Sand	Swedish wood char	CO was found to not directly inhibit char gasification. Partial pressure of H_2 had a significant influence on fuel conversion through dissociative H_2 adsorption under the experimental conditions used. Hence, OCs with better reactivity towards H_2 would exhibit better performance.	[63]
64	TGA	FeO Fused iron mixed with Kentucky coal fly ash	10% H_2, 15% CO and 20% CO_2 with balance Ar Beneficiated coal char	Ash also functioned as an OC due to the presence of iron. Higher ash concentration led to increased porosity in the OC and improved redox reaction rates. Carbon removal was found to improve with increasing ash concentration in the OC.	[64]
65	FzB	Ilmenite Fe_2O_3-$MgAl_2O_4$	Columbian bituminous coal	Coal particle size decreased with increasing residence time in the reactor.	[65]
66	TGA	CuO	Illinois #6 bituminous coal and char	It was found that solid-solid reactions between the fuel and OC can be completed at much lower temperatures at acceptable rates provided sufficient contact existed between the fuel and OC. Carbon induced the Cu-O bond breaking process.	[66]
67	FzB	CVRD iron ore	Xuzhou bituminous coal	Carbon conversion was approximately constant with increasing reaction cycles. Carbon conversion was found to increase with increasing reaction pressures. No agglomeration was detected.	[67]

68	CFB	Ilmenite	Mexican petroleum coke South African coal	A mass-based kinetic model was developed to determine the reaction rate constant for char conversion to describe the behaviour of the CFB. The reaction rate constant for the Mexican petroleum coke was 8.2 wt%/min at 950°C and 28.8 wt%/min at 970°C. Reaction rate constant for the South African coal was 26.1 wt%/min at 950°C.	[68]
69	TGA	Fe_3O_4	Shenhua bituminous coal Straw coke Natural coke	Reduction conversion increased with increasing temperatures with 37.1% at 800°C and 54.1% at 950°C. Fe_3O_4 sintering occurred after 950°C. Solid fuels with higher volatile matter contents and more developed pore structures showed greater reactivity with the OCs.	[69]
70	TGA	$CuFe_2O_4$	Bituminous coal	$CuFe_2O_4$ had better reactivity than Fe_2O_3. The reactivity of $CuFe_2O_4$ increased when Al_2O_3 was added.	[70]
71	FzB	CuO-θ-alumina	Hambach lignite and char	The impregnated OC was found to be durable over 20 redox cycles. Even though the BET surface area fell from 60 m^2/g to 6 m^2/g after 20 cycles, it did not affect the overall reaction rate. The rate was controlled by the much slower gasification rate of the solid fuel. The gasification rate was much faster in the presence of the OC as there was less CO inhibiting the gasification of the fuel. At 900°C, CuO decomposed to gas phase O_2 and Cu_2O. Both of these could react with the CO produced from gasification.	[71]
72	FzB	Hematite	Coal	Slight sintering observed on the surface of the OC particle but agglomeration was absent.	[72]
73	TGA	Fe_2O_3-	Coal char	Rapid reaction was found to occur	[73]

		Al_2O_3		at 880°C. Sintering was observed on the surface of the OC.	
74	FxB	Iron ore	Xuzhou bituminous coal	Higher operating pressures resulted in higher CO_2 yields during the reduction reaction. Under pressurized conditions, the initial coal pyrolysis process was suppressed while the char gasification and reduction with the iron ore was enhanced, which improved the overall reaction rate of CLC. Under pressurized conditions, the OC particles became porous but maintained their structure and size after several cycles with no evidence of agglomeration.	[74]
75	FzB	Fe_2O_3	Hambach lignite char	The accumulation of carbon in the bed, the product gas concentrations, the gasification kinetics of char in the presence of CO_2 and the inhibiting effect of CO on char gasification was successfully modelled using the two-part Langmuir-Hinshelwood rate expression that was developed.	[75]
76	SFB	NiO-Al_2O_3	Shenhua bituminous coal	95% CO_2 capture efficiency obtained at 985°C. Higher temperatures resulted in more SO_2 and less H_2S being formed in the FR.	[76]
77	FzB	CuO	Taldinskaya bituminous coal Illinois #5 bituminous coal Hambach lignite	Lignite char was much more reactive than bituminous char and there was no build-up of char in the bed over multiple cycles. The bituminous coal gasification rates were primarily controlled by intrinsic chemical kinetics and not by the rate of external mass transfer. At the reaction temperature, the OC alternated between Cu and Cu_2O.	[77]

				Agglomeration of the OC particles was not observed.	
78	FxB	Iron ore	Xuzhou bituminous coal	More pyrolysis gases were oxidized with increasing redox cycles. With increasing number of cycles, the reduction extent of the OC increased. The OC particles became more porous but the deposition of coal ash on the OC surface also increased. Outlet CO_2 fraction increased from 80% to 90% after 10 redox cycles at atmospheric pressures. The average CO_2 fraction at elevated pressures stabilized close to the equilibrium value of 95.75%.	[78]
79	FxB	Fe_2O_3	Municipal solid waste	Conversion of HCl in municipal solid waste to chlorine can be supressed through the addition of Fe_2O_3.	[79]
80	TGA	Fe_3O_4	Shenhua coal	Fe_3O_4 fully reduced to FeO with a certain amount being further reduced to Fe. Reduction conversion rates of 29.5%, 40.8%, 46.5% and 46.6% obtained for 5:95, 10:90, 15:85 and 20:80 fuel to OC ratios.	[80]
81	CFB	Ilmenite	Mexican petroleum coke	Higher FR temperatures of around 1000°C enhanced carbon capture and solid fuel conversion. Most of the oxygen demand was associated with the reactor design. A fuel feeding method which improves the contact between the solid fuel and the OC material could potentially increase the conversion.	[81]
82	FzB	Mt. Wright iron ore Glodskal oxide scale	Mexican petroleum coke Indonesian coal	Iron ore and oxide scales worked well as OCs for CLC. The gasification rate doubled in the presence of the OCs because of the removal of gasification inhibitors such as H_2.	[82]

			Colombian coal German lignite Swedish wood char	Agglomeration, sintering or change in the structure of the OC after the reaction was not observed.	
83	FzB	Fe_2O_3	Shenhua bituminous coal	Reactivity of Fe_2O_3 was enhanced in the operating temperature range of 800-950°C. Fe_2O_3 was found to only reduce to Fe_3O_4. The sintering of the OC gradually increased with increasing redox cycles.	[83]
84	TGA FzB FxB	CuO Fe_2O_3 Co_3O_4 NiO Mn_2O_3	Illinois #6 bituminous coal	CuO showed the best properties relative to the other OCs. The reduction reaction started at 500°C and combustion of coal was found to be complete by 700°C. Complete re-oxidation of the reduced Cu was found to be finished by 700°C. The separation of fly ash would be a necessary step for the successful operation of CLC.	[84]
85	FzB	NiO-Al_2O_3	Sawdust	Temperatures above 820°C increased the combustion efficiencies. The OC showed strong recyclability over 100 hours of operation.	[85]
86	CFB	NiO-Al_2O_3	Shenhua bituminous coal	At temperatures higher than 960°C, there was an observed loss in the surface area and porosity of the reacted Ni-based OC, leading to a deterioration in its reactivity. The effect of coal ash and sulphur on the reactivity deterioration of the OC was less significant relative to the effect of sintering. Due to the high temperatures that were used in the AR, sintering of	[86]

				the OC was also found to occur.	
87	FzB	Fe_2O_3	Coal	95% outlet CO_2 concentration was achieved.	[87]
88	TGA	NiO Fe_2O_3 CoO CuO	Beneficiated coal char	Fe_2O_3 based OCs were found to possess rapid reduction rates which increased with an increase in the concentration of the reducing gases. Combined with other properties such as low tendency for agglomeration, low cost and high durability over multiple cycles, Fe_2O_3-based OCs were found to be suitable candidates for use in CLC with solid fuels. Fe_2O_3 was found to be capable of oxidizing the carbon in the char, even in an inert environment, removing 88% of the carbon in the char.	[88]
89	SFB	NiO	Shenhua bituminous coal	A 92.8% carbon conversion and 80% CO_2 capture efficiency was achieved at operating temperatures of around 960-970°C. Low carbon conversion and CO_2 capture efficiency was attributed to the reactor design, which resulted in easy elutriation of fines and bypassing of gases from the FR to the AR.	[89]
90	FzB	NiO-$NiAl_2O_4$	Coal	OC was found to react rapidly at temperatures in excess of 850°C.	[90]
91	FzB	NiO	Shenhua bituminous coal	Reduction rates were very low at temperatures less than 800°C. CO_2 concentration at the outlet increased with increasing temperatures. Reactivity of NiO decreased with increasing redox cycles. Approximately 95% CO_2 purity in the outlet gas was obtained at optimum conditions.	[91]
92	FzB	Fe_2O_3	Chinese Baorixile	Reduction of Fe_2O_3 to FeO by char was found to be feasible for	[92]

			char	the production of H_2 through the steam-iron process.	
93	FzB	NiO	Coal	CO_2 concentration over 92% was achieved.	[93]
94	10 kW_{th} FzB	Ilmenite	Mexican petroleum coke	CO_2 capture ranged from 60-75% due to insufficient residence time in the FR for the reduction of the solid fuel by the OC. Low solid fuel conversions, 66-78%, were obtained due to the inefficiencies of the small cyclones. Ilmenite exhibited strong resistance to attrition.	[94]
95	TGA	NiO-$NiAl_2O_4$	Chinese Shenfu char	Char reacted rapidly with the OC at temperatures above 850°C. NiO was found to be a feasible OC for CLC because it maintained its reactivity over single and multicycle redox reactions, showed good recyclability and strong resistance to sintering while maintaining its porous structure.	[95]
96	TGA	NiO-$NiAl_2O_4$	Coal char	OC structure over after both single cycle and multicycle redox reactions without any evidence of sintering.	[96]
97	FxB	Fe_2O_3	Chinese Baorixile lignite	Fe_2O_3 fully reduced to Fe_3O_4 by coal pyrolysis and gasification products provided that the molar ratio of the carbon in char to the OC was 1:6. Purity of CO_2 in outlet gas was 85% during coal pyrolysis but increased to 95% during char gasification by steam. Rate limiting step was attributed to the char gasification reaction, which was much slower compared to the reaction between the char gasification intermediates and the OC. Addition of 10% K and Ca increased the gasification rates of	[97]

				the fuel, possibly by reducing the activation energy of the gasification reaction.	
98	FzB	Fe_2O_3-$MgAl_2O_4$	Mexican Cadereyta petroleum coke	Reaction rate was found to be highly dependent on steam and SO_2 concentrations as well as operating temperatures. The gasification rate of petroleum coke was enhanced in the presence of metal oxides. An OC inventory of less than 2000 kg/MW_{th} was estimated for a CLC process using the Fe-based OC.	[98]
99	CFB	Ni-NiO	Xuzhou bituminous coal	Thermodynamic analysis of the OC reduction reaction by the solid fuel indicated that NiO would be a suitable OC for CLC. Optimal operating temperature range was found to be 1050-1150°C in the AR and 900-950°C in the FR. Sulphur in coal converted to H_2S at lower temperatures and to SO_2 at higher temperatures.	[99]
100	MB	Fe_2O_3	Pittsburg #8 coal	A high H_2 production rate of 0.183kg H_2/kg coal was achieved. High temperatures, high OC flow rates and low oxygen demands were found to be optimal for high H_2 production rates. A high carbon conversion and CO_2 purity was obtained. Over 99% sulphur capture obtained through the addition of CaO to the OC. Production of NO_x was below detectable limits.	[100]
101	TGA	CuO	Sub-bituminous Powder River Basin coal Wood Low density polyethylene	Results strongly supported the use of CuO-based OCs for CLC. CuO reduction was found to start at temperatures as low as 500°C. Highly reactive solid fuels containing a large amount of volatile matter would be the desired type of fuel for the	[101]

				development of CLC using solid fuels.	
102	FzB	Fe_2O_3-Al_2O_3	Lignite	Various OC preparation methods such as freeze granulation, spray drying, mechanical mixing and impregnation were compared. For large scale OC production, the favourable preparation methods were determined to be freeze granulation and spray drying when considering the productivity, preparation duration, physical and chemical characteristics as well as reactivity.	[102]
103	FzB	Iron ore Limonite	Yallourn brown coal	Limonite showed the most promising results for use in a CLC process with Victorian brown coal because of its high reactivity and porosity. No agglomeration was detected over the duration of the experiments.	[103]
104	FzB	Sol-gel derived Fe_2O_3-Al_2O_3	Xiao Longtan lignite	A highly reactive OC was synthesized using the sol-gel process. High steam concentrations were found to enhance the char gasification rates. The presence of the OC also increased the char gasification rates. An oxygen carrier inventory of 600 kg/MW_{th} was estimated to enable 99% char combustion to be obtained using the sol-gel derived Fe_2O_3-Al_2O_3.	[104]
105	CFB	Bauxite waste	El Bierzo anthracite Terual lignite	In the FR, the fraction of vaporized mercury from coal depended on the reactor temperature and coal type, which increased with increasing temperatures. Mercury was predominantly emitted in the gas phase as Hg^0. In the AR, mercury was mainly emitted as Hg^{2+}.	[105]

				Although there was a significant decrease in the Hg emissions here relative to that obtained in conventional combustion, measures should be taken to further reduce the amount of Hg^0 present in the CO_2 stream.	
106	CFB	Spanish iron ore	El Bierzo anthracite El Cerrejon bituminous coal Terual lignite	Highest combustion efficiency obtained using iron ore compared to ilmenite and bauxite waste. CaO in the iron ore was capable of removing sulphur during the first few hours of operation.	[106]
107	FzB TGA	Commercial Fe_2O_3 mixed with: 20 wt% CuO 20 wt% Mn_2O_3 20 wt% NiO	Yallourn brown coal	Bimetallic OCs were synthesized. All synthetic OCs showed enhanced performance and reactivity over Fe_2O_3. Fe_2O_3 impregnated with NiO had the highest CO_2 conversion efficiency. The viability of generating synthetic OCs need to be considered from an economic point of view.	[107]
108	TGA	NiO CuO	Loy Yang brown coal	At 950°C, CuO could not reoxidize to its original state due to sintering. Hence, an operating temperature of 800°C was chosen when using CuO. A weight loss of 4.4-7.5% was detected after each redox cycle when using NiO but no weight loss was detected when using CuO. The use of CuO resulted in a greater extent of coal combustion relative to NiO.	[108]
109	TGA FzB	Fe_2O_3	Loy Yang brown coal	The OC particle size range of 100-150 µm yielded the best carbon conversion and this increased with increasing temperatures and CO_2 concentrations.	[109]
110	TGA	NiO	Loy Yang	A weight loss of 4.4-7.5% was	[110]

			brown coal	detected after each redox cycle using the NiO OC. 67% coal combustion was achieved. Minimal agglomeration between coal ash and NiO observed due to the low ash content in the coal.	
111	TGA	Fe_2O_3	Loy Yang brown coal	Study on the effect of operating conditions on the performance of a CLC system was done using Aspen Plus modelling. The general trends predicted by the model agreed with the results from literature.	[111]
112	FzB	Fe_2O_3	Hambach lignite char	Two models were developed to describe the gasification rates of lignite char. For temperatures below 850°C, an excellent agreement was found between the predictions by the model and the experimental results. Gasification kinetics of the lignite char was significantly faster in the presence of the OC due to the rapid oxidation of CO to CO_2, removing CO and maintaining a higher mole fraction of CO_2 in the gas mixture around the char particle.	[112]
113	CFB	$CuO-Al_2O_3$	Rhenish lignite dust	Study of a CLC system having a two-stage FR was undertaken with a solids circulation rate of 17-45 kg/m^2s. The two-stage FR design worked well, with 94% CO_2 concentration obtained in the flue gas.	[113]
114	CFB	$CuO-Al_2O_3$	Rhenish lignite dust	Using a two-stage FR, the simulation results showed that the fuel did not mix with the OC bed material in the lower stage of the FR. This led to the detection of large quantities of combustible gases in the flue gas stream of the first FR stage.	[114]

115	CFB	Australian ilmenite	Rhenish lignite dust	Study was done using a CFB configuration with a two-stage FR. The two-stage FR performed well, achieving over 90% CO_2 concentration in the flue gas stream. A solids circulation rate between 56-70 kg/m^{2}s was required. Only 1.5-6.5 wt% of the fixed carbon in the coal was detected in the AR.	[115]
116	TGA FzB	Iron ore mixed with: 5 wt% Mn_2O_3 10 wt% Mn_2O_3 20 wt% Mn_2O_3	Yallourn brown coal	Study on the performance of Mn_2O_3-Fe_2O_3 OCs prepared via physical mixing and impregnation. Mn_2O_3 had a positive effect on the performance of Fe_2O_3 in terms of the reactivity, carbon conversion and CO_2 yield, which improved with increasing Mn_2O_3 loading contents.	[116]

References

1. Bao, J., Z. Li, and N. Cai, *Interaction between iron-based oxygen carrier and four coal ashes during chemical looping combustion.* Applied Energy, 2014. **115**: p. 549-558.
2. Wang, B., C. Gao, W. Wang, F. Kong, and C. Zheng, *TGA-FTIR investigation of chemical looping combustion by coal with CoFe2O4 combined oxygen carrier.* Journal of Analytical and Applied Pyrolysis, 2014. **105**: p. 369-378.
3. Arjmand, M., H. Leion, T. Mattisson, and A. Lyngfelt, *Investigation of different manganese ores as oxygen carriers in chemical-looping combustion (CLC) for solid fuels.* Applied Energy, 2014. **113**(0): p. 1883-1894.
4. Bao, J., Z. Li, and N. Cai, *Experiments of char particle segregation effect on the gas conversion behavior in the fuel reactor for chemical looping combustion.* Applied Energy, 2014. **113**: p. 1874-1882.
5. Markström, P., C. Linderholm, and A. Lyngfelt, *Operation of a 100kW chemical-looping combustor with Mexican petroleum coke and Cerrejón coal.* Applied Energy, 2014. **113**: p. 1830-1835.
6. Luo, S., S. Bayham, L. Zeng, O. McGiveron, E. Chung, A. Majumder, and L.-S. Fan, *Conversion of metallurgical coke and coal using a Coal Direct Chemical Looping (CDCL) moving bed reactor.* Applied Energy, 2014. **118**: p. 300-308.
7. Ksepko, E., *Sewage sludge ash as an alternative low-cost oxygen carrier for chemical looping combustion.* Journal of Thermal Analysis and Calorimetry, 2014. **116**(3): p. 1395-1407.
8. Zhang, S., Shen, L., Gu, H., Liu, W. & Ge, H., *Chemical-looping combustion of coal in interconnected fluidized bed using Na-loaded iron ore as oxygen carrier*. Huagong Xuebao/CIESC Journal, 2013. **64**(11): p. 4187-4195.
9. Di, H., Wang, C., Zhang, J., Zhang, S. & Huang, F. , *Study on cycling performance of coal/straw blending chemical looping combustion with oxygen carrier Fe2O3.* Dongli Gongcheng Xuebao/Journal of Chinese Society of Power Engineering, 2013. **33**(11): p. 902-906.
10. Abad, A., J. Adánez, L.F. de Diego, P. Gayán, F. García-Labiano, and A. Lyngfelt, *Fuel reactor model validation: Assessment of the key parameters affecting the chemical-looping combustion of coal.* International Journal of Greenhouse Gas Control, 2013. **19**: p. 541-551.
11. Mendiara, T., A. Abad, L. de Diego, F. García-Labiano, P. Gayán, and J. Adánez, *Biomass combustion in a CLC system using an iron ore as an oxygen carrier.* International Journal of Greenhouse Gas Control, 2013. **19**: p. 322-330.
12. Zhang, S., R. Xiao, Y. Yang, and L. Chen, *CO2 Capture and Desulfurization in Chemical Looping Combustion of Coal with a CaSO4 Oxygen Carrier.* Chemical Engineering & Technology, 2013. **36**(9): p. 1469-1478.
13. Azis, M.M., H. Leion, E. Jerndal, B.M. Steenari, T. Mattisson, and A. Lyngfelt, *The Effect of Bituminous and Lignite Ash on the Performance of Ilmenite as Oxygen Carrier in Chemical‐Looping Combustion.* Chemical Engineering & Technology, 2013. **36**(9): p. 1460-1468.
14. Wang, B., H. Zhao, Y. Zheng, Z. Liu, and C. Zheng, *Chemical looping combustion of petroleum coke with CuFe2O4 combined oxygen carrier.*
15. Saucedo, M.A., J.Y. Lim, J.S. Dennis, and S.A. Scott, *CO2-gasification of a lignite coal in the presence of an iron-based oxygen carrier for chemical-looping combustion.* Fuel, 2014. **127**: p. 186-201.

16. Song, T., L. Shen, W. Guo, D. Chen, and J. Xiao, *Enhanced reaction performance with hematite/Ca2Al2SiO7 oxygen carrier in chemical looping combustion of coal.* Industrial & Engineering Chemistry Research, 2013. **52**(28): p. 9573-9585.
17. Zhang, S.-., Gu, H.-., Shen, L.-. & Xiao, J. , *Chemical looping combustion of coal with hematite oxygen carrier improved with potassium.* Kung Cheng Je Wu Li Hsueh Pao/Journal of Engineering Thermophysics, 2012. **33**(9): p. 1627-1630.
18. Gu, H., L. Shen, J. Xiao, S. Zhang, T. Song, and D. Chen, *Iron ore as oxygen carrier improved with potassium for chemical looping combustion of anthracite coal.* Combustion and Flame, 2012. **159**(7): p. 2480-2490.
19. Saha, C. and S. Bhattacharya, *Chemical looping combustion of low-ash and high-ash low rank coals using different metal oxides - A thermogravimetric analyser study.* Fuel, 2012. **97**: p. 137-150.
20. Wang, B.W., H.B. Zhao, Y. Zheng, Z.H. Liu, R. Yan, and C.G. Zheng, *Chemical looping combustion of a Chinese anthracite with Fe2O3-based and CuO-based oxygen carriers.* Fuel Processing Technology, 2012. **96**: p. 104-115.
21. Wang, B., Zhao, H., Zheng, Y., Liu, Z., Zheng, C. & Yan, R. , *Effect of inert support Al2O3 on the chemical looping combustion of coal with Fe2O3 and CuO-based oxygen carrier.* Zhongguo Dianji Gongcheng Xuebao/Proceedings of the Chinese Society of Electrical Engineering, 2011. **31**(32): p. 53-61.
22. Cuadrat, A., A. Abad, F. García-Labiano, P. Gayán, L. De Diego, and J. Adánez, *The use of ilmenite as oxygen-carrier in a 500W< sub> th</sub> Chemical-Looping Coal Combustion unit.* International Journal of Greenhouse Gas Control, 2011. **5**(6): p. 1630-1642.
23. Chen, D., Shen, L., Xiao, J., Song, T., Gu, H., Zhang, S. , *Experiments on chemical-looping combustion of coal with cement-decorated iron ore as oxygen carrier.* Zhongguo Dianji Gongcheng Xuebao/Proceedings of the Chinese Society of Electrical Engineering, 2013. **33**(20): p. 40-45.
24. Thunman, H., F. Lind, C. Breitholtz, N. Berguerand, and M. Seemann, *Using an oxygen-carrier as bed material for combustion of biomass in a 12-MW< sub> th</sub> circulating fluidized-bed boiler.* Fuel, 2013. **113**: p. 300-309.
25. Cheng, Y., Liu, Y., Tian, H., Guo, Q., *Chemical-looping gasification reaction characteristics and mechanism of coal and Fe-based composite oxygen carriers.* Huagong Xuebao/CIESC Journal, 2013. **64**(7): p. 2587-2595.
26. Song, T., L. Shen, S. Zhang, D. Chen, and J. Xiao, *Performance of hematite/Ca2Al2SiO7 oxygen carrier in chemical looping combustion of coal.* Industrial & Engineering Chemistry Research, 2013. **52**(22): p. 7350-7361.
27. Gu, H.-M., Wu, J.-H., Shen, L.-H., Xiao, J., *Chemical looping combustion of coal in interconnected fluidized bed with Nio/Al2O3 oxygen carrier.* Ranliao Huaxue Xuebao/Journal of Fuel Chemistry and Technology, 2013. **41**(6): p. 649-656.
28. Song, T., Chen, D.-Q., Zhang, H.-F., Shen, L.-H., Xiao, J., *Characterization of anthracite in chemical looping combustion with iron.* Kung Cheng Je Wu Li Hsueh Pao/Journal of Engineering Thermophysics, 2013. **34**(6): p. 1179-1183.
29. Luo, M., S. Wang, L. Wang, M. Lv, L. Qian, and H. Fu, *Experimental investigation of co-combustion of coal and biomass using chemical looping technology.* Fuel processing technology, 2013. **110**: p. 258-267.
30. Yu, Z., C. Li, X. Jing, Q. Zhang, Y. Fang, J. Zhao, and J. Huang, *Effects of CO2 Atmosphere and K2CO3 Addition on the Reduction Reactivity, Oxygen Transport Capacity, and Sintering of CuO and Fe2O3 Oxygen Carriers in Coal Direct Chemical Looping Combustion.* Energy & Fuels, 2013. **27**(5): p. 2703-2711.

31. Gu, H., Wu, J., Shen, L. & Xiao, J., *Defluidization of iron-based oxygen carrier during chemical looping combustion of coal in continuous reactor.* Dongnan Daxue Xuebao (Ziran Kexue Ban)/Journal of Southeast University (Natural Science Edition), 2013. **43**(3): p. 531-535.
32. Kim, H.R., D. Wang, L. Zeng, S. Bayham, A. Tong, E. Chung, M.V. Kathe, S. Luo, O. McGiveron, and A. Wang, *Coal direct chemical looping combustion process: Design and operation of a 25-kWth sub-pilot unit.* Fuel, 2013. **108**: p. 370-384.
33. Siriwardane, R., H. Tian, T. Simonyi, and J. Poston, *Synergetic effects of mixed copper–iron oxides oxygen carriers in chemical looping combustion.* Fuel, 2013. **108**: p. 319-333.
34. Bayham, S.C., H.R. Kim, D. Wang, A. Tong, L. Zeng, O. McGiveron, M.V. Kathe, E. Chung, W. Wang, and A. Wang, *Iron-based coal direct chemical looping combustion process: 200-h continuous operation of a 25-kWth subpilot unit.* Energy & Fuels, 2013. **27**(3): p. 1347-1356.
35. Song, T., M. Zheng, L. Shen, T. Zhang, X. Niu, and J. Xiao, *Mechanism Investigation of Enhancing Reaction Performance with CaSO4/Fe2O3 Oxygen Carrier in Chemical-Looping Combustion of Coal.* Industrial & Engineering Chemistry Research, 2013. **52**(11): p. 4059-4071.
36. Saha, C., S. Zhang, K. Hein, R. Xiao, and S. Bhattacharya, *Chemical looping combustion (CLC) of two Victorian brown coals–Part 1: Assessment of interaction between CuO and minerals inherent in coals during single cycle experiment.* Fuel, 2012.
37. Zhang, S., Shen, L., Xiao, J., Gu, H. & Song, T. , *Influence of alkaline earth metals of Ca loaded on iron ore in chemical-looping combustion of coal.* Zhongguo Dianji Gongcheng Xuebao/Proceedings of the Chinese Society of Electrical Engineering, 2013. **33**(2): p. 39-45.
38. Mendiara, T., F. García-Labiano, P. Gayán, A. Abad, L. de Diego, and J. Adánez, *Evaluation of the use of different coals in Chemical Looping Combustion using a bauxite waste as oxygen carrier.* Fuel, 2013. **106**: p. 814-826.
39. Abad, A., A. Cuadrat, T. Mendiara, F. García-Labiano, P. Gayán, L. de Diego, and J. Adánez, *Low-Cost Fe-Based Oxygen Carrier Materials for the i G-CLC Process with Coal. 2.* Industrial & Engineering Chemistry Research, 2012. **51**(50): p. 16230-16241.
40. Mendiara, T., R. Pérez, A. Abad, L. de Diego, F. García-Labiano, P. Gayan, and J. Adanez, *Low-Cost Fe-Based Oxygen Carrier Materials for the i G-CLC Process with Coal. 1.* Industrial & Engineering Chemistry Research, 2012. **51**(50): p. 16216-16229.
41. Shi, S., Dong, C., Qin, W., Wang, L., Li, W. & Yang, Y. , *Experimental and theoretical study of Fe2O3/coal ash oxygen carrier in CLC system.* Huagong Xuebao/CIESC Journal, 2012. **63**(12): p. 4010-4018.
42. Azimi, G., M. Keller, A. Mehdipoor, and H. Leion, *Experimental evaluation and modeling of steam gasification and hydrogen inhibition in Chemical-Looping Combustion with solid fuel.* International Journal of Greenhouse Gas Control, 2012. **11**: p. 1-10.
43. Guo, Q.J., J.S. Zhang, and H.J. Tian, *Recent Advances in CaSO4 Oxygen Carrier for Chemical-Looping Combustion (CLC) Process.* Chemical Engineering Communications, 2012. **199**(11): p. 1463-1491.
44. Rydén, M., C. Linderholm, P. Markström, and A. Lyngfelt, *Release of Gas-Phase O_2 from Ilmenite during Chemical-Looping Combustion Experiments.* Chemical Engineering & Technology, 2012. **35**(11): p. 1968-1972.

45. Zhang, S.-., Shen, L.-., Xiao, J., Gu, H.-. & Song, T. , *Catalytic combustion of coal using alkali and transition metals loaded on iron ore oxygen carrier.* Ranliao Huaxue Xuebao/Journal of Fuel Chemistry and Technology, 2012. **40**(10): p. 1179-1187.
46. Xiao, R., L.Y. Chen, C. Saha, S. Zhang, and S. Bhattacharya, *Pressurized chemical-looping combustion of coal using an iron ore as oxygen carrier in a pilot-scale unit.* International Journal of Greenhouse Gas Control, 2012. **10**: p. 363-373.
47. Gu, H.-., Shen, L.-., Xiao, J., Zhang, S.-. & Song, T. , *Cycle experiments on chemical looping combustion of coal using potassium-improved iron ore as oxygen carrier.* Ranliao Huaxue Xuebao/Journal of Fuel Chemistry and Technology, 2012. **40**(8): p. 927-934.
48. Rubel, A., Y. Zhang, J.K. Neathery, and K.L. Liu, *Comparative Study of the Effect of Different Coal Fly Ashes on the Performance of Oxygen Carriers for Chemical Looping Combustion.* Energy & Fuels, 2012. **26**(6): p. 3156-3161.
49. Wang, S.Z., M. Luo, G.X. Wang, L.F. Wang, and M.M. Lv, *Analysis of Reactivity of a CuO-Based Oxygen Carrier for Chemical Looping Combustion of Coal.* Energy & Fuels, 2012. **26**(6): p. 3275-3283.
50. Saha, C., S. Zhang, R. Xiao, and S. Bhattacharya, *Chemical Looping Combustion (CLC) of two Victorian brown coals - Part 2: Assessment of interaction between CuO and minerals inherent in coals during multi cycle experiments.* Fuel, 2012. **96**: p. 335-347.
51. Arjmand, M., H. Leion, A. Lyngfelt, and T. Mattisson, *Use of manganese ore in chemical-looping combustion (CLC)-Effect on steam gasification.* International Journal of Greenhouse Gas Control, 2012. **8**: p. 56-60.
52. Yu, Z.L., C.Y. Li, Y.T. Fang, J.J. Huang, and Z.Q. Wang, *Reduction Rate Enhancements for Coal Direct Chemical Looping Combustion with an Iron Oxide Oxygen Carrier.* Energy & Fuels, 2012. **26**(4): p. 2505-2511.
53. Chen, D.-q., L.-h. Shen, J. Xiao, T. Song, H.-m. Gu, and S.-w. Zhang, *Experimental investigation of hematite oxygen carrier decorated with NiO for chemical-looping combustion of coal.* Journal of Fuel Chemistry and Technology, 2012. **40**(3): p. 267-272.
54. Sim, C.Y., T. Brown, Q. Chen, V. Sharifi, J. Swithenbank, J. Dennis, and S. Scott, *Particle characterisation in chemical looping combustion.* Chemical Engineering Science, 2012. **69**(1): p. 211-224.
55. Cuadrat, A., A. Abad, F. Garcia-Labiano, P. Gayan, L.F. de Diego, and J. Adanez, *Effect of operating conditions in Chemical-Looping Combustion of coal in a 500 W-th unit.* International Journal of Greenhouse Gas Control, 2012. **6**: p. 153-163.
56. Zhang, S., C. Saha, Y.C. Yang, S. Bhattacharya, and R. Xiao, *Use of Fe2O3-Containing Industrial Wastes As the Oxygen Carrier for Chemical-Looping Combustion of Coal: Effects of Pressure and Cycles.* Energy & Fuels, 2011. **25**(10): p. 4357-4366.
57. Teyssie, G., H. Leion, G.L. Schwebel, A. Lyngfelt, and T. Mattisson, *Influence of Lime Addition to Ilmenite in Chemical-Looping Combustion (CLC) with Solid Fuels.* Energy & Fuels, 2011. **25**(8): p. 3843-3853.
58. Wang, B.W., R. Yan, H.B. Zhao, Y. Zheng, Z.H. Liu, and C.G. Zheng, *Investigation of Chemical Looping Combustion of Coal with CuFe2O4 Oxygen Carrier.* Energy & Fuels, 2011. **25**(7): p. 3344-3354.
59. Bao-wen, W., W. Wei-shu, G. Chuan-chang, Z. Hai-bo, Z. Ying, and Z. Chu-guang. *TGA-FTIR investigation of the chemical looping combustion by coal with a CuO-Fe 2 O 3 combined oxygen carrier*. in *Electric Information and Control Engineering (ICEICE), 2011 International Conference on*. 2011. IEEE.

60. Wang, B.W., R. Yan, Y. Zheng, H.B. Zhao, and C.G. Zheng, *Mechanistic investigation of chemical looping combustion of coal with Fe2O3 oxygen carrier.* Fuel, 2011. **90**(7): p. 2359-2366.
61. Bao-wen, W., G. Chuan-chang, W. Wei-shu, Z. Hai-bo, Z. Ying, and Z. Chu-guang. *Investigation of Chemical Looping Combustion of Coal with Fe2O3 Oxygen Carrier*. in *Power and Energy Engineering Conference (APPEEC), 2011 Asia-Pacific*. 2011. IEEE.
62. Nakagaki, T., *Enhanced Hydrogen Production Process from Coal Integrated with CO2 Separation Using Dual Chemical Looping.* 10th International Conference on Greenhouse Gas Control Technologies, 2011. **4**: p. 324-332.
63. Keller, M., H. Leion, T. Mattisson, and A. Lyngfelt, *Gasification inhibition in chemical-looping combustion with solid fuels.* Combustion and Flame, 2011. **158**(3): p. 393-400.
64. Rubel, A., Y. Zhang, K. Liu, and J. Neathery, *Effect of Ash on Oxygen Carriers for the Application of Chemical Looping Combustion to a High Carbon Char.* Oil & Gas Science and Technology-Revue D Ifp Energies Nouvelles, 2011. **66**(2): p. 291-300.
65. Iggland, M., H. Leion, T. Mattisson, and A. Lyngfelt, *Effect of fuel particle size on reaction rate in chemical looping combustion.* Chemical Engineering Science, 2010. **65**(22): p. 5841-5851.
66. Siriwardane, R., H.J. Tian, D. Miller, G. Richards, T. Simonyi, and J. Poston, *Evaluation of reaction mechanism of coal-metal oxide interactions in chemical-looping combustion.* Combustion and Flame, 2010. **157**(11): p. 2198-2208.
67. Wenguang, X.R.Z.S.Z. and S.Q.Y. Yichao, *Pressurized chemical-looping combustion of coal: cyclic performance and characterization of iron ore oxygen carrier.* Journal of Southeast University (Natural Science Edition), 2010. **5**: p. 021.
68. Markstrom, P., N. Berguerand, and A. Lyngfelt, *The application of a multistage-bed model for residence-time analysis in chemical-looping combustion of solid fuel.* Chemical Engineering Science, 2010. **65**(18): p. 5055-5066.
69. Sun, X.Y., W.G. Xiang, S. Wang, W.D. Tian, X. Xu, Y.J. Xu, and Y.H. Xiao, *Investigation of Coal Fueled Chemical Looping Combustion Using Fe3O4 as Oxygen Carrier: Influence of Variables.* Journal of Thermal Science, 2010. **19**(3): p. 266-275.
70. Wang, B., Y. Zheng, Z. Liu, H. Zhao, C. Zheng, and R. Yan, *Investigation of chemical looping combustion of coal with Fe2O3-based combined oxygen carrier.* Journal of Engineering Thermophysics, 2010. **31**(8): p. 1427-1430.
71. Dennis, J.S. and S.A. Scott, *In situ gasification of a lignite coal and CO2 separation using chemical looping with a Cu-based oxygen carrier.* Fuel, 2010. **89**(7): p. 1623-1640.
72. Gu, H.-M., J.-H. Wu, J.-G. Hao, L.-H. Shen, and J. Xiao. *Experiments on chemical looping combustion of coal in interconnected fluidized bed using hematite as oxygen carrier*. in *Zhongguo Dianji Gongcheng Xuebao(Proceedings of the Chinese Society of Electrical Engineering)*. 2010. Chinese Society for Electrical Engineering.
73. Jiang, L., Zhao, H., Zhang, S., Wang, J. & Zheng, C., *Fe2O3/Al2O3 oxygen carriers for chemical looping combustion fueled by coal char.* Kung Cheng Je Wu Li Hsueh Pao/Journal of Engineering Thermophysics, 2010. **31**(6): p. 1053-1056.
74. Xiao, R., Q.L. Song, M. Song, Z.J. Lu, S.A. Zhang, and L.H. Shen, *Pressurized chemical-looping combustion of coal with an iron ore-based oxygen carrier.* Combustion and Flame, 2010. **157**(6): p. 1140-1153.
75. Brown, T.A., J.S. Dennis, S.A. Scott, J.F. Davidson, and A.N. Hayhurst, *Gasification and chemical-looping combustion of a lignite char in a fluidized bed of iron oxide.* Energy and Fuels, 2010. **24**(5): p. 3034-3048.

76. Shen, L.H., J.H. Wu, Z.P. Gao, and J. Xiao, *Characterization of chemical looping combustion of coal in a 1 kW(th) reactor with a nickel-based oxygen carrier.* Combustion and Flame, 2010. **157**(5): p. 934-942.
77. Dennis, J.S., C.R. Müller, and S.A. Scott, *In situ gasification and CO2 separation using chemical looping with a Cu-based oxygen carrier: Performance with bituminous coals.* Fuel, 2010. **89**(9): p. 2353-2364.
78. Xiao, R., Q.L. Song, S.A. Zhang, W.G. Zheng, and Y.C. Yang, *Pressurized Chemical-Looping Combustion of Chinese Bituminous Coal: Cyclic Performance and Characterization of Iron Ore-Based Oxygen Carrier.* Energy & Fuels, 2010. **24**: p. 1449-1463.
79. Zhang, J., C. Dong, L. Wang, and Y. Yang. *The interaction between HCl and Fe 2 O 3 during the chemical looping combustion of MSW*. in *Sustainable Power Generation and Supply, 2009. SUPERGEN'09. International Conference on*. 2009. IEEE.
80. Xlang, W., X. Sun, S. Wangt, W. Tian, X. Xu, Y. Xu, and Y. Xiao. *Investigation of Coal Fueled Chemical Looping Combustion Using Fe3O4 as Oxygen Carrier*. in *Proceedings of the 20th International Conference on Fluidized Bed Combustion*. 2010. Springer.
81. Berguerand, N. and A. Lyngfelt, *Chemical-Looping Combustion of Petroleum Coke Using Ilmenite in a 10 kWth Unit−High-Temperature Operation.* Energy & Fuels, 2009. **23**(10): p. 5257-5268.
82. Leion, H., E. Jerndal, B.-M. Steenari, S. Hermansson, M. Israelsson, E. Jansson, M. Johnsson, R. Thunberg, A. Vadenbo, T. Mattisson, and A. Lyngfelt, *Solid fuels in chemical-looping combustion using oxide scale and unprocessed iron ore as oxygen carriers.* Fuel, 2009. **88**(10): p. 1945-1954.
83. GAO, Z.-p., L.-h. SHEN, J. XIAO, M. ZHENG, and J.-h. WU, *Analysis of reactivity of Fe-based oxygen carrier with coal during chemical-looping combustion.* Journal of Fuel Chemistry and Technology, 2009. **37**(5): p. 513-520.
84. Siriwardane, R., H.J. Tian, G. Richards, T. Simonyi, and J. Poston, *Chemical-Looping Combustion of Coal with Metal Oxide Oxygen Carriers.* Energy & Fuels, 2009. **23**(8): p. 3885-3892.
85. WU, J., L. SHEN, J. XIAO, L. WANG, and J. HAO, *Chemical looping combustion of sawdust in a 10 kW_ (th) interconnected fluidized bed [J]*. Journal of the Chemical Industry and Engineering Society of China, 2009. **8**: p. 033.
86. Shen, L.H., J.H. Wu, Z.P. Gao, and J. Xiao, *Reactivity deterioration of NiO/Al2O3 oxygen carrier for chemical looping combustion of coal in a 10 kW(th) reactor.* Combustion and Flame, 2009. **156**(7): p. 1377-1385.
87. Lai-Hong, G.Z.-P.S. and X.J.W. Jia-Hua, *MULTICYCLE REDUCTION OF COAL AS FUEL FOR CHEMICAL-LOOPING COMBUSTION WITH Fe-BASED OXYGEN CARRIER.* Journal of Engineering Thermophysics, 2009. **7**: p. 048.
88. Rubel, A., K.L. Liu, J. Neathery, and D. Taulbee, *Oxygen carriers for chemical looping combustion of solid fuels.* Fuel, 2009. **88**(5): p. 876-884.
89. Shen, L.H., J.H. Wu, and J. Xiao, *Experiments on chemical looping combustion of coal with a NiO based oxygen carrier.* Combustion and Flame, 2009. **156**(3): p. 721-728.
90. Zhao, H., Liu, L., Xu, D., Zheng, C., Liu, G. & Jiang, L. , *NiO/NiAl2O4 oxygen carriers for chemical looping combustion fueled by coal.* Ranshao Kexue Yu Jishu/Journal of Combustion Science and Technology, 2009. **15**(1): p. 22-27.
91. Gao, Z.P., L.H. Shen, J. Xiao, C.J. Qing, and Q.L. Song, *Use of Coal as Fuel for Chemical-Looping Combustion with Ni-Based Oxygen Carrier.* Industrial & Engineering Chemistry Research, 2008. **47**(23): p. 9279-9287.

92. Yang, J.B., N.S. Cai, and Z.S. Li, *Hydrogen production from the steam-iron process with direct reduction of iron oxide by chemical looping combustion of coal char.* Energy & Fuels, 2008. **22**(4): p. 2570-2579.
93. Gao, Z., L. Shen, and J. Xiao, *Chemical looping combustion of coal based on NiO oxygen carrier.* JOURNAL OF CHEMICAL INDUSTRY AND ENGINEERING-CHINA-, 2008. **59**(5): p. 1242.
94. Berguerand, N. and A. Lyngfelt, *The use of petroleum coke as fuel in a 10kWth chemical-looping combustor.* International Journal of Greenhouse Gas Control, 2008. **2**(2): p. 169-179.
95. Zhao, H., L. Liu, B. Wang, D. Xu, L. Jiang, and C. Zheng, *Sol–gel-derived NiO/NiAl2O4 oxygen carriers for chemical-looping combustion by coal char.* Energy & Fuels, 2008. **22**(2): p. 898-905.
96. Zhao, H., Liu, L., Xu, D. & Zheng, C. *Study on Ni-based oxygen carriers for chemical looping combustion by coal char*. in *24th Annual International Pittsburgh Coal Conference*. 2007. Johannesburg, South Africa.
97. Yang, J.B., N.S. Cai, and Z.S. Li, *Reduction of iron oxide as an oxygen carrier by coal pyrolysis and steam char gasification intermediate products.* Energy and Fuels, 2007. **21**(6): p. 3360-3368.
98. Leion, H., T. Mattisson, and A. Lyngfelt, *The use of petroleum coke as fuel in chemical-looping combustion.* Fuel, 2007. **86**(12–13): p. 1947-1958.
99. Shen, L., M. Zheng, J. Xiao, H. Zhang, and R. Xiao, *Chemical looping combustion of coal in interconnected fluidized beds.* Science in China Series E: Technological Sciences, 2007. **50**(2): p. 230-240.
100. Gupta, P., L.G. Velazquez-Vargas, F. Li, and L.-S. Fan. *Chemical looping reforming-an efficient process for the production of hydrogen from coal*. in *American Institute of Chemical Engineers Annual Conference, San Francisco, CA*. 2006.
101. Cao, Y., B. Casenas, and W.-P. Pan, *Investigation of Chemical Looping Combustion by Solid Fuels. 2. Redox Reaction Kinetics and Product Characterization with Coal, Biomass, and Solid Waste as Solid Fuels and CuO as an Oxygen Carrier.* Energy & Fuels, 2006. **20**(5): p. 1845-1854.
102. Guo, L., H.-b. Zhao, J.-c. Ma, D.-f. Mei, and C.-g. Zheng, *Comparison of large-scale production methods of Fe_2O_3/Al_2O_3 oxygen carriers for Chemical-Looping Combustion.* Chemical Engineering Technology, 2014. **37**(7): p. 1211-1219.
103. Karlsson, T., *A study of three iron-based oxygen carriers in a Chemical Looping Combustion process with a Victorian brown coal*. 2014, Chalmers University of Technology: Gothenburg, Sweden.
104. Mei, D., A. Abad, H. Zhao, J. Adanez, and C. Zheng, *On a highly reactive Fe_2O_3/Al_2O_3 oxygen carrier for in-situ gasification Chemical Looping Combustion.* Energy and Fuels, 2014. **28**(11): p. 7043-7052.
105. Mendiara, T., M.T. Izquierdo, A. Abad, P. Gayan, F. Garcia-Labiano, L.F.d. Diego, and J. Adanez, *Mercury release and speciation in Chemical Looping Combustion of coal.* Energy and Fuels, 2014. **28**(4): p. 2786-2794.
106. Mendiara, T., L.F.d. Diego, F. García-Labiano, P. Gayán, A. Abad, and J. Adánez, *On the use of a highly reactive iron ore in Chemical Looping Combustion of different coals.* Fuel, 2014. **126**: p. 239-249.
107. Rajendran, S., S. Zhang, R. Xiao, and S. Bhattacharya, *Use of synthetic oxygen carriers for Chemical Looping Combustion of Victorian brown coal.* Proceedings of the Combustion Institute, 2014. **In Press, Corrected Proof**.

108. Saha, C. and S. Bhattacharya, *Comparison of CuO and NiO as oxygen carrier in Chemical Looping Combustion of a Victorian brown coal.* International Journal of Hydrogen Energy, 2011. **36**: p. 12048-12057.
109. Saha, C. and S. Bhattacharya, *Experimental investigation of fluidized bed chemical looping combustion of Victorian brown coal using hematite.* Journal of Environmental Chemical Engineering, 2014. **2**: p. 1642–1654.
110. Saha, C., B. Roy, and S. Bhattacharya, *Chemical looping combustion of Victorian brown coal using NiO oxygen carrier.* International Journal of Hydrogen Energy, 2011. **36**: p. 3253-3259.
111. Saha, C., A.I.A. Raisi, and S. Bhattacharya, *Coal direct chemical looping combustion: Experimental investigation and assesment of operating conditions*, in *Chemeca 2011: Engineering a Better World*. 2011: NSW, Australia. p. 1852-1861.
112. Saucedo, M.A., J.S. Dennis, and S.A. Scott, *Modelling rates of gasification of a char particle in chemical looping combustion.* Proceedings of the Combustion Institute, 2014. **In Press, Corrected Proof**.
113. Thon, A., M. Kramp, E.-U. Hartge, S. Heinrich, and J. Werther. *Operation of a coupled fluidized bed system for Chemical Looping Combustion of solid fuels with a synthetic Cu-based oxygen carrier*. in *The 14th International Conference on Fluidization - From Fundamentals to Products*. 2013. Noordwijkerhout, The Netherlands.
114. Kramp, M., A. Thon, E.-U. Hartge, S. Heinrich, and J. Werther. *Simulation of the Chemical Looping Combustion process of coal with a synthetic Cu-based oxygen carriers*. in *The 14th International Conference on Fluidization - From Fundamentals to Products*. 2013. Noordwijkerhout, The Netherlands.
115. Thon, A., M. Kramp, E.-U. Hartge, S. Heinrich, and J. Werther, *Operational experience with a system of coupled fluidized beds for Chemical Looping Combustion of solid fuels using ilmenite as oxygen carrier.* Applied Energy, 2014. **118**: p. 309-317.
116. Zhang, S., S. Rajendran, R. Xiao, and S. Bhattacharya, *Chemical-Looping Combustion of Victorian brown coal using mixed oxygen carriers of iron and manganese oxides*, in *Chemeca 2013: Challenging Tomorrow*. 2013: Brisbane, Qld. p. 130-136.